Spring 1-1-2021

Model-free Optimization of Trajectory And Impedance Parameters on Exercise Robots With Applications To Human Performance And Rehabilitation

Humberto De las casas zolezzi
Cleveland State University

MODEL-FREE OPTIMIZATION OF TRAJECTORY AND IMPEDANCE PARAMETERS ON EXERCISE ROBOTS WITH APPLICATIONS TO HUMAN PERFORMANCE AND REHABILITATION

HUMBERTO DE LAS CASAS ZOLEZZI

Master of Science in Mechanical Engineering

Cleveland State University

August 2017

Bachelor of Science in Mechatronics Engineering

Pontificia Universidad Catolica del Peru

December 2013

submitted in partial fulfillment of requirements for the degree

DOCTOR OF PHILOSOPHY IN MECHANICAL ENGINEERING

at the

CLEVELAND STATE UNIVERSITY

MAY 2021

We hereby approve this dissertation for

HUMBERTO DE LAS CASAS ZOLEZZI

Candidate for the Doctor of Philosophy in Mechanical Engineering degree for the

Department of Mechanical Engineering and

CLEVELAND STATE UNIVERSITY'S

College of Graduate Studies by

Hanz Richter, Ph.D, Dissertation Committee Chairperson
Department of Mechanical Engineering

Antonie van den Bogert, Ph.D, Dissertation Committee Member
Department of Mechanical Engineering

Eric Schearer, Ph.D, Dissertation Committee Member
Department of Mechanical Engineering

Kenneth Sparks, Ph.D, Dissertation Committee Member
Department of Health and Human Performance

Douglas A Wajda, Ph.D, Dissertation Committee Member
Department of Health and Human Performance

Date of Defense: March 16, 2021

This student has fulfilled all requirements for the
Doctor of Philosophy in Engineering degree.

Chandra Kothapalli, Ph.D, Doctoral Program Director

ACKNOWLEDGMENTS

I thank, above all, God. His blessing has always accompanied me allowing me to share, learn, and connect with incredible people (family, professors, and friends) to whom I owe my present and future. It is amazing how many people cross our lives. But it is more amazing how we grow up personally and professionally thanks to each of them. In the end, we are the results of the people we met.

I want to thank the professors at Cleveland State University, and especially my committee members whom I chose not only for their great knowledge and experience, but also because of what they have meant to me as inspiration, perseverance, and hard work. Dr. Richter, thank you for accepting me as your student, and thank you especially for your patience and be always guiding me on the right path. I promise you, I will never disappoint you and you will be very proud of the person that you helped me become. Thank you so much, it is simply impossible to express the enormous gratitude and appreciation I have for you. Dr. van den Bogert, thank you for your willingness to help me with everything I needed. Despite not having all the answers, you never had your door closed or an unanswered email for your students. I will never forget searching together for the answers on the internet and old paper, as well as I will never forget your patience and great intelligence. Dr. Schearer, thank you for so many funny anecdotes during your very creative classes. I will never forget my first graduate-level class, Intelligent Control Systems, where I realized this journey was not going to be only academic but also very fun. Also thank you for the way you promoted teamwork during the interactive sessions where I learned a lot working with you and my classmates. Please, don't stop doing it. Dr. Sparks, thank you for your fun classes and wise advices. I feel blessed to have had the opportunity to be your student. I learned and laughed so much under your guidance. You are an

amazing teacher and your patience, charisma, and passion will never be forgotten by the lucky students you have mentored. Dr. Wajda, thank you for inspiring me as a multidisciplinary engineer. Being good in one area is not easy, but being good in multiple areas of science and engineering is just extraordinary. Thank you very much for such that inspiration and your constructive criticism. I hope to work again with each of you one day. Being your collaborator would be a tremendous honor.

Thank you to my labmates, who more than that are my friends. Thank you Poya Khalaf, Amin Ghorbanpour, Erivelton Gualter dos Santos, Holly Warner, and Santino Bianco for your support, teachings, and advices. I hope we will work together again one day.

Finally, I want to thank my complete family. They are the best gift that God has been able to give me. Thank you to my wife Laura for always being there; to my father Humberto for being my strongest motivation, support, and example to follow; to my mother Carmen for always being in my care; to my siblings Marife and Alonso for inspiring encouragement and optimism; to my grandparents for taking care of me from heaven. Thanks to all of you for making this possible by giving me love, patience, and support throughout this time. No word can define how grateful and how much love I have for each of you.

MODEL-FREE OPTIMIZATION OF TRAJECTORY AND IMPEDANCE PARAMETERS ON EXERCISE ROBOTS WITH APPLICATIONS TO HUMAN PERFORMANCE AND REHABILITATION

HUMBERTO DE LAS CASAS ZOLEZZI

ABSTRACT

This dissertation focuses on the study and optimization of human training and its physiological effects through the use of advanced exercise machines (AEMs). These machines provide an invaluable contribution to advanced training by combining exercise physiology with technology. Unlike conventional exercise machines (CEMs), AEMs provide controllable trajectories and impedances by using electric motors and control systems. Therefore, they can produce various patterns even in the absence of gravity. Moreover, the ability of the AEMs to target multiple physiological systems makes them the best available option to improve human performance and rehabilitation.

During the early stage of the research, the physiological effects produced under training by the manual regulation of the trajectory and impedance parameters of the AEMs were studied. Human dynamics appear as not only complex but also unique and time-varying due to the particular features of each person such as its musculoskeletal distribution, level of fatigue, fitness condition, hydration, etc. However, the possibility of the optimization of the AEM training parameters by using physiological effects was likely, thus the optimization objective started to be formulated.

Some previous research suggests that a model-based optimization of advanced training is complicated for real-time environments as a consequence of the high level of

complexity, computational cost, and especially the many unidentifiable parameters. Moreover, a model-based method differs from person to person and it would require periodic updates based on physical and psychological variations in the user. Consequently, we aimed to develop a model-free optimization framework based on the use of Extremum Seeking Control (ESC).

ESC is a non-model based controller for real-time optimization which its main advantage over similar controllers is its ability to deal with unknown plants. This framework uses a physiological effect of training as bio-feedback. Three different frameworks were performed for single-variable and multi-variable optimization of trajectory and impedance parameters. Based on the framework, the objective is achieved by seeking the optimal trajectory and/or impedance parameters associated with the orientation of the ellipsoidal path to be tracked by the user and the stiffness property of the resistance by using weighted measures of muscle activations.

TABLE OF CONTENTS

LIST OF TABLES

LIST OF FIGURES

CHAPTER I

INTRODUCTION

1.1 Motivation

Today's demanding society forces human beings to be in a continuous search for better and faster results mainly aimed at education, fitness performance, and health. Human Performance Improvement (HPI) refers to the tools used to adjust physical and psychological factors to achieve higher levels of human function. HPI has been a popular area widely used in different fields from education to health and fitness. HPI in education contributes to long-run increases in productivity. The key reason for education demanding is the fact that education affects earning generating interest from both employers and employees [43]. On the other side, HPI has also shown popularity and beneficial contributions to the health and fitness industry. HPI focused on Conditioning For Strength And Human Performance (CSHP) includes applications for leisure, rehabilitation recovers, and job requirements. For instance, some jobs such as firefighters, police, prison guards, and military are physically demanding requiring high-efficiency training for personal welfare [132].

This work focuses in CSHP aiming to enhance current exercise procedures by providing more efficient and safer training. Only in the US, over 450 thousand injuries were reported as a result of exercise training in the year 2019 [65]. Simi-

larly, more than 114 deaths were reported up to the year 2007 [86] estimating that more than 2 of 5 gym users have had at least one injury while working out [118]. Therefore, safety enhancements for CSHP could be beneficial to considerably reduce the number of reported cases associated with injuries and deaths as a result of the exercise training. Additionally, the high demand for the health and fitness industries generates a high economic impact worldwide. Only in North America, 71.06 billion dollars has been accounted for in the sports market during the year of 2018 [142] (see Figure 1). This market value includes, but is not limited to, gate revenues, media rights, merchandising, sponsorship, and exercise equipment . These latter segments (sponsorship and exercise equipment) are the ones with the largest share as a result of their largest contribution to athletes' performance, sportsmanship, and equipment developments. The market size for fitness equipment was estimated at more than $2.5 billion with an estimated compound annual growth rate of 5.01% by 2020 [52, 51]. The market of rehabilitation systems and equipment has also evidenced promising economic impacts. Only in the United States, there are over 38,000 clinics providing services such as physical therapy, occupational therapy, speech therapy, and audiology supporting this massive market with more than 30 billion dollars in market share and a growth forecast of 7% average annual pace [130, 69] (see Figure 2). Finally, in addition to the economic impact, CSHP can be of significant benefit to people experiencing chronic illness, obesity, or reduced motor abilities. This additional strong motivation is priceless providing invaluable contributions to these people's lives and their families.

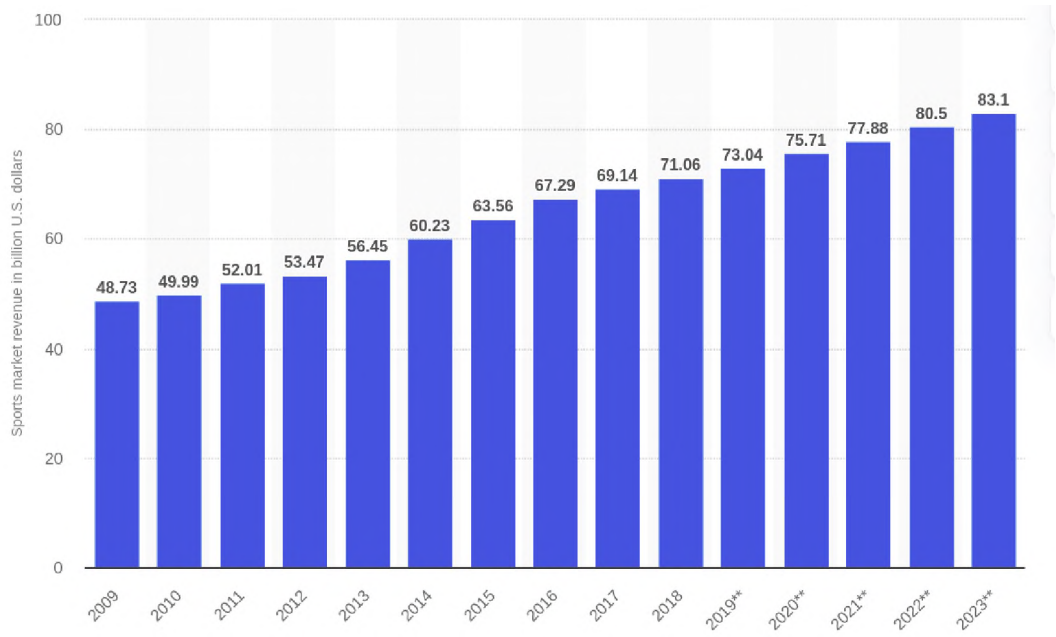

Figure 1: North America sports market size from 2009 to 2023 (in billion U.S. dollars) [142].

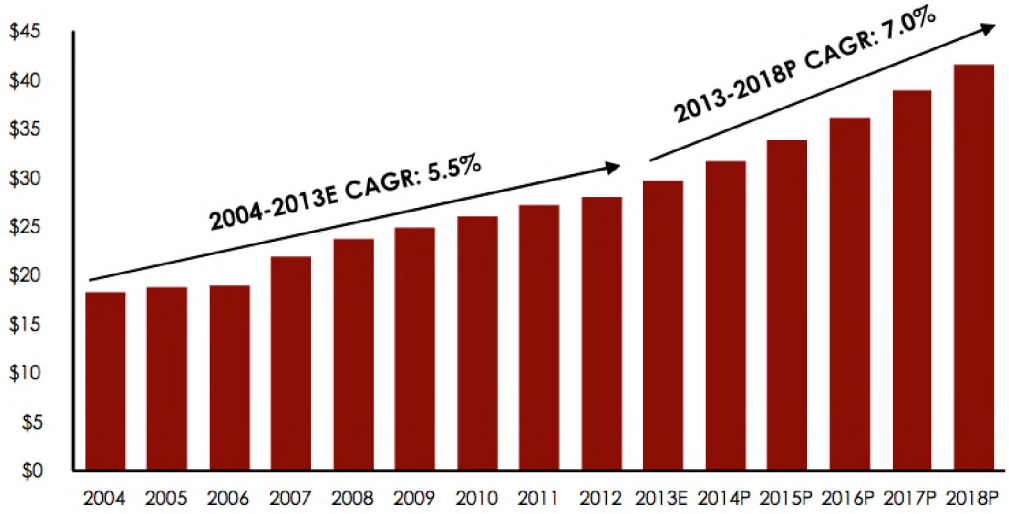

Figure 2: North America physical therapy market size from 2004 to 2018 (in billion U.S. dollars) [130].

It is important to highlight that the greatest developments in CSHP have been accomplished through the interaction between humans and machines (human-machine interaction or HMI). These developments have become highly relevant be-

cause of their growth potential and opportunities oriented toward human performance and rehabilitation. Some applications include interactive environments using advanced exercise machines (AEMs), virtual reality, and information technology as a means of measuring, supporting, and enhancing human exercise and rehabilitation practices [77, 76, 58]. This technology aims to improve the strength, flexibility, and/or manipulation skills of people with disabilities as well as high-level athletes.

One of the first robots aiding exercise and rehabilitation was the MIT-Manus (MITM) (see Figure 3). This system was introduced in 1991 to study and quantify the potential of robot assistance in rehabilitation. Since then, MITM has assisted thousands of stroke patients in improving their reduced motor skills. The subject using this robot fits his or her lower arm and wrist into a brace attached to the robot arm. Then, this subject is required to follow a trajectory provided by the system. The activity integrating the human and robot seems to help the subject by developing new neural connections that eventually support the re-learning process of the muscles [62, 61]. Several expansions and new configurations following similar approaches to the concept of the MITM have been developed over the years. For instance, robots for upper-limb rehabilitation [96, 120] providing an increased efficiency by achieving partial/fully recovery on disable people through robot-assisted technology [16, 129]; exoskeleton for neurorehabilitation [14] overcoming the single joint control of rehabilitation patients by allowing the full control of the arm kinematics; and advanced exercise machines [10, 78] enhancing the exercise performance by empowering different training patterns [151, 30].

Figure 3: NMIT-MANUS (Interactive Motion Technologies, Cambridge, MA). [36].

The biggest limitation of most of the current AEMs is the manual or semi-automatic regulation of the system parameters requiring the professional assistance of trainers or therapists to handle the different machine parameters, which in most cases, are results of guesses [101, 45]. Besides, the increasing of cardiovascular problems as a result of heart diseases, core health behaviors (lack of physical activity, smoking, and unbalanced diet), and health factors (high levels of cholesterol, glucose, and blood pressure) is causing more and more severe disabilities around the world and consequently a higher demand for professional therapists [75, 152]. Another crucial limitation is related to the efficiency which is low because of the current exercise protocols based on weights, elastic, and pneumatic resistances with manual or semi-automatic regulations [139].

An optimal or more efficient training could potentially help to diminish or suppress the current alteration in the musculoskeletal loading and the muscle toning

of the astronauts as a result of the lack of gravity for long periods of time [114]. Currently, these microgravity alterations and their health consequences represent one of the most important limitations for space exploration. These consequences include but are not limited to motion sickness, muscle degeneration (atrophy), loss of bone mineral density (BMD), and change in body fluids, responding on losing mass proportional to the time of exposition to the microgravity with an average of 1% BMD per month [106, 57, 153]. Finally, the development of a new generation of smart systems for automatic regulations of AEMs will motivate future research overcoming several of the current limitations on human performance and rehabilitation while providing valuable contributions.

1.2 Literature Review

1.2.1 Exercise and Rehabilitation Practices

The physiological effects associated with human training are the natural response of the body to remain in the homeostasis state (steady internal conditions) [131]. The presence of any internal or external disturbance such as a higher muscle energy demand, changes in the intensity and/or duration of the exercise, and environmental conditions (such as temperature, humidity, and even colors) produces an alteration on these effects [12]. For instance, a person running requires oxygen in the muscles to produce muscle contractions. To satisfy this demand (recover the homeostasis state), the body inhales more oxygen while the heart increases its pumping rate. Several physiological effects of multiple biological systems are associated with exercise training. However, this research focus on the study of the effects of the musculoskeletal (muscle activation), cardiorespiratory (oxygen consumption), and cardiovascular (heart rate) systems [41].

Physiological effects have been used as performance metrics in CSHP for

several years. In early research, these effects were manipulated through conventional methods based on post-training measurements. For instance, the level of glucose in the serum, plasma, or urine was widely used to measure the intensity of training [72]. Other methods a little more sophisticated used to include invasive electrodes [34]. Some years later, HMI began to receive more attention because of its several benefits. Thus, the areas of rehabilitation and physical conditioning started to grow by including better sensors and equipment such as AEMs.

AEMs provide an invaluable contribution to human performance and rehabilitation by combining exercise physiology with technology [71]. Unlike conventional exercise machines, AEMs provide controllable trajectories and resistances through the use of electric motors and control systems with the capacity to produce workloads even in lack of gravity. Thus, these machines would become very effective under microgravity conditions by allowing astronauts operating in space to receive a similar stimulus as they would otherwise obtain while under the effects of gravity. Finally, the ability of the AEMs to target multiple systems makes them the best option available to improve human performance and rehabilitation practices by providing a rich variety of training effects.

AEMs have been used for many and varied applications. Some applications have been developed as portable orthotic devices to provide stability and alignment for the body while including real-time control and monitor of patients [97]. Other developments have been developed as home-based systems to aid in the functional recovery of post-stroke patients from the comfort of home [167]. Some more novel applications including graphical user interfaces have been used through teleoperation for remote rehabilitation [166]. Rehabilitation machines developed based on the Internet of Things (IoT) technology have been also reported claiming to be able to mitigate problems associated with the lack of health professionals [40]. Other research focus-

ing on human fitness improvement has reported a variety of physiological effects on the musculoskeletal, cardiovascular and cardiorespiratory systems as a result of the manual variation of trajectory and impedance parameters [30, 28, 27].

AEM has always been part of HMI by connecting the human and machine through conventional and smart processes. The smart integration between humans and machines which has been used in this study is the smart-HMI (S-HMI) [56, 99]. S-HMI considers the human dynamics inside of the closed-loop system enabling the integration of human science together with mechanical, electrical, and information technology. Most of the applications have been mainly focused on the integration between human and IoT technologies [109, 54]. However, S-HMI provides endless applications in different areas with multiple benefits for quality of life.

S-HMI research oriented to rehabilitation has been reported for systems with learning capabilities and biological model estimations [9, 154]. For instance, muscular activations have been previously used to enhance rehabilitation results by regulating joint trajectory and/or torque in a rehabilitation robot system for lower limbs [2]. This system requires training sessions where the subject is required to follow some special procedures while an artificial neural network model is fitted for posterior probability estimations. Results show good performances but, besides the training requirements, performance is time-sensitive because of the loss of accuracy in the model over time. Other S-HMI research has shown promising results compared to the conventional practices by using a semi-automatic selection of machine parameters based on biofeedback such as exoskeletons and active prostheses [53]. The use of biofeedback on this application guarantees the enhancement of human mobility by identifying the optimal exoskeleton or prostheses assistance to minimize energy cost during walking and running [163]. The optimization is performed by finding patterns related to the required assistance while parameters are manually customized for each

need. On the other side, S-HMI research oriented to fitness performance has been reported with applications such as heart rate control during exercise with treadmills [123, 145, 146, 147]. The feasibility and the methods of these studies have been experimentally demonstrated. Most of these works are based on a PID controller for heart rate regulation. Although improvements in human performance have been reported, there is not any evidence about the optimization of training based on these results. A possible reason for this conclusion could be the fact that there is not an optimal heart rate. Heart rate depends on several parameters including the physiology of a person including age, gender, physical condition, and the kind of training to be performed. Other S-HMI researches have been oriented to synergy optimization. The concept of muscle synergy was introduced to divide muscle activations into a lower-dimensional synergy space. This synergy space defines the possible combinations of muscle activations to control the movement [160, 138].

1.2.2 Virtual Populations Analysis (VPA)

In addition to human subjects, this study has been supported by using Virtual Population Analysis (VPA). The objective of this technique is not to replace the analyses using real populations, but to support it by providing a faster and simpler data analysis especially when the required population is large and/or it is not easily available. The first VPA studies were conducted by Gulland and they date back to around the 1960s as a cohort statistical technique mainly used for fisheries science [94]. In these studies, historical reconstructions of fish populations were performed to estimate the numbers of fish based on individual births and deaths during each year [116]. Although these studies did not turn out to be very accurate during the early stages due to wrong assumptions associated with lack of parameters and random fluctuations in the natural mortality of the species, VPA immediately garnered much broader interest and its popularity continued to grow and spread to more areas of research

[150, 70].

There are lots of popular areas where VPAs have been used including but not limited to manufacture, medicine, and social sciences. These industries are highly dynamic as a result of rationally changing environments. For instance, VPA in the manufacturing industry (or Functional Virtual Population as it is also known) was proposed to assist the scheduling knowledge for systems by using techniques including machine learning such as artificial neural networks [87]. Regarding VPA in the medicine industry, computational whole-body human models were developed for several applications from electromagnetic exposure evaluations to closed-loop glucose control developments for subjects with type 1 diabetes [50, 55, 70]. This technique has become very useful by allowing the inclusion of different models needed for reliable, effective, and safe diagnostic and therapeutic applications.

The virtual population used in this research includes 50 human models with 25 female and 25 male models. The model description, the generation process, and the list of them can be seen in Appendix A.

1.2.3 Model-Free Training Optimization and Rehabilitation

The first research about model-free training optimization including human dynamics in the closed-loop system was reported in 1996 [89, 88]. This work used a single degree of freedom (DOF) manipulator with variable speed (see Figure 4). The optimization objective was the maximization of a performance function based on the biomechanical configuration of the user (estimated by its force-velocity relationship in Figure 5).

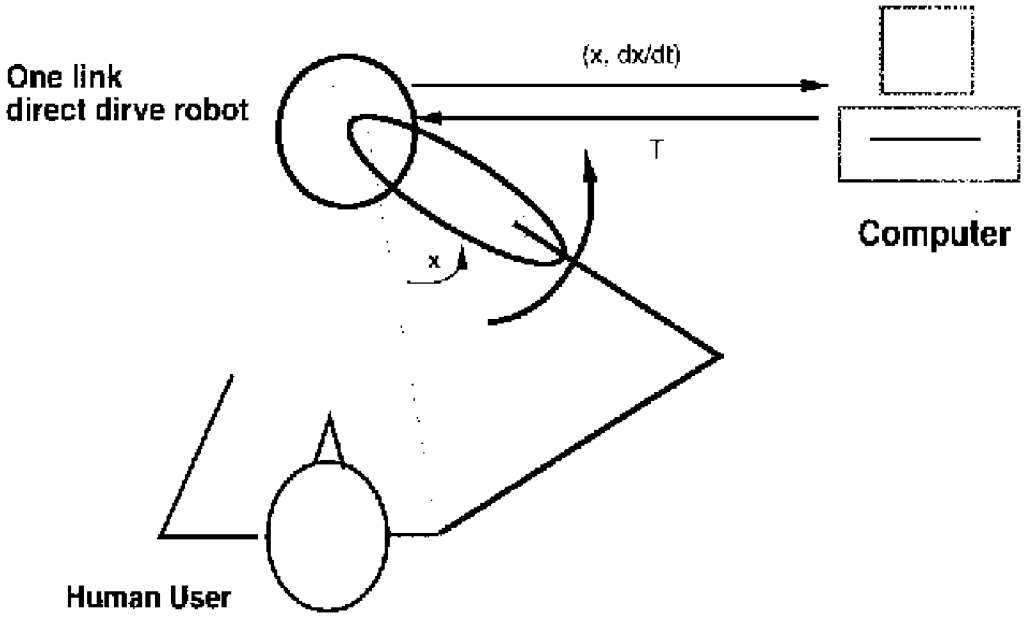

Figure 4: 1 DOF machine setup on the research [89].

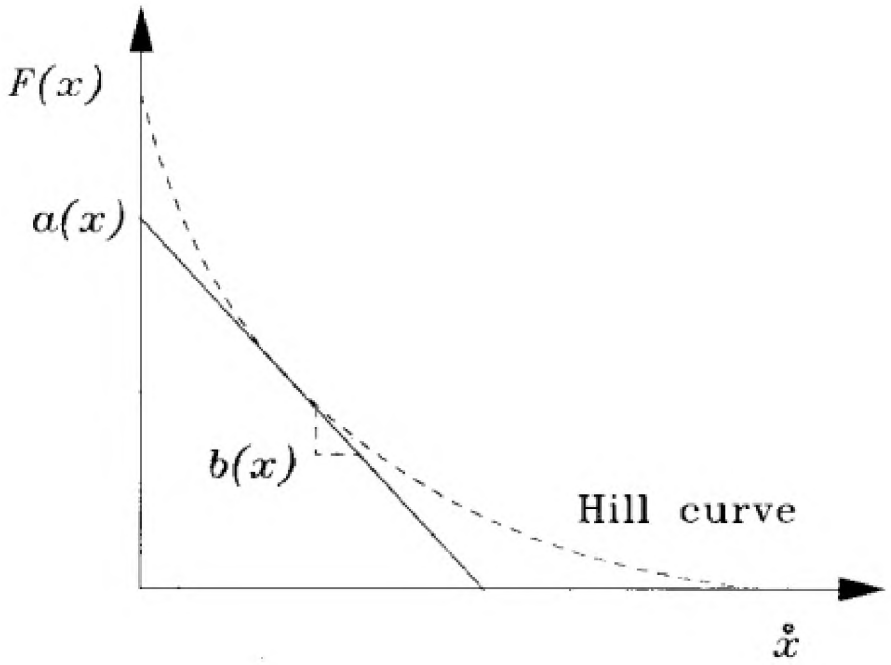

Figure 5: Hill muscle curve. Force-velocity relationship [89].

The performance function (J_p) to be maximized was based on the user's power output as follows:

$$J_p(F, x, \dot{x}) = F\dot{x}^{\rho}, \tag{1.1}$$

where F is the interaction force, and x and $\dot{x}$ are the angular position and velocity respectively. The parameter ρ is a gain parameter which allows to emphasizes or de-emphasizes the interaction force with respect to the angular velocity. For instance, a ρ-value lower than 1 ($\rho < 1$) de-emphasizes the force, a ρ-value higher than 1 ($\rho > 1$) emphasizes force, and a ρ-value equal to 1 ($\rho = 1$) emphasizes power.

As a graphical example emphasizing the user power ($\rho = 1$), the power cost function would have a parabolic shape (see Figure 6). Based on the force-velocity relationship (see Figure 7) and Eq. 1.1, the optimal velocity and force can be derived as follows:

$$F = (x, \dot{x}) = a(x) - b(x)\dot{x}, \tag{1.2}$$

where $a(x)$ and $b(x)$ are the intercept with the vertical axis and slope of the Hill muscle curve in Figure 5 respectively.

$$J_p = a(x)\dot{x}^{\rho} - b(x)\dot{x}^{\rho+1} \tag{1.3}$$

$$\frac{\partial J_p}{\partial t} = 0 = \rho a(x)(V^*)^{\rho+1} - (\rho + 1)b(x)(V^*)^{\rho} \tag{1.4}$$

$$V^*(x) = \frac{\rho}{(\rho + 1)}\frac{a(x)}{b(x)} = \frac{1}{2}\frac{a(x)}{b(x)}, \tag{1.5}$$

where V^* is the optimal velocity to be tracked and the optimal force becomes

$$F^*(x) = \frac{a(x)}{2} \tag{1.6}$$

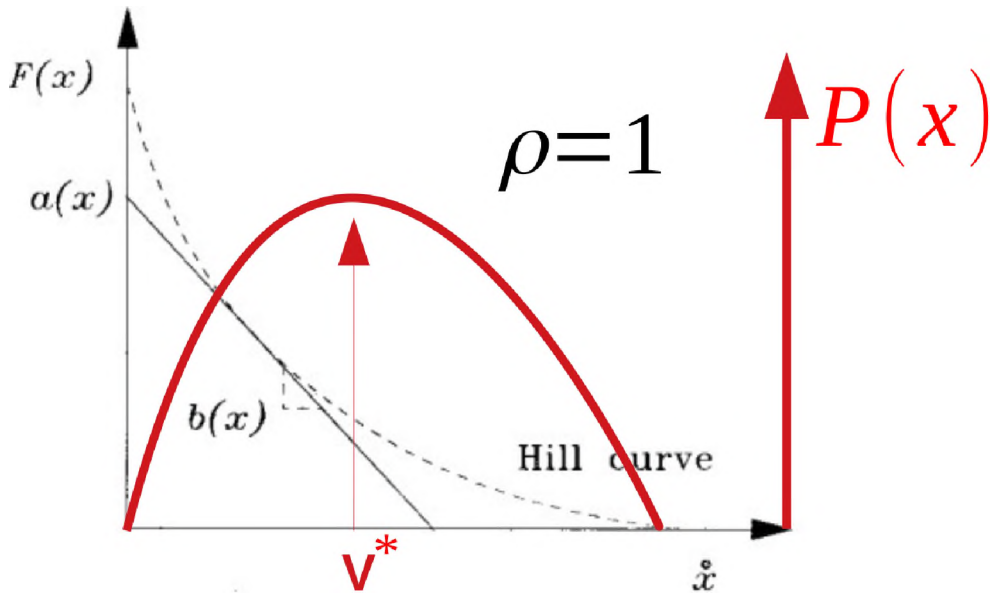

Figure 6: Power function over the Hill muscle curve [89].

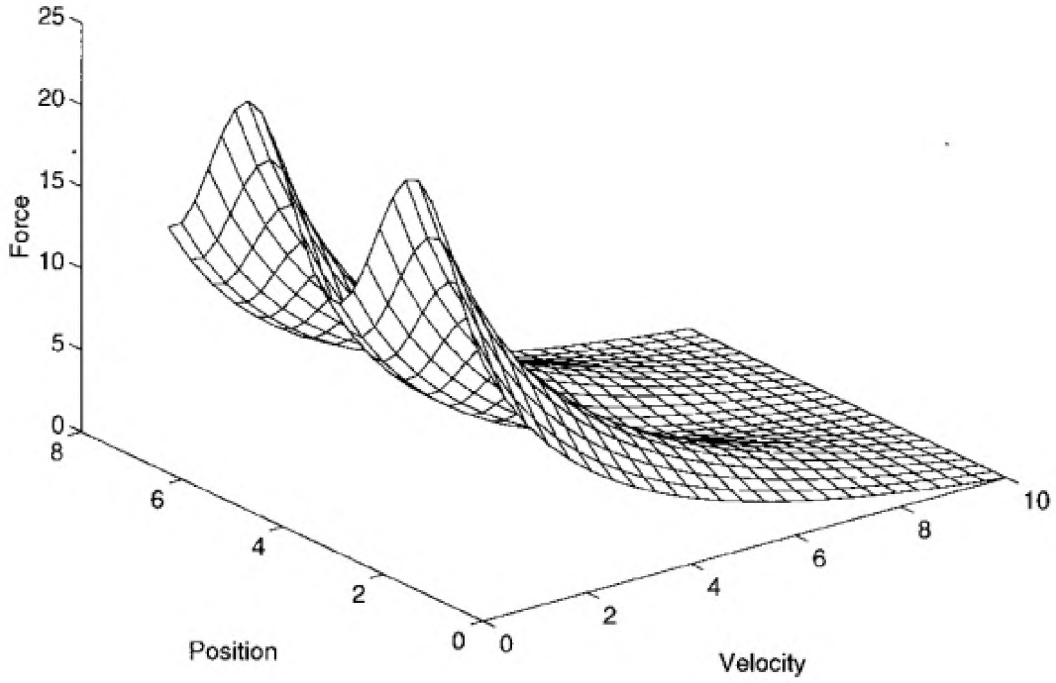

Figure 7: 3D-state relationship. Force-position-velocity relationship [89].

Results reported on this research showed an accurate tracking of the desired velocity. However, the biomechanical parameters $a(x)$ and $b(x)$ were not known ac-

curately. Besides, these parameters were wrongly used as constant when they are time-variable as a result of physiological factors during exercise training such as fatigue, body temperature, and level of hydration. Consequently, the maximization of the performance function or the optimality of the training was not proved.

The previous research was replicated 8 years later and reported in 2 different papers [164, 165]. The AEM used was a 1 DOF rotational handle similar to the original from [89] (see Figure 8). For this approach, two Extremum Seeking Control (ESC) algorithms were used. The first algorithm was used to maximize the user's power output under the assumption that the user's torque is available, and the second algorithm was used to estimate the user torque.

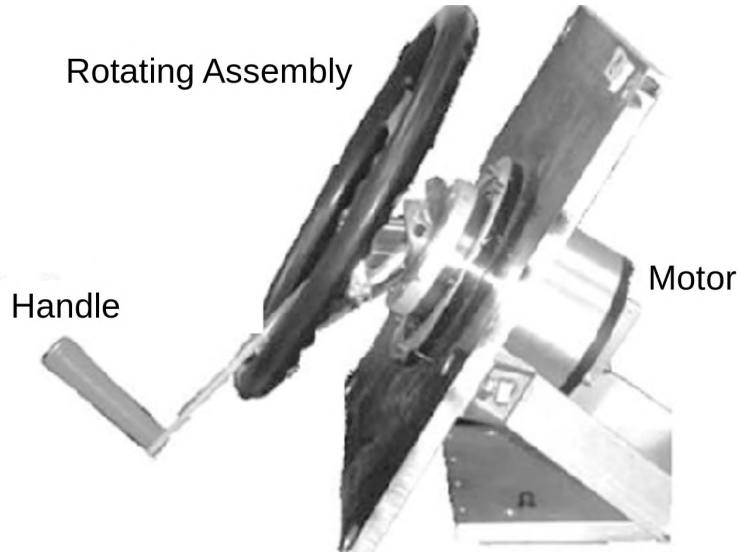

Figure 8: 1 DOF machine setup on the research [165].

The results obtained from this research showed that the desired velocity to be tracked was close to the one presented in the previous research (see Figure 9). However, based on the same considerations previously made, the optimal velocity can not be constant but depending on other variables. Besides, since the biomechanical parameters are unique in each person, different subjects should produce different solutions.

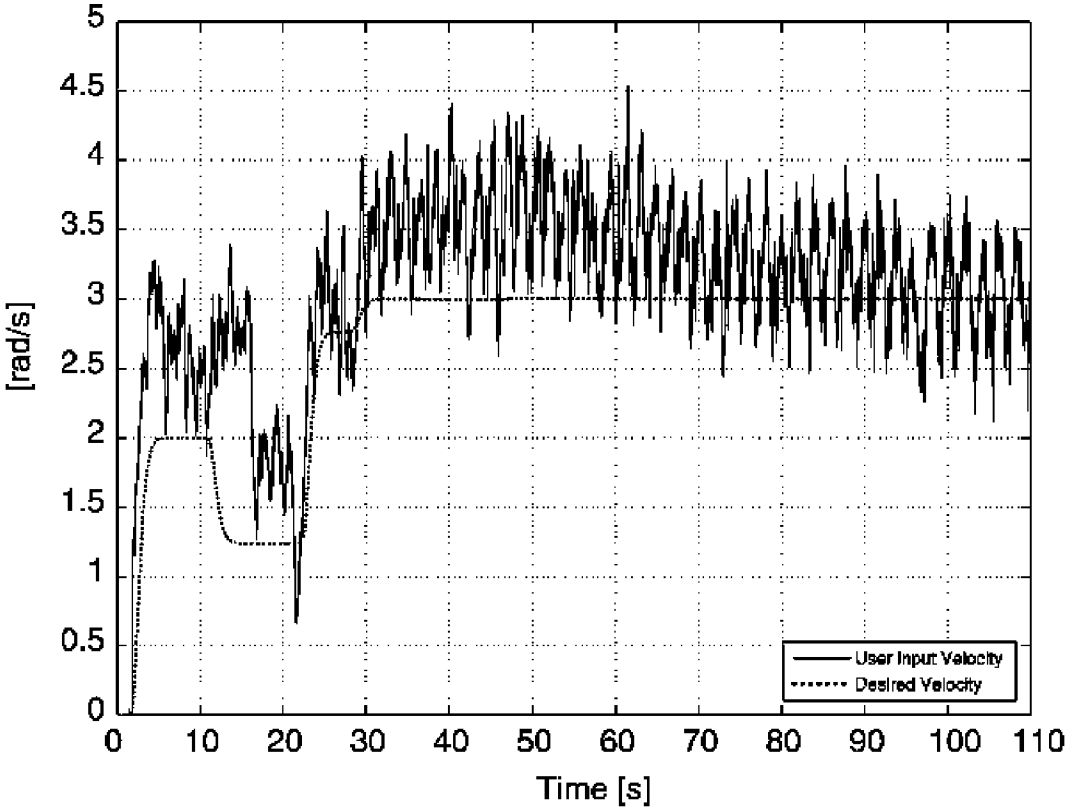

Figure 9: Velocity tracking for the training optimization [165].

Some model-free optimization applications have also been developed for prostheses. For several years, the setting parameters on prostheses, which are important to achieve a good balance between performance and comfort, have been manually configured by trial and error. A proposed ESC for the auto-tuning of these parameters in a powered prosthetic leg was reported [82] (see Figure 10). The use of ESC successfully improved the control of the prostheses at different walking speeds and conditions achieving optimal settings only using tracking errors as feedback. This model-free approach supports the personalized configuration process between people achieving a desirable performance without specific knowledge about the subject.

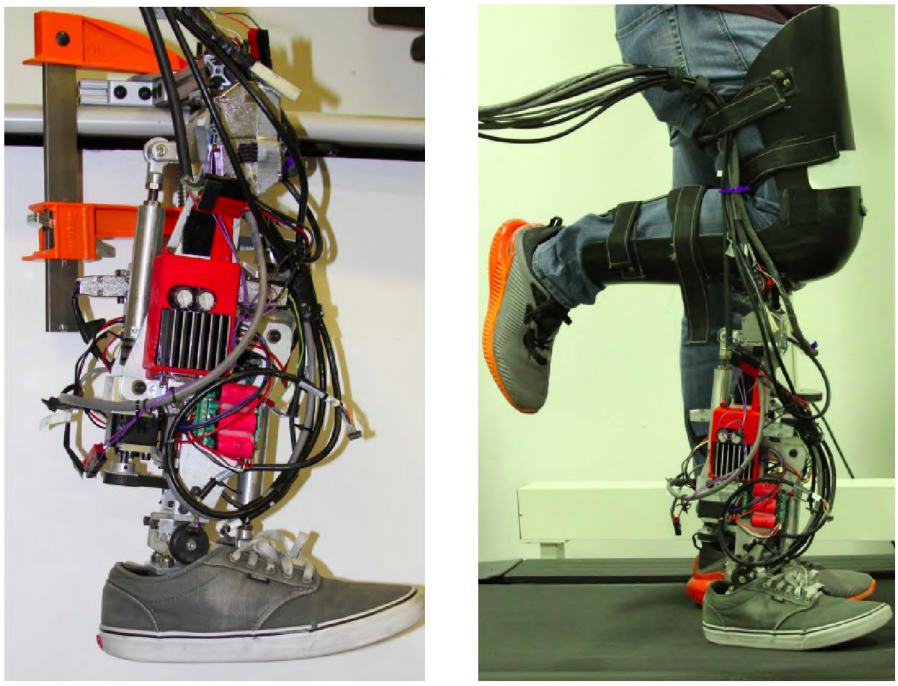

Figure 10: Prosthesis leg auto-tuned by ESC [82].

Rehabilitation systems have made use of both, model-based and model-free, approaches in a wide range of applications but mainly based on functional electrical stimulation (FES) (see Figure 11). FES is a promising procedure to restore movement in people following spinal cord injury (SCI) by reanimating their paralyzed muscles [161]. The development and setting of FES controllers can become very challenging because of the multiple variables and muscles involved in the approach [127]. Among the smart and optimization systems developed for FES, some of them have been oriented to maximize the extraction of data associated with the recruitment curve parameters [126], others to predict joint torques using musculoskeletal positions, velocities, and the electrical stimulation applied to the muscles [128], and some others to optimize the integrated controllers working simultaneously with them. For instance, neuromuscular electrical stimulation (NMES) systems are mainly controlled by a proportional derivative integral controller (PID) and its performance lies in the right selection of these parameters (which requires knowledge, experience, and some

trial and error). However, since the human dynamics are nonlinear, these parameters are not constant depending on some biological factors. Based on that limitation, a model-free methodology based on ESC was proposed to auto-tune the PID parameters. The auto-tune was achieved by minimizing a cost function reflecting the desired performance attributes. The work has been presented in 4 different stages. The first stage was a proof of concept using a multi-variable and deterministic ESC approach which was was successfully tested in healthy people [110]. Later, the work was replicated with eight post-stroke patients. A reduced root-mean-square error (RMSE) tracking and improvements were reported compared to the initial evaluation cycle [112]. Then, the multi-variable approach was replaced by a stochastic ESC. This approach was tested with healthy and post-stroke patients. Results seem to be similar to those previously reported [113]. Finally, the stochastic approach was replaced by the original deterministic. New experiments were conducted with healthy volunteers and stroke patients. Significant advances compared to the previous approach were reported [121]. Similar research using ESC together with NMES has also been developed to optimize the frequency and voltage modulation of the electrical stimulation. The stimulation was applied to the quadriceps muscles producing desired knee joint displacements. Experimental results illustrating the real-time positioning performance have been reported with better results compared to the traditional methods using manual modulation [144].

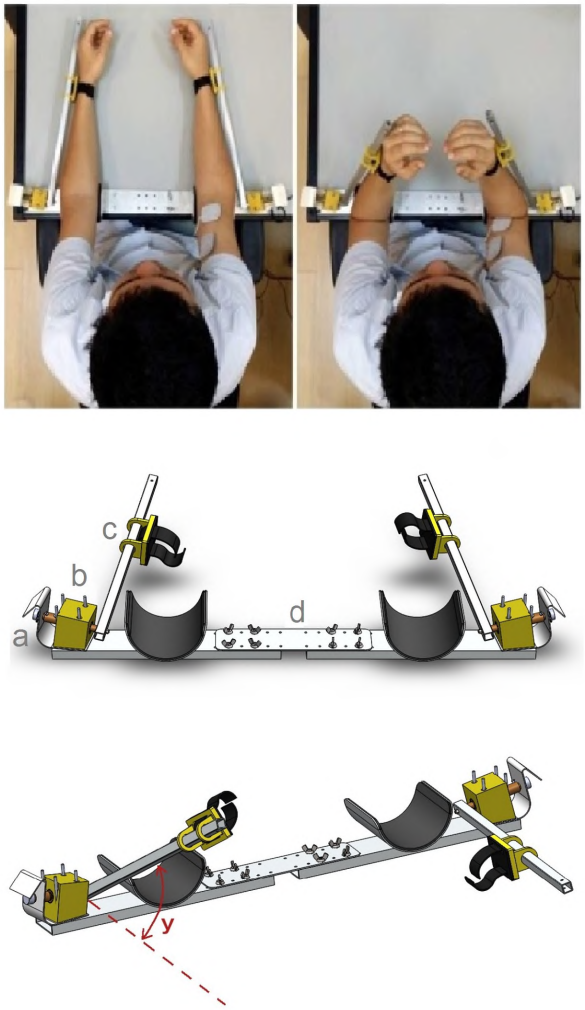

Figure 11: Mechanical system operated with ESC and PID to neuromuscular electrical stimulation [121].

Some studies on exercise optimization have also been developed based on the use of ESC [117]. This work was developed in a simulation environment to support the feasibility of model-free exercise optimizations in real-time experiments. ESC was proposed to fulfill the need for an automated resistance able to optimize muscle performance. This resistance was produced by a variable impedance control proportional to the position tracking error (stiffness impedance). The performance function to be maximized was the average of the squared power of muscles. The

model-free controller was simulated against two muscle-actuated linkages models. The first model was a single DOF manipulator actuated by two antagonistic muscles (see Figure 12). This first model under the action of a stiffness impedance revealed the existence of a local maximum. The solution was achieved under specific parameters and initial conditions close to the local maximizer. The second model was a two DOFs manipulator actuated by seven muscles (see Figure 13). Unlike the first linkage model, the second was not able to find an optimizer. After several iterations evaluating the performance function using different parameters, the controller was unable to locate an optimum point. In some cases, it was shown that an optimum did not exist. Although the optimization was not achieved for all the cases, the proposed framework encouraged this work by presenting its partial feasibility.

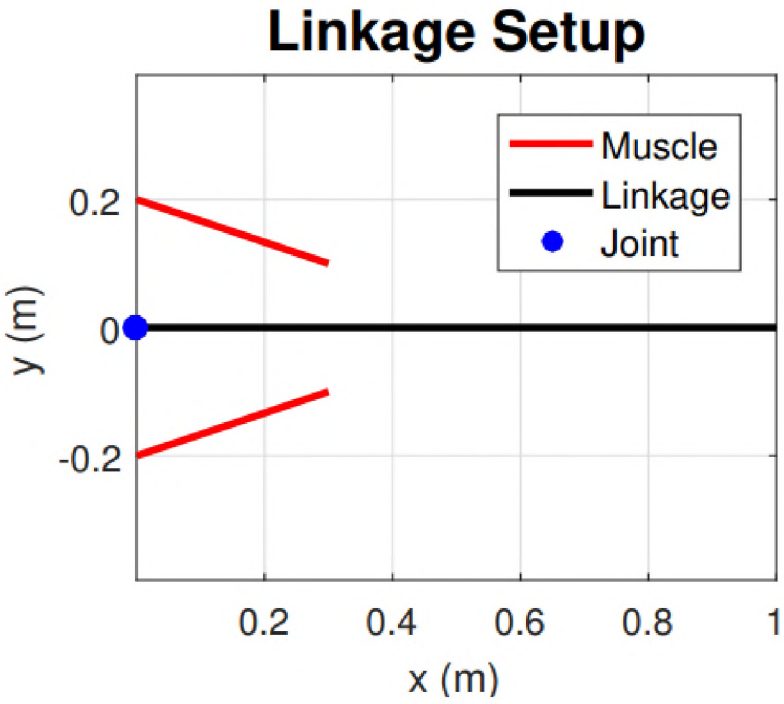

Figure 12: Single DOF manipulator actuated by two antagonistic muscles [117].

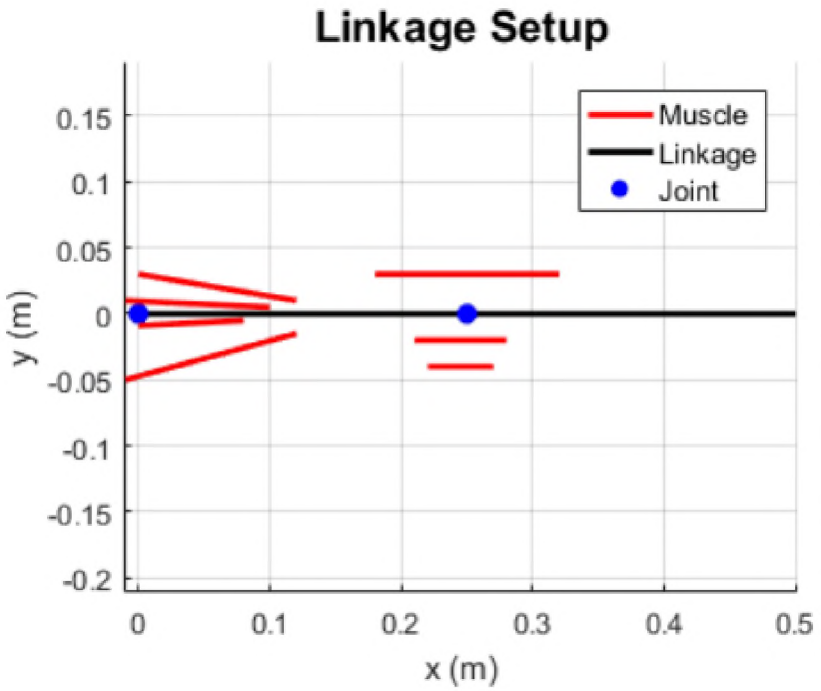

Figure 13: Two DOFs manipulator actuated by seven muscles [117].

1.2.4 Extremum Seeking Control and Applications

Extremum seeking control (ESC) is a branch of adaptive control developed for optimization. This control aims to the output of a dynamical system to converge to unknown maximum or minimum operating points. Several ESC algorithms have been developed and studied since their first appearance in the 1920's [5]. Some of them are model-based methods. However, the popularity of ESC lies in its model-free optimization algorithms and its ability to operate in real-time.

The ESC algorithm works by applying a variable input ($a\sin(\omega t)$ in Figure 14) while measuring the output (y in Figure 14) as a result of those variations. If the input and output are in phase (the input value increases together with the output), by applying a zero-mean normalization to both variables, and then, by multiplying them together, the direction towards the optimization variable is defined as positive. Oppositely, if the input and output are out of phase (the input value increases while

the output value decreases), the direction towards the optimization variable is defined as negative. If the direction is defined as positive, the maximizer/minimizer is greater/lower than the estimated variable ($\hat{\theta}$), and if the direction is defined as negative, the maximizer/minimizer is lower/greater than the estimated variable.

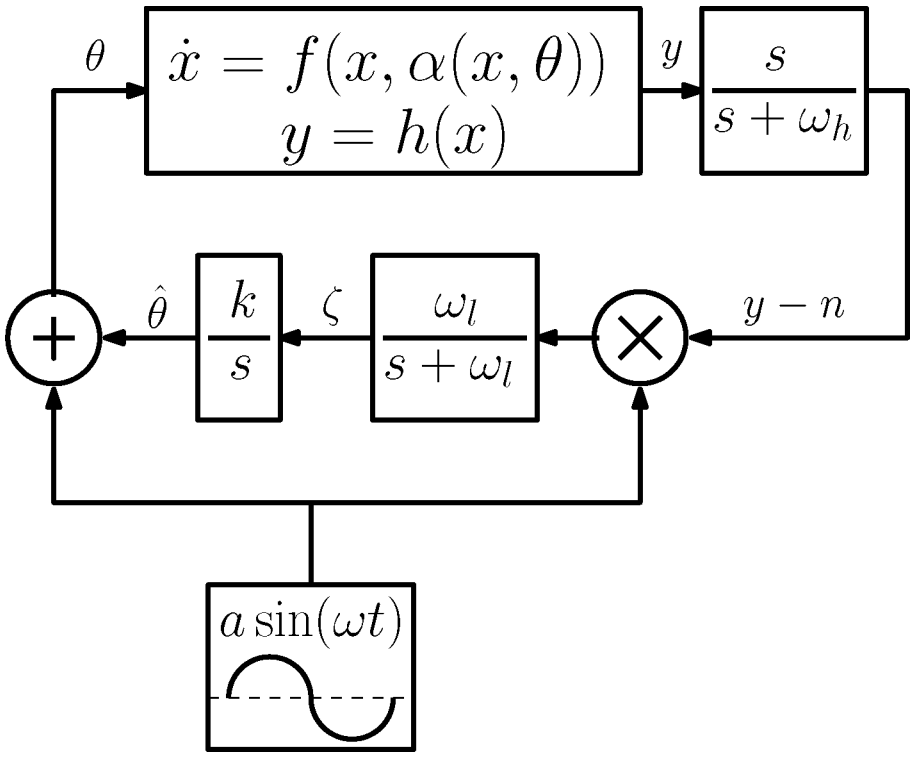

Figure 14: Deterministic perturbation-based ESC scheme [162].

For more details, see the application example presented in Appendix B.

Summary of Theoretical Results on ESC

In this summary, the model-free deterministic perturbation ESC is presented [162, 44]. This method of ESC has been the most popular because of its fast adaptation and easy implementation.

For a general nonlinear system

$$\dot{x} = f(t, x, u), \tag{1.7}$$

and the following performance output

$$y = J(t, x), \tag{1.8}$$

where t is the time, $x^T = [x_1, x_2, ..., x_n]$ is the state vector, u is the input, and the functions $f : D \times \mathbb{R} \to \mathbb{R}^n$ and $J : D \to \mathbb{R}$ are sufficiently smooth on $D \subseteq \mathbb{R}^n$, ESC is designed to find the optimizer (x^*) maximizing/minimizing the performance function.

It is important to highlight that the performance output $\Big(y = J(x)\Big)$ is not the same as the plant output. This output related to plant behavior is the variable to be minimized or maximized. Comparable to any other optimization method, the basis of the ESC development is provided by the following optimal conditions:

Theorem 1 (First-order Necessary Conditions [108])

If x^* is a local minimizer (or maximizer) and J is continuously differentiable in the neighborhood of x^*, then $\nabla J(x^*) = 0$.

Theorem 2 (Second-order Necessary Conditions [108])

If x^* is a local minimizer (or maximizer) and $\nabla^2 J$ is continuous in the neighborhood of x^*, then $\nabla J(x^*) = 0$ and $\nabla^2 J(x^*)$ is positive semi-definite (or negative semi-definite).

Theorem 3 (Second-order Sufficient Conditions [108])

If $\nabla J(x^*) = 0$, $\nabla^2 J$ is continuous in the neighborhood of x^* and $\nabla^2 J(x^*)$ is positive definite (or negative definite), then x^* is a strict local minimizer (or maximizer) of J.

Theorem 4 [108]

If J is convex, then any local minimizer (or maximizer) x^* is a global minimizer (or global maximizer) of J. If also J is differentiable, then any stationary point x^* is a global minimizer (or global maximizer) of J.

These conditions have to be satisfied to guarantee a local minimizer (or maximizer). Although determining a global minimizer (or maximizer) is possible, is generally difficult. Therefore, the convergence of the solution to a stationary point can only be guaranteed.

Assuming stability on the system (or being stabilizable) at each of the equilibrium points by a local feedback controller, a control law of the form

$$u = \alpha(x, \theta) \tag{1.9}$$

is taken, where θ is a scalar parameter. The closed-loop system becomes

$$\dot{x} = f\Big(t, x, \alpha(x, \theta)\Big), \tag{1.10}$$

therefore, the equilibrium points of the system will be parameterized by θ.

The following additional assumptions about the closed-loop system are made:

Assumption 1.

There is a smooth function $l : \mathbb{R} \to \mathbb{R}^n$ such that

$$\dot{x} = 0 \quad \text{if and only if} \quad x = l(\theta) \tag{1.11}$$

Assumption 2.

For each $\theta \in \mathbb{R}$, the equilibrium of the system $x = l(\theta)$ is locally exponentially stable.

Assumption 3.

For the optimal parameter $\theta^* \in \mathbb{R}$

$$(J \; o \; l)(\theta^*)' = 0 \tag{1.12}$$

$$(J \; o \; l)(\theta^*)'' < 0 \text{ for maximization.} \tag{1.13}$$

Therefore, the output of the equilibrium map $y = J\big(l(\theta)\big)$ has a maximum at $\theta = \theta^*$.

For the case of this study, the closed-loop system represents the human-machine system including the human, the robot, and interaction between them during the exercise; the training parameter to be optimized is represented by θ, and the system states including the muscle activations as a result of the exercise are represented by the vector x where they are optimal when the training parameter is also optimal $\big(x^* = l(\theta^*)\big)$.

The system is shown as stable and the stability analysis is derived and proven in [79, 5].

Multi-variable ESC

The basis of the ESC algorithm for multi-variable systems is provided by the same optimal conditions presented for the single-variable optimization case and the same assumptions about the closed-loop system. The main differences with the scalar method are the inclusion of new parameters and dynamic estimators depending on the multi-variable methodology.

Multi-variable ESC methodologies are robust algorithms that operate with multiple variables in dynamic maps. The efficiency of these methods mainly lies in the frequencies of perturbations. These frequencies have to be higher than the frequency of change of the dynamic map. Since the change in human dynamics is slow compared to computer speeds, this model shows a promising performance to deal with the multi-variable approach.

Two multi-variable ESC optimization methods were selected for performance evaluation. These methods were the multi-variable perturbation-based ESC and the multi-variable Newton-based ESC.

Multi-variable perturbation-based ESC

The stability analysis and convergence for the multi-variable perturbation-based ESC method are proved in [4]. This methodology for the two-variables case uses two single-variable models with different perturbation frequencies. As a result, the single perturbation with the lowest frequency will seek convergence at a slow rate. Meanwhile, the single perturbation with the highest frequency considers the slow perturbation as a part of the dynamic system. Thus, the controller will optimize each variable independently without relating one variable to the other. The scheme of this model can be seen in Figure 15. The model parameters are the same as for the single-variable perturbation-based model.

Regarding the selection of all the parameters, except for the frequencies of perturbation, they only need to be real nonzero values. In addition to the previous requirement, the frequencies of perturbation require some additional requirements. For instance, for a multi-variable system with n variables, n number of perturbation frequencies have to be selected (ω_1, ω_2,..ω_n). For distinct i, j, and k, the requirements for the perturbation frequencies are:

- ω_i/ω_j has to be rational.
- $\omega_i \neq \omega_j$.
- $\omega_i + \omega_j \neq \omega_k$

For our case, where we only have 2 variables (ω_1 and ω_2), the requirement for the frequencies is their values to be 2 different real and rational nonzero numbers.

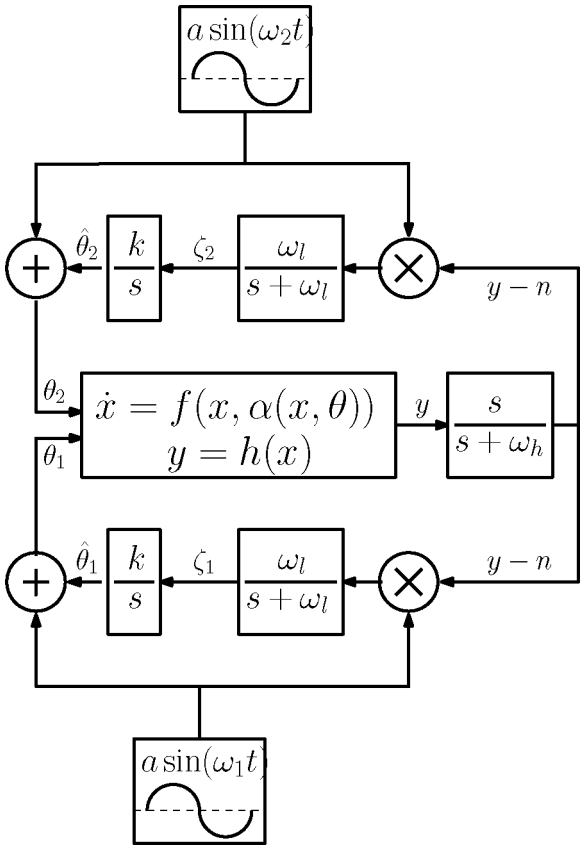

Figure 15: Multi-variable perturbation-based ESC scheme for 2 variables.

Newton-based ESC

The Newton-based approach is one of the fastest algorithms in Extremum Seeking Control. Its speed lies in the fact that the Newton-based convergence is independent of the Hessian which significantly matters in model-free methodologies (where the Hessian is unknown). This approach has three important parts: the perturbation

$M(t)$, which produces an estimation of the gradient ($\hat{G}$), the perturbation $N(t)$, which produces an estimation of the Hessian ($\hat{H}$), and the Riccati equation, which produces an estimation of the inverse of the Hessian (Γ). In this approach, the optimization is performed by a Newton-step calculated as $-\Gamma\hat{G}$, where Γ is the inverse of the Hessian and $\hat{G}$ is the estimated gradient. Particularly, for the case of two variables, the Newton-based approach works as follow:

The input perturbation works the same as in the single variable approach, except for the fact that this input is a vector of 2 perturbations as follows:

$$S(t) = [a\sin(\omega_1 t), a\sin(\omega_2 t)]^T, \tag{1.14}$$

where a is the amplitude of perturbation, and ω_1 and ω_2 are different perturbation frequencies ($\omega_1 \neq \omega_2$).

Based on the stability calculations presented in [100, 47], the estimated Gradient ($\hat{G}$) and Hessian ($\hat{H}$) are obtained as long as the zero-mean removed output (high pass filtered) is multiplied by the right selection of $M(t)$ and $N(t)$. To illustrate the specific two-variable case, the following vector and matrix respectively would be:

$$M(t) = \left[\frac{2}{a}\sin(\omega_1 t), \frac{2}{a}\sin(\omega_2 t)\right]^T \tag{1.15}$$

$$N(t) = \begin{bmatrix} \frac{16}{a^2}\left(\sin^2(\omega_1 t) - \frac{1}{2}\right) & \frac{4}{a^2}\sin(\omega_1 t)\sin(\omega_2 t) \\ \frac{4}{a^2}\sin(\omega_1 t)\sin(\omega_2 t) & \frac{16}{a^2}\left(\sin^2(\omega_2 t) - \frac{1}{2}\right) \end{bmatrix} \tag{1.16}$$

After the estimation of the Hessian, the Riccati equation for the estimation

of Γ is derived using the following derivative filter:

$$\dot{\mathscr{H}} = -\omega_r \mathscr{H} + \omega_r \hat{H}, \tag{1.17}$$

where ω_r is the frequency of the derivative filter (positive real number). It can be seen the state converges to $\hat{H}$ (Hessian estimate). Furthermore, since Γ is the estimation of the inverse of the Hessian:

$$\Gamma = \mathscr{H}^{-1}, \tag{1.18}$$

Eq. 1.18 can be differentiated and replaced in Eq. 1.17 to obtain the Riccati Eq:

$$\dot{\Gamma} = -\Gamma \dot{\mathscr{H}} \Gamma, \tag{1.19}$$

$$\dot{\Gamma} = \omega_r \Gamma - \omega_r \Gamma \hat{H} \Gamma, \tag{1.20}$$

which using an initial condition positive definite for Γ, it can be solved in real-time.

The Newton-based scheme can be seen in Figure 16.

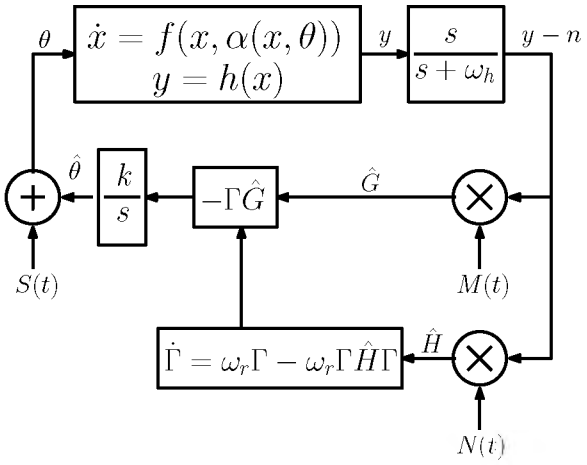

Figure 16: Newton-based ESC scheme.

Multi-variable methodology comparison and selection

The performances of the two multi-variable methodologies were impartially evaluated using the same parameter configurations and results are presented in the Appendix C.

To summarize, both methodologies showed some advantages and disadvantages. The perturbation-based approach proved to be more robust against different combinations of configuration parameters and cost functions by keeping good performance. The Newton-based approach proved to be faster (up to 15 times faster under the same configuration parameters) but at the cost of stability. During the simulation tests, the Newton-based method worked under a very limited range of configuration parameters showing to be highly unstable. Besides, Newton-based showed to be very sensitive to the parameter selection by requiring good parameter guesses which are not possible for this research involving highly nonlinear dynamics from the human body.

Factors such as the computational cost and processing time can always be part of improvements and future research, so they did not represent part of our design requirements. Therefore and since the stability and robustness of the system are the most important factors for the selection of the methodology because they are strictly related to the safety of the training environment, it was decided to use the multi-variable perturbation-based ESC for this research.

1.3 Hypothesis

It is postulated that each person requires a unique combination of trajectory and resistance parameters to achieve a desired muscular effort distribution. This combination of parameters, which seems to depend on the unique physical features of each person such as force capacity, musculoskeletal distribution, body mass index

(BMI), and flexibility, supports the proposed training personalization concept of this dissertation. The fact that the training personalization exists and that it can be set automatically through the use of muscle activations as biofeedback is the main reason and objective of this study. For that reason, simulation tests have been analytically conducted to test the following null hypothesis:

There is no statistically significant correlation between the differences in musculoskeletal parameters and the differences between optimal training parameters.

The null hypothesis would indicate that optimization in models with neighboring musculoskeletal parameters does not lead to similar optimal training parameters. The outcome variable accepts "true" or "false" values if there is sufficient evidence to accept or reject the null hypothesis at a significance level of 5%. The hypothesis testing was conducted using Continuous-Analysis-of-Variance (CANOVA) [155] and Kendall rank correlation coefficient [135] and is presented in Chapter V Section 5.2.

1.4 Specific Aims

Objective 1: Investigate the physiological effects as a result of different exercise protocols with different exercise machines.

We aim to investigate the physiological effects on subjects of different ages, genders, and fitness levels by measuring them during experimental exercise training. The aim of this investigation includes the study of exercise protocols and training machines used to perform these exercises. Thereby, we aim to measure the physiological effects on people performing cardio-based and resistance-based training using a powered rowing machine and robotic systems respectively. The physiological effects selected for this study were muscle activations, heart rate, and oxygen consumption associated

with the musculoskeletal, cardiovascular, and cardiorespiratory systems respectively.

Objective 2: Develop a model-free framework for single-variable optimization of a trajectory parameter using muscle activations as biofeedback.

Using the outcomes from previous investigations suggesting that muscle activations can be controlled leading to a maximization of training performance for fitness and rehabilitation, the methodology was proposed. We aim to develop a single-variable optimization framework using perturbation-based ESC for automatic regulation of the ellipsoidal trajectory orientation to be tracked by the subject exercising. The objective required to follow a model-free approach using muscle activation as biofeedback. We aim to evaluate the performance in simulation using a human arm model and in real-time experiments with a human controlling 2 different robots.

Objective 3: Develop a model-free framework for single-variable optimization of an impedance parameter using muscle activations as biofeedback.

Using the model-free methodology from the previous objective as a starting point, we aim to adapt the framework for impedance regulation. For this objective, we aim to use a fixed ellipsoidal trajectory orientation with a variable impedance automatically regulated using muscle activation as biofeedback. Unlike trajectory parameters, impedance parameters are sensitive to the system stability (especially the damping and inertia parameters). Therefore, we aim to regulate only the stiffness impedance parameter while keeping damping and inertia constant. We also aim to evaluate the performance in simulation using a human arm model and in real-time experiments conducted with a human controlling a robot.

Objective 4: Develop a model-free framework for multi-variable optimization of trajectory and impedance parameters using muscle activations as biofeedback.

We aim to extend the single-variable framework to include multi-variable capabilities for simultaneous regulation of trajectory and impedance parameters. For this objective, we aim to develop two new model-free frameworks based on the use of perturbation-based and Newton-based ESC. Both frameworks had the target of automatically and simultaneously regulating the ellipsoidal trajectory orientation and the stiffness impedance to find the best parameter combination optimizing muscle activations. We also aim to evaluate the performance in simulation of each framework to select the best one based on specific criteria. Finally, we aim to evaluate the performance in simulation using a human arm model and in real-time experiments conducted with a human controlling a robot.

1.5 Organization

The proposal is organized as follows: Chapter II - Background Knowledge on Human Exercise and Exercise Machines outlines each of the different exercise machines and devices used in the research. This chapter includes technical descriptions of their performance, dynamics, and control design. Chapter III - Physiological Effects Under Advanced Training presents the methodology followed for the data acquisition including a technical description of the systems and devices used in this study. This chapter also presents the physiological effects of the cardiorespiratory, cardiovascular, and musculoskeletal systems as a result of cardio-based and resistance-based training. Chapter IV - Model-free Optimization Frameworks of Training Parameters in Advanced Training presents the model-free frameworks developed for the single-variable and multi-variable optimization of the robotic training parameters by using muscle activation as biofeedback. This chapter is subdivided into 2 parts; first, the frame-

works are presented including the systems, methodology, and configurations; second, a performance evaluation conducted in a simulation environment is presented. Chapter V - Training Personalization presents evidence that supports the idea of the unique combination of optimal training parameters for each person. Besides, the necessity of automatic training personalization is supported based on the presence of complex and time-varying human dynamics encountered in parameter estimations using artificial neural networks. Chapter VI - Real-time Optimization Experiments presents the results from real-time experiments performed by using the single-variable and multi-variable optimization frameworks in 4 different phases. The experimental trials were performed using both of the subject body's sides for performance comparison between the dominant and the non-dominant side. Some discussions are presented specifically for each environment and generally for both.

CHAPTER II

BACKGROUND KNOWLEDGE ON HUMAN EXERCISE AND EXERCISE MACHINES

2.1 Overview

Muscles have the ability to produce positive and negative work. Positive work is produced when the muscle is contracting concentrically and negative work when the muscle is contracting eccentrically. A muscle can be considered to be concentrically contracting when the muscle is active and the attachments are drawing closer together or shortening (see Figure 17). A muscle can be considered to be eccentrically contracting when the muscle is active and the attachments are drawn farther apart or lengthening (see Figure 18) [66].

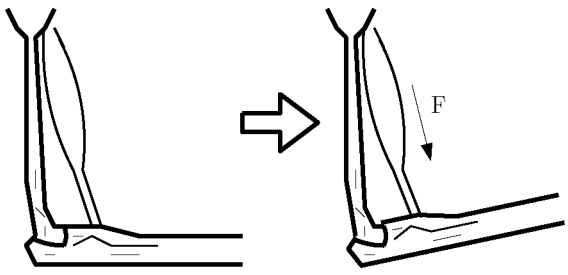

Figure 17: Concentric contraction (muscles shorten with force is generated).

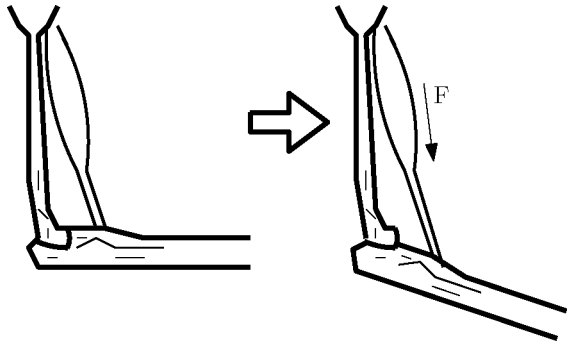

Figure 18: Eccentric contraction (muscles lengthen with force is generated).

Eccentric loading is an important and known exercise modality for its significant contribution to the efficacy of training. Eccentric contractions can generate greater amounts of force while requiring a lessened metabolic demand in comparison with concentric contractions. Consequently, a high metabolic demand caused by only eccentric workloads may involve training with a force greater than the maximum concentric capacity. Thus, high eccentric contractions are normally difficult to perform with conventional exercise machines (CEMs), but they can be easily produced by using advanced exercise machines (AEMs). Eccentric contractions can lead to muscle growth and remodeling through the microdamage produced by its practice [63]. Besides, eccentric training is particularly important in microgravity environments because it allows muscles to lengthen under load imitating the effects of gravity. Thus, it has the potential to aid in solving two critical problems currently experienced: loss of bone mineral density (BMD) and muscle atrophy [57, 153].

2.2 Conventional Exercise Machines (CEMs)

Conventional exercise machines produce load as a result of weight, elastic, or pneumatic resistance (see Figure 19). One of the limitations of the CEM is their lack of control over the resistance making it difficult to isolate one type of contraction, vary the resistance in the middle of the exercise, or even make the exercise dangerous.

During exercise protocols with CEM, the resistance is affected by the mechanical configuration of the machine producing a higher resistance (targeting) one type of contraction while the other contraction receives a resistance equal or lower.

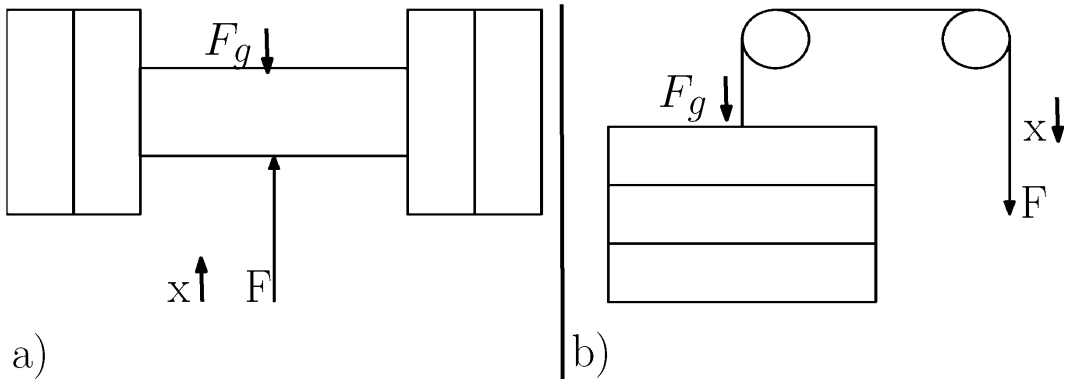

Figure 19: Conventional exercise machines with resistances based on weights. a) Free weight. b) Weight machine.

2.2.1 Dynamics

The resistance produced by a 1 degree-of-freedom (DOF) CEM can be modeled as follows:

$$F = F_g + M\ddot{x} + B\dot{x} + Kx + F_r \text{sign}(\dot{x}), \tag{2.1}$$

where F is the force applied by the user, F_g is the force produced by the gravity effect on the weight ($F_g = Mg$), M is the mass of the weight, B and F_r are the viscous and Coulomb frictions in the cables and pulleys (for weight machines), K is the stiffness property in the cables or springs (if any), and x is the position of the weight. From Eq. 2.1, it can intuitively be seen that the resistance produced will be unbalanced depending on the action direction. As a result, one contraction will be targeted (a higher resistance) and the other one will be untargeted (a lower resistance).

The magnitude of the difference in the workloads will be proportional to the magnitude of the acceleration. For that reason, bodybuilders recommend training in slow-motion as close as possible to a constant speed. A slow-motion training makes it

possible to produce a similar resistance to both kinds of contractions. However, even assuming a slow motion training ($\dot{x}$ and $\ddot{x}$ close to zero), targeted and untargeted resistances can be modeled as:

$$F_{target} = \begin{cases} F, & \text{for } \dot{x} \geq 0 \quad \text{, where} \quad (F \geq F_g) \\ 0, & \text{for } \dot{x} < 0, \end{cases} \tag{2.2}$$

$$F_{nontarget} = \begin{cases} 0, & \text{for } \dot{x} \geq 0 \\ F, & \text{for } \dot{x} < 0 \quad \text{, where} \quad (F \leq F_g) \end{cases} \tag{2.3}$$

Both the concentric and eccentric exercises are very important to make exercise sessions shorter and more effective. However, exercise with conventional machines produces a higher workload in one contraction than the other one. The difference in the loads and the lack of control over them are what makes the traditional training inefficient. Another limitation in CEMs is their ability to produce constant resistances during training. The only way to change the resistance on these machines is by adding or removing weights, changing the elastics, or regulating the pneumatic pressure. This lack of versatility limits the efficiency of the training and increases the exercise setup duration. Regarding safeties during exercise, weightlifting is one of the most common causes for injuries in athletes [81, 119]. The injuries are mainly caused by the inflexibility and improper technique of even experts and well-trained lifters [107]. Statistically, 68% of sportsmen have had an injury related to weight lifting [83]. Therefore, CEMs are not only inefficient but also unsafe. Due to these limitations, AEMs were selected to work on the optimization of exercise training parameters.

2.3 Conventional Rowing Machine

Before starting to develop AEMs, CEMs were analyzed and studied. The first conventional machine used in this research was a rowing machine. A conventional rowing machine is a cardiovascular exercise training machine. The following four main movements form the rowing pattern [13]: catch (see Figure 20-a), drive (see Figure 20-b), finish (see Figure 20-c), and recovery (see Figure 20-d).

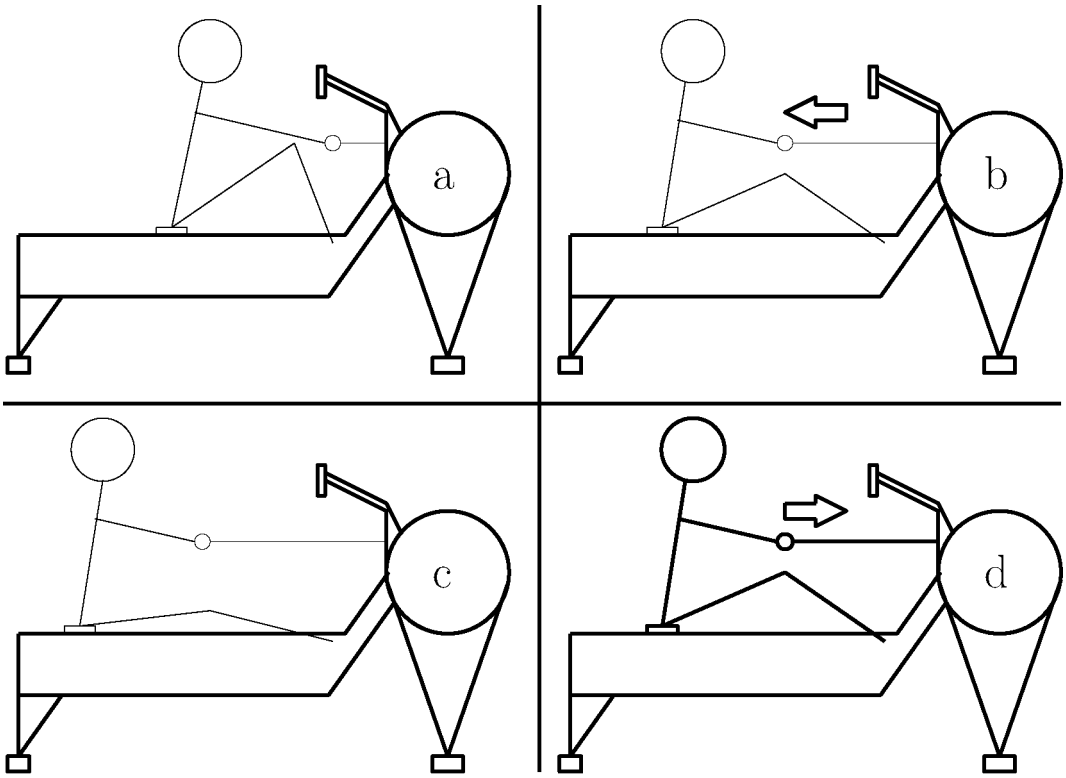

Figure 20: Biomechanics of the rowing machine training.

In order to complete the rowing exercise successfully, the user begins the position with the lower back relaxed to allow for trunk flexion, flexed knees, ankles dorsiflexed, and arms extended as the catch begins with the user pulling the handle with both hands. In the next phase, the drive can be subdivided into (1) leg emphasis, (2) body swing emphasis, and (3) arm pull through emphasis. The drive is initiated by extending the legs and plantarflexion of the ankles against the foot pads

and pulling the handle towards the upper body as the muscles of the shoulder are contracting. As the knees are reaching full extension, the hips begin to extend, and back extension occurs. In the upper body, elbow flexion is also occurring. The knees achieve full extension, the ankles are planter flexed, while the hips and back are finishing extension. During this time, there is high activation of the upper body to finish the drive. During the finish, the knees and ankles maintain extension and plantarflexion respectively, while the muscles of the back and upper arms are contracting. The recovery occurs as the user allows the body to shift back into the starting position by allowing the arms to extend, legs and hips flex, and the ankles dorsiflexed.

It is important to understand the biomechanics of rowing, as this exercise requires the coordination of many muscles at once to produce a smooth and fluid movement to achieve its benefits. Traditional rowing biomechanics is not capable of eccentrically loading (lack of resistance on the return stroke), which limits the use of eccentric exercise. The user allows the body to return back with no resistance, and may even have to slightly engage muscles (concentrically) to help them return to the starting position.

2.3.1 Dynamics

The resistance of the rowing machine is more complex than weight-based machines (see Figure 21). The resistance is the result of the physical interaction between the handle and the internal components (resistance to air flow and flywheel inertia). The resistance produced by a rowing machine can be described as a function of some parameters (see Table I) as follows:

Table I: Rowing machine parameters.

Parameter	Description	Original value	Units
r_s	Sprocket radius	13.5	mm
M_h	Handle mass	1	kg
K_s	Spring stiffness	14.85	N/m
J_F	Flywheel inertia	550	kg
b_F	Flywheel linear friction	5	Ns/m
C_F	Flywheel low quadratic friction	30	Ns^2/m^2
C_F	Flywheel medium quadratic friction	60	Ns^2/m^2
C_F	Flywheel high quadratic friction	90	Ns^2/m^2

$$F = \begin{cases} J_F\ddot{x}_1 + b_f\dot{x}_1 + C_F|\dot{x}_1|\dot{x}_1 + K_s x_1, & \text{for } \dot{x}_1 \geq 0 \text{ (pull phase)}, \\ K_s x_1, & \text{for } \dot{x}_1 < 0 \text{ (return phase)}, \end{cases} \tag{2.4}$$

where x the position of the handle.

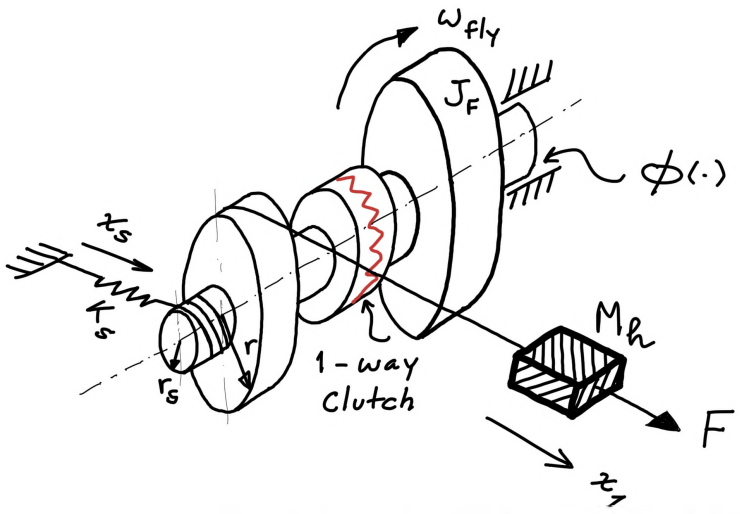

Figure 21: Resistance in a conventional rowing machine.

In conventional machines, all parameters except the air flow resistance (C_F in Table I) are constant. This parameter (C_F) can be set by opening or closing the air vents around the flywheel.

2.4 Powered Rowing Machine

The powered rowing machine was the first AEM used in this study. It was developed based on an ordinary rowing machine modified to include an electric motor and an impedance controller (see Figure 22). The combination between the electric motor and the controller made it possible to mimic the behavior of the original rowing machine and to increase its versatility. The motorized rowing machine has programmable parameters independent for each stroke (for the pull and return strokes). Unlike conventional rowing machines, this motorized rowing machine can produce controlled forces during the return stroke, empowering the eccentric exercise. The powered rowing machine forces the subjects to resist the motor as they return back to the starting position, leading to a more complete, demanding exercise session. This exercise protocol makes it possible to maximize the effects of eccentric training without sacrificing the concentric action. This ultimately could provide better methods for countering the ill effects of microgravity and improve the rehabilitation process.

Figure 22: Powered rowing machine.

2.4.1 Dynamics

In the powered rowing machine, the dynamics behavior can be programmed arbitrarily, to produce resistance patterns which differ from the original rowing machine if so desired. Dynamics can include new features such as pure stiffness on the pull stroke or friction on the return stroke. Therefore, the resistance can be defined as any function depending on machine states such as chain position and velocity. All the resistance parameters in the powered rowing machine are flexible even during the exercise. As a result, the resistance can change during the same stroke or between

the pull and return stroke. The resistance produced is modeled as follows:

$$F = \begin{cases} f_p(x, \dot{x}, \theta), & \text{for } \dot{x}_1 \geq 0 \text{ (pull phase)}, \\ f_q(x, \dot{x}, \theta), & \text{for } \dot{x}_1 < 0 \text{ (return phase)}, \end{cases} \tag{2.5}$$

where θ can be any system variable or set of variables such as acceleration of the handle.

The resistances used in this study for the pull and return stroke were generated according to the following equations:

$$F = \begin{cases} K_{s1}x_1 + b_{f1}\dot{x}_1 + C_F\dot{x}_1|\dot{x}_1|, & \text{for } \dot{x}_1 \geq 0 \text{ (pull phase)}, \\ K_{s2}x_1 + b_{f2}\dot{x}_1, & \text{for } \dot{x}_1 < 0 \text{ (return phase)}, \end{cases} \tag{2.6}$$

For instance, an increase in eccentric workloads can be achieved by increasing the stiffness during the return stroke (K_{s2}).

2.4.2 Sliding Mode Robust Impedance Controller

The controller developed for the powered rowing machine was a robust impedance control. A basic impedance controller works regulating the relationship between force and velocity without ensuring that the impedance obtained is as expected. A robust impedance controller is an approach that makes it possible to control this relationship despite disturbances or inaccurate estimates of the parameters. The full control of the programmed impedances is very important for the safety of the users operating the machine (stability) and the validation and reliability of the results (accuracy). These reasons supporting the use a robust approach are summarized below:

- During the parameter estimations, the accuracy is never optimal.

- During the mathematical modeling, some parameters could be missed.
- During the experiments, disturbances can be produced.
- A robust approach empowers stability.

A robust controller works by compensating for those uncertainties while guaranteeing stability and providing an adequate and proper operation [15, 38]. The designing process for this controller was based on the sliding-mode approach [134]. A sliding mode is a nonlinear control method that works by altering the dynamics of the system by regulating the control signal. The control signal forces the system to compensate for the errors by "sliding" their values to zero. The performance of the controller can be easily estimated by measuring the slide (or switching) variable related to the estimation error variable. For the development of this controller, a previously-published sliding mode impedance control [15] was suitably modified and adapted for the powered rowing machine. The modifications performed include the integration of a nonlinear parameter (nonlinear damper) and the hybrid performance. The hybrid condition on this controller is related to the integration of continuous and discrete variables working together. This integration made it possible to switch the controller according to the phase of motion and the target impedances but keeping a single sliding variable. The robust sliding mode controller developed has been presented in [30, 24].

2.5 WAM Arm Robot

WAM is a 4 DOFs articulated linkage robot developed by Barrett Advanced Robotics [8]. This lightweight cable-driven manipulator is exceptionally dexterous, low-friction naturally backdrivable. Therefore, the robot is able to provide an almost negligible interaction resistance with the human. Its end-effector position was used to track and

feedback the user position by sending the encoder information to a Graphical User Interface (GUI) during the experiment.

Figure 23: WAM arm robot.

2.5.1 Dynamics

The dynamics of this robot [103] given in joint coordinates are derived as:

$$D(q)\ddot{q} + C(q,\dot{q})\dot{q} + g(q) = \tau + J^T F_{ext}, \tag{2.7}$$

where $q = [q_1, q_2, q_3, q_4]$ is a vector of joint displacements, $D(q)$ is the inertia matrix, $C(q,\dot{q})$ is the centripetal and Coriolis effects, $g(q)$ is the gravity vector, τ is the control torque, J is the Jacobian, and F_{ext} is the external force representing the interaction force between subject and robot.

2.5.2 PD and Gravity Compensation Control

This robot was operated with a PD-gravity compensator controller. In order to restrict the robot workspace to an almost planar ellipsoidal trajectory, 2 of the 4 joints of the robot were fixed by applying a PD controller acting on the third and fourth joints as follows:

$$\tau_{PD} = k_P q + k_D \dot{q}, \tag{2.8}$$

where P_{gain} and D_{gain} are diagonal PD gain matrices (zero diagonal values for the first 2 DOFs), and e is the error vector between the desired and the current joint positions.

For the 2 active (movable) DOFs, a gravity compensation was applied to increase the robot maneuverability. The control law was defined as:

$$\tau = P_{gain} e + D_{gain} \dot{e} + g(q), \tag{2.9}$$

$$\tau_g = g(q), \tag{2.10}$$

Thus, the control torque resulted as follows:

$$\tau = \tau_{PD} + \tau_g \tag{2.11}$$

2.6 4OptimX

The 4OptimX is a robot developed at Cleveland State University to provide a platform for research in the areas of human performance and rehabilitation (see Figure 24). It is a 4 DOFs robot consisting of two identical arms with fixed lengths whose pivot

points are horizontally separated by a fixed distance and are at an identical vertical distance from the ground. The end effectors of the robot can move independently on two spherical surfaces. Each DOF (horizontal and vertical on each robot arm) is powered and controlled by an individual electric motor in torque-mode. These motors provide resistance to the user, replacing the traditional weights. Moreover, arbitrary impedances can be synthesized digitally by adjusting the control algorithm. Torque sensors are installed on each axis for use as feedback by the control system. The resistances are controlled by a robust impedance controller.

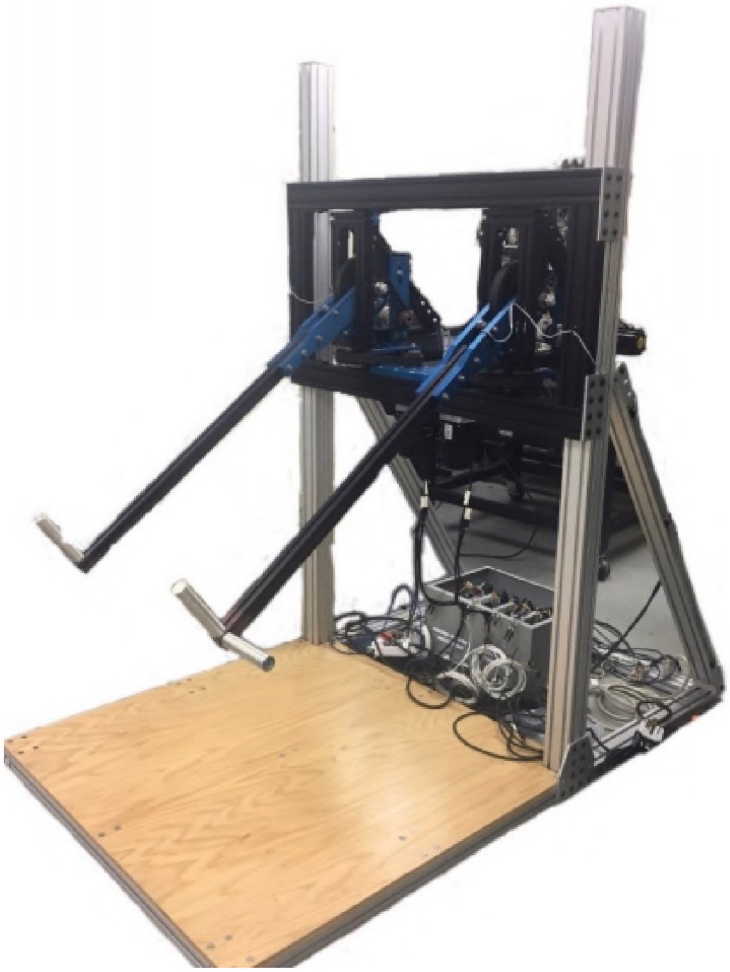

Figure 24: 4OptimX CSU robot.

2.6.1 Dynamics

The dynamics of this robot [103] given in joint coordinates are derived as:

$$\begin{bmatrix} \tau_{12} \\ \tau_{34} \end{bmatrix} = \begin{bmatrix} D(q_{12})\ddot{q}_{12} + C(q_{12}, \dot{q}_{12})\dot{q}_{12} + g(q_{12}) \\ D(q_{34})\ddot{q}_{34} + C(q_{34}, \dot{q}_{34})\dot{q}_{34} + g(q_{34}) \end{bmatrix} \tag{2.12}$$

where $q_{12} = [q_1, q_2]^T$ and $q_{34} = [q_3, q_4]^T$ are the vectors of joint displacements for the left and right side of the robot respectively. Each joint was modeled independently. Therefore, $D(q)$ is the inertia diagonal matrix, $C(q, \dot{q})$ counts for the damping and the centripetal and Coriolis effects diagonal matrix, $g(q)$ is the gravity vector, and τ is the control torque.

2.6.2 Control Design

The 4OptimX is operated with a robust sliding mode impedance controller with trajectory tracking [10]. The controller was designed decoupled and identically for each DOF of the robot. The impedance controller was developed for the human-robot interaction. However, due to the lack of accuracy on the parameter identification and disturbance anomalies evidenced due to electrical noise, a sliding mode approach was developed to add robustness.

Sliding Mode Impedance Control

The controller was developed based on a sliding mode impedance controller, which regulates the dynamic response of the training resistance and the manipulator deviation from a reference trajectory [60, 38, 15]. In the absence of human-robot interaction (no external force), the controller tracks a reference trajectory. However, as a result of manipulator interaction (deviation from the reference position, velocity, or acceleration) the robot imposes a training resistance. The robot controller gives the system

robustness and global stability against the inaccurate and unmodeled plant dynamics and disturbance associated with the real-time environments. Robustness is important to ensure that the prescribed impedance is accurately achieved in the presence of inaccurately modeled or unmodeled plant dynamics. Stability is important to ensure the safety of the user during the exercise protocols.

The controller targets the impedance as follows:

$$I(\dot{\omega}_m - \dot{\omega}_d) + B(\omega_m - \omega_d) + K(\theta_m - \theta_d) = \tau_{ext}, \tag{2.13}$$

where the subscripts m and d represent the measured and desired trajectories respectively, I is target inertia, B is target damping, K is target stiffness, and τ_{ext} is the torque produced externally (by the user). From the previous equation, the equality has to match to achieve the target impedance. Consequently, a sliding surface based on the difference between them is developed as follows

$$s = \int I(\dot{\omega}_m - \dot{\omega}_d) + B(\omega_m - \omega_d) + K(\theta_m - \theta_d) - \tau_{ext} = 0, \tag{2.14}$$

where s has a relative degree of one with respect to the control input (Eq. 2.13). The current development makes it possible to avoid the use of the measured joint acceleration ($\dot{\omega}_m$) which is not reliable due to the noise.

2.7 Human Subject - Performance

In many aspects, human performance and engineering go hand-in-hand as the body is engineered to move efficiently and effectively. Human performance is concerned with measuring and perfecting the efficiency of human movement. This efficiency is strictly correlated to the physiological effects associated with human exercise. Typical physiological measurements collected for human performance research and involved in

this research are electromyography (EMG), heart rate (HR), and oxygen consumption (VO_2). Despite the simplicity of their measurements, physiological effects are complex as everyone has varying physiological functioning. They depend on the unique features of each person (organismic variables) such as force capacity, musculoskeletal distribution, body mass index, and flexibility. Besides, they display time-varying dynamics due to fatigue, body temperature, level of hydration, etc. As a result, modeling and controlling muscle performance is challenging but necessary in some areas of research.

2.7.1 Dynamics

Human dynamics are the description of the mechanical, physical, and biochemical behavior of the human body to determine current and future states associated with actions and reactions. Human dynamics is a very wide term, but in this research, they will be focused on the human reaction to the interaction with an AEM during advanced exercise.

Biological Factors

Human dynamics during exercise are very complex and time-varying because of the several biological factors affecting these dynamics such as, for example:

- Interaction force between human and machine (impedance magnitude).
- Musculoskeletal position, speed, and orientation.
- Musculoskeletal distribution (lengths, weights, etc).
- Fitness level (strength, flexibility, stamina, etc).
- Level of hydration.

- Body temperature.
- Muscle fatigue.
- Mood and psychological behavior.

Human dynamics as a result of exercise are reflected as physiological effects. These effects are presented below.

Muscle Activations

The muscle contractions generating the movement are produced by electrical signals transmitted from the motor neurons to the muscle fibers. This electrical activity can be measured using different techniques including contact-based, contact-free, invasive, and non-invasive sensing. In this study, muscle activations were only measured by using surface electromyography.

Muscle dynamics are based on the biological factors described in 2.7.1 and it might be modeled as follows:

$$\dot{M}(t) = f_1(M(t), u_m(t)), \tag{2.15}$$

where $M(t) = [M_1(t), M_2(t), ..., M_n(t)]$ is a vector of n muscle activations and $u_m(t)$ is a nonlinear time-varying function including all variables affecting muscle activations. Due to the complexity of the muscle dynamics, this study doesn't aim to model or estimate the activations. Thus, they are measured by using electromyography sensing as biofeedback.

Electromyography is the best-known electro-diagnostic technique used to measure the electrical activity produced in the musculoskeletal system. This technique provides non-invasive access to the internal physiological processes causing the

muscles to generate force and movement which is helpful for studies in human performance and most of the rehabilitation practices [93]. Rehabilitation research with electromyography is normally more complex, especially when it is associated with diseases of motor units that require the integration of electromyography with the nerve conduction process. In those cases, electromyography might require invasive measurements including physical insertion and movement of needles for electrical signal recording [21].

Electromyography sensors, better known as EMG sensors or EMGs, have electrodes to be in contact with the user skin above the muscle fiber to be measured. The muscle activity is then reflected by the electrical signals detected with electrodes. EMGs are becoming very popular because of their potential applications including prostheses, rehabilitation machines, sports, and human-machine interactions [18]. For instance, EMGs for fitness and performance are used for identification of muscle activity, effort, fatigue, etc [98]; and for rehabilitation by identifying interactions with rehabilitation robots, prostheses, and exoskeletons [42].

In this study, individual EMGs are directly used as biofeedback. However, this study could be extended to encompass training optimization based on specific synergies. In the last years, researches have been performed to understand the relationship between the central nervous system (CNS) and the control of the muscles to perform a specific task [148, 143]. Most of these researches have been used for rehabilitation purposes. For instance, neuroprostheses with FES for people with paraplegia have been developed to help them walk again. The synergy principle made it possible to optimize the FES having multiple effectors [3]. Other researches have focused on the synergy analysis for the identification of people particularities [122]. The analysis and identification of these synergy patterns as physiological markers empowered to development of better rehabilitation plans and approaches[17].

The human body has muscle redundancy as a result of having more muscles than mechanical DOFs. Therefore, CNS can choose between different muscle combinations to achieve the desired movement. This flexibility provides multiple possibilities with different efficient behaviors. Furthermore, this capability allows the avoidance of some muscle groups without affecting the achievement of the movement [133]. For instance, controlling the movement of the arm to reach an object requires the coordination of multiple muscles acting on many joints. CNS simplifies the control by directly driving initial states to the final ones through the combination of muscle synergies [22].

Heart Rate (HR)

Heart rate, also known as pulse, quantifies the number of heartbeats per minute (BPM) in a person. A normal HR in adults is in the range from 60 to 100 BPM. Their values can vary based on several factors including but not limited to gender, age, and health. For instance, females have a higher HR than males as a result of their smaller heart [33, 23]; and overweight and pregnant people usually have the highest HR.

The main variables in the HR dynamics and widely used on human performance are BPM and maximum heart rate (HR_{max}). Some training plans are designed to reach specific BPM values (known as HR zones or target zones) where the performance capacity is at optimal levels [48, 73]. Sometimes the target value is selected as the HR_{max} as the most demanding way of exercise. A common way to estimated the maximum heart rate is by subtracting your age from 220. However, the best option (and safer) is by performing a cardiovascular experiment.

Heart rate dynamics can be expressed as follows:

$$\dot{HR}(t) = f_2(BPM(t), HR_{max}, u_{hr}(t)), \tag{2.16}$$

where f_2 is a unique function on each person, BPM and HR_{max} are the main heart rate variables, and $u_{hr}(t)$ is the nonlinear time-varying function including all the unknown and unmeasurable parameters affecting heart rate. Same as muscle activations, heart rate dynamics are complex and unpredictable. So, they are not usually estimated, but measured by heart rate monitors.

Oxygen Consumption (VO_2)

Oxygen consumption is a metabolic variable that quantifies the oxygen taken by the body per minute. The measurements of metabolic variables can involve direct and indirect calorimetry using open-circuit and closed-circuit respirometry methods. Open-circuit methods include flow chambers where the subject trains inside. Closed-circuit methods are more common. They are laboratory-based and include gas analysis systems [95, 156]. Other measured variables with the metabolic system are carbon dioxide production (CO_2), and respiratory exchange ratio (RER). The device reads the data and transmits it at the end of the experiment for future analysis. The limitation of the available metabolic units is their lack of capacity to interface with other devices in real-time. Nonetheless, VO_2 can be estimated based on HR as a way of integration with other systems.

Most research related to the estimation of VO_2 based on HR is oriented to the maximum oxygen consumption (VO_{2-max}). VO_{2-max} is the highest rate of oxygen that a person can consume during incremental exercise and also one of the best indicators of performance in a subject. The best reference to determine that a VO_{2-max} has been reached is a leveling off in the VO_2 despite an increase in the

intensity of the exercise (see Figure 25).

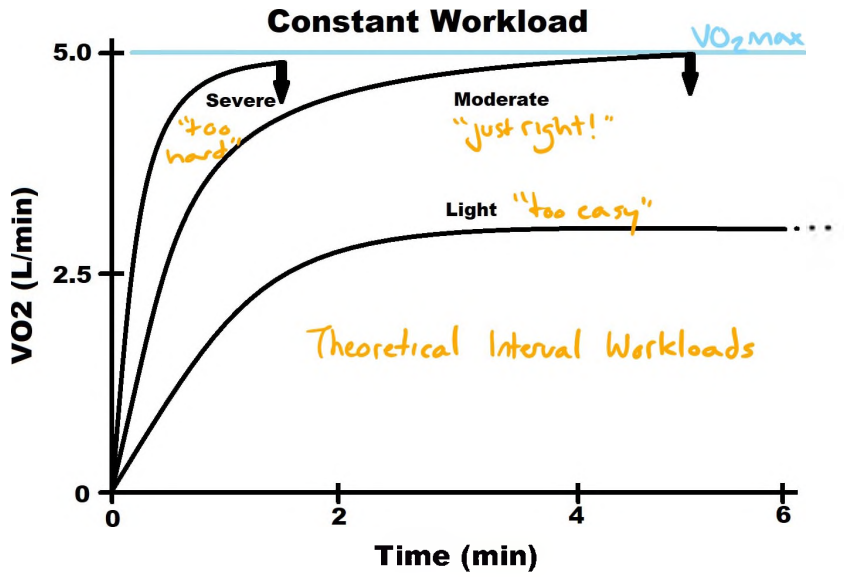

Figure 25: Example of maximum oxygen consumption (VO_{2-max}) [68].

Researches related to VO_{2-max} are mainly used for fitness planning [140] [125]. Some others are developed for estimation of cardiovascular risk factors [64]. However, the continuous oxygen consumption estimation is valuable to be able to monitor the intensity of the physical activities. Therefore, some algorithms also HR-based have been developed but limited for specific activities such as walking and cycling commuting [124, 141]. More versatile algorithms capable of providing better estimations have been reported [91, 92], but they are private for commercial purposes.

It is known that the VO_2 dynamics, as well as any other physiological effect, depends on several factors. Thus, its dynamics can be described as follows

$$\dot{VO_2}(t) = f_3(W, H, A, HR(t), \dot{HR}(t), HR_{max}, VO_{2-max}), \tag{2.17}$$

where f_3 is a unique function on each person; W, H, and A are constants related to weight, height, and age of the subject respectively; $BPM(i)$ is the number of beats

per minute, $\dot{HR}(t)$ is the variation of the heart rate respect to time, and HR_{max} and VO_{2-max} are constant obtained from a VO_{2-max} experiment.

Same as the previous physiological effects (muscle activations and heart rate) the oxygen consumption dynamics are complex and unpredictable, so, they are mainly measured by closed-circuit respirometry methods.

CHAPTER III

PHYSIOLOGICAL EFFECTS UNDER ADVANCED TRAINING

3.1 Overview

The study of the physiological effects associated with training plays a key role in this work because of the strict correlation between exercise performance and training effects. It is important to note that every training pattern produces a unique combination of training effects. For instance, resistance-based training such as weight lifting does not produce the same effects on the cardiovascular and cardiorespiratory system as cardio-based training such as aerobic fitness. Therefore, real-time experiments were performed under these 2 different training patterns.

Experiments were carried out using a similar HMI multi-system network (see the scheme in Figure 26). This network includes computers, robots, cameras, and physiological sensors. Each of these components is required for the success of the experiments. These systems and devices are presented below.

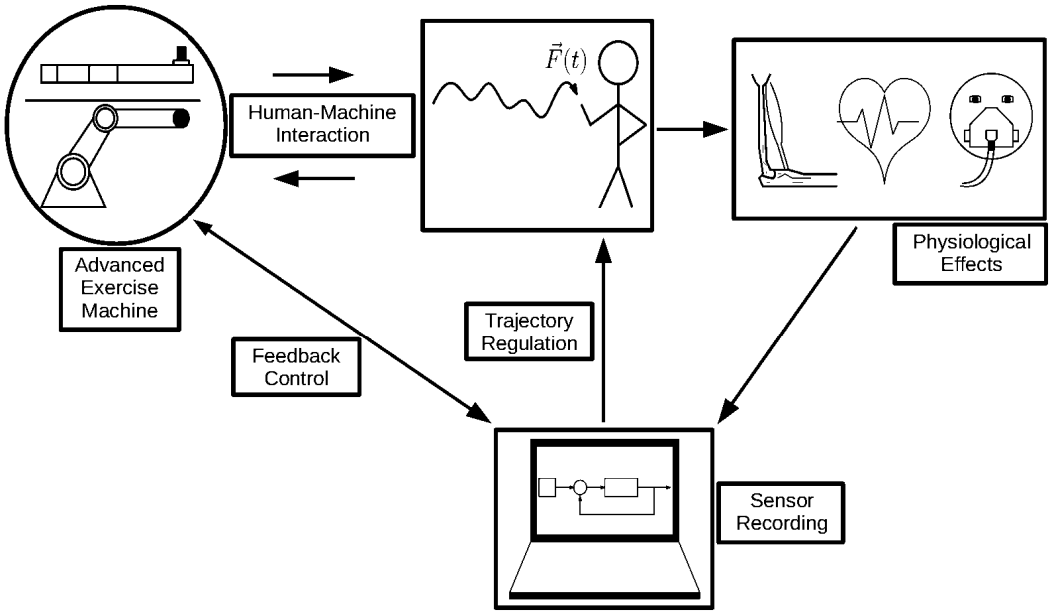

Figure 26: Scheme of the HMI network for real-time experiment.

3.2 Real-time experiment systems and devices

dSpace MicroLabBox

The dSpace MicroLabBox is a system class that provides a high-performance control, test, and measurements [37]. It is a simple and fast system at a compact size. It has a Freescale QorlQ P5020 dual-core 2 GHz processor with 1 GB DRAM and 128 MB flash memory. It admits until 32 analog-inputs, 16 analog-outputs with ± 10 V and ± 8mA and 48 bidirectional digital channels with functionality for:

- 6 x Encoder sensor input
- 2 x Hall sensor input
- 2 x EnDat interface
- 2 x SSI interface
- Synchronous multi-channel PWM

- Block commutational
- PWM

Figure 27: dSpace MicroLabBox [37].

The MicroLabBox (see Figure 27) is used as the central controller. Its main function is to run the main programs, control the robots and devices, and record the data from the network.

Load cell or F/T sensors

Load cells or F/T sensors are transducers which convert force and torque into an electrical signal.

Figure 28: Example of a load cell.

These transducers are used to measure the interaction force between the human and the robot at the point of contact during the experiments.

Polar Beat monitor

The Polar Beat monitor (see Figure 29) is a heart rate sensor [115].

Figure 29: Heart rate monitor Polar Beat [115].

The heart rate measurements can be performed in real-time or recording for later study. For the current experiments, heart rates have been recorded for later study.

Cosmed K4b2

Cosmed is an organization specialized in metabolic and cardiorespiratory diagnostics. The Cosmed K4b2 (see Figure 30) is the device used in the experiment to quantify the cardiorespiratory effects of metabolic diagnostic [19].

Figure 30: Standard ambulatory metabolic system COSMED K4b2 [19].

The measurements of this machine provide useful estimations about the physiological effects associated with the metabolic cost and energy expenditure during

training.

Wireless Delsys System

The Delsys Trigno Wireless EMG system (see Figure 31) is a high-performance device capable of measuring EMG signals easily and reliably [32].

Figure 31: Trigno wireless EMG system [32].

A total of 16 EMGs can be used. Each of them has to be placed in line with the muscle fibers for a correct measurement. The muscle selection depends on the kind of training to be performed.

Cortex System

The Cortex system (see Figure 32) is a group of 10 infrared cameras capable of recording and processing the movement of objects and people.

Figure 32: Cortex Camera System in Parker-Hannifin Human Motion and Control Laboratory - CSU. Adapted from [111]

Cortex system works measuring the position of reflective markers strategically located at each point of motion interest. This system is used when human movement analysis is required. Previous research has made use of this system for model fitting and analysis of human movement during training.

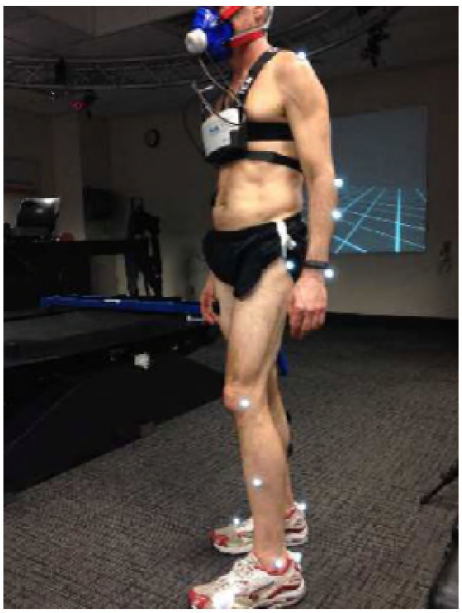

Figure 33: Subject before test in the at the Parker-Hannifin Motion and Control Lab, Cleveland State University.

An example of a subject with motion markers and EMGs can be seen in Figure 33.

LabJack T7 and U3-HV

Figure 34: Labjack T7 [84] and LabJack U3-HV [85].

The LabJack T7 is the most accurate DAC of the LabJack family. It has three communication interfaces (USB, Ethernet, and WiFi), and numerous built-in firmware features [84]. The LabJack T7 is used to interface between any system and the computer connected to the projector. Its main function is to read the data and send it to the graphical user interface for visualization.

The Labjack U3 is a versatile DAC with configurable analog and digital I/O for accurate measurement and control within simple analog and digital systems [85]. The version HV (high voltage) reduces slightly its accuracy but supporting voltage up to 10 volts. As well as the Labjack T7, the LabJack U3 is used to interface between systems. When more than one DAC is required, the U3 is used.

3.3 Cardio-Based Training with a Powered Rowing Machine

During these experimental trials, we aimed to investigate the physiological effects (muscle activation, heart rate, and oxygen consumption) as a result of the variations

in the impedance parameters associated with the eccentric workloads generated by a powered rowing machine. Thereby, the impedance during the return stroke was increased through the stages, while the pull stroke remained almost constant.

3.3.1 Methodology

This study had an IRB which covers for Ethical Approval. It was provided by Cleveland State University with reference number 30305-RIC-HS. An informed consent form was signed by each subject conducting the experiment (see Appendix D).

The methodology of the study was experimental and presented in detail in [28, 27]. The two cardio-based exercise trials were a full-body row (FBR) and low-body row (LBR) (see Figure 35). They were performed on different and non-consecutive days. Each of them consisted of 12 minutes of training including four stages with different eccentric workloads. Greater eccentric muscular contractions and metabolic costs were expected by increasing only the eccentric workloads.

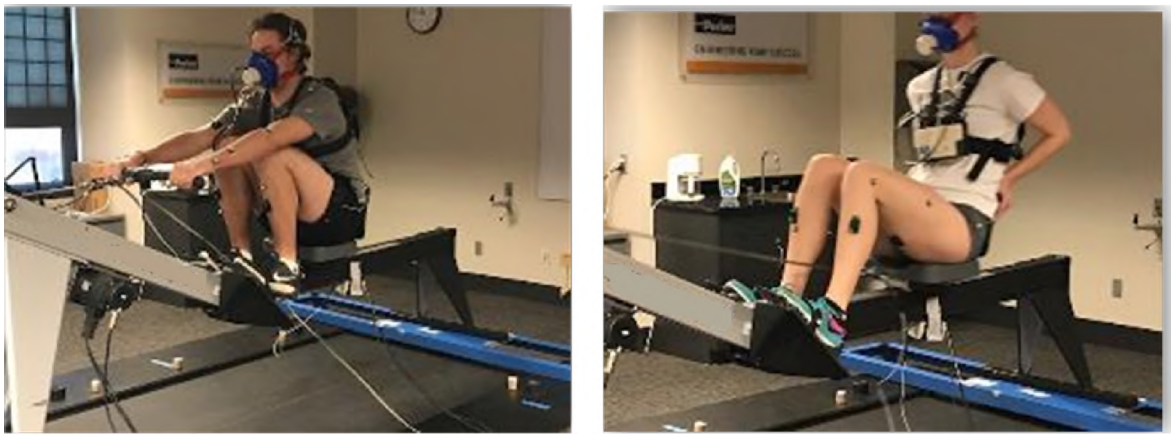

Figure 35: Full-body and low-body rowing configuration (LBR and FBR respectively).

Ten participants (5 males and 5 females) between the ages of 18 and 60 with an average age of 26.3 $\pm$ 6.63 years, height of 66.5 inches, and weight of 139.97 pounds were recruited through a convenience sample through word of mouth, social

media, and flyers. To participate in the study, subjects had to be free of any musculoskeletal injuries, cardiovascular disease, and/or any limitations that prevented them from participating in regular exercise. These subjects were subjected to a four-stage, 12-minute rowing protocol. After each stage (3 minutes), the average eccentric workload was increased, while the average concentric workload remained constant (the concentric and eccentric resistances used on the trials can be seen in Table II and III).

Table II: Average power per stroke in FBR.

Stage	Concentric (W)	Eccentric (W)
1	150	100
2	150	120
3	150	155
4	150	190
Cadence:	60 strokes/min	

Table III: Average power per stroke in LBR.

Stage	Concentric (W)	Eccentric (W)
1	80	65
2	80	110
3	80	135
4	80	175
Cadence:	70 strokes/min	

Figure 36 shows an example of the power and forces produced during training with a conventional rowing machine. As it can be seen in Figure 37, the powered rowing machine programmed with low eccentric resistance replicates the behavior of the conventional rowing machine. Figure 38 shows an example of the power and forces produced during training with high eccentric workloads.

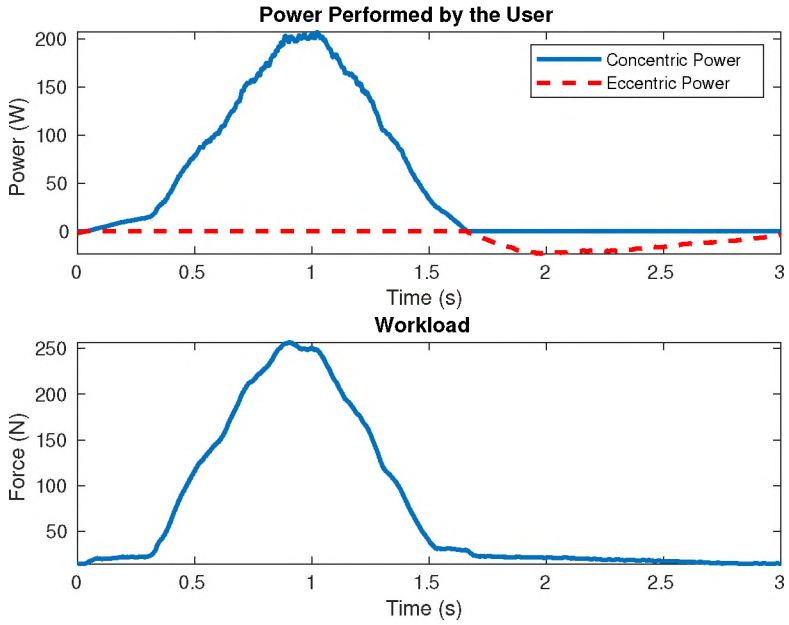

Figure 36: Typical example of the concentric and eccentric power and force in a conventional rowing machine.

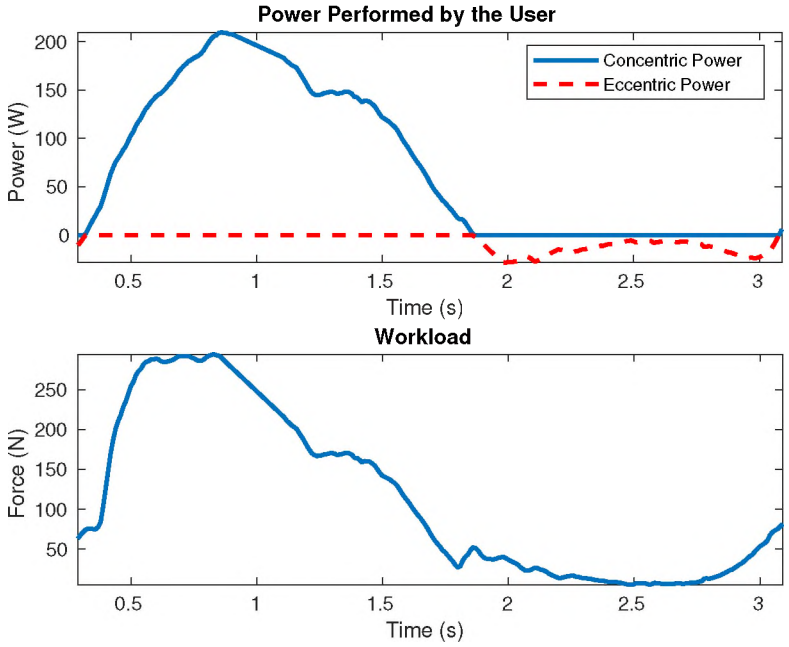

Figure 37: Typical example of the concentric and eccentric power and force during stage-1 with the powered rowing machine at a low eccentric setting.

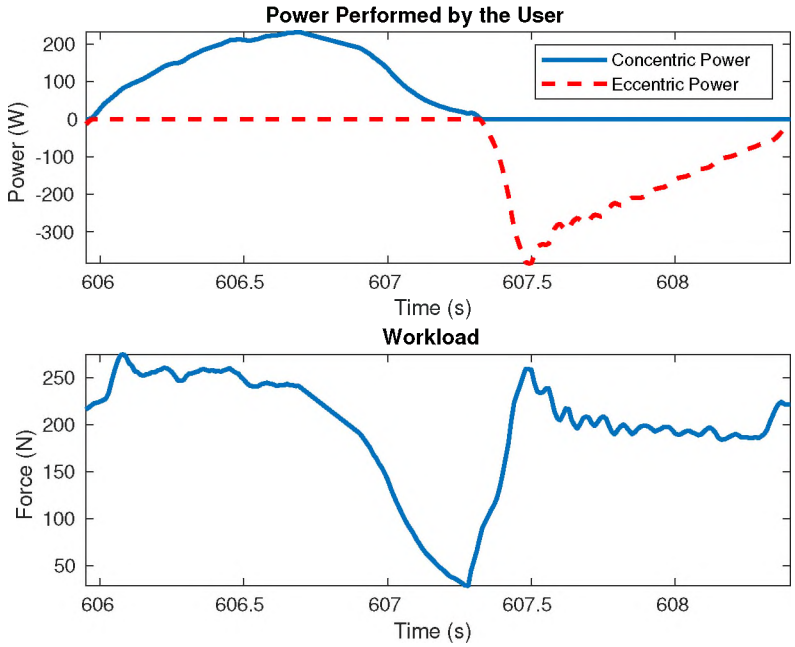

Figure 38: Typical example of the concentric and eccentric power and force during stage-4.

During the training sessions, the following physiological effects were measured to examine the effectiveness of the powered rowing machine were:

1. Cumulative EMG: muscle activations from both contractions (concentric and eccentric) were collected as a single raw signal. First, the data was normalized by removing the mean and dividing each value by its maximum activation. Then, the resulting data was rectified to obtain a positive signal. Finally, the measurement values of the data were added for each of the 3-minute trials. As a result, the cumulative EMG provides information about the total activation for both contractions. The same procedure was performed for each of the following eight muscles selected for the experiment:

   (a) Rectus Femoris (RF).

   (b) Biceps Femoris (BF).

(c) Gastrocnemius (GM).

(d) Tibialis Anterior (TA).

(e) Biceps Brachii (BB).

(f) Posterior Deltoid (PD).

(g) Trapezius (LT).

(h) Latisimus Dorsi (LD).

2. Metabolic data: oxygen (O_2) consumption was collected through a mobile metabolic system. The measurements presented are the average recorded during each stage.

3. Heart rate (HR): heart rate was monitored by using a heart rate sensor. The measurements presented are the average recorded during each stage.

For this study, the experiment trials required the use of a dSpace MicroLabBox real-time data acquisition and control system (dSPACE GmbH, Paderborn, Germany), a COSMED K4b2 portable metabolic unit (The Metabolic Company, Rome, Italy), a heart rate sensor (Polar USA, United States), and a set of wireless EMG sensors (Trigno Wireless EMG, Delsys Inc.). The MicroLabBox was utilized for controlling and operating the powered rowing machine, while also allowing for the recording of all data related to the experiments. The COSMED K4b2 collected and wirelessly transmitted metabolic diagnostics (heart rate and oxygen consumption) to the K4b2 software, while the Delsys Trigno Wireless EMG system aided in collecting the EMG (muscle) activity of the eight muscles selected for the study. Eight wireless EMG sensors transmitted data back to the Delsys EMGworks data acquisition software for further analysis.

Following the study, 1-way repeated measures of ANOVA were used for the statistical analysis of the mean, standard deviation, mean difference, and level of significance of oxygen consumption (VO2) and heart rate (HR). The level of marginal significance selected to determine the difference in metabolic variables was 0.05 (statistically significant). The statistical difference was evaluated between each stage where the eccentric workload was increased. The statistical analysis for both, FBR and LBR, were performed separately.

3.3.2 Results - Four Levels of Eccentric Impedance

Upon completion of the powered rowing machine sessions, our initial aim was achieved by acquiring a variety of physiological effects as a result of the impedance variations. Increases in muscle activation, oxygen consumption, and heart rate were witnessed through each stage, thus displaying the effectiveness of the system's ability to harness the effects of eccentric exercise. Muscle activation was shown to increase for all muscles with each stage through the use of EMGs for both, the LBR (see Figure 41) and the FBR (see Figure 42). It is important to consider that there are variations in the biomechanics of each subject - especially when none of the participants were avid rowers - thus affecting to what extent each subject targeted each particular muscle. For example, those who showed smaller activation of the lower body muscles generally compensated by utilizing more of their upper body. Despite this, with each increasing eccentric workload, the overall muscle activation of all subjects continued to increase. Rectus femoris (RF) and biceps femoris (BF) increased dramatically with the eccentric load. These muscles have exactly opposite functions, so this suggests a large increase in antagonistic co-contraction. This is likely the result of the task becoming difficult to control (intrinsically unstable), and because the human neural system has large time delays, the joints are stiffened by co-contraction, so the series elastic elements operate at a higher point in their nonlinear force-length relationship.

Oxygen consumption also revealed a significant increase ($p<0.05$), seen between stages one and two for both the FBR and LBR, and continued to increase through the third stage for the FBR sessions (see Figure 39). Heart rate significantly increased ($p<0.05$) as well through each stage for both configurations (see Figure 40). When calculated for the percentage of maximum heart rate (MHR), subjects showed an increase from 61.5% to 75.4% of MHR during the FBR and from 55.8% to 67.3% of MHR during the LBR sessions, thus demonstrating an effective training effect on the cardiovascular system.

Positive training effects on the cardiorespiratory, cardiovascular, and musculoskeletal systems were exhibited, suggesting that the powered rowing machine can lead to effective training protocols. The powered rowing machine was capable of maximizing the return stroke through a controllable resistance parameter and maximizing the strength of muscles when they are eccentrically contracting. With no change in the concentric phase of the rowing stroke, it can be assumed that the increased metabolic demand during the sessions was a result of the eccentric muscle contractions during the return phase of the rowing stroke. This is also true of the increased muscle activation, as the muscles were only targeted with a heavier workload when performing negative work. The ability to have great control over the parameters of the movement in a fluid and dynamic manner provides a great tool that can contribute to human performance, injury prevention, and rehabilitation.

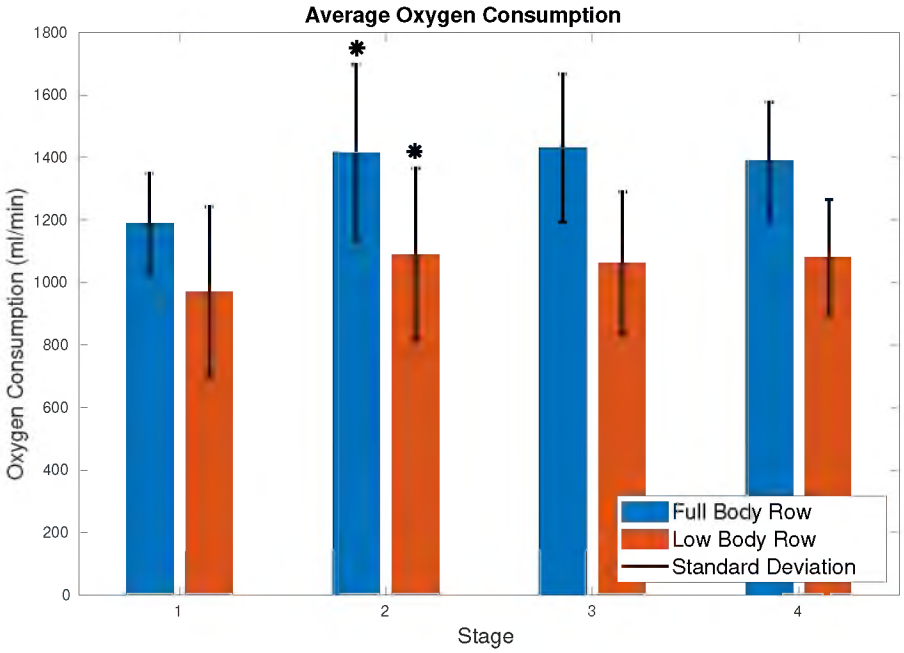

$*$ Denotes a significant increase ($p < 0.05$) with respect to the previous stage.

Figure 39: Oxygen consumption average for each stage during FBR and LBR.

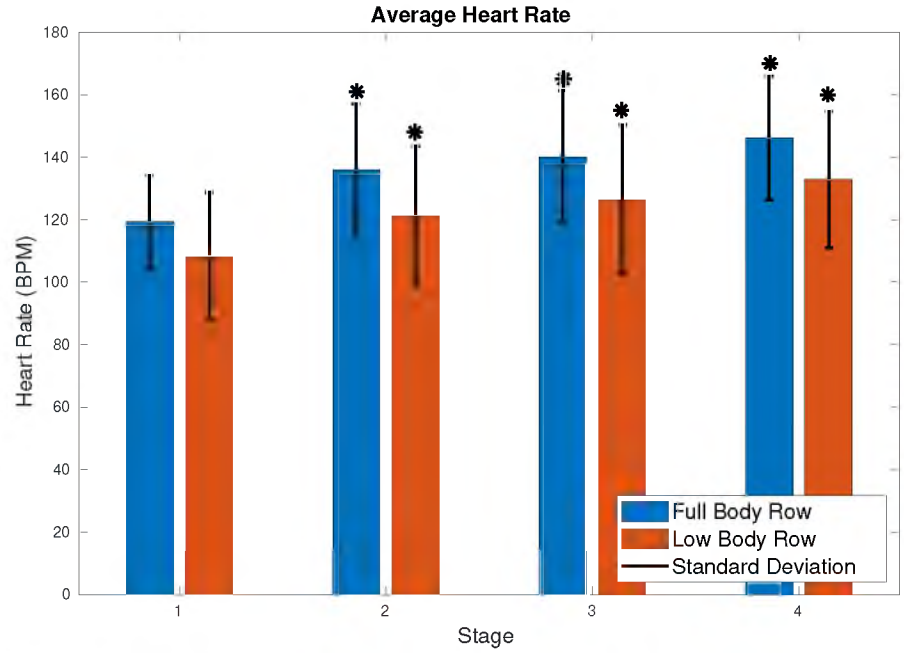

$*$ Denotes a significant increase ($p < 0.05$) with respect to the previous stage.

Figure 40: Heart rate average for each stage during FBR and LBR.

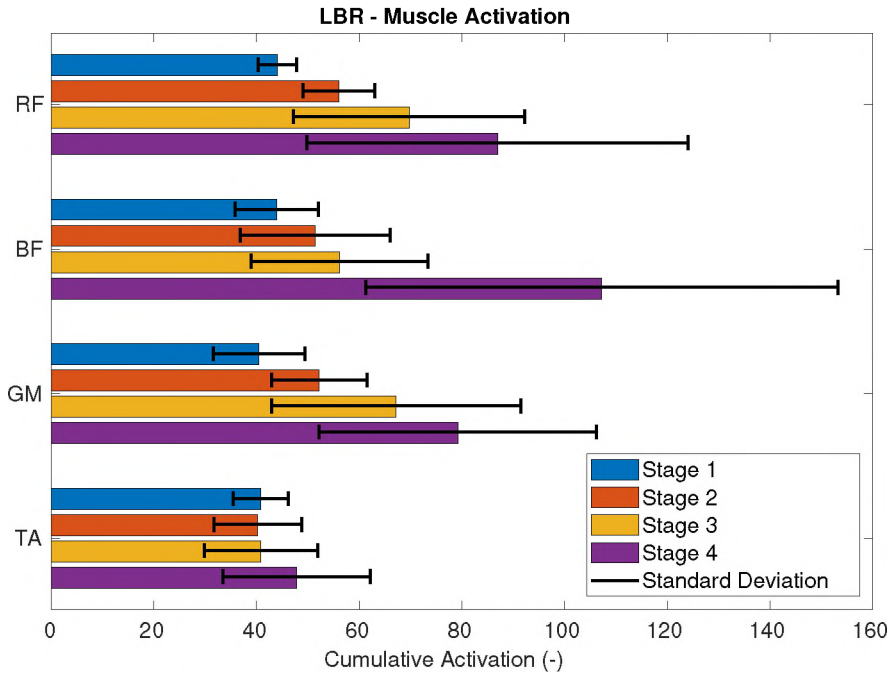

Figure 41: Cumulative activation average for each stage during LBR.

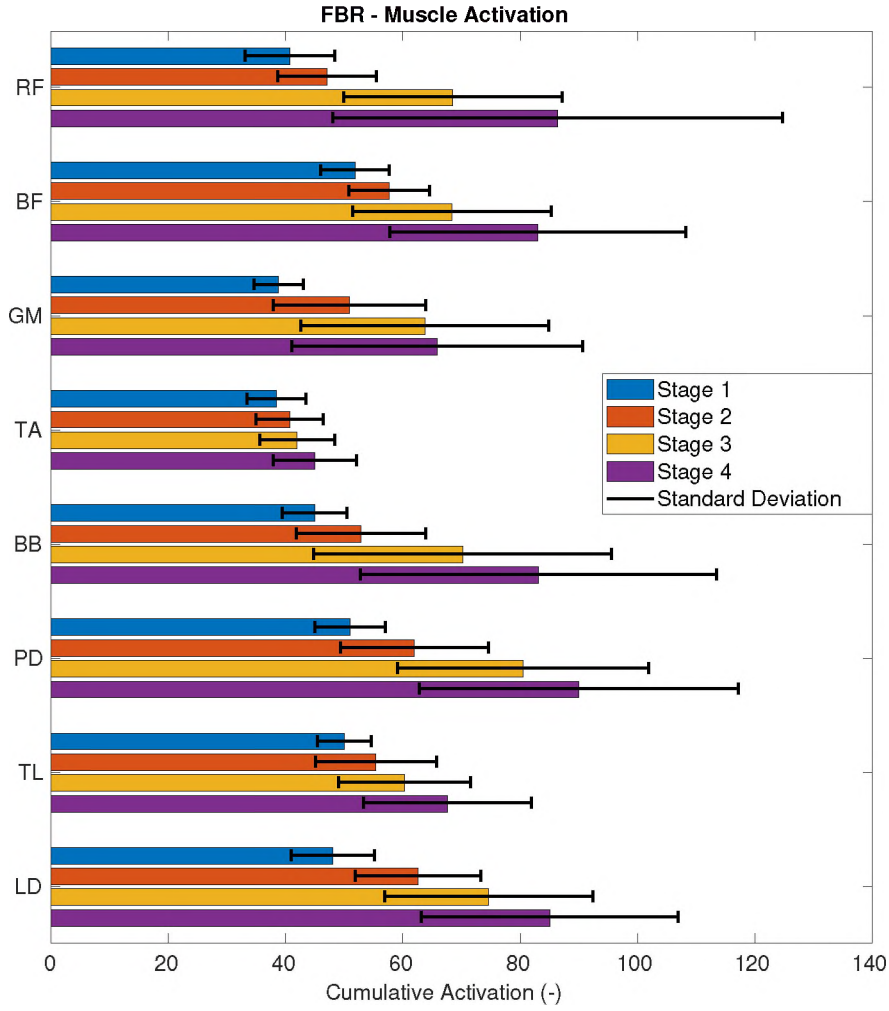

Figure 42: Cumulative activation average for each stage during FBR.

With its ability to utilize eccentric exercise, a powered machine shows much promise in the improvement of human performance in a variety of settings. In a microgravity environment, a powered machine offers to be an effective tool that allows for both resistance and aerobic exercise in one, lightweight apparatus. The adaptability of the machine is its strongest asset. For instance, based on the same functionality principle, the machine can be adapted for a different type of training similar to ARED [105], a resistive exercise device developed for microgravity that

uses a rowing machine-like mechanism. Besides, by its ability to maximize eccentric training through customized resistance, the powered rowing machine could serve as a starting point to develop better training methods or rehabilitative tools.

3.4 Resistance-Based Training with the 4OptimX

During these experimental trials, we aimed to investigate the physiological effects (muscle activation, heart rate, and oxygen consumption) as a result of the variations in the trajectory and impedance parameters from the robot. The robot used was the 4OptimX and the variable parameters related to the trajectory and impedance were the orientation of the ellipsoidal training trajectory and the stiffness impedance respectively.

3.4.1 Methodology

This study had an IRB which covers for Ethical Approval. It was provided by Cleveland State University with reference number 30305-RIC-HS. An informed consent form was signed by each subject conducting the experiment (see Appendix E).

The experimental procedure followed a conventional calibration process consisting of a warm-up and isometric tests [7] (trial 0 in Table IV). The isometric tests are used to assess muscle strength for the EMG sensor calibration. The subject is required to maintain a constant position where muscles are capable of producing maximum forces [46]. Then, the experiment proceeds with a 36-minute protocol of 17 1-minute trials. Each 1-minute workout (odd-number trials from 3 to 35 in Table IV) was followed by a 1-minute rest (even-number trials).

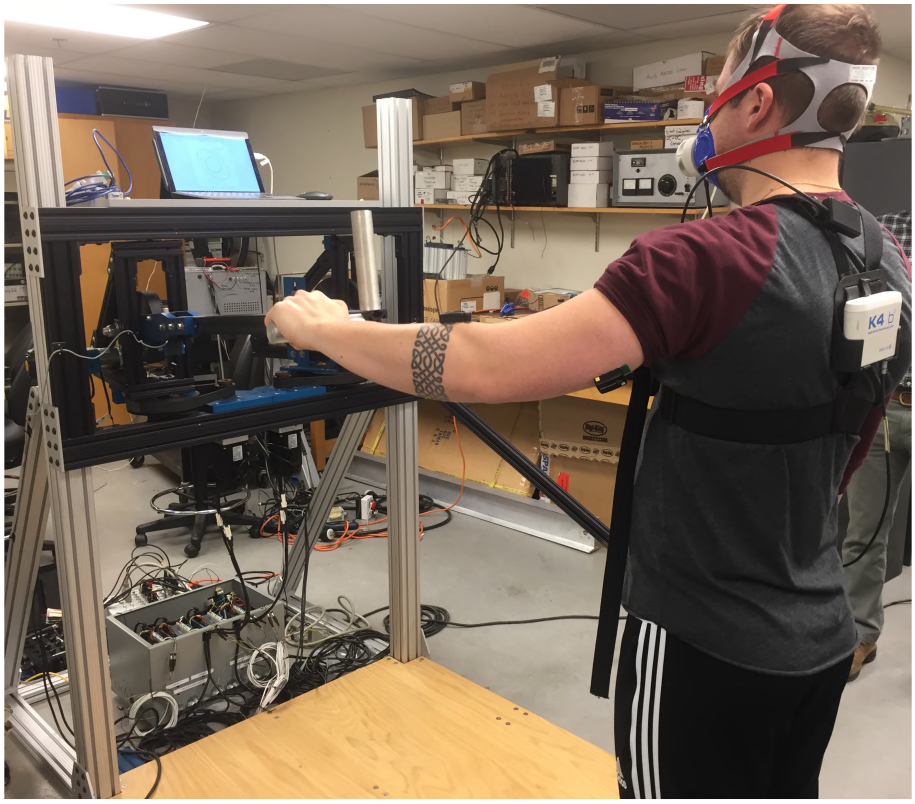

Figure 43: 4OptimX experiment configuration.

Table IV: 4OptimX experiment planning (reference in Table V and VI

Trial	Impedance	Speed	Ellipse orientation (deg)
1	(Warm up)	(Warm up)	(Warm up)
3	Low	Low	90
5	Low	Low	45
7	Low	Low	0
9	Low	Low	-45
11	High	Low	90
13	High	Low	45
15	High	Low	0
17	High	Low	-45
19	High	High	90
21	High	High	45
23	High	High	0
25	High	High	-45
27	Low	High	90
29	Low	High	45
31	Low	High	0
33	Low	High	-45
35	Low	Super-high	0

One male participant of 22 years old, height of 180 cm, and weight of 91.8 kg was recruited. To participate in the study, he had to be free of any musculoskeletal injuries, cardiovascular disease, and/or any limitations that prevented him from participating in regular exercise. The 17 workout trials were resistance-based training including different levels of resistance and speeds of the trajectory (see resistance and speed parameters in Table V and VI). Greater eccentric muscular contractions and metabolic costs were expected by increasing the impedance and the speed of the trajectory.

Table V: Impedance reference for the 4OptimX experiment planning (the same parameter for each DOF).

Impedance	Inertia (kgm^2/rad)	Damping (Nms/rad)	Stiffness (Nm/rad)
Low	0.035	0.4	1
High	0.035	0.4	7

Table VI: Speed reference for the 4OptimX experiment planning.

Speed	Period of revolution (s)
Low	8
High	4
Super-high	2

During the protocol, the user is asked to follow a path against the machine's neutral path and resistance. The robotic machine establishes a zero-effort circular path, and the subject is asked to follow an elliptical trajectory of 90 and 60 centimeters of axes. The control system produces a user-defined resistance based on the deviations from the neutral path and the force/torque applied by the subject. The trajectories and positions involved in the training protocol can be seen in Figure 44. The target position (X_d) is labeled with a blue dot which moves periodically over a blue ellipsoidal curve of fixed axis lengths and programmable orientation. The user position (X_a) is labeled with a green dot and tries to follow the blue dot except on the simulation environment where the user performs a perfect tracking (in simulation

the user position is equal to the desired position). The red label (X) moving periodically over a red circular curve of a radius of 40 centimeters represents the machine's trajectory where the impedance is zero. Any deviation from the machine's trajectory produces an interaction force by impedance control as follows:

$$\begin{aligned} F_{ext} &= I\ddot{e} + B\dot{e} + Ke, \\ \ddot{e} &= \ddot{X} - \ddot{X}_a, \\ \dot{e} &= \dot{X} - \dot{X}_a, \\ e &= X - X_a, \end{aligned} \tag{3.1}$$

where X_a, and X are the 2 dimensional vectors of the actual user (green dot) and the machine reference position (red dot) respectively; I is the acceleration gain (inertia impedance in Table V); B is the velocity gain (damping impedance in Table V); and K is the position gain (stiffness impedance in Table V).

It is important to note that results depend on the relative position of the subject with respect to the machine. Thus, a mark was placed on the ground to make the subject have the same relative position with respect to the machine during all the trials.

Meanwhile the subject is following the protocol, his/her muscle activations are measured and recorded. Since the supplied trajectories were in various ellipsoid patterns (horizontal, vertical, and angled), the major movements involved were flexion and extension in the sagittal plane, horizontal abduction and adduction in the transverse plane, and anterior circumduction movement. Therefore, some glenohumeral muscles [11] (see Figure 45) were selected for the study in the following order:

1. Brachialis.

2. Posterior deltoid.

3. Anterior deltoid.

4. Biceps.

5. Triceps.

6. Chest.

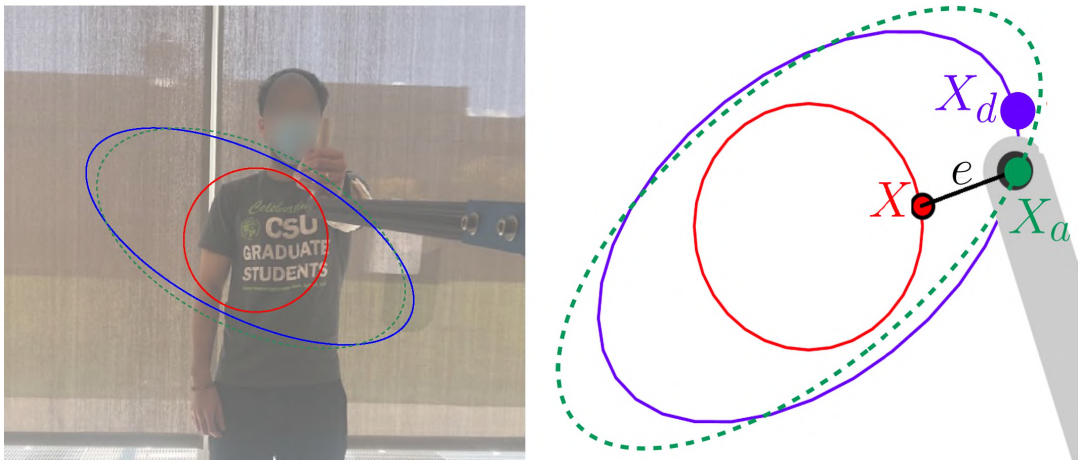

Figure 44: Positions involved in the training protocol: user position (green dot or X_a), target position (blue dot or X_d), and robot trajectory (red dot or X).

The brachialis and triceps, despite not belonging to the glenohumeral muscles, were chosen because of their relationship with the elbow movement. This relationship is able to provide information about involuntary rotations. The anterior and posterior deltoids were chosen because they are the main glenohumeral drivers. They are responsible for the space motion of the extended arm. The biceps brachii was chosen because of its synergistic work with the deltoid muscles. The chest was chosen because it is the main contributor in the glenohumeral adduction and stabilization of the shoulder.

During the resistance-based training session, the following physiological effects were measured:

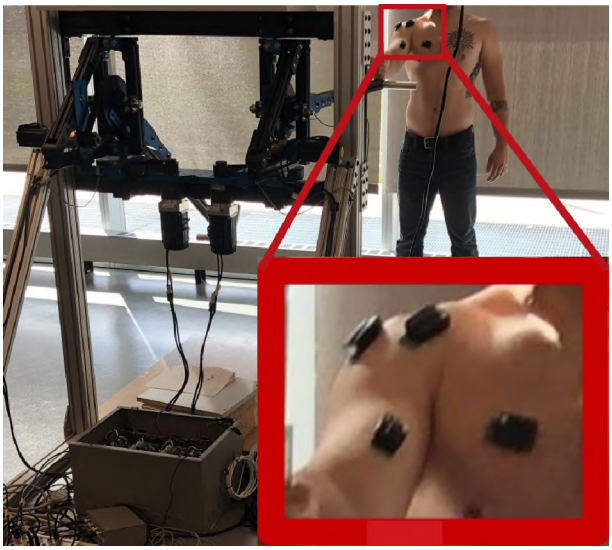

Figure 45: EMG location on the glenohumeral muscles.

1. Muscle activation: the raw muscle signals were recorded at a frequency of 2 kHz and real-time processed to obtain the muscle activations. First, they were normalized by removing the mean and dividing each value by its maximum activation (isometric test in trial 1). Then, a bandpass second-order Butterworth filter between 30 and 950 Hz is applied. Later, a full-wave rectification was performed. Finally, a low pass second-order Butterworth filter at 50 Hz was performed. The same procedure is performed for each of the 6 selected muscles.

2. Metabolic data: the VO_2, and CO_2 were collected through a mobile metabolic system. The measurements presented are the average recorded during each stage.

3. Heart rate: heart rate was monitored using a heart rate sensor. The measurements presented are the average recorded during each stage.

For this study, the experiment trials required the use of a dSpace MicroLabBox real-time data acquisition and control system (dSPACE GmbH, Paderborn, Germany), a COSMED K4b2 portable metabolic unit (The Metabolic Company,

Rome, Italy), a heart rate sensor (Polar USA, United States), a set of wireless EMG sensors (Trigno Wireless EMG, Delsys Inc.), and a Labjack data acquisition system. The MicroLabBox was utilized for controlling and operating the 4OptimX, while also allowing for the recording of all data related to the experiments. The COSMED K4b2 collected and wirelessly transmitted metabolic diagnostics (VO_2, CO_2, and HR) to the K4b2 software, while the Delsys Trigno Wireless EMG system aided in collecting the EMG (muscle) activity of the six muscles selected for the study. Six wireless EMG sensors transmitted data back to the Delsys EMGworks data acquisition software for further analysis. The Labjack was used to interface between the human and the robot providing a graphical user interface (GUI) for visualization.

3.4.2 Results

Upon completion of the experimental trials, our initial aim was achieved by acquiring a variety of physiological effects as a result of the changes in the trajectory and impedance parameters. These changes were witnessed in muscle activation, oxygen consumption, and heart rate but in different shapes and magnitudes. The results from each physiological system are presented below.

Effects in the Musculoskeletal System

The complete muscle activations from each trial can be seen in Appendix F. For better visualization, the muscle activations from each trial have been averaged and presented below:

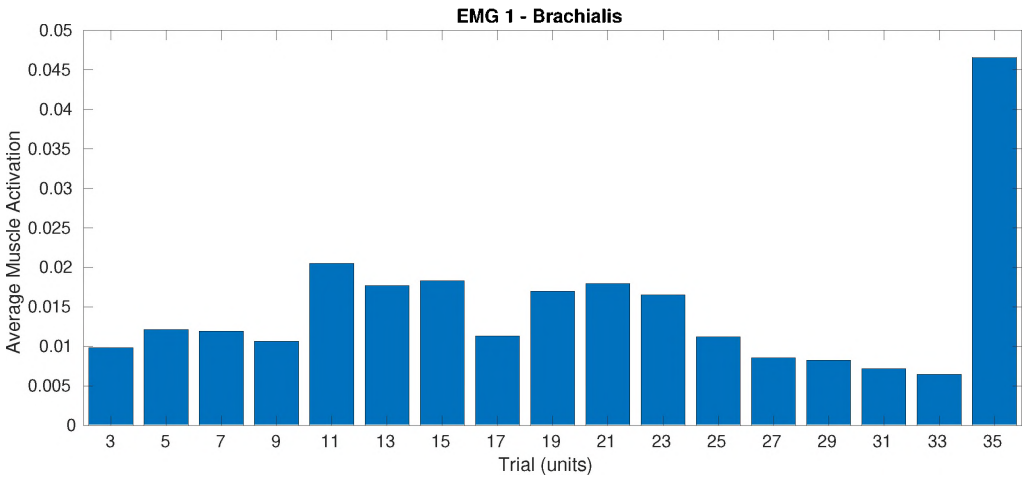

Figure 46: Average muscle activation on the brachialis (EMG-1) during each of the training trials.

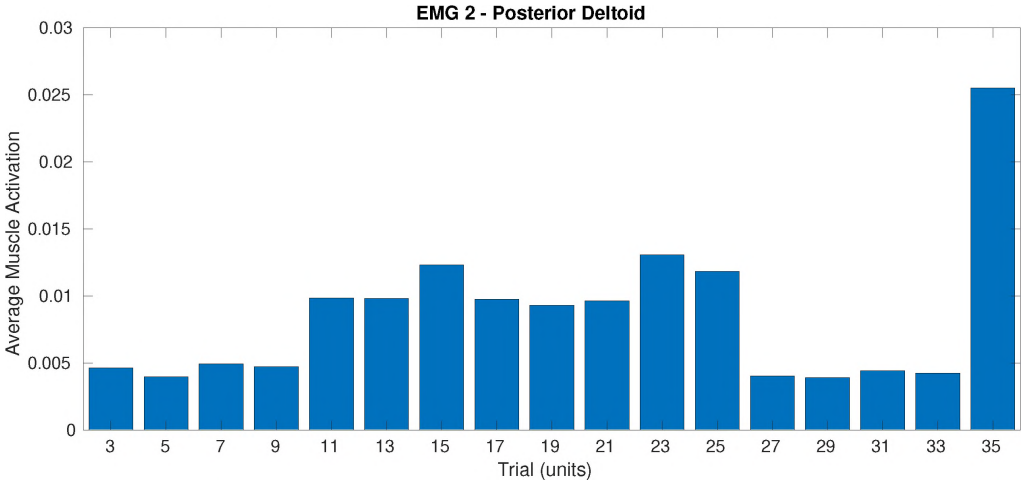

Figure 47: Average muscle activation on the posterior deltoid (EMG-2) during each of the training trials.

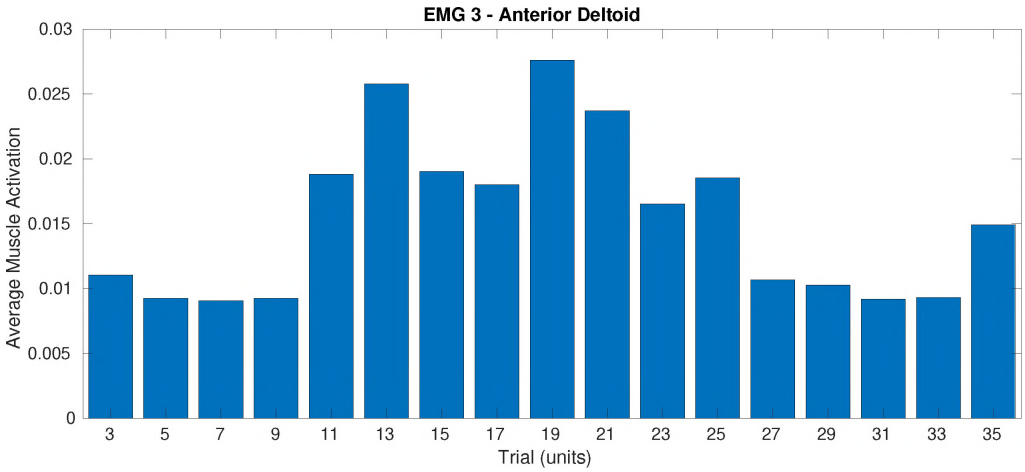

Figure 48: Average muscle activation on the anterior deltoid (EMG-3) during each of the training trials.

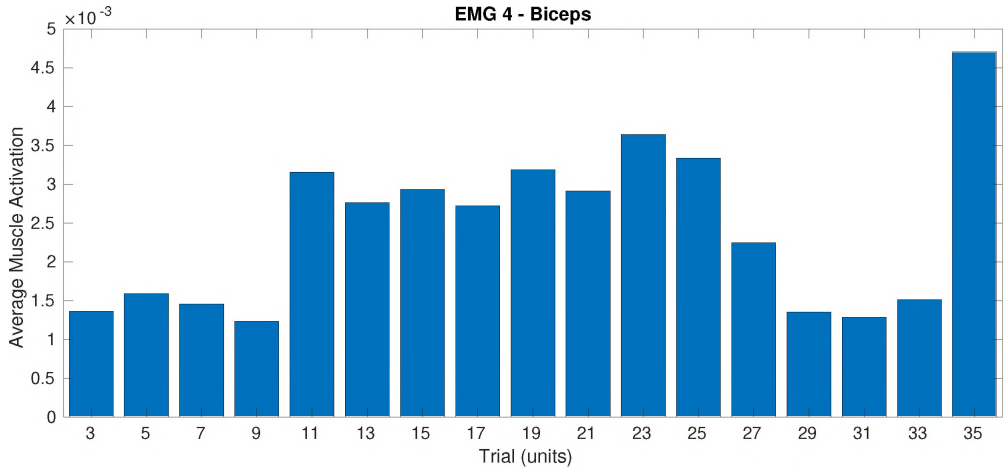

Figure 49: Average muscle activation on the biceps (EMG-4) during each of the training trials.

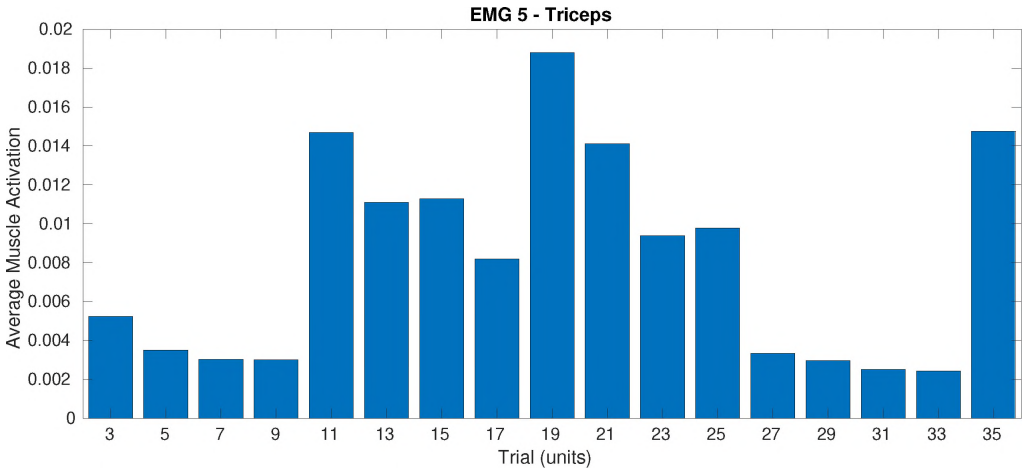

Figure 50: Average muscle activation on the triceps (EMG-5) during each of the training trials.

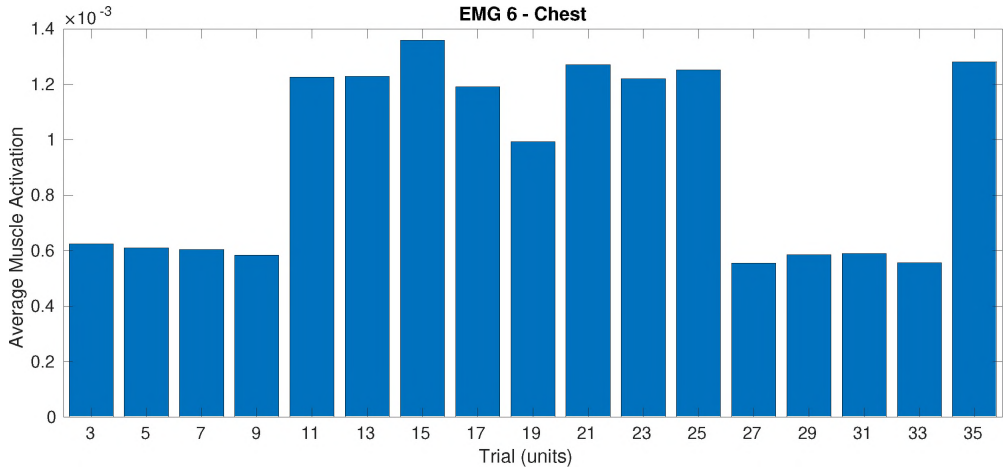

Figure 51: Average muscle activation on the chest (EMG-6) during each of the training trials.

Analyzing the results, the highest average muscle activation on the brachialis, posterior deltoid, and biceps (see Figures 46, 48, and 49) were observed in trial number 35 (the trial with the highest speed of trajectory). As a result, it could be seen that these three muscles are the most sensitive to the speed of the trajectory (more sensitive than by the impedance). On the other side, the anterior deltoid, triceps, and chest were mostly affected by the impedance.

Regarding the trajectory variations, under the same conditions of resistance and speed, higher activations were measured on the trials with an ellipsoidal orientation of 45^o (trials: 5, 13, 21, and 29) and -45^o (trials: 9, 17, 25, and 33). These results seem to suggest that inclined ellipsoidal trajectories produce a higher muscle effort. If that is the case, training protocols could be designed based on this finding.

Effects in the Cardiovascular and Cardiorespiratory Systems.

The HR (see Figure 52), VO_2 (see Figure 53), and CO_2 (see Figure 54) from each of the trials have been averaged and are presented below:

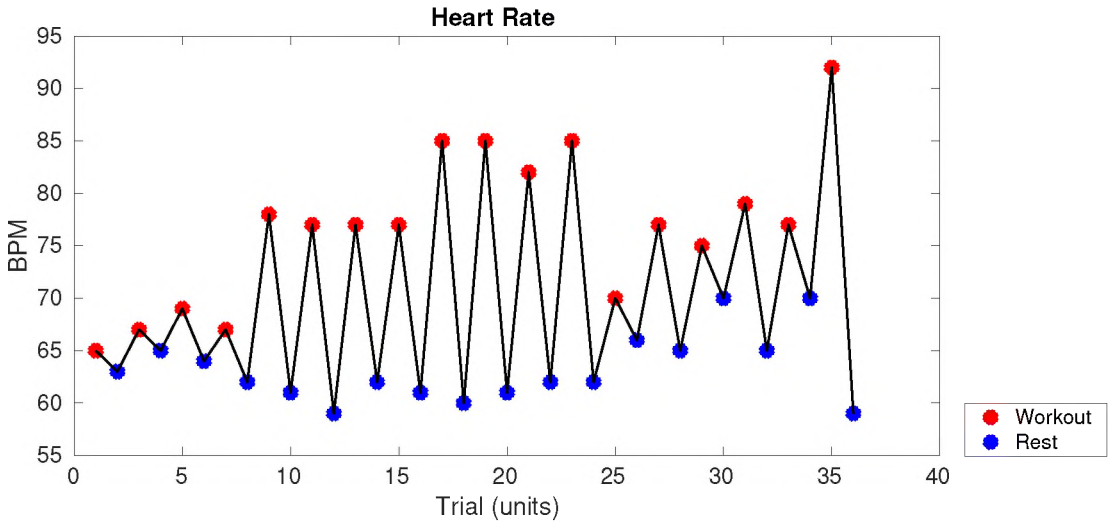

Figure 52: Heart rate during each of the training trials.

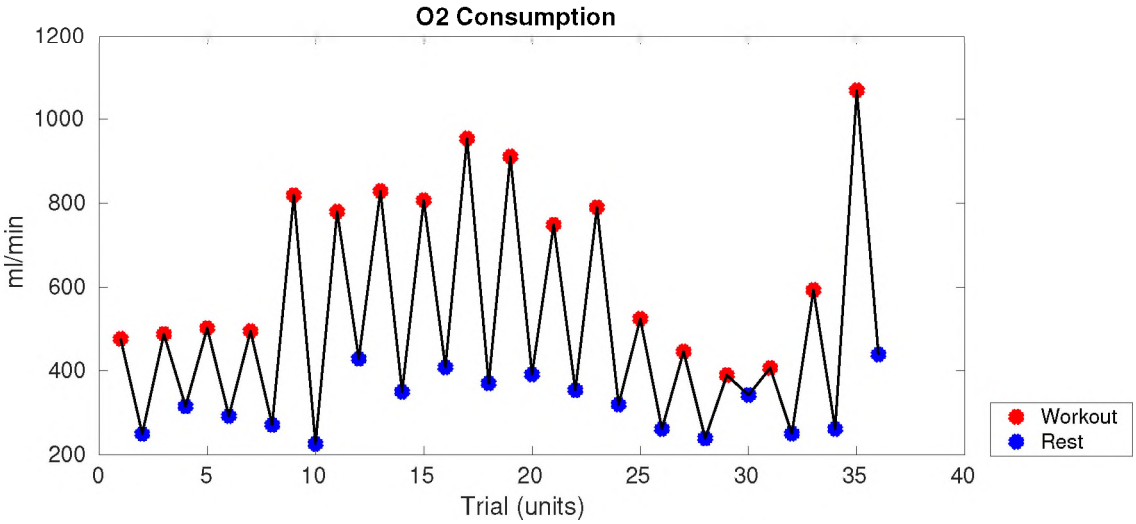

Figure 53: Oxygen consumption during each of the training trials.

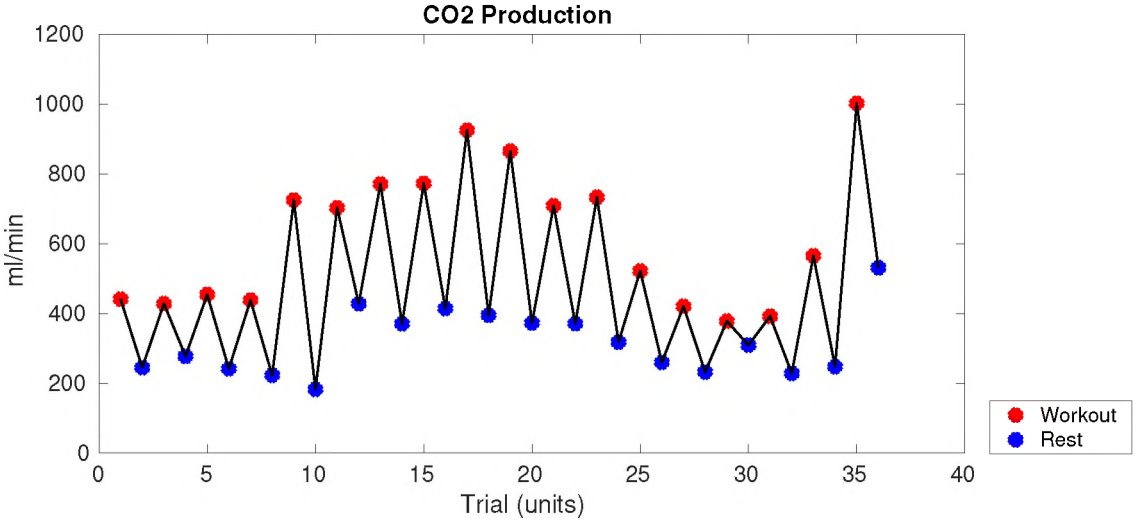

Figure 54: Carbon dioxide production during each of the training trials.

The physiological effects on the cardiovascular and cardiorespiratory systems experienced an expected behavior. In addition to trial 35 (the trial with the highest speed), the trials which produced the highest values for all of the systems were from 9 and 23 (related to the trials with the high impedance). However, although the values were high, they were well below the maximum biological values showing a marked difference between resistance-based and cardio-based training. The peak values for

the heart rate and oxygen consumption during the experiments were 92 BPM and 1069 ml/min; and based on the subject data, the estimated HR_{max} and VO_{2-max} should be around 198 BPM and 4590 ml/min (50 ml/kg/min for a subject with 91.8 kg) respectively. In conclusion, the resistance-based experiment was able to reach 46.5% of the HR_{max} and 23.3% of the maximum VO_{2-max} suggesting that the resistance-based training is not adequate for controlling cardiovascular and cardiorespiratory physiological effects.

3.4.3 General Discussions

Upon completion of the 4OptimX trials, a great variety of results was evidenced during the trials. Furthermore, unique combinations of physiological effects per each combination of training parameters were observed. It is also important to consider that the resistance and speed of trajectory were not the only parameters affecting the muscle activation. Some biological factors such as fatigue, hydration, and mood play a crucial role in physiological dynamics. Nonetheless, this diversity of training effects shows the potential for training optimization by the optimal regulation of these training parameters.

It is important to note that the trajectory tracking was not perfect, but very consistent. There were not a lot of variations product of the impedances or trajectory speeds (see Figure 55). An RMS tracking error of 0.2792 ± 0.0077 (mean $\pm$SD) meters was measured during the 17 workout trials. Since the interface is similar to a 3D game, it is required to make the subject practice before the experiments to develop some good tracking skills.

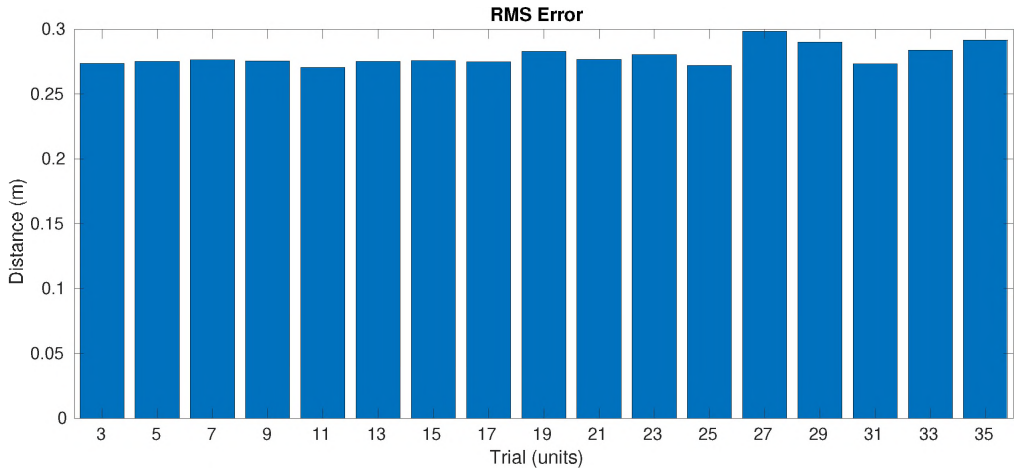

Figure 55: RMS error on the tracking trajectory during each of the training trials.

CHAPTER IV

MODEL-FREE OPTIMIZATION FRAMEWORKS OF TRAINING PARAMETERS IN ADVANCED TRAINING

4.1 Overview

This chapter presents the model-free frameworks for single-variable and multi-variable optimization. Then, the framework performance is evaluated in simulation against another model-free approach based on the use of the global evolutionary optimizer Biogeography-Based Optimization (BBO). This last framework promises a good performance as a result of exhaustive searches but with a high computational cost limiting its use on real-time experiments.

The purpose of the validation was to evaluate the framework performance by comparing its results against the other model-free optimizer. The performance validation is conducted by comparing the optimal results between these 2 methods by using five human arm models from our virtual population. An average of less than 5 degrees for the absolute difference between the optimal trajectory parameters is expected for the validation.

4.2 Model-free Optimization Frameworks

The model-free approaches are based on the use of Extremum Seeking Control (ESC) as the real-time optimizer and they were designed to work with advanced exercise protocols. During these protocols, the user is required to follow the same procedure as previosuly presented in Section 3.4.1 where he/she is required to follow a path against the machine's neutral path and resistance. This subject is asked to follow an elliptical trajectory while the robotic machine establishes a zero-effort circular path. A user-defined resistance is produced by the controller based on the interaction force/torque and the deviations from the neutral path.

As previously defined, the model-free framework is a multi-system structure including a robot as an advanced exercise machine, an electromyography (EMG) system, a real-time processor, and a data acquisition system (DAQ) (see Figure 56). These 4 systems and their connectivity are illustrated in the block diagram in Figure 57 and presented below.

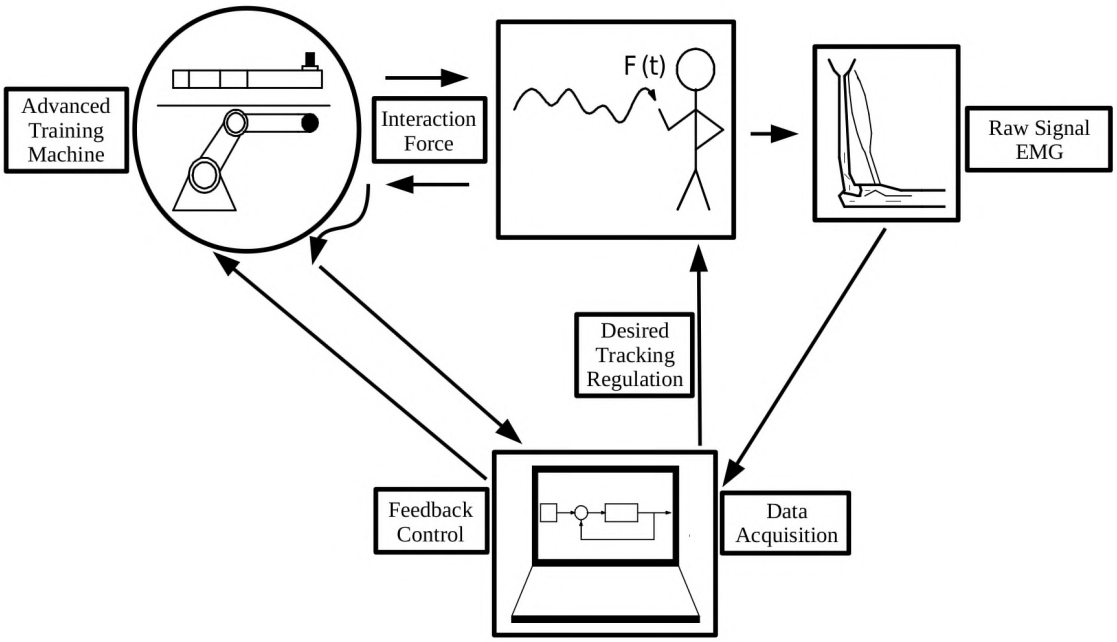

Figure 56: Graphical representation of the model-free optimization framework.

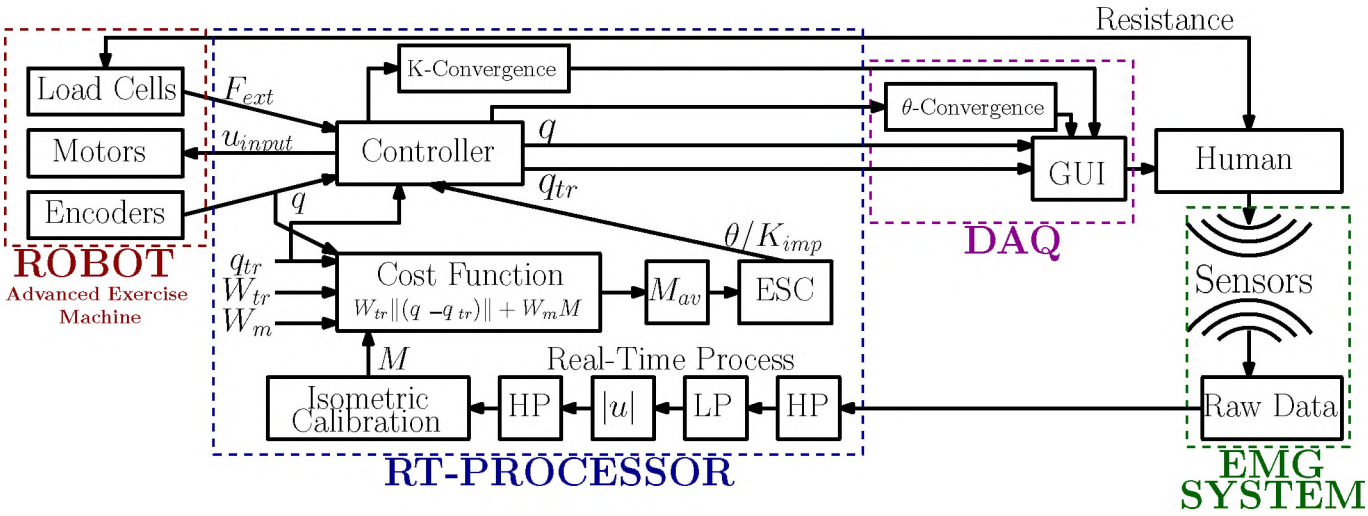

Figure 57: Summarized block diagram of the model-free optimization framework.

Robot:

The robot interacts with the human while it is been controlled by the RT processor. The human-robot interaction produces external forces (F_{ext}) and alterations in the robot positions (q) which are acquired by using load cells and encoders respectively. The acquired data is automatically transmitted to the RT processor to feedback the controller and produce the required motor inputs (u_{input}) to achieve the desired training performance.

DAQ:

The DAQ receives from the RT processor the user and desired positions, the impedance parameter convergence status, and the ellipse orientation. In the case of training parameter optimization, the DAQ also processes the convergence criterion by analyzing its variation over a period of time. Finally, a script using the data builds the graphical user interface (GUI) (see Figure 58) which serves as visual feedback to the user. In this GUI, the convergence status is shown in 2 digital LEDs (red and green). When the convergence status is negative ("NO" in the GUI), the red LED is ON and the

green LED is OFF (shown as black). Oppositely, when the convergence status is positive ("YES" in the GUI), the green LED is ON and the red LED is OFF (shown as black).

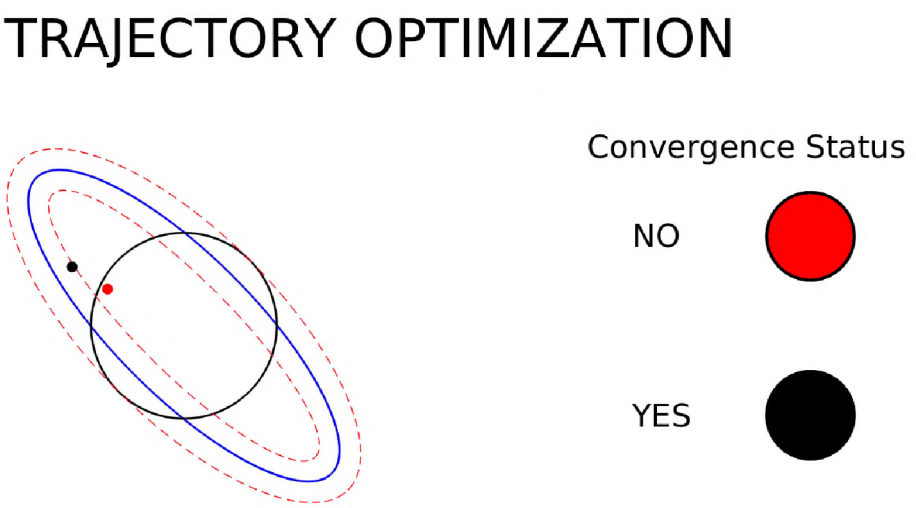

Figure 58: Example of the GUI shown to the user during a negative convergence status (red LED ON and green LED OFF).

EMG System:

The EMG system measures wirelessly the raw muscle signals from the sensors located in the subject's skin over his/her muscles. Then, the signals are sent to the RT processor.

RT-Processor

The RT processor measures the human-robot interaction forces and positions (F_{ext} and q respectively) to control the robot and run the optimization framework. The process starts by measuring the raw muscle signals from the EMG system and real-time processing into muscle activations. Then, the muscle activations are calibrated (M) and used in the performance function which is defined as the sum of the multiplication of a tracking weight vector and the tracking error ($W_{tr}(\|q - q_{tr}\|)$) and the

multiplication of a muscle weight vector and the muscle activations ($W_m M$). The resulted value is then moving averaged to estimate the average cost per trajectory revolution. The complete moving averaged cost function is presented below:

$$\min_{\theta} \qquad y = \frac{t_s}{t_{rev}} \sum_{i=t-t_{rev}/t_s}^{t} \Big(W_{tr}(\|q - q_{tr}\|) + W_m M \Big), \tag{4.1}$$

where θ is the optimization variable (trajectory and/or impedance parameter), t_s is the simulation sample time, t_{rev} is the period of rotation for the reference cursor (blue or red dot), t is the time, M is the vector of muscle activations, and W_n is the muscle weight vector. For instance, a value of $[-1, 1, 1, 1, 1, 1]$ forces the optimization framework to maximize the first muscle; meanwhile, the last five muscles are minimized. The muscle objective can be professionally selected by a therapist to emphasize or de-emphasize certain muscle groups. Next, the moving averaged cost function works as an input to the ESC algorithm.

The ESC algorithm is based on the approach (single-variable or multi-variable framework). The single-variable approach uses a single perturbation-based model following the diagram in Figure 59.

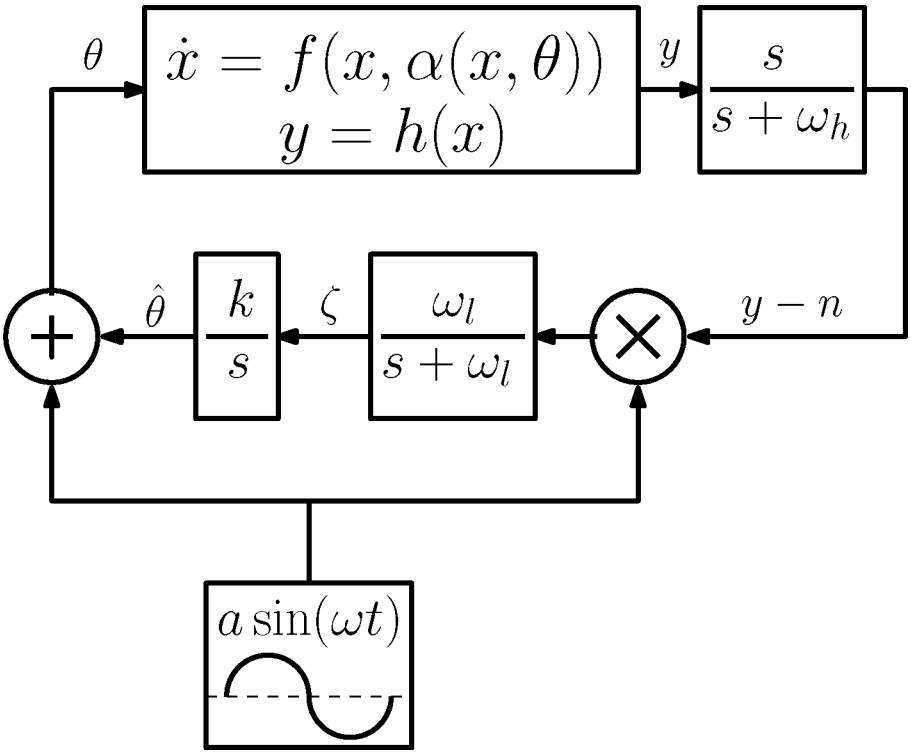

Figure 59: Block diagram extension from the block "ESC" for single-variable optimization framework in Figure 57. The output parameter θ represents the optimization training parameter (the trajectory or impedance parameter), a, ω, ω_h, ω_l, and k are the configuration parameters (amplitude of perturbation, frequency of perturbation, high-pass filter, low-pass filter, and gain respectively).

The multi-variable framework follows a similar process as the single-variable framework except for the fact that it uses 2 estimators working in parallel (see Figure 60). A special rule about the parameter selection in the multi-variable framework is to not use the same value for the perturbation frequencies ($\omega_1 \neq \omega_2$) because, assuming a choice where $\omega_1 > \omega_2$, the algorithm works by treating the second perturbation system as a dynamic map of slow frequency.

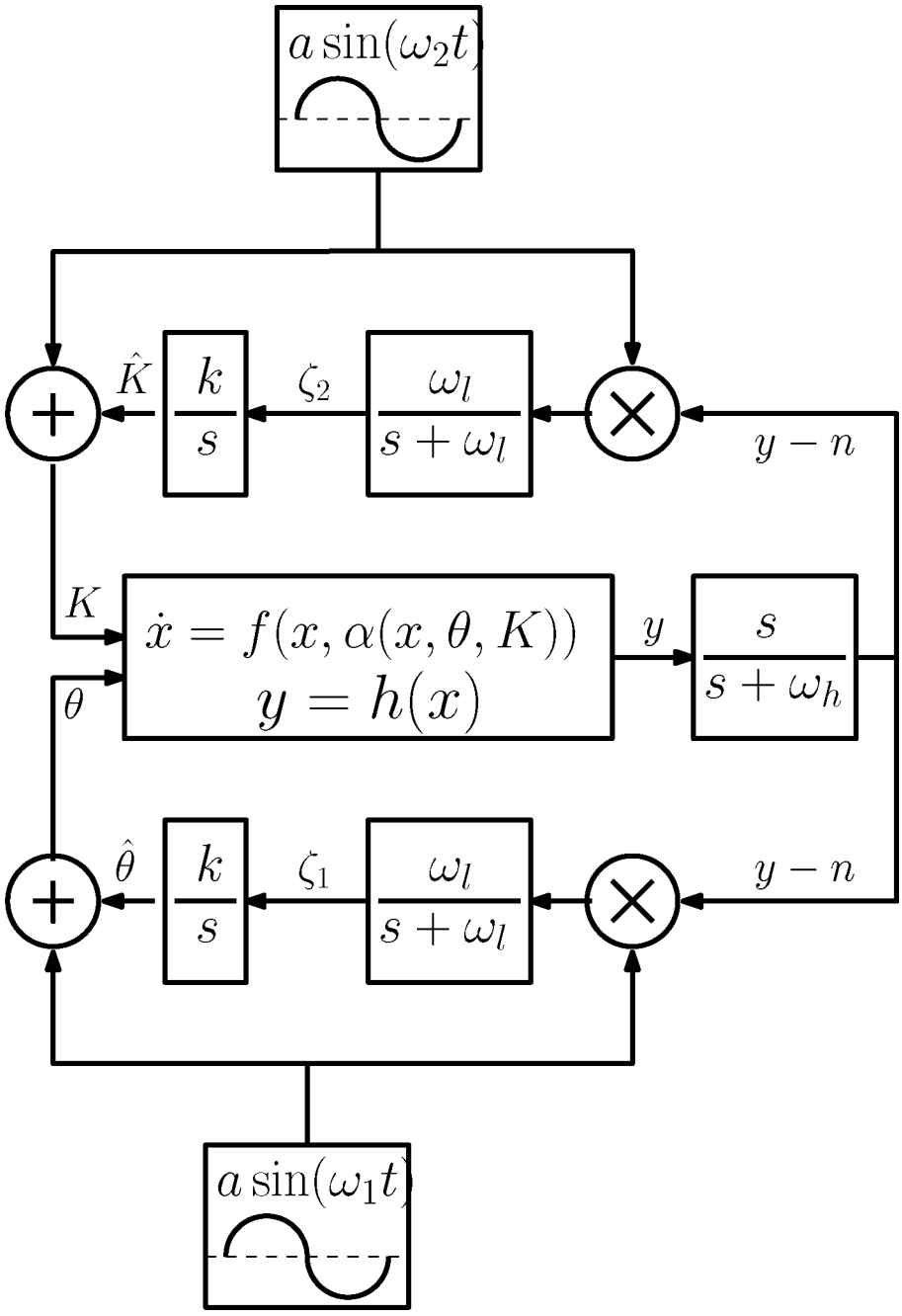

Figure 60: Block diagram extension from the block "ESC" for the multi-variable optimization framework in Figure 57. The output parameters θ and K represent the optimization training parameter (the trajectory or impedance parameter respectively), a, ω_1, ω_2, ω_h, ω_l, and k are the configuration parameters (amplitude of perturbation, first and second frequency of perturbation, high-pass filter, low-pass filter, and gain respectively).

Based on the framework and the training parameter at the output of the

ESC block, the RT processor will redirect the signal for convergence testing. For the case of the trajectory optimization, it sends the parameter value and tracking positions to the DAQ. For the case of the impedance parameter optimization, the RT processor performs the convergence criterion and it sends the tracking positions and the digital convergence result (5 volts or high for positive convergence status and 0 volts or low for a negative convergence status).

4.2.1 Convergence Criteria

Two different approaches were developed for the convergence criteria. It is important to highlight that the reason for those 2 (one for each single-variable framework) was to provide 2 different alternatives for convergence identification. Both work equally well and they can be used interchangeably.

It is also important to note that the convergence criterion might be affected by the presence of biological factors (time-varying dynamics) or special circumstances such as critical environmental conditions, exercise with untrained people, or using the wrong combination of configuration parameters. The configuration parameters play a key role especially for the success of the convergence criteria. For instance, a high framework gain might accelerate the convergence process, but introducing disturbances that are not recommended because of undesired performances. On the other hand, a low framework gain might the convergence process slow or even unable to achieve convergence. These configuration parameters can be selected by performing pre-tests following the same exercise protocol of the experiments.

An average of less than 1 degree for the absolute difference between the optimal trajectory parameters is expected for the validation.

Single-Variable Convergence Criterion - Trajectory Parameter

The convergence criterion for the trajectory parameter (θ) optimization is performed in the DAQ subsystem and it works by computing the absolute value of the maximum difference (θ_{diff}) between the θ parameter and its last n samples (where n is a configuration parameter). Once that difference remains under the threshold (θ_{th}) for more than the trigger time (t_{tr}), the convergence is accomplished and the converged value becomes the average value between the last n θ values (θ_{av}). The reason to use θ_{av} instead of θ is for considering the convergence value as an intermediate value between the value at the trigger time (when the variable starts to remain between the thresholds) and the final value.

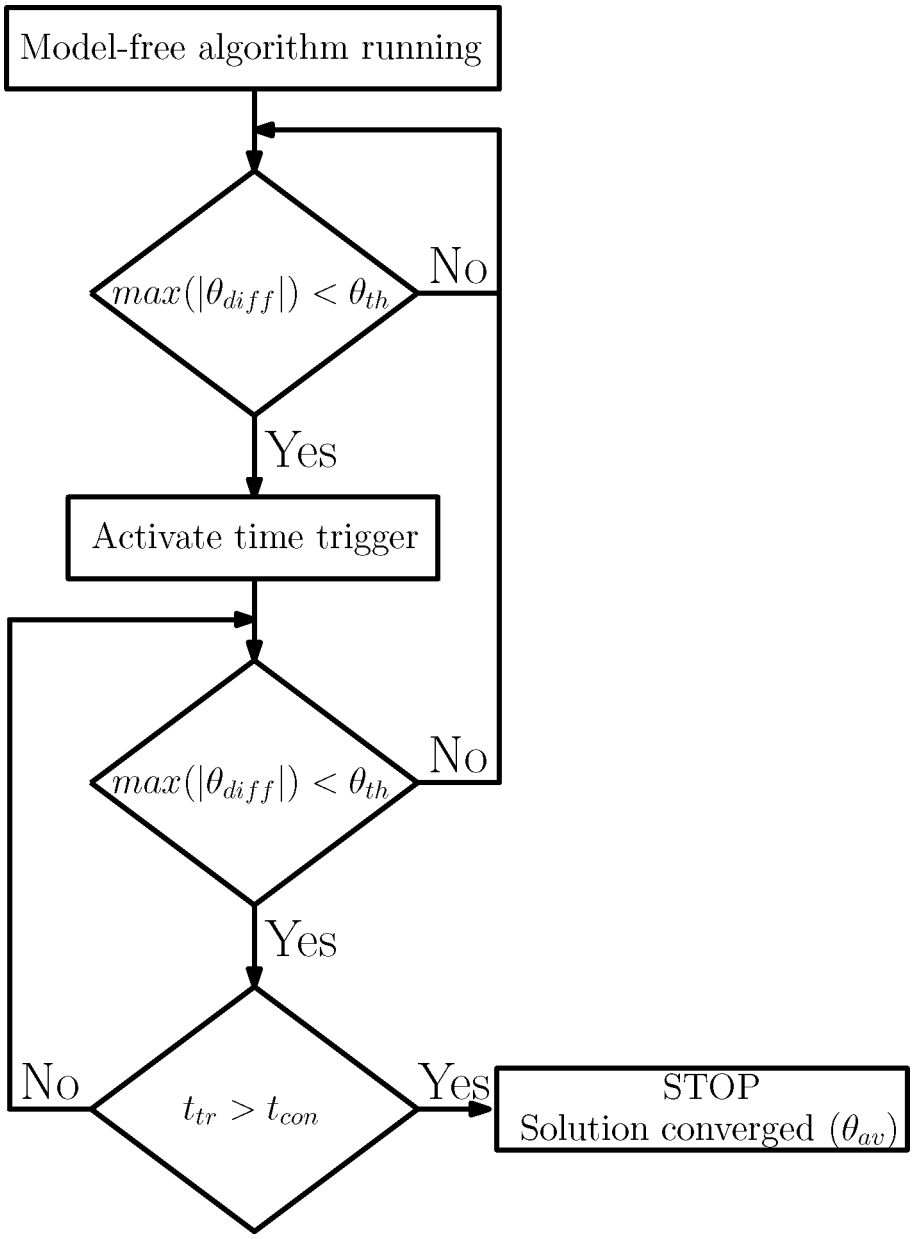

Figure 61: Block diagram of the convergence criterion for the trajectory parameter.

An example of a trajectory parameter convergence can be seen in the Figure below:

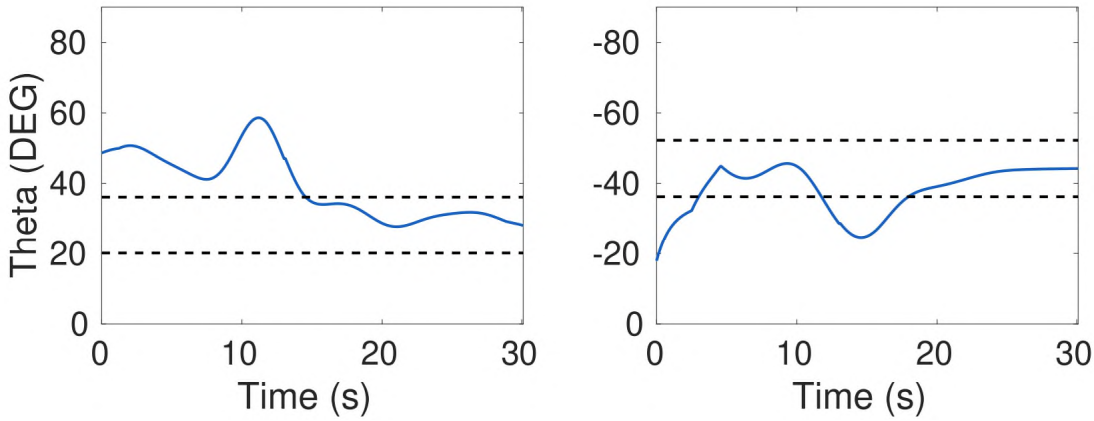

Figure 62: Two different examples of trajectory parameter convergence with $\theta_{th} = 15°$ and $t_{tr} = 10$ seconds.

Single-Variable Convergence Criterion - Impedance Parameter

The convergence criterion for the impedance parameter optimization was developed based on a previous work applied for Unmanned Aerial Vehicles (UAVs) [6]. This convergence criterion is performed in the RT processor subsystem and it works by high-pass filtering the stiffness parameter ($K \rightarrow K_{HP}$). The high-pass filter will attenuate low frequencies producing a signal with zero-mean. This signal will become smaller as the oscillations are reduced. Therefore, when the impedance oscillations are reduced and the high-pass filtered value becomes smaller, the time threshold is activated. When the high–pass filtered remains under the threshold (δ_{th}) for a specific time, the exercise protocol ends. Finally, the obtained stiffness value (K) is compared with the stiffness tolerance K_{toll} (one of the safety-parameters used to avoid negative impedance during the exercise protocol) to define the convergence result. If the difference between the impedance value and the impedance tolerance is higher than the tolerance threshold ($|K - K_{toll}| > T_{th}$), the convergence is accomploshed, but if not, the convergence fails.

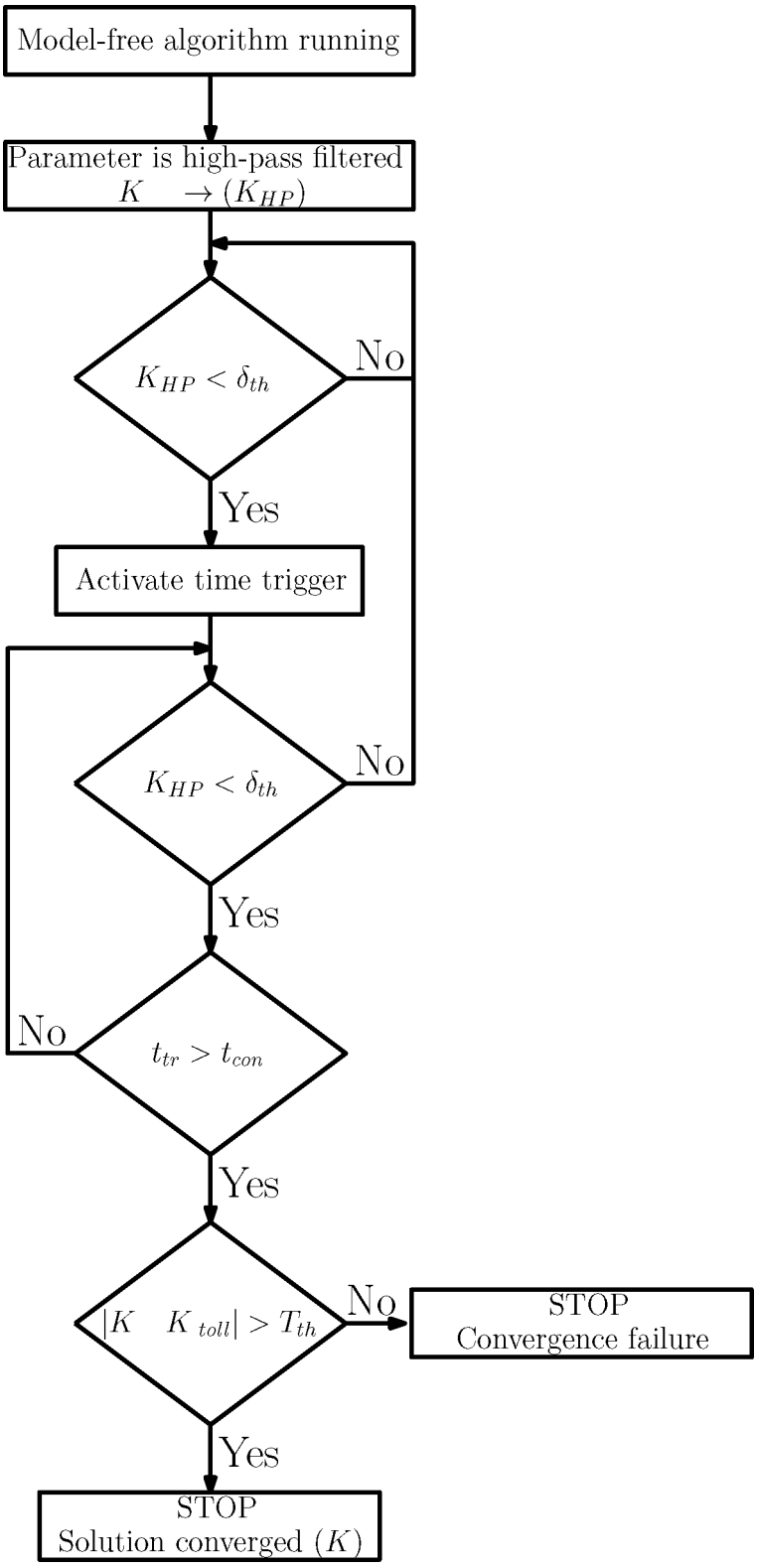

Figure 63: Block diagram of the convergence criterion for the impedance parameter.

An example of an impedance parameter convergence can be seen in the Figure below:

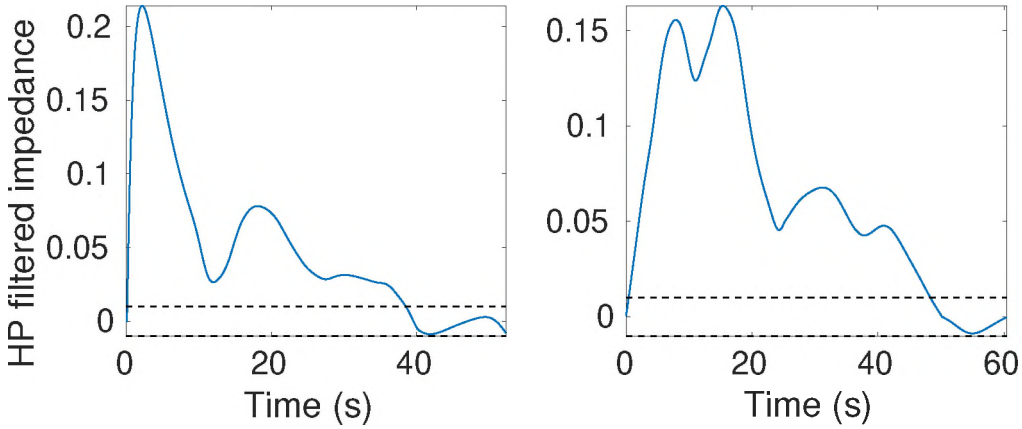

Figure 64: Two different examples of impedance parameter convergence with $\delta_{th} = 0.01$ and $t_{tr} = 10$ seconds.

Multi-Variable Convergence Criterion - Trajectory and Impedance Parameter

The convergence criterion for the multi-variable framework encompasses each of the individual criteria including as a final condition the simultaneous convergence of each criterion (see Figure 63). Therefore, even after one of the conditions has been met, this can be broken while waiting for the others to converge.

In addition to the previous complications related to the convergence process (presented at the beginning of this Section 4.2.1), the multi-variable approach results more demanding becoming more difficult to meet. For that reason, it is highly recommended to use lower framework gain with the multi-variable approach.

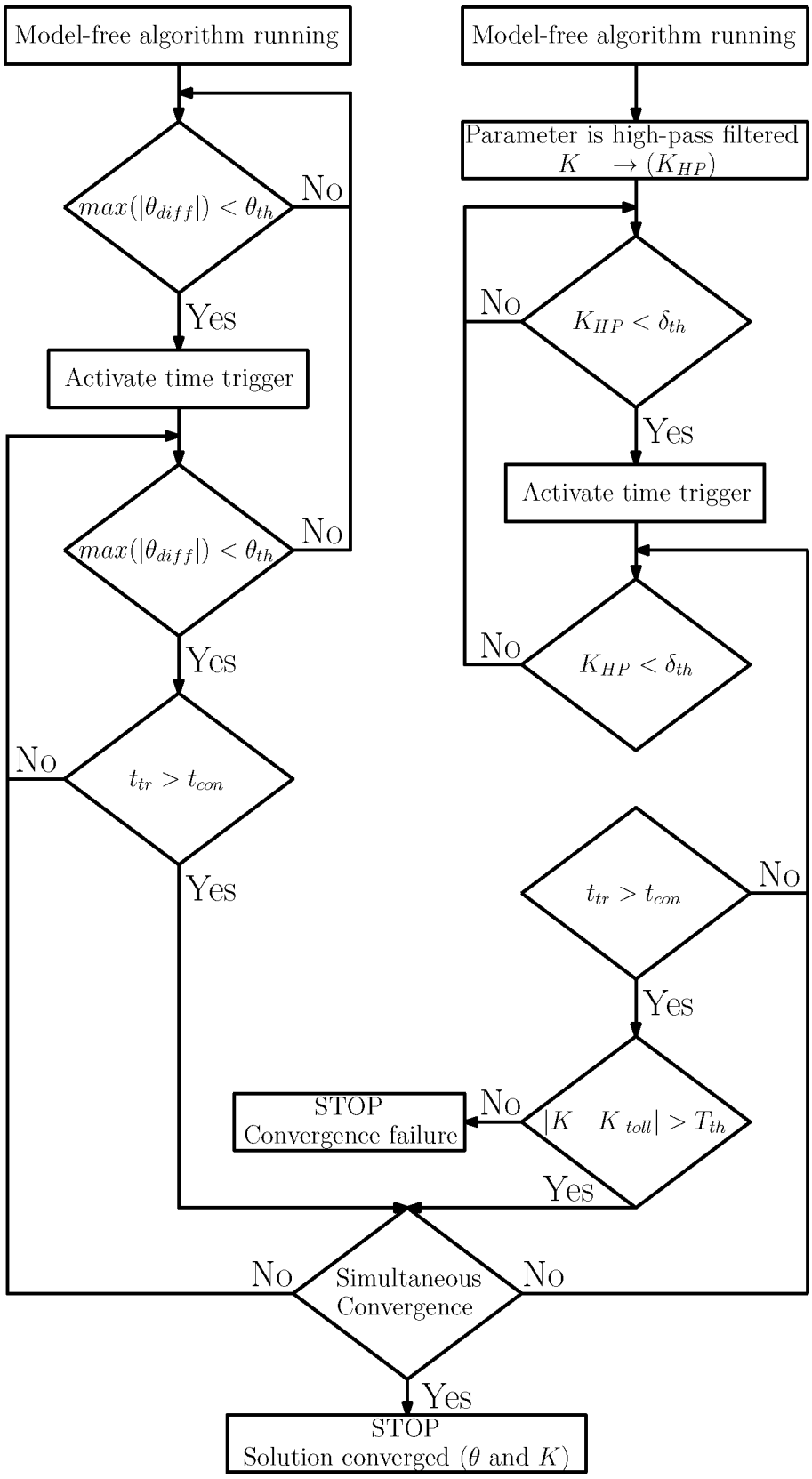

Figure 65: Block diagram of the simultaneous convergence criterion for the trajectory and impedance parameter.

4.3 Performance Evaluation

The performance of the model-free approach was evaluated in a simulation environment by using a muscle-actuated linkage model with 5 human arm models from our virtual population. Previously, evident effects on muscle activations have been reported as a result of the regulation of trajectory and impedance settings [101]. Between those parameters, the trajectory parameter related to the ellipsoidal trajectory orientation resulted to be the most influential exercise parameter [25]. Thus, the optimization of this parameter (ellipsoidal orientation) was selected for the performance comparison between the single-variable optimization approach with ESC and BBO [31].

4.3.1 Biogeography-based optimization (BBO)

BBO is an evolutionary nature-inspired optimization method based on the study of the geographical distribution of biological life forms [136, 137]. The performance of this method lies in the biogeography mathematical models observed in the animal world relating the emigration and immigration of species from one isolated habitat to another one.

BBO works by defining habitats with a set of Suitability Index Variables (SIVs) representing their environmental features such as resource availability (food and water), space, climate, etc. Then, based on the features previously described, the suitability of the habitat is calculated by the Habitat Suitability Index (HSI). Each habitat is different and its capacity is based on the HSI, where the higher the HSI, the more species can become established, leading to abundant emigration (emigration from high HSI habitats to others). Therefore, the habitat's immigration rate becomes affected by mainly the number of species there. For instance, when there aren't any species, the habitat is full of space and resources producing a maximum immigration

rate. As the number of species increases, the habitat's resources start to run out making it difficult the survive and decreasing the immigration rate. Thus, when a habitat is full of species (at maximum capacity), the immigration rate becomes zero.

Analogously in the optimization problems, each possible optimal solution is a habitat, its cost function is the HSI, and its features are the SIVs. The methodology is performed sequentially by generations where the first is randomly initialized. The best n solutions (where n is a configuration parameter) are stored, and its features are shared. In order to reduce the probability of finding a local optimizer, some features from possible solutions are probabilistically mutated, and the best solutions are sorted and added to the population. On the other side, the worst n solutions are then eliminated. The resulting populations from each generation are used to initialize the next generation.

The effectiveness of this algorithm has been proven even for complex applications involving auto-setting of training parameters [149] and has been served as a starting point for multiple new approaches. However, the slow processing speed of BBO limits its use in real-time applications.

4.3.2 Simulation Setup

Simulation Environment

The simulation environment includes the human arm models from the virtual population (see Appendix A for details), the exercise trajectories, and the resistance force acting at the end of arm model.

In the simulation environment, the linkage model receives the target position and the interaction force in order to compute the muscle activations required to accomplish the motion.

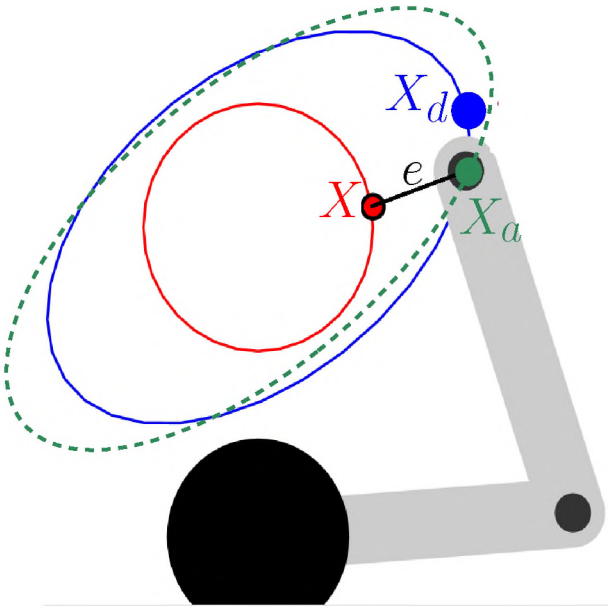

Figure 66: Simulation environment including the human arm, user position (green dot X_a), target position (X_d blue dot), and the machine's trajectory (X red dot).

The simulation environment (see Figure 66) The target position is labeled with a blue dot which moves periodically over a blue ellipsoidal curve of fixed axis lengths and programmable orientation. The user position (labeled with a green dot) follows the blue dot except on the simulation environment where the user performs a perfect tracking (user position equal to the desired position). The red label moving periodically over a red circular curve represents the machine's trajectorMuscle activations were not known a priori. The muscle activations were simulated but their values were not recorded because the objective was oriented to compare the performance of the frameworks by comparing their optimal results and cost but not the resulted muscle activations.y where the impedance is zero. Therefore, by impedance

control the external force (F_{ext} in Eqs. A.1) becomes:

$$\begin{aligned} F_{ext} &= I\ddot{e} + B\dot{e} + Ke, \\ \ddot{e} &= \ddot{X} - \ddot{X}_a, \\ \dot{e} &= \dot{X} - \dot{X}_a, \\ e &= X - X_a, \end{aligned} \tag{4.2}$$

where X_a, and X are the user position (green dot) and the machine reference trajectory (red dot) respectively; I is the acceleration gain (inertia impedance); B is the velocity gain (damping impedance); and K is the position gain (stiffness impedance).

Simulation Parameters

To make an impartial evaluation, each of the frameworks was tested using the same simulation parameters. The selection of these parameters was randomly performed and they can be seen in Table VII.

Table VII: Simulation parameters.

Variable	Value	Units
Ellipsoidal axes	[0.25, 0.15]	m
Ellipse center	[0, 0.3]	-
Ellipse orientation	between [0.1, 2π]	rad
Zero-impedance circle radius	0.12	m
Zero-impedance circle center	[0, 0.3]	-
Frequency of rotation	between [0, 1]	Hz
Trajectory direction	Counterclockwise	-
Inertia Impedance (I)	100	kg
Damping Impedance (B)	1	kg/s
Stiffness Impedance (K)	50	N/m
Muscle weight vector (W_m)	[-1,1,-1,1.-1,1]	-

From our virtual populations, 5 female arm models were used for the simulations. The arm model parameters associated with these 5 models can be seen in Table VIII. The first and second links on each model ($L1$ and $L2$) represent the elements

joining the shoulder with the elbow and the elbow with the wrist, respectively.

Table VIII: Arm model parameters. The subscripts M, I, L, and CM represent the mass, inertia, length, and center of mass properties of the links respectively.

Model	$L1_M$ (kg)	$L2_M$ (kg)	$L1_I$ (kgm)	$L2_I$ (kgm)	$L1_L$ (m)	$L2_L$ (m)	$L1_{CM}$ (m)	$L2_{CM}$ (m)
1	1.9159	1.7175	0.0219	0.0389	0.28930	0.3258	0.1319	0.2297
2	1.9767	1.7876	0.0236	0.0421	0.29350	0.3277	0.1313	0.2214
3	2.1124	1.7835	0.0220	0.0392	0.2963	0.3292	0.1262	0.2329
4	2.0423	1.8957	0.0219	0.0427	0.3002	0.3317	0.1295	0.2200
5	2.1022	1.8281	0.0231	0.0423	0.3063	0.3363	0.1359	0.2357

4.3.3 Optimization objective

The objective of the optimization frameworks was designed to find the orientation of the ellipsoidal curve that minimizes a performance function. Both of the frameworks are completely model-free making only use of the estimation of the muscle activations. Therefore, the regulation of the orientation is automatically performed using these activations as biofeedback.

BBO frameworks optimize by exhaustive searches using complete cycles. Thus, the performance function was defined as the multiplication of a muscle weight vector and the muscle activations, and it is derived as follows:

$$\min_{\theta} \qquad y = \Big(W_m M_{act} \Big), \tag{4.3}$$

where M_{act} is the vector of muscle activations calculated from the muscle-actuated linkage model, and W_n is the muscle weight vector.

Unlike BBO, ESC optimizes at each instant of time (at each sample time), therefore the same performance function (Eq. 4.3) was adapted by using the moving average of the multiplication of a muscle weight vector and the muscle activations,

and it is derived as follows:

$$\min_{\theta} \qquad y = \frac{t_s}{t_{rev}} \sum_{i=t-t_{rev}/t_s}^{t} \Big(W_m M_{act} \Big), \tag{4.4}$$

where t_s is the simulation sample time, t_{rev} is the period of rotation for the reference cursor (blue or red dot), t is the time, and M_{act} and W_n are the same variables previously defined.

4.3.4 Results

The optimal ellipsoidal orientations obtained from the simulations with the BBO and ESC frameworks are presented in Figure 67 (exact results in Table IX).

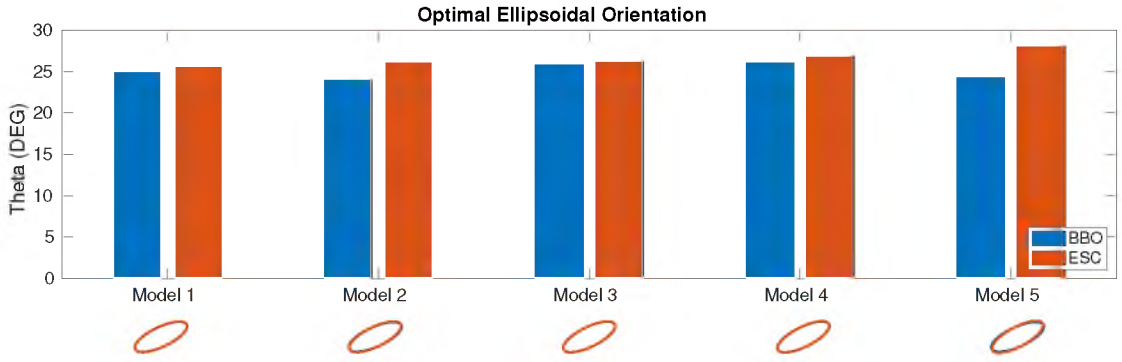

Figure 67: Results obtained from the simulations with each arm model.

Table IX: Comparison of the optimal ellipsoidal orientation solution between the model-free optimization frameworks.

Model Number	BBO Final Cost	ESC Final Cost	BBO Optimal Orientation	ESC Optimal Orientation	Absolute Difference
1	-0.0377	-0.0738	25.065°	25.767°	0.702°
2	-0.0352	-0.0705	23.999°	26.026°	2.027°
3	-0.0398	-0.0684	25.799°	26.309°	0.510°
4	-0.0413	-0.0654	26.062°	26.895°	0.833°
5	-0.0432	-0.0609	24.292°	28.039°	3.747°
Mean					1.564°
Standard Deviation					1.357°

Upon completion of the experiments, the feasibility of the optimization of training parameters by using biological factors as biofeedback (automatic training personalization) was tested. Both frameworks (BBO and ESC) found similar solutions supporting the fact that they were able to find the optimal ellipsoidal orientations. Besides, as was expected, different optimal solutions were obtained with each human arm model suggesting the existence of a unique combination of optimal training parameters for each person/model.

Despite the variety of optimal orientations observed in the simulation and real-time results, all of them were in the neighborhood of 26°. Results seem to suggest that an inclined ellipsoidal orientation in the neighborhood of 26 ° might produce desirable muscle efforts for the selected glenohumeral muscles. However, more simulations with a bigger population would be required to provide stronger conclusions. Given the case of a deeper study, human performance and rehabilitation practices could use this information for muscle training optimization by muscle activation maximization (fitness improving) and muscle activation minimization (muscle-isolation or rehabilitation practices).

It is important to point out that the BBO optimization performance takes over 5 hours for a single optimization run with the human arm model simulator. On the other hand, ESC takes about 2 minutes. For that reason, even though both proved to be effective by finding the optimal training parameters, ESC is more suitable for real-time experiments. It is also important to consider that the BBO and ESC frameworks use a different approach (despite both working on the same optimization objective). On one side, BBO provides the results for a fixed ellipsoidal orientation. Meanwhile, ESC provides variable orientation (small oscillations after convergence is achieved).

These results were important to go forward into research related to the

model-free optimization of training parameters by training personalization.

CHAPTER V

TRAINING PERSONALIZATION

5.1 Overview

Personalized fitness and rehabilitation are two popular research areas with several developments mainly focused on providing to the user more and better training tools. For instance, it is estimated that most of the gym centers upgrade their equipment at least once every 5 years (in addition to the purchase of the latest technology equipment) [102]. These upgrades are implemented because of the improvements in the training features offered by the new training machines to increase the potential of the exercise. However, to the best of my knowledge, this is the first time that an improvement is performed by providing automatic regulations of training parameters using robots and physiological parameters as biofeedback.

Training personalization is not only important but also required for most of the training protocols and rehabilitation practices. The necessity of personalized training is the reason why personal coaches have become very popular lately. They adapt their customer's workouts to maximize their performance by manually changing their training parameters (trajectories and resistances) based on the subject's goal, experience, and condition. Currently, these adaptations provide great results, but they are manually performed at the coach's suboptimal criteria [35, 104]. Similarly,

personalized rehabilitation is a necessity because every patient has a particular diagnosis which, sometimes, this diagnosis can be difficult to determine even by the most experienced therapists. In effect, rehabilitation treatments and procedures become even harder. Currently, different kinds of rehabilitation robots work with several patients trying to personalize their treatment as best as possible [101, 45]. The rehabilitation tools normally utilized with these robots include training programs that are unique and suitable for each patient. These training programs are based on the subject's body features and condition (such as degree of motor dysfunction). However, the adaptability of the training program requires a therapist. Thus, it is expected that automatic training personalization using robots and physiological parameters as biofeedback will enhance fitness and rehabilitation.

This chapter introduces the concept of training personalization by presenting early evidence about the unique combination of optimal training parameters that exists for each person/model. Additionally, evidence suggesting the presence of complex and time-varying human dynamics is presented based on the variety of the optimal parameters with respect to time.

5.2 Training Parameter Variations Based on Different Musculoskeletal Distributions

5.2.1 Methodology

It is not only believed that each person/model has a unique combination of optimal training parameters, but also this combination is a function of biological factors including the musculoskeletal distribution. In this study, the musculoskeletal parameters associated with the lower and upper arms (including their lengths, masses, inertias, and centers of mass) were considered.

It is expected that people/models with similar musculoskeletal distributions

tend to have similar optimal training parameters. To test this theory, a null hypothesis was defined as follows: *There is no statistically significant relationship between the difference in people/models' musculoskeletal parameters and the difference between their combination of optimal training parameters.* The outcome variable accepts "true" or "false" values if there is sufficient evidence to accept or reject the null hypothesis at a significance level of 5%.

To successfully test the hypothesis, first, the variety in optimal training parameters in the virtual population was evaluated by using the 50 arm models. The optimal training parameters associated with each arm model were measured by using the model-free optimization frameworks (single-variable trajectory, single-variable impedance, and multi-variable optimization) and the same simulation approach including the muscle-actuated linkage system with the simulation environment presented in Section 4.3.2. The total virtual population of 50 human arm models includes 25 females (see Table XXXIII) and 25 males models (see Table XXXIV) and it can be seen in detail in Appendix A. The training parameter optimization was performed by using 2 different weight muscle vectors in order to compare results with the effect of the optimization objective. The first weight muscle vector was $[1, -1, 1, -1, 1, -1]$ that maximize the second, fourth, and sixth muscles (Posterior Deltoid, Triceps Brachii-long head, and Brachialis); and the other vector was $[-1, 1, -1, 1, -1, 1]$ that maximize the first, third, and fifth muscles (Anterior Deltoid, Biceps Brachii, Triceps Brachii-short head).

Given the number of arm models (25 male and 25 female models), a total of 1200 comparisons between the musculoskeletal parameters and the optimal training parameters of the 2 models can be conducted. This total results from the 4 sets of models. Each set, including 25 models each, results in a total of 300 comparisons by comparing one model to the other. The 4 sets include two sets of males and 2 sets of

females each of them with a different weight muscle vector. These comparisons were conducted by obtaining the difference between their arm lengths, mass, inertia, and center of mass as a vector, obtaining the difference between their optimal training parameters as a vector, computing the norms of these vectors, and evaluating the possible correlation between them by using Continuous-Analysis-of-Variance (CANOVA) [155] and Kendall rank correlation coefficient [135] (see Section 5.2.3).

Each optimal parameter is presented with an independent color from black to red where black is the optimal parameter associated with the smallest arm model, and red with the largest one. Based on the musculoskeletal parameters considered for this study, the model size is defined as the norm of the vector including them as follows:

$$M = [L1, L2], \tag{5.1}$$

where $L1$ and $L2$ are the arm lengths associated with the lower and upper arm respectively. Thus, the smallest model is identified as the model with the lowest norm value and the largest as the one with the highest norm value.

5.2.2 Results

The optimal training parameters encountered from the simulation experiments with the virtual population are presented below.

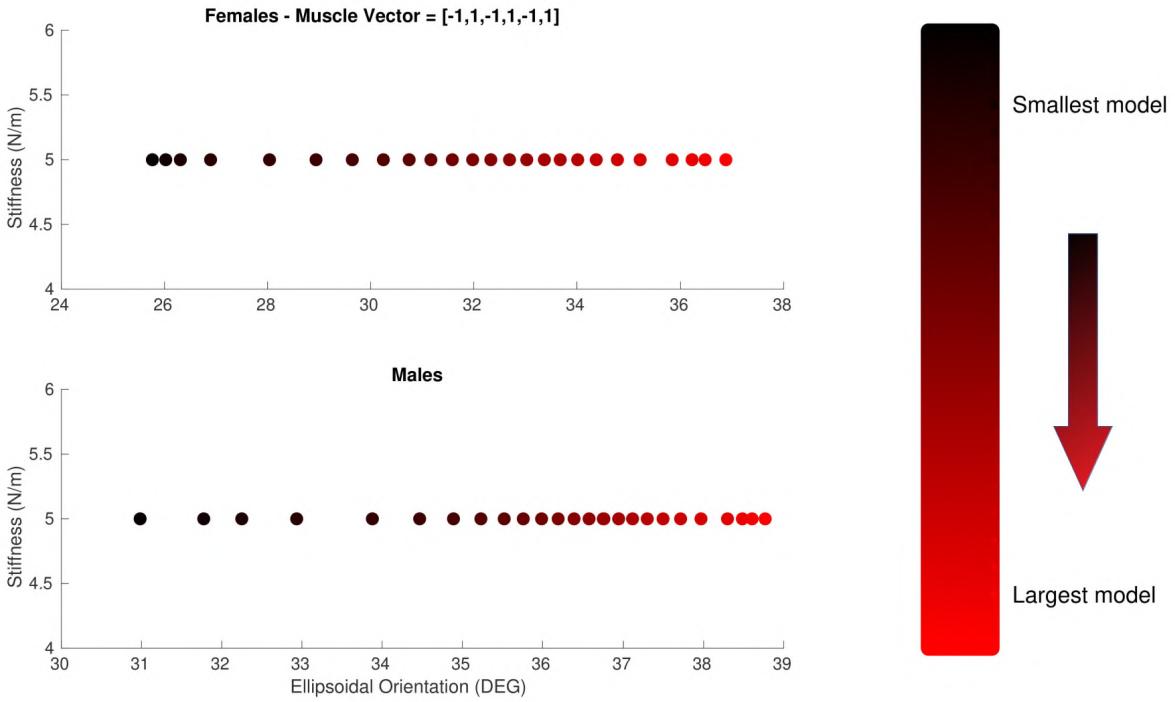

Figure 68: Optimal trajectory parameters for the virtual population with the first muscle weight vector ([-1,1,-1,1,-1,1]).

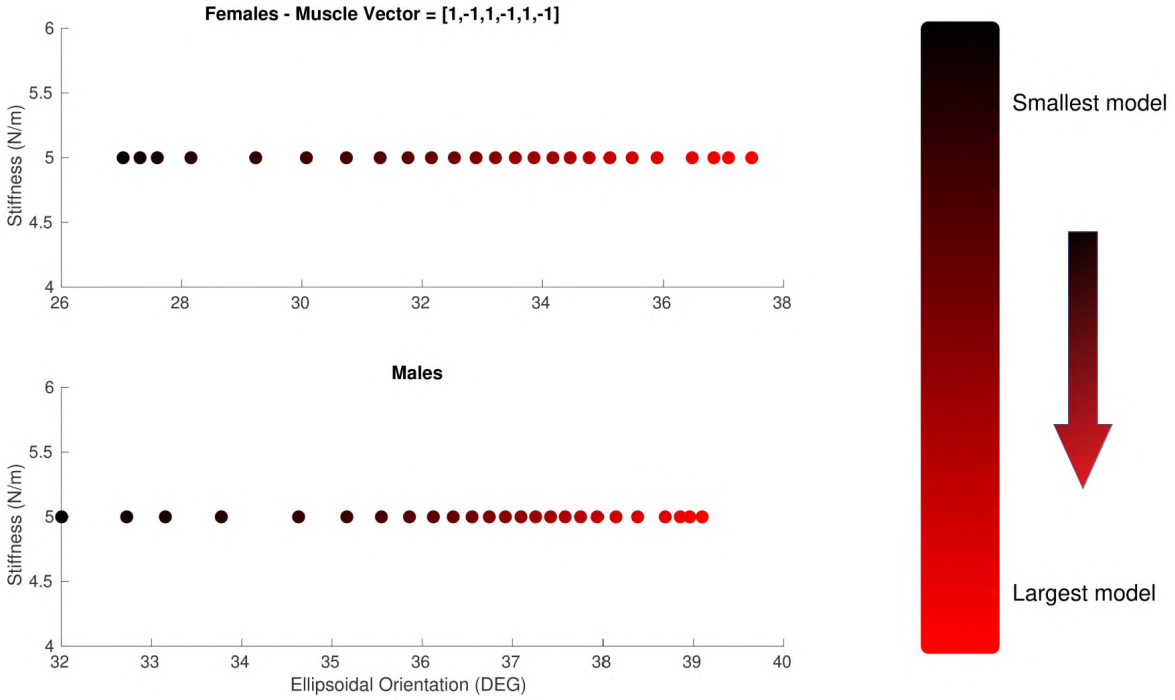

Figure 69: Optimal trajectory parameters for the virtual population with the second muscle weight vector ([1,-1,1,-1,1,-1]).

At a first glance, results suggest that there is a pattern relating models and their optimal training parameters. For instance, figures 68 (muscle weight vector $[-1, 1, -1, 1, -1, 1]$) and 69 (muscle weight vector $[1, -1, 1, -1, 1, -1]$) show how the optimal trajectory parameter increases as the human model becomes larger for both weight muscle vectors in males and females. These results don't mean that the optimal trajectory parameter will always become bigger as the person/model becomes larger, but it provides strong evidence about the existence of this trend.

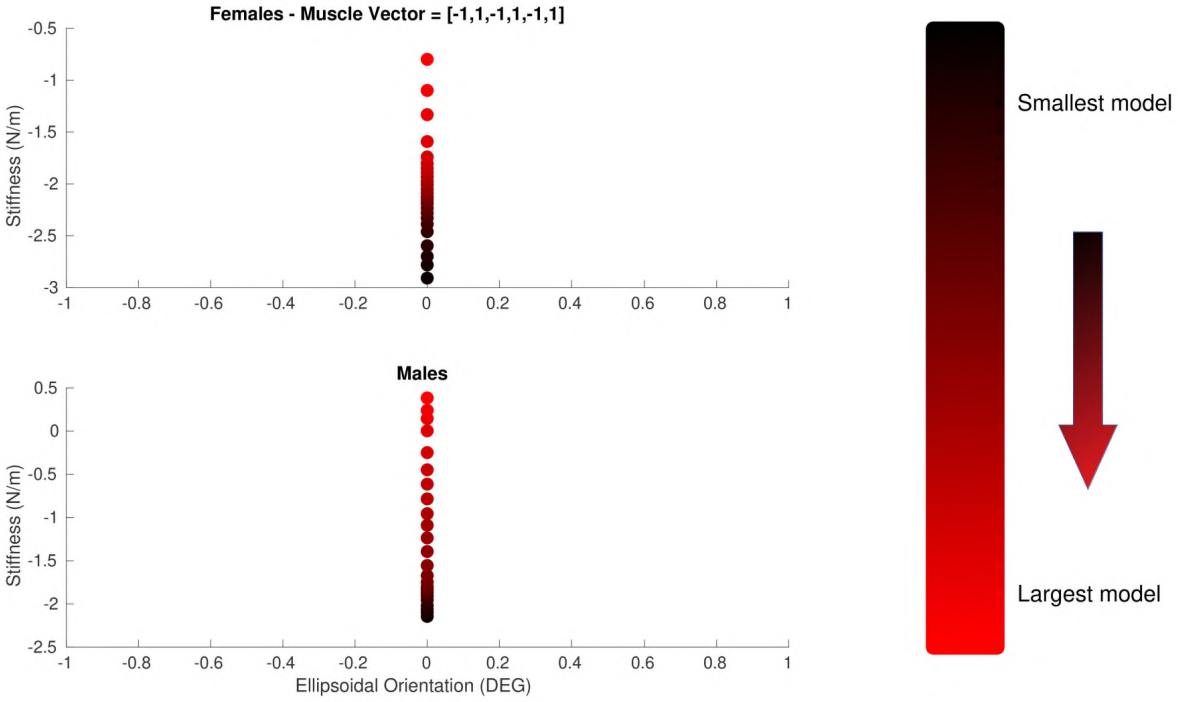

Figure 70: Optimal impedance parameters for the virtual population with the first muscle weight vector ([-1,1,-1,1,-1,1]).

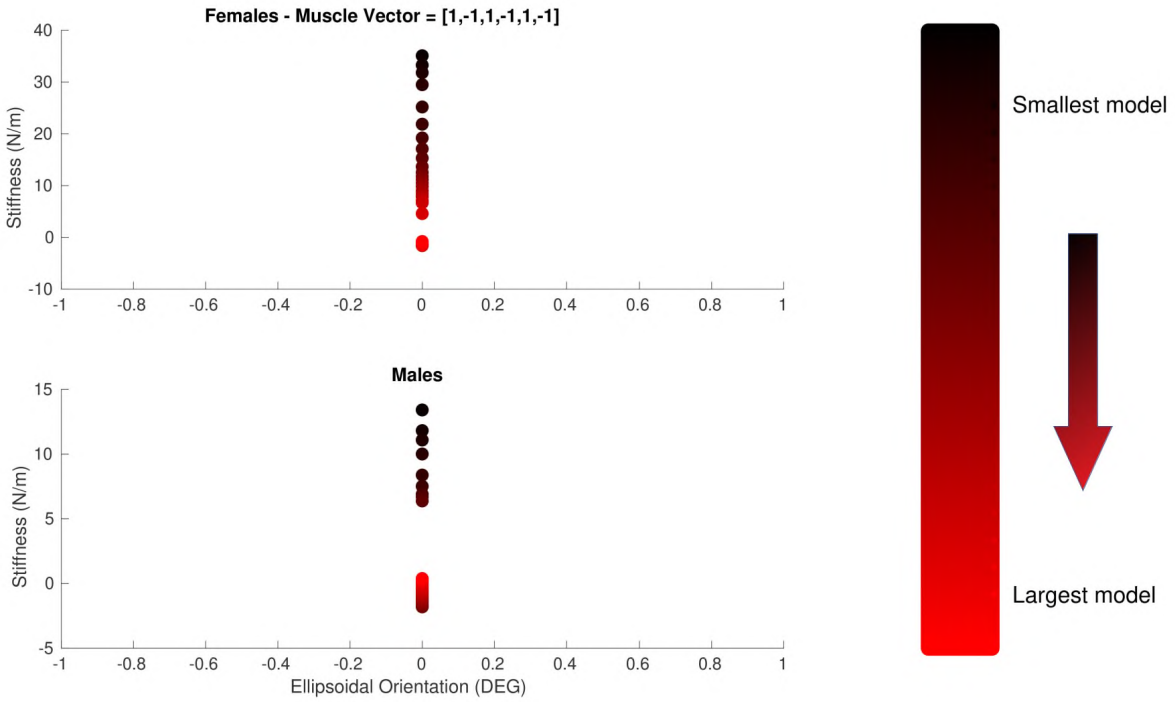

Figure 71: Optimal impedance parameters for the virtual population with the second muscle weight vector ([1,-1,1,-1,1,-1]).

Unlike the trajectory parameter optimization, figures 70 and 71 show how the optimal impedance parameter increases and decreases as the human model becomes larger for both (male and female models) depending on the weight muscle vector. For instance, Figure 70 (muscle weight vector $[-1, 1, -1, 1, -1, 1]$) shows that the optimal impedance parameter increases together with the size of the model, while Figure 71 (muscle weight vector $[1, 1, -1, 1, -1, 1, -1]$) shows the opposite effect. Although the increase in value is not equally proportional in value either in direction, a clear pattern can be identified.

Besides the correlation, it is important to highlight that, as a result of the unconstrained optimization during the simulation experiments, the results show how some optimal impedance parameters converged to positive values while some others to negatives. Considering that the zero-effort path (the circular trajectory of zero

impedance) was located inside of the ellipsoidal tracking trajectory, a positive stiffness impedance produces resistance forces acting centripetally, while negative stiffness impedance produces resistance forces acting centrifugally. Therefore, based on the skeletal distribution and the weight muscle vector, some optimal resistances might result in centripetal efforts and some others centrifugal efforts. In these cases, results associated with the weight muscle vector $[-1, 1, -1, 1, -1, 1]$ show that the largest models for both, males and females, have centripetal efforts as optimal impedance while the smallest models have centrifugal efforts. Contrarily, results associated with the weight muscle vector $[1, -1, 1, -1, 1, -1]$ show that the largest models have centrifugal efforts as optimal impedance while the smallest models have centripetal efforts.

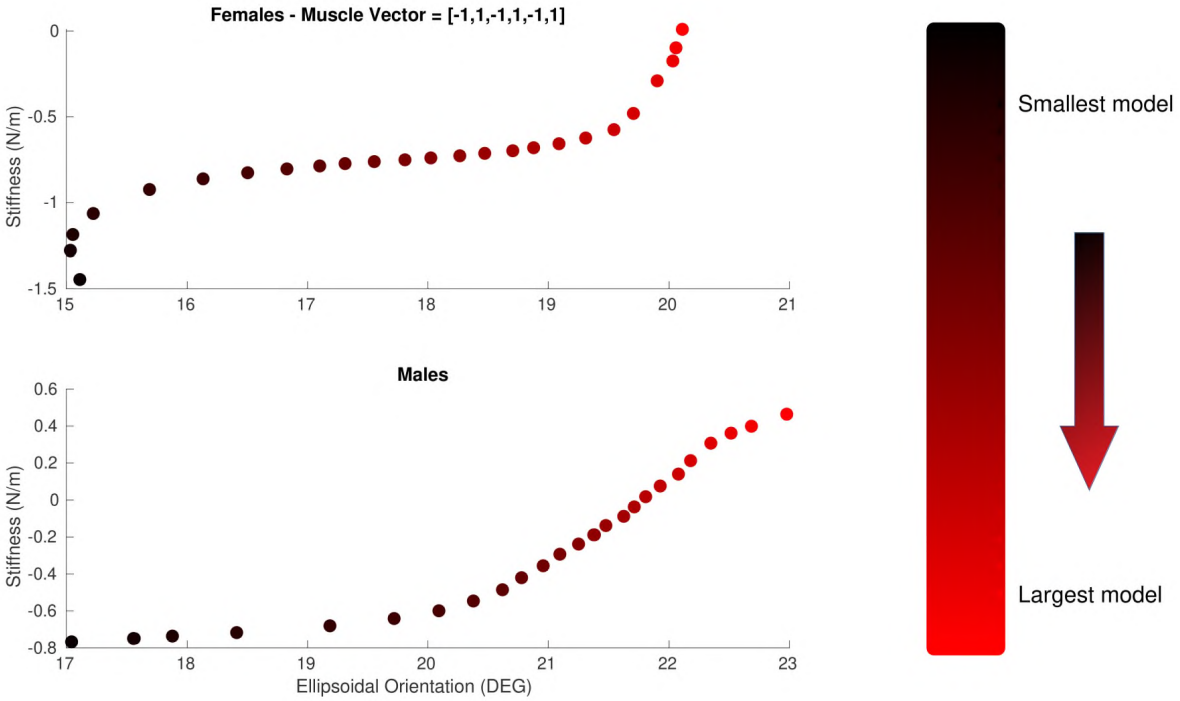

Figure 72: Optimal training parameters for the virtual population with the first muscle weight vector ([-1,1,-1,1,-1,1]).

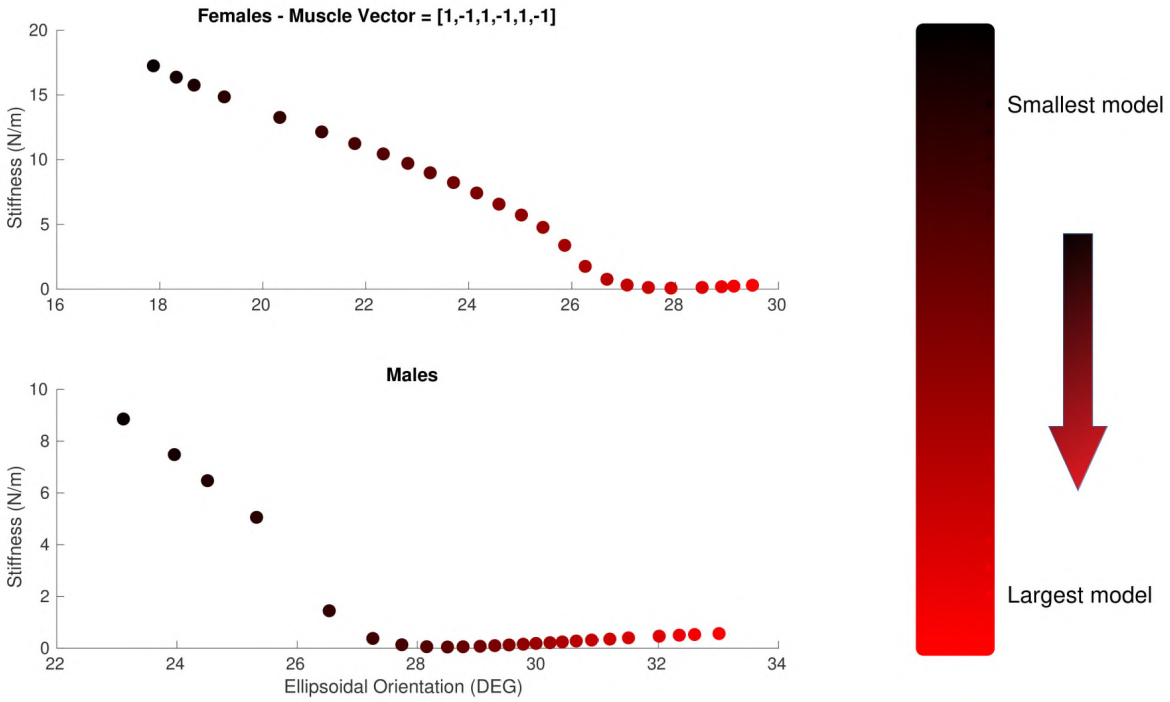

Figure 73: Optimal training parameters for the virtual population with the second muscle weight vector ([1,-1,1,-1,1,-1]).

For the multi-variable case, figures 72 (muscle weight vector $[-1, 1, -1, 1, -1, 1]$) and 73 (muscle weight vector $[1, -1, 1, -1, 1, -1]$) show how the pattern becomes more complicated. The optimal training parameters increase and decrease in different directions and proportions as the human model becomes larger based on the gender and weight muscle vector. Emphasizing the fact that the 2 weight muscle vectors have an opposite muscle objective (one maximizes the muscles that the other minimizes), a possible correlation is suggested, but it can't be ensured at this point.

From these last 2 figures, it is important to also highlight that the optimal trajectory and impedance parameters obtained from the single-variable optimization frameworks were not the same as the ones obtained with the multi-variable optimization frameworks. Consequently, it can be concluded that there is a unique combination of optimal training parameters, or put another way, for each trajectory

parameter there is a unique optimal impedance parameter and vice versa. It can also be concluded that the optimal training parameters depend on the musculoskeletal distribution, the optimization objective, and others. However, further study is still required to identify how strict the relationship between these parameters is, and thus, evaluate the feasibility of a relationship estimator. Being able to estimate the optimal parameters offline would provide the benefit of the initial conditions during real-time experiments avoiding large oscillations that normally occurred when the optimization variables are not close to the optimizers.

5.2.3 Hypothesis Testing

Before choosing the hypothesis testing approach, some graphical correlations were performed by plotting the musculoskeletal differences ($\|\delta M\|$) against the training parameter differences ($\|\delta\phi\|$) for each model comparison. The musculoskeletal differences were obtained by computing the norm of the vector representing the normalized difference between the arm link lengths of the 2 models as follows:

$$\delta M = [(L1_i - L1_j)/(L1_{max-d}), (L2_i - L2_j)/(L2_{max-d})], \tag{5.2}$$

where $L1_i$ and $L2_i$ are the upper and lower arm lengths of the model number i respectively, and the subscript "$max - d$" is the maximum difference obtained from the difference between the maximum and the minimum value.

The training parameter differences were obtained by computing the norm of the vector representing the normalized difference between the optimal training parameters as follows:

$$\delta\phi = [(\theta_i^* - \theta_j^*)/\theta_{max-d}, (K_i^* - K_j^*)/K_{max-d}], \tag{5.3}$$

where θ_i^* and K_i^* are the optimal trajectory parameter (optimal orientation) and the optimal stiffness impedance of of the model number i respectively, and the subscript "$max-d$" is the maximum difference obtained from the difference between the maximum and the minimum value.

These differences were computed for each of the total 1200 comparisons. This total number is the result of the 2 weight muscle vectors and the 25 male and 25 female models used in this study (300 per comparisons per each combination of gender and weight muscle vector as seen in Figure 74).

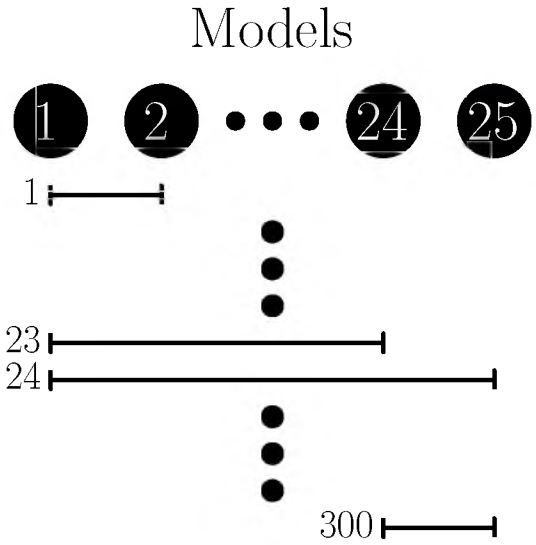

Figure 74: Total of model comparisons per each combination of gender and weight muscle vector.

Graphical correlation - trajectory parameter (single-variable)

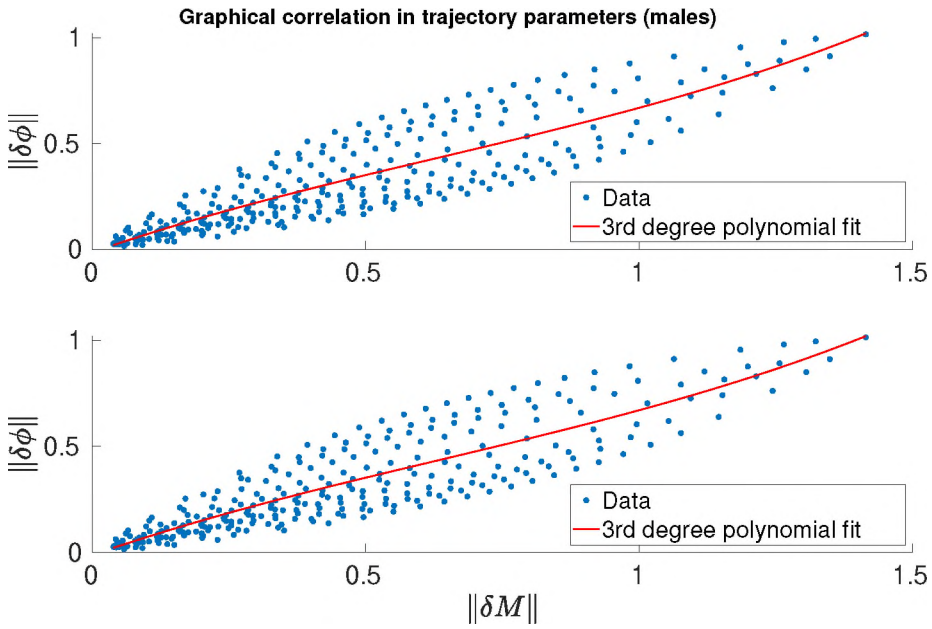

Figure 75: Graphical relationship for the trajectory parameter in males. Subplots present the results related to the muscle weight vectors [-1,1,-1,1,-1,1] and [1,-1,1,-1,1,-1] respectively.

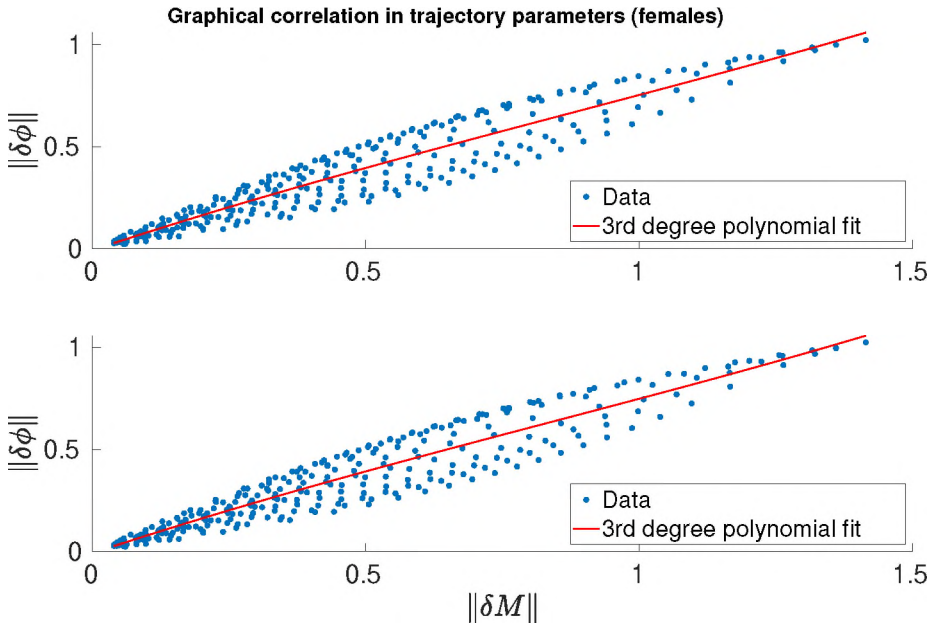

Figure 76: Graphical relationship for the trajectory parameter in females. Subplots present the results related to the muscle weight vectors [-1,1,-1,1,-1,1] and [1,-1,1,-1,1,-1] respectively.

Graphical correlation - impedance parameter (single-variable)

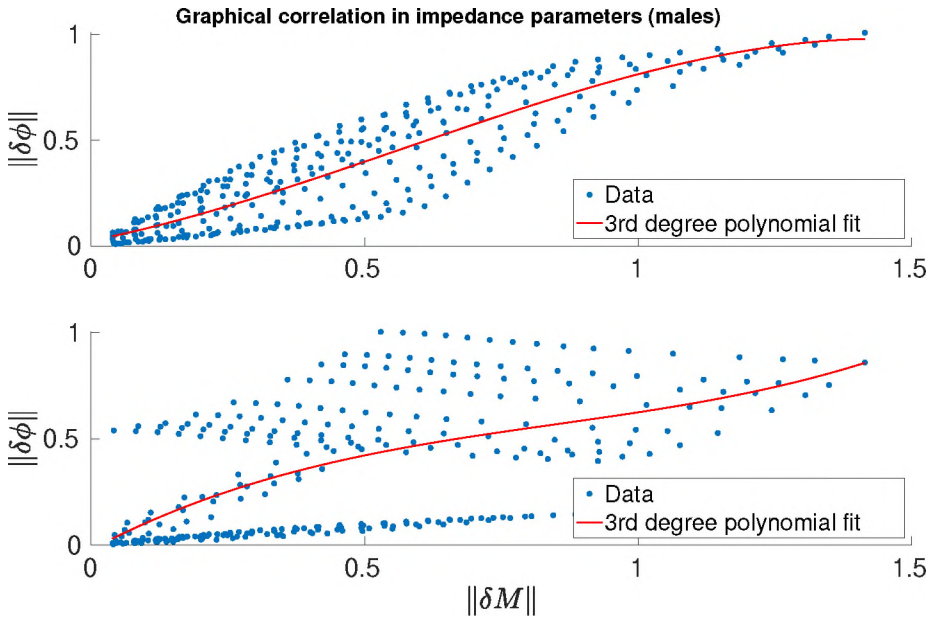

Figure 77: Graphical relationship for the impedance parameter in males. Subplots present the results related to the muscle weight vectors [-1,1,-1,1,-1,1] and [1,-1,1,-1,1,-1] respectively.

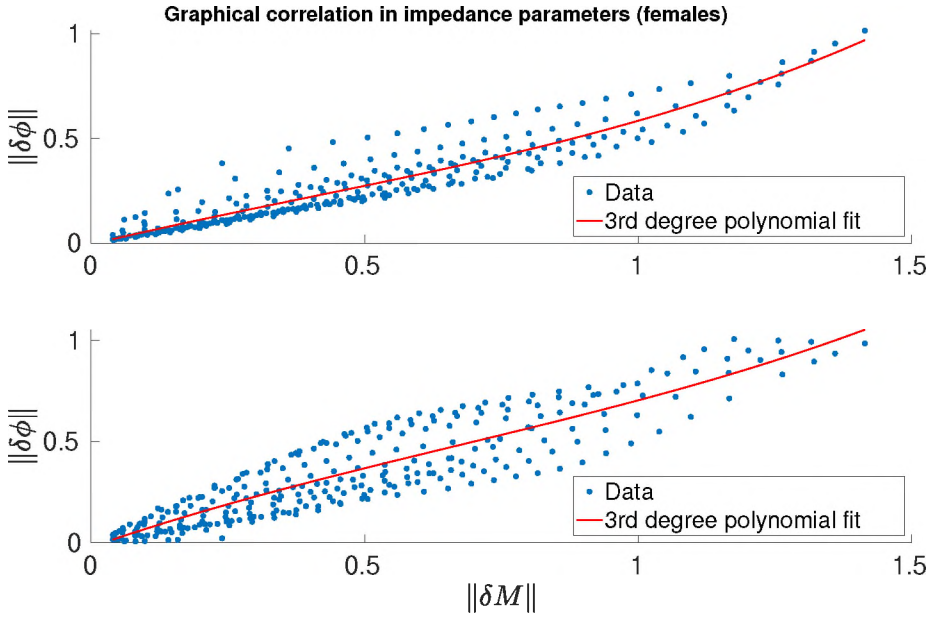

Figure 78: Graphical relationship for the impedance parameter in females. Subplots present the results related to the muscle weight vectors [-1,1,-1,1,-1,1] and [1,-1,1,-1,1,-1] respectively.

Graphical correlation - trajectory and impedance parameters (multi-variable)

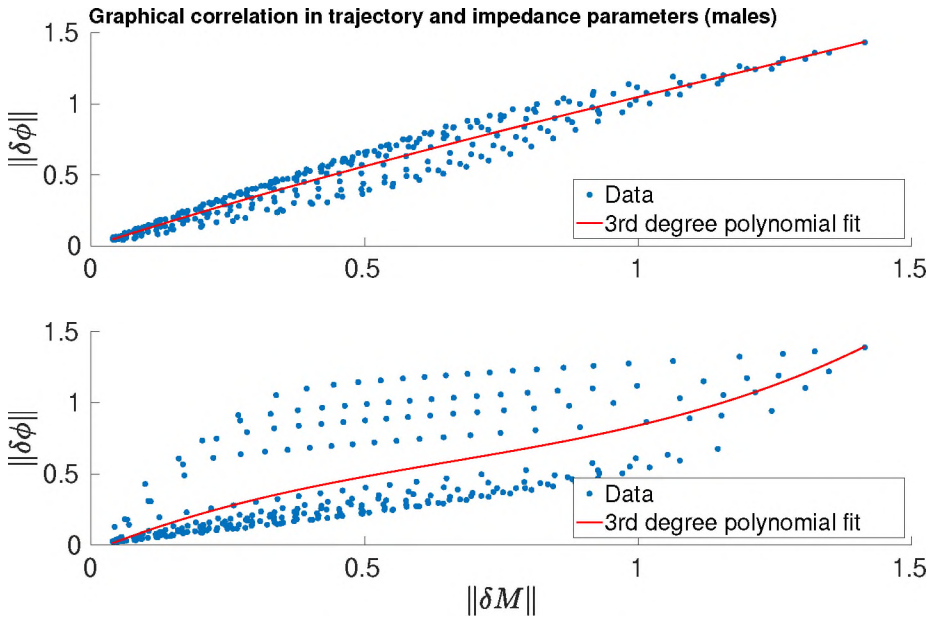

Figure 79: Graphical relationship for the trajectory and impedance parameters in males. Subplots present the results related to the muscle weight vectors [-1,1,-1,1,-1,1] and [1,-1,1,-1,1,-1] respectively.

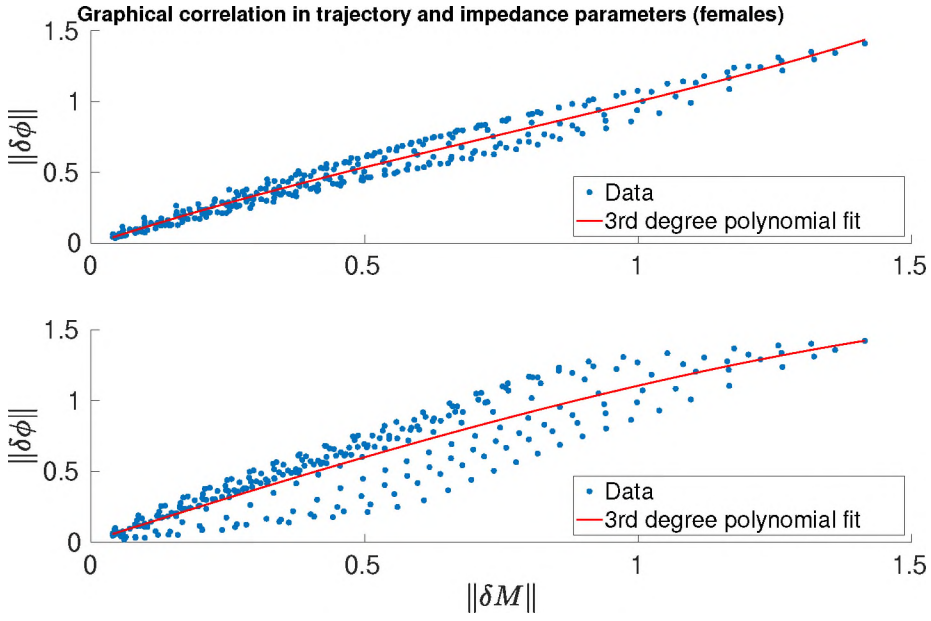

Figure 80: Graphical relationship for the trajectory and impedance parameters in females. Subplots present the results related to the muscle weight vectors [-1,1,-1,1,-1,1] and [1,-1,1,-1,1,-1] respectively.

Regarding the trajectory parameter in figures 75 and 76, a correlation can be graphically seen between the difference in the optimal training parameter and the difference in the musculoskeletal distribution for male and female models with both weight muscle vectors. Although this correlation seems to be linear for the most part, some non-linearities are also evident, especially at the beginning and at end of the graphs, where the musculoskeletal differences are small and large in magnitude. Regarding the impedance parameter, it is essential to note that the level of correlation between the differences in the optimal impedance parameters and the difference in the musculoskeletal distribution is less in comparison to the trajectory parameter. Nonetheless, figures 77 and 78 suggest its existence especially in the polynomial fit estimation. Regarding the multivariable case, a similar pattern was evidenced in figures 79 and 80. As a result of the previous plots, the hypothesis was tested for nonlinear dependencies by using CANOVA and Kendall rank correlation coefficient.

CANOVA is a novel method for testing nonlinear dependencies and correlations between 2 variables [155]. The framework works by defining a neighborhood for each data point, calculating the variance among the data points neighborhood, and finally, performing permutations to evaluate the significance of the observations within the neighborhood variance. CANOVA's performance has been compared to six other methods (Pearson, Kendall, Spearman, Distance Correlation, Hoeffding, and MIC) showing not only outstanding results but also a more agile performance by providing a low computational cost making it potentially useful for big data. However, given the fact that CANOVA is a new framework, Kendall's rank correlation coefficient was also used to support the results.

In hypothesis testing, the robustness of an estimator is very important but it normally comes at the price of an increased computational cost. However, Kendall correlation combines robustness (small gross error sensitivity) with high efficiency

(small asymptotic variance) [135, 20] making it one of the most preferred frameworks for nonlinear dependence. Kendall's framework works by evaluating the similarity between two variables given to the same set of objects and calculating a coefficient based on the number of required inversions of pairs of objects to transform one variable into the other [1].

After testing the hypothesis, the p-values for each of the 12 cases (trajectory, impedance, and multivariable for the 2 genders and 2 muscle weight vectors) were 10^{-6} (very small values). The results reject the null hypothesis that there is no statistically significant relationship between the difference in the musculoskeletal parameters and the difference in the optimal training parameters.

Parameter	τ-value	z-value	Conclusion (null hypothesis)
Trajectory - Male	0.8581	22.1637	Reject
Impedance - Male	0.7222	18.6552	Reject
Multivariable - Male	0.7107	18.3580	Reject
Trajectory - Female	0.8869	22.9078	Reject
Impedance - Female	0.8114	20.9570	Reject
Multivariable - Female	0.8240	21.2837	Reject

Table X: Muscle weight vector $[-1, 1, -1, 1, -1, 1]$.

Parameter	τ-value	z-value	Conclusion (null hypothesis)
Trajectory - Male	0.6604	17.0588	Reject
Impedance - Male	0.7250	18.7266	Reject
Multivariable - Male	0.4926	12.7244	Reject
Trajectory - Female	0.7697	19.8808	Reject
Impedance - Female	0.8103	20.9301	Reject
Multivariable - Female	0.7360	19.0111	Reject

Table XI: Muscle weight vector $[1, -1, 1, -1, 1, -1]$.

From the above tables, it can be seen that all the z-values are large enough (higher than 1.96) to reject the null hypothesis. Consequently, like the CANOVA framework, Kendall's results favor the alternative hypothesis supporting the fact that there is a relationship between training parameters and musculoskeletal parameters.

Given this fact, the next objective became to test the feasibility of a correlation estimator between these 2 variables.

5.3 Nonlinear Correlation Validation with Artificial Neural Networks

5.3.1 Approach

The objective of this part of the research is to estimate the nonlinear correlation between the musculoskeletal parameters and the optimal training parameters encountered previously. The successful identification of this correlation is very important because:

- It supports even stronger the existence of the correlation previously identified (reducing the probability of a type I hypothesis testing error).
- It provides additional information including a mathematical model of the correlation of the musculoskeletal parameters and training parameters.
- It makes it possible to estimate the neighborhood of the optimal parameters to be used as initial parameter guesses during real-time experiments.

As a result, a model estimator based on Artificial Neural Networks (ANNs) was developed.

Two datasets, each of them with a different weight muscle vector, including the total virtual population of 50 human arm models were used for the development and testing of the estimator. Each total dataset was split into training (80%) and testing (20%) data. The ANN algorithm was developed based on the feedforward neural network presented in [80]. The framework was built to use 8 inputs (one per each musculoskeletal parameter), 2 outputs (one per each training parameter), and a hidden layer with 6 nodes (selected experimentally). The complete scheme can be

seen in Figure 81.

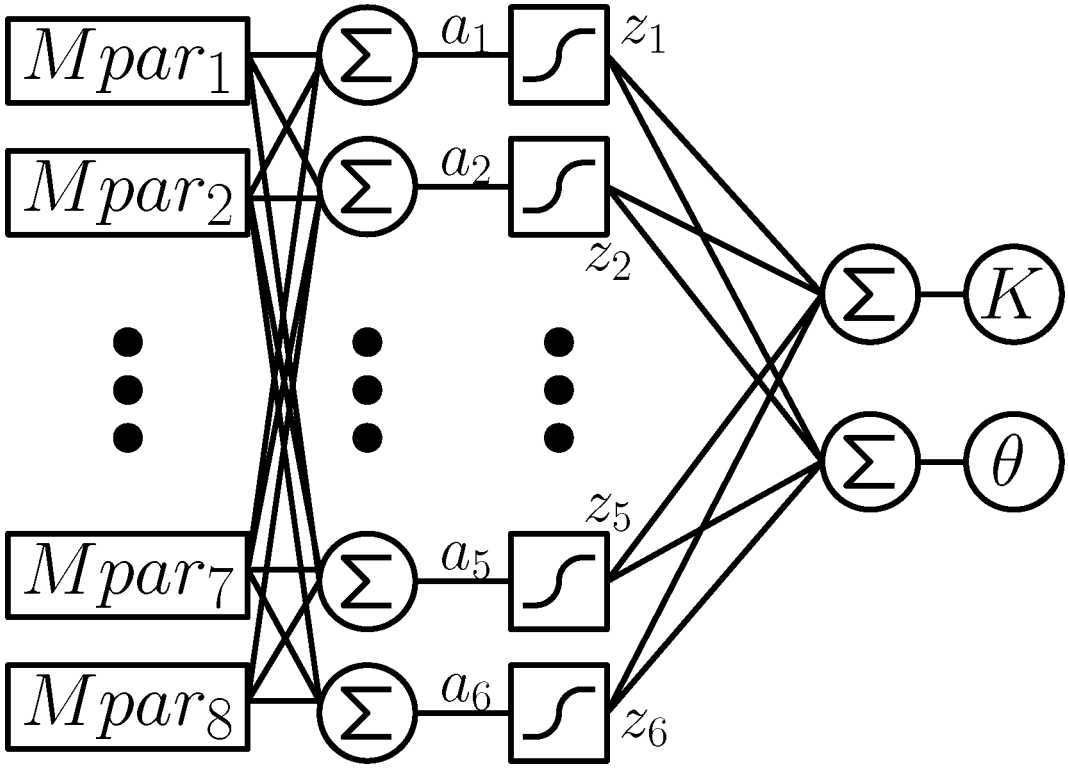

Figure 81: ANN scheme for the relationship estimator between musculoskeletal distribution and optimal training parameters.

From this figure, the 2 internal ANN parameters, a and z, are defined as follows:

$$a_i = \sum_{j=1}^{8} Mpar_j W_{in-ij}, \tag{5.4}$$

$$z_i = \frac{1}{1 + e^{-a_i}}, \tag{5.5}$$

where $Mpar$ is the vector of musculoskeletal parameters, i is the hidden layer node number, j is the parameter number, and W_{in-ij} is the value from the input weight matrix of the order (i, j). The output is calculated as follows:

$$\hat{Y}_k = \sum_{i=1}^{6} z_i W_{out-ki}, \tag{5.6}$$

where $\hat{Y}$ is the estimated output vector $[\hat{K}, \hat{\theta}]^T$, k is the output number, and W_{out-ki} is the value from the output weight matrix of the order (k, j).

The accuracy of the estimation relies on the calibration of the two weight matrices (W_{in} and W_{out}) performed through data training. Thus, the calibration was performed using the training data and the recommended backpropagation-of-error method from [80].

5.3.2 Results

Optimal Trajectory Estimation

The results from the estimations by using the testing data are presented in 4 different plots. All the trajectory parameter estimations (10 from the single-variable and 10 from the multi-variable optimization with male and female models) are presented in figures 82 and 83 (one plot per each weight muscle vector).

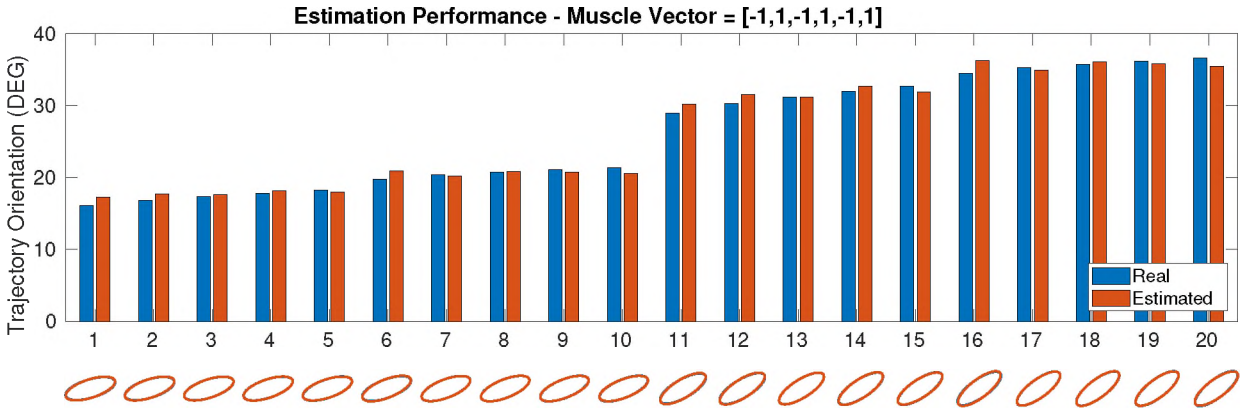

Figure 82: Optimal trajectory parameter estimation with a weight muscle vector equal to $[-1, 1, -1, 1, -1, 1]$.

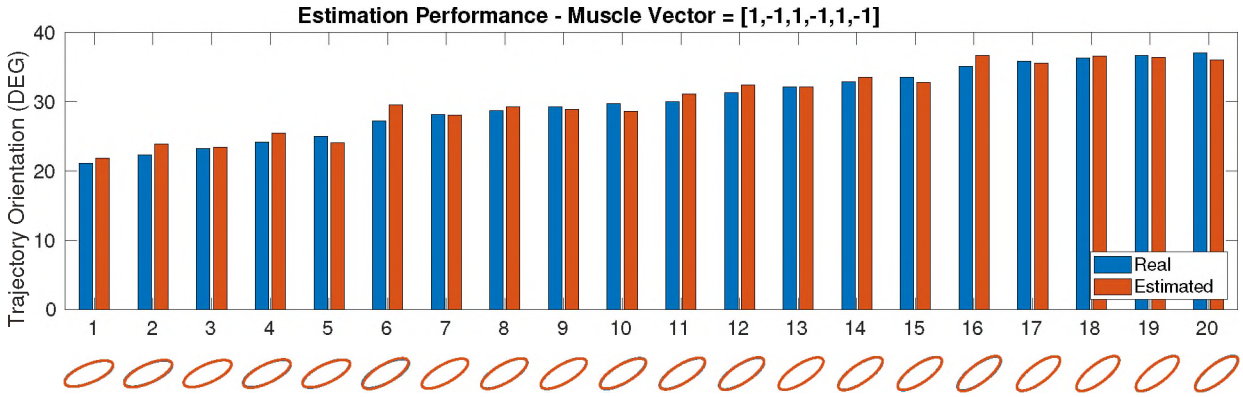

Figure 83: Optimal trajectory parameter estimation with a weight muscle vector equal to $[1, -1, 1, -1, 1, -1]$.

Figures 82 and 83 show the estimations for the 2 weight muscle vectors with RMS errors of 0.8306 and 0.9906 degrees respectively.

It is important to note that previous studies [31] have shown similar cost values in training protocols following ellipsoidal orientations reflected with respect to the axes (as showing in Figure 84 suggesting the existence of local minima. Therefore, although it was not the case, further research could lead to this scenario.

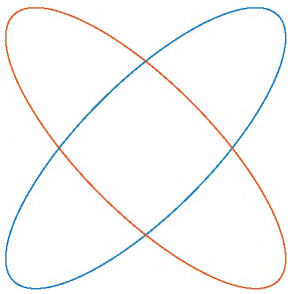

Figure 84: Ellipsoidal orientations with similar cost.

In a conclusion, the results show an acceptable estimation performance for potential use as an initial orientation during real-time experiments. Besides, they support the feasibility of an estimator for optimal trajectory parameters based on the musculoskeletal distribution of a human/model.

Optimal Impedance Estimation

Similarly, all the impedance parameter estimations (10 from the single-variable and 10 from the multi-variable optimization with male and female models) are presented in figures 85 and 86.

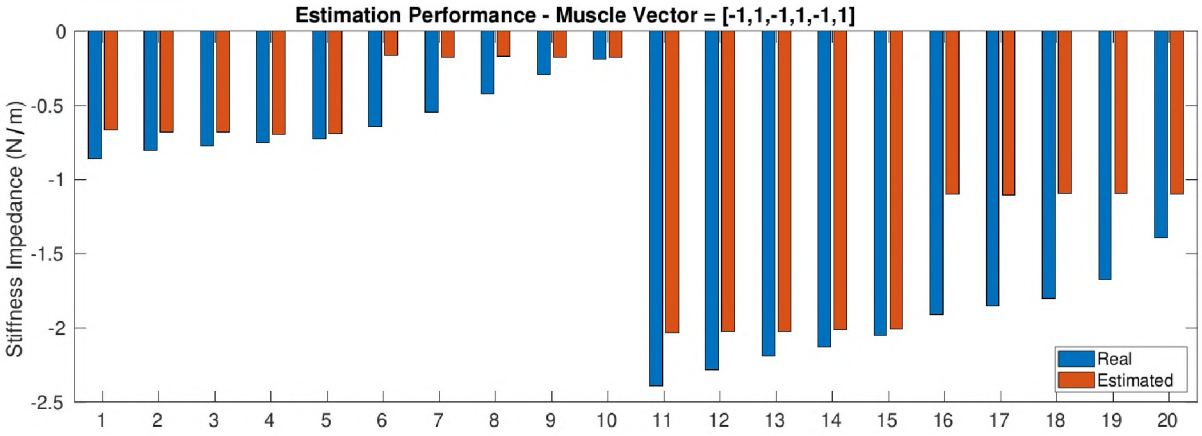

Figure 85: Optimal impedance parameter estimation with a weight muscle vector equal to $[-1, 1, -1, 1, -1, 1]$.

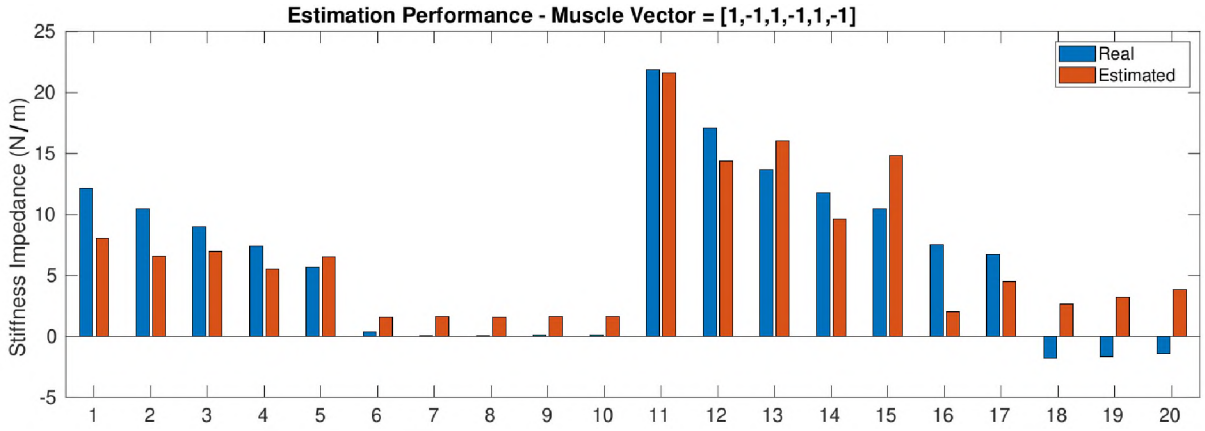

Figure 86: Optimal impedance parameter estimation with a weight muscle vector equal to $[1, -1, 1, -1, 1, -1]$.

Figures 85 and 86 show the estimations for the 2 weight muscle vectors with RMS errors of 0.3792 and 3.1096 Newton/meters respectively. Unlike the trajectory, the impedance seems to not have multiple local optima points and the impedance estimator seems to support this fact. In a conclusion, these results also show an acceptable estimation performance for potential using as an initial impedance parameter during real-time experiments. However, more information, supported by real-time experiments, seems to be required to prove the feasibility of an impedance estimator *only* based on the musculoskeletal distribution of a human/model.

5.4 Time-Varying Dynamics present in Training Personalization

5.4.1 Approach

The objective of this work is to identify the presence of time-varying dynamics during exercise by relating muscle effort distributions to trajectory and resistance settings over time. To achieve this goal, the dataset from the real-time experiments presented in Section 3.4 was re-used. As a revision of this experiment, 17 trials of 1 minute each were conducted. One male participant of 22 years old, height of 180 cm, and weight of 91.8 kg free of any injuries, cardiovascular disease, and/or any other physical limitation was recruited. The trials were resistance-based training including different levels of resistance and speeds of the trajectory.

The muscular effort distributions, representing the participation of each muscle in the training activity, were estimated based on the muscle activations. The complete process from the raw signals to the muscle effort distributions involves the following steps:

1. The raw signals are recorded at a frequency of 2 kHz.

2. A normalization is performed on the signals by removing the mean and dividing

each value by its maximum activation (isometric test in trial 0).

3. A second-order Butterworth band-pass filter between 30 and 950 Hz is used to clean the data.

4. A full-wave rectification is implemented to convert the signal into only positive values.

5. A second-order Butterworth low-pass filter at 50 Hz is used to attenuate the signal.

6. A normalization of each muscle activation is performed with respect to the sum of all activations to obtain the muscle effort distribution as follows:

$$M = \frac{[M_1, M_2, M_3, M_4, M_5, M_6]}{\sum_{i=1}^{6} M_i}, \tag{5.7}$$

where M is the vector of muscle effort distribution. For instance, a muscle vector equal to $M = [0.1, 0.1, 0.2, 0.2, 0.2, 0.2]$ represents a muscle effort distribution where the 2 first muscles and the last 4 muscles perform 10% and 20% of the total effort respectively.

The dataset including 1-minute trials was split into training (75%) and testing (25%) data. To observe the performance of the estimated model over time, the testing data was used as segments and as a whole. The testing data used by segments was built from 3 equally-divided periods of 15 seconds each and they were labeled in the plots as "First", "Second", and "Third" for the first, second, and third 15-seconds respectively. The whole data results are labeled in the plots as "Whole".

The ANN algorithm was developed based on the feedforward neural network and the calibration was performed using the training data and the recommended

backpropagation-of-error method presented in [80]. The ANN scheme was built with 6 inputs (one per each muscle), 2 outputs (one per each training parameter), and a hidden layer with 6 nodes (selected experimentally). The complete scheme can be seen in Figure 87. From this figure, the 2 internal ANN parameters, a, z, and $\hat{Y}$ (estimated output vector) are defined as the same as in Eqs. 5.4, 5.5, and 5.6 respectively.

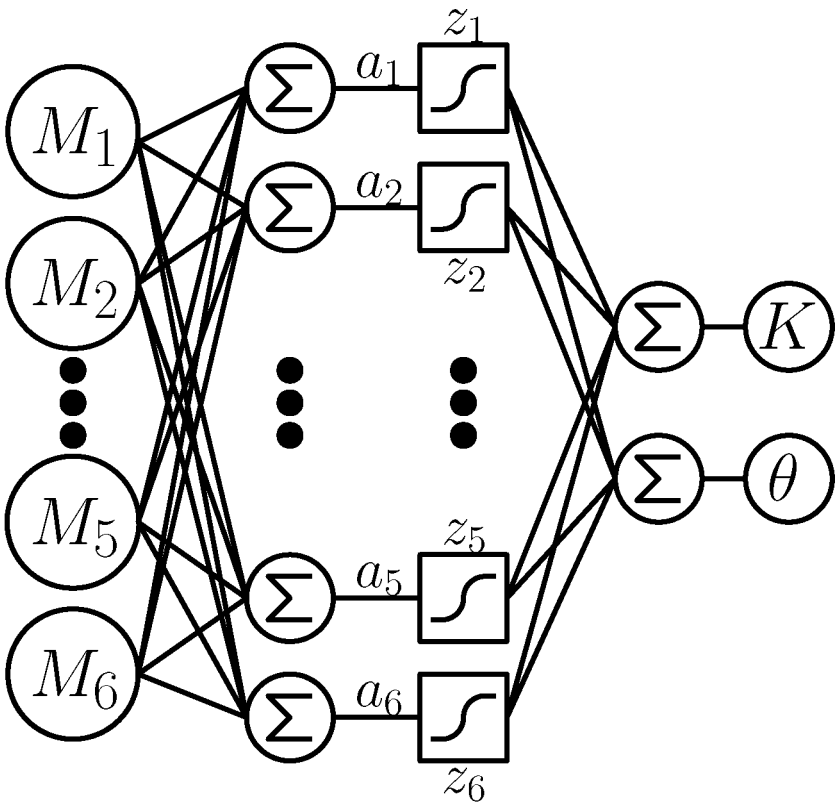

Figure 87: ANN scheme for the relationship estimator between muscle effort distribution and training parameters.

5.4.2 Results

The average muscle effort distributions during each trial with low (see Figure 88) and high (see Figure 89) impedances are presented below.

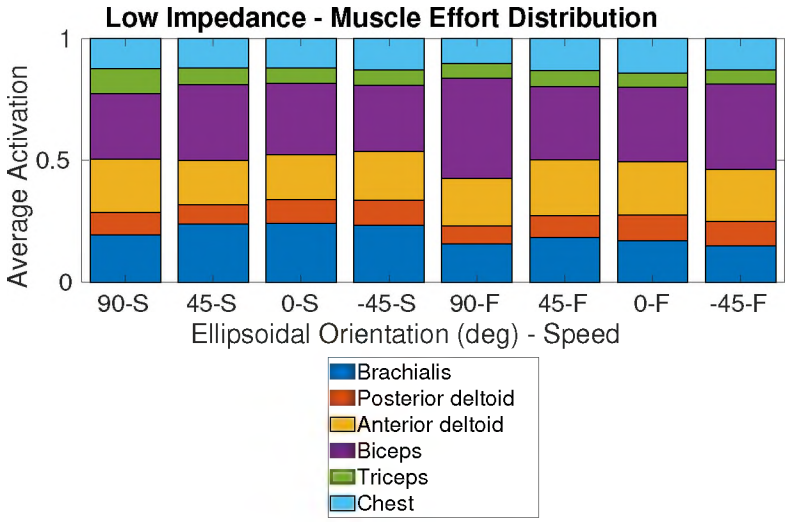

Figure 88: Average muscle effort distribution during the training trials with low impedance. The speed label "S" refers to the trials with slow frequency (periods of rotation of 8 seconds).

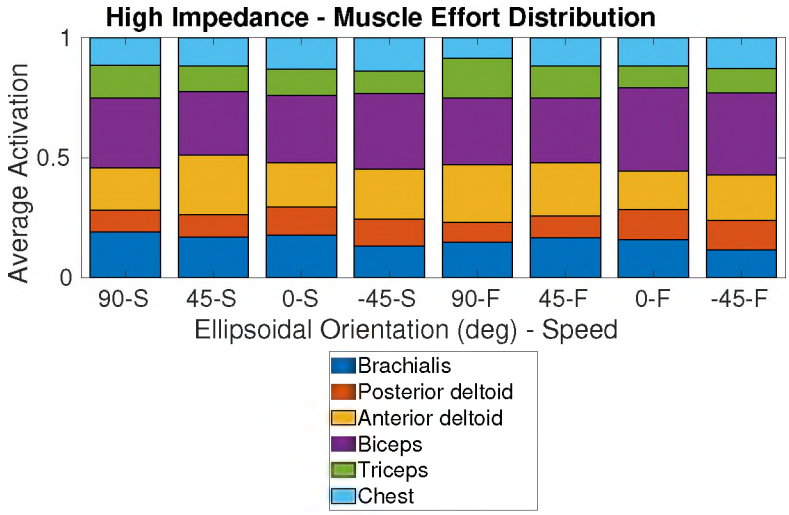

Figure 89: Average muscle effort distribution during the training trials with high impedance. The speed label "F" refers to the trials with fast frequency (periods of rotation of 4 seconds).

The results from the root-mean-square (RMS) error between the real output and the estimated output are presented in Figures. 90 and 91.

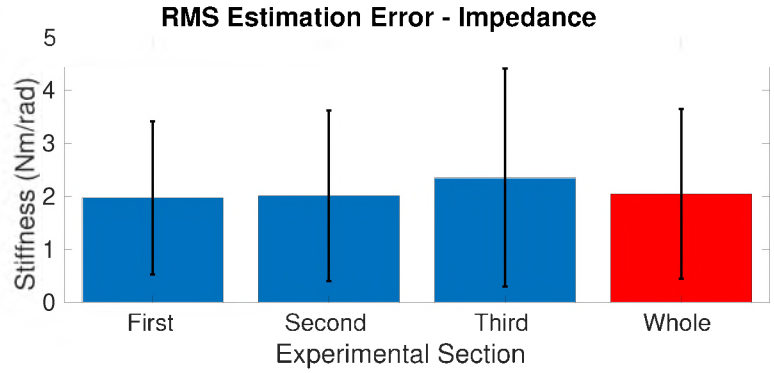

Figure 90: RMS error in the estimation of the impedance parameter.

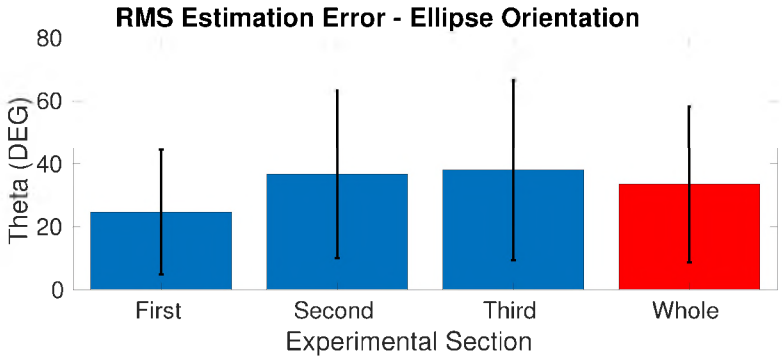

Figure 91: RMS error in the estimation of the ellipse.

The previous figures show a good estimation for the training parameters based on the low magnitude of the errors and the similar magnitude values in the 3 sections ("First", "Second", and "Third") and the complete testing data ("Complete"). However, it is important to highlight the fact that the best estimation was achieved in the first section (the estimation in the first 15 seconds). For the impedance estimation, the RMS error went from 1.97 Nm/rad in the first section to 2.0 and 2.36 for the second and third sections respectively. For the ellipse orientation, the RMS error went from 24.68 deg in the first section to 36.7 and 38.05 for the second and third sections respectively. These results evidence that the prediction accuracy of the model is lost over time. These outcomes show the complexity of the muscle dynamics for long-term estimations suggesting the existence of time-varying dynamics playing

an important role in the relationship with the training parameters.

It is suggested that organismic and intervening variables such as musculoskeletal distribution, performance status, level of hydration, and mood produce an effect on the muscles. However, biological dynamics like muscle temperature or fatigue seem to potentially introduce time-varying dynamics depending on biological factors associated with training such as fatigue, body temperature, and level of hydration.

It is important to also consider that the trajectory tracking was not perfect possibly introducing variation in the muscle effort distribution during each trial, and consequently affecting the model estimation. Besides, the over-actuated nature of the human body (having more muscle actuators than position variables) makes it possible to reach a target position with infinite possible musculoskeletal orientations (see Figure 92). Therefore, part of the changes in the model estimation could also be attributed to the involuntary elbow rotations able to generate a completely new muscle effort distribution. These involuntary rotations could occur because of muscle fatigue or simply distraction.

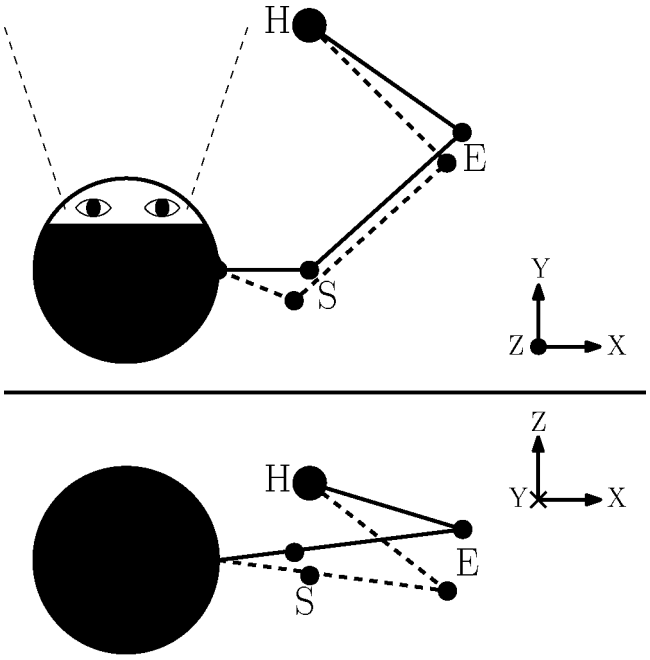

Figure 92: Example for the redundancy on the musculoskeletal orientation. (S, E, and H represents shoulder, elbow, and hand respectively).

CHAPTER VI

REAL-TIME OPTIMIZATION EXPERIMENTS

6.1 Overview

The main purpose of the study was to show the feasibility of the 3 model-free optimization approaches by evaluating their performance in real-time experiments. Besides, we aimed to generate some discussions, identify limitations, and provide potential improvements towards future developments. Regarding these experiments, 2 robots (WAM and 4OptimX) were used. The first experiments were conducted using the WAM robot because it is lighter and more user-friendly than the 4OptimX providing an easier and safer environment to test the model-free for the first time. Later, in order to fully test the capabilities of the proposed model-free frameworks, the 4OptimX, which is stronger (it supports higher iteration forces), more versatile (it can be integrated with other systems), and more precise (it supports a higher sampling rate), was used for the succeeding experiments.

Experiments were performed in 4 different phases to release new features progressively based on feedback and data from previous phases. These 4 phases were:

1. Single-variable trajectory optimization without impedance: The WAM robot operated with its PD and gravity-compensation control (see Section 2.5) was

used during this stage. The main objective of this phase was to test the feasibility of the model-free approach in a safe environment.

2. Single-variable trajectory optimization with impedance: The 4OptimX robot operated with its impedance control (see Section 2.6.2) was used during this phase. The main objective of this phase was to test the model-free approach for trajectory optimization with a fixed impedance acting based on the human behavior.

3. Single-variable impedance optimization: The 4OptimX robot was also used during this phase. The main objective of this phase was to test the model-free approach for impedance optimization with a fixed trajectory orientation.

4. Multi-variable trajectory and impedance optimization: The 4OptimX was also used during this phase. The main objective of this phase was to test all the features previously tested simultaneously with the multi-variable model-free optimization approach involving trajectory and impedance variables.

For each real-time experiments, the following dependent and organismic variables (in Tables XII and XIII respectively) were measured and collected:

Table XII: Dependent variables from the experimental data.

Variable	Description
Convergence status	Yes/No
Solution	Ellipse orientation and/or stiffness value
Convergence time	Time to meet the convergence criterion

Table XIII: Organismic variables about subjects.

Variable	Description
Height	In centimeters
Weight	In kilograms
Gender	Male (M) or female (F)
Age	In years
Side dominant	Left (L), right (R), or both (B)
Upper arm length	From shoulder to elbow in centimeters
Forearm length	From elbow to wrist in centimeters

6.2 Experimental Protocol

This study had an IRB which covers for Ethical Approval. It was provided by Cleveland State University with reference number 30305-RIC-HS. An informed consent form was signed by each subject conducting the experiment (see Appendix E). However, due to the pandemic situation with SARS-CoV-2, the experiments performed after March 2020 (phases 2, 3, and 4) were self-conducted. That means I played the role of the subject and the experimenter simultaneously during these experiments.

Except for the first phase (the feasibility test) which was conducted with only the dominant side of the body, the experiments were conducted by using both sides of the body (the right and left arm). For an accurate analysis, no more than 1 phase was performed on the same day and they were performed following the same protocol:

1. Fill the Table XIII with the measurements from the subject.

2. Warm-up for 2 minutes.

3. Place the EMGs in one of the upper body side (side randomly selected).

4. A minimum of 2 isometric tests for each EMG are performed for calibration.

5. Start the first test of the day. The initial values for the optimization variables are randomly set.

6. Wait for the solution to converge. If convergence is not achieved in less than 4 minutes, the experimental test results in a convergence failure, and no optimal parameters are obtained. Regardless of the success or failure of convergence, the next step follows.

7. Rest for 2 minutes.

8. Start the second test of the day. The initial values for the optimization variables are randomly set.

9. Wait for the solution to converge. If convergence is not achieved in less than 4 minutes, the experimental test results in a convergence failure, and no optimal parameters are obtained. Regardless of the success or failure of convergence, the next step follows.

10. Remove and place the EMGs in the other upper body side.

11. A minimum of 2 isometric tests for each EMG are performed for calibration.

12. Start the third test of the day. The initial values for the optimization variables are randomly set.

13. Wait for the solution to converge. If convergence is not achieved in less than 4 minutes, the experimental test results in a convergence failure, and no optimal parameters are obtained. Regardless of the success or failure of convergence, the next step follows.

14. Rest for 2 minutes.

15. Start the fourth and last test of the day. The initial values for the optimization variables are randomly set.

16. Wait for the solution to converge. If convergence is not achieved in less than 4 minutes, the experimental test results in a convergence failure, and no optimal parameters are obtained. Regardless of the success or failure of convergence, the next step follows.

17. Save all the data.

18. Fill the Table XII with the results from the subject.

The trajectory pattern was supplied in an ellipsoid pattern (horizontal, vertical, and angled). The major movements involved were flexion and extension in the sagittal plane, as well as horizontal abduction and adduction in the transverse plane. Together these movements combined into an anterior circumduction movement. Therefore, the primary drivers for the glenohumeral joint [11] were selected for this study (see Figure 93) in the following order:

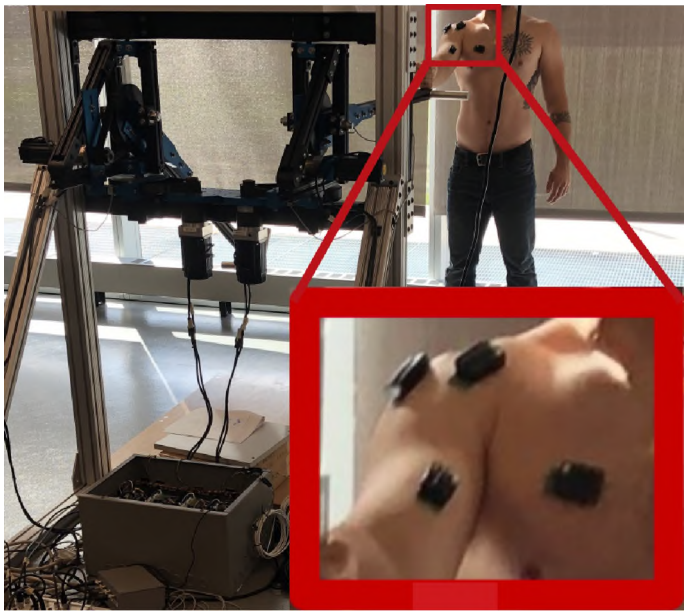

Figure 93: Elbow immobilizers for shoulder muscles isolation.

For the first phase:

1. Anterior deltoid.
2. Lateral deltoid.
3. Biceps brachii.
4. Pectoralis major.

For the second, third, and fourth phase:

1. Anterior deltoid.
2. Lateral deltoid.
3. Posterior deltoid.
4. Pectoralis major.

The deltoid muscles (lateral, anterior, and posterior) were chosen because they are the main glenohumeral drivers and responsible for the motion of the arm in the three dimensions. The chest was chosen because it is the main contributor to the stabilization and adduction of the shoulder. The bicep was initially chosen (only for the first stage) as it works synergistically with the anterior deltoid to hold the lower arm in a fixed position while the upper arm is moved into flexion or extension about the glenohumeral joint. Besides, the bicep has a relationship with the elbow flexion providing information about undesired rotations causing loss of focus in the glenohumeral action. However, its low effort distribution and the use of elbow immobilizers in the second, third, and fourth phases removed the need to continue to use this muscle for the study.

It is important to note that optimal solutions depend on the relative position of the subject with respect to the machine. Thus, a mark was placed on the ground and the subject was required to stand on it during the trials from the same phase to validate the results (similar converged solutions). However, it is also important to highlight that the framework is designed to achieve convergence independently of the relative position of the subject with respect to the machine.

The muscle activations from these glenohumeral muscles were computed from the raw signals recorded with EMGs at a frequency of 2 kHz. Then, they were real-time processed to obtain the muscle activations as follows:

1. Bandpass second-order Butterworth filter between 30 and 950 Hz.

2. Full-wave rectification.

3. Low-pass second-order Butterworth filter at 50 Hz.

Given the objective of these experiments was to show the feasibility of the model-free framework, the muscle weight vector (used to focus or defocus a muscle or group of muscles) was randomly choose during each stage. However, it is important to highlight that some muscles work synergistically better with some muscles than with others. Thus, for best results and maximum efficiency, it is recommended the muscle weight vector be professionally selected by a professional trainer or therapist.

As previously noted, the involuntary inclusion of other muscles (while conducting experiments) potentially affects the results. For this reason, elbow immobilizers were used to guarantee muscle group isolation (see Figure 94).

There were a total of 2 advanced exercise protocols. The first one was only used on the first phase where there wasn't a zero-effort path (it was zero-effort in the complete robot's workspace). The regulated trajectory was a geometric path to

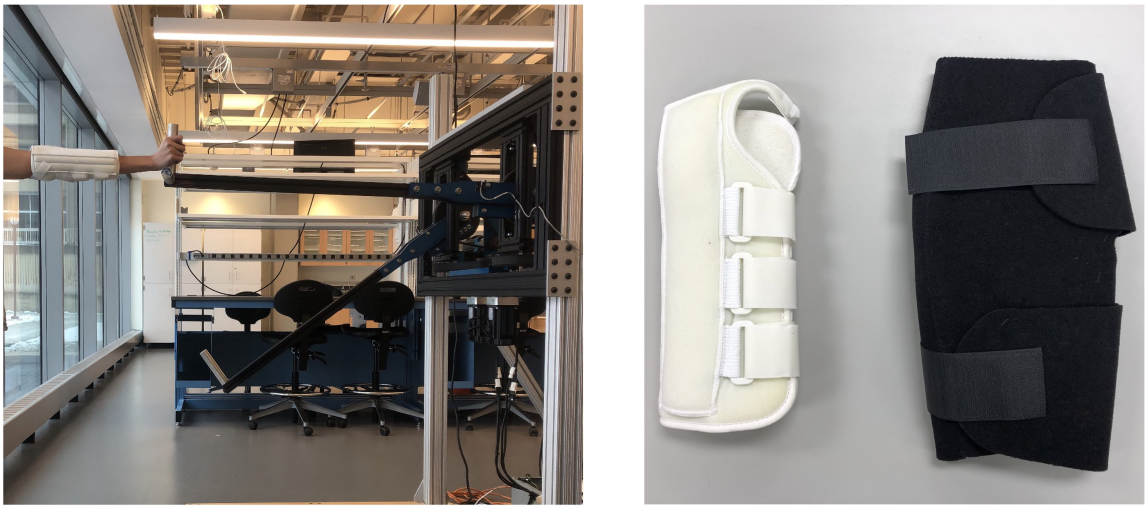

Figure 94: Elbow immobilizers for shoulder muscles isolation.

be tracked by the user (see Figure 95). User and desired positions were represented in the map by a red and a blue dot respectively. On the same figure, the blue line represents the ellipsoidal curve of 80 cm and 40 cm of axes. The desired position (blue dot) moves periodically over the blue ellipse while this curve rotates.

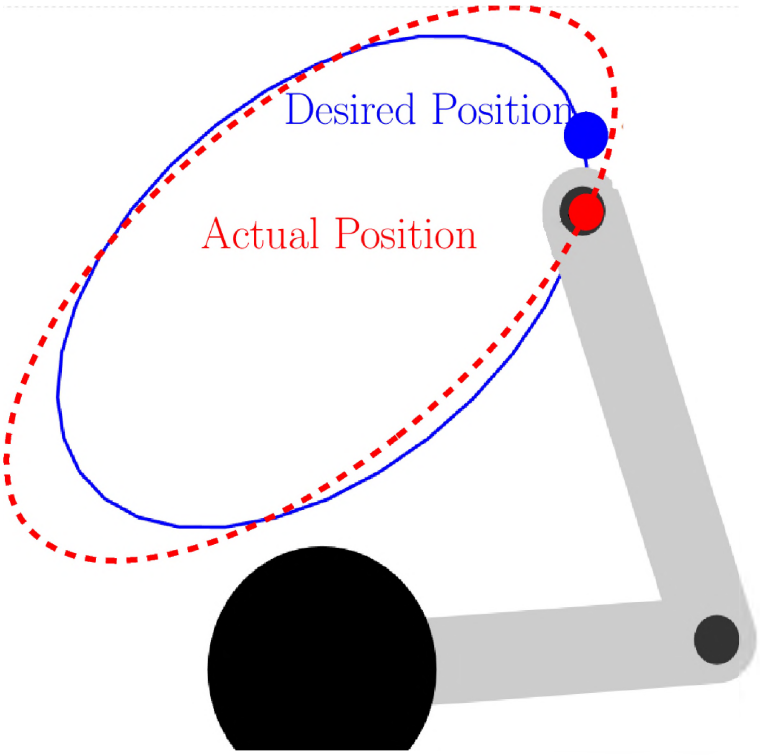

Figure 95: Ellipsoidal path to be tracked by the user.

The second advanced exercise protocol was followed in the second, third, and fourth phases. During these phases, the robotic exercise machine establishes a zero-effort circular path (machine's neutral path) of 40 cm of radius producing a controlled impedance against the subject asked to follow an elliptical trajectory path. This elliptical trajectory path has 30 and 90 cm of axes. The user-defined impedance produced by the controller is based on the deviations from the neutral path and the force/torque applied by the subject. The positions and trajectories involved in the training protocol can be seen in Figure 96. The machine's neutral position (X) is labeled with a red dot and it moves periodically over a red circular curve representing the machine's trajectory where the impedance is zero. The target position (X_d) is labeled with a blue dot moving periodically over a blue ellipsoidal curve of fixed axis lengths and programmable orientation. The user position (X_a) is labeled with a green dot and tries to follow the blue.

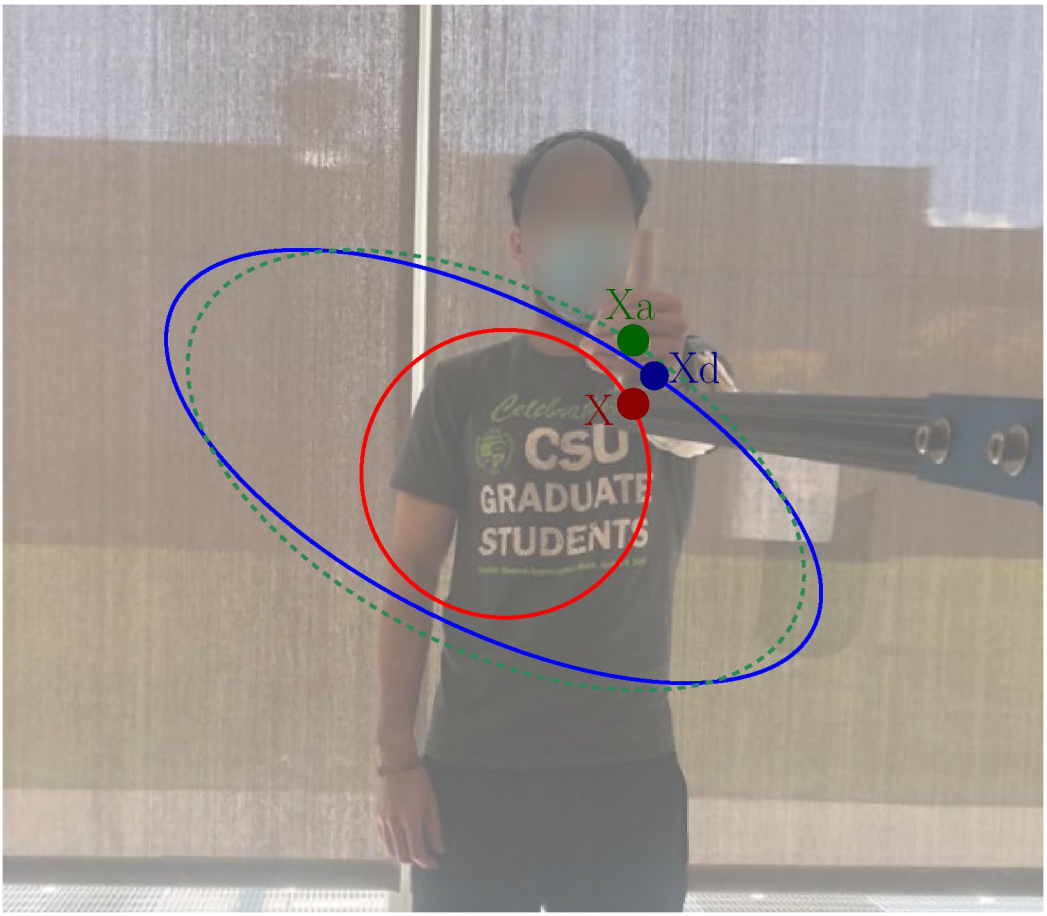

Figure 96: Positions involved in the training protocol: robot trajectory (red dot or X), target position (blue dot or X_d), and user position (green dot or X_a).

6.3 Phase I - Single Variable Trajectory Optimization No-Impedance

6.3.1 Methodology

During the first phase, the objective was to maximize all the activations from the involved muscles but assigning different weights (priorities) to each of them [26]. The model-free approach was implemented for performance maximization and the performance function was defined as the moving average of the multiplication of a muscle weight vector and the muscle activation derived as follows:

$$\max_{\theta} \quad J(t) = \frac{t_s}{t_{rev}} \sum_{(i=t-t_{rev}/t_s)}^{t} \Big(W_m M(t) \Big), \tag{6.1}$$

where θ is the ellipse orientation, t_s is the sample time set at 5×10^{-4} seconds, t_{rev} is the period of revolution of the blue dot (dot along the ellipsoidal path), t is the current time, W_m is the muscle weight vector, and M the vector of muscle activations.

One subject of the age of 23 (see Table XIV) performed 3 sets of experiments on 3 different days (see Figure 97). During each day, one set of 2 trials (one trial next to the other one) was performed by using the same parameter configuration. The first set of experiments used the muscle weight vector $W_m = [1, 5, 3, 5]$. This set gave the highest priority to the anterior deltoid and pectoralis major, medium priority to the biceps brachii, and the lowest priority to the lateral deltoid. The second set used the muscle weight vector $W_m = [3, 5, 1, 1]$. This set gave the highest priority to the anterior deltoid, medium priority to the lateral deltoid, and the lowest to biceps brachii and pectoralis major. And the third set used the muscle weight vector $W_m = [1, 1, 5, 5]$). This latest set gave the highest priority to the biceps brachii and pectoralis major and the lowest to the lateral and anterior deltoid.

Figure 97: Experiment of human training with AEM.

Table XIV: Organismic variables about the first subject.

Variable	Description
Height	180.4 cm
Weight	93.2 kg
Gender	Male (M)
Age	23
Side dominant	Right (R)
Upper arm length	33.0 centimeters
Forearm length	24.2 centimeters

The ESC parameters used on this project (related to Figure 14) can be seen in Table XV.

Table XV: Framework settings and configuration parameters for the first phase of experiments.

Parameter	Description	Value	Units
a	Perturbation amplitude	0.1	-
ω	Perturbation frequency	1	rad/s
ω_l	Low-pass filter cutoff frequency	0.1	rad/s
ω_h	High-pass filter cutoff frequency	0.5	rad/s
k	Gain	1000	-
θ_{th}	Convergence tolerance for trajectory	10°	deg
t_{con}	Convergence time threshold	10	s

6.3.2 Results and Discussion

The results from the first phase of the experimental sets are presented in the plots and tables below:

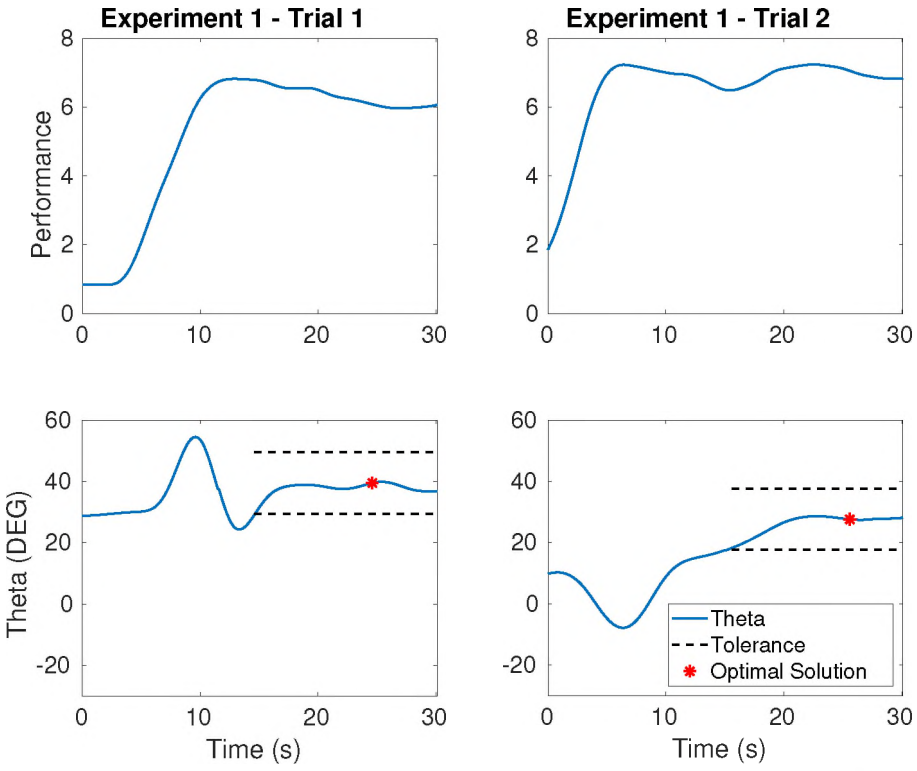

Figure 98: First set of experiments with the muscle weight vector $W = [1, 5, 3, 5]$

Table XVI: Table of the experimental results for the first set ($W = [1, 5, 3, 5]$).

Arm side	Trial	Convergence status	Solution (°)	Convergence time (s)
Dominant	1	Yes	39.50	24.6
Dominant	2	Yes	27.60	25.6

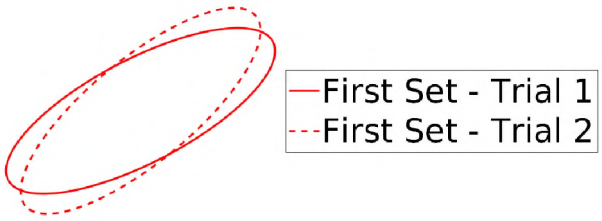

Figure 99: Convergence solutions from the first set of experiments ($W = [1, 5, 3, 5]$).

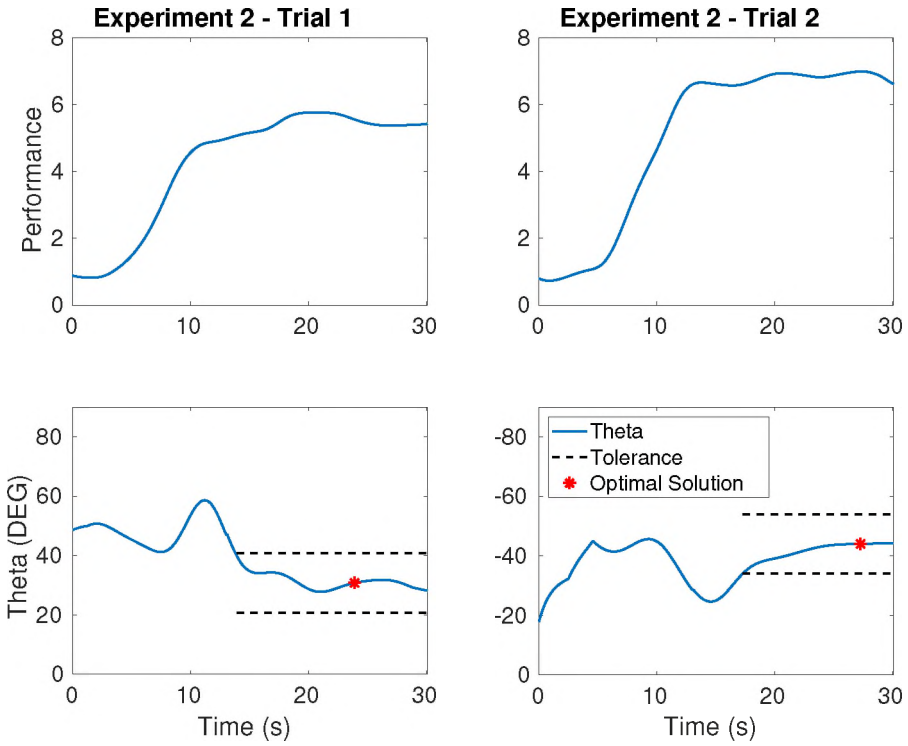

Figure 100: Second set of experiments with the muscle weight vector $W = [3, 5, 1, 1]$

Table XVII: Table of the experimental results for the second set ($W = [3, 5, 1, 1]$).

Arm side	Trial	Convergence status	Solution (°)	Convergence time (s)
Dominant	1	Yes	30.77	23.9
Dominant	2	Yes	-44.09	27.3

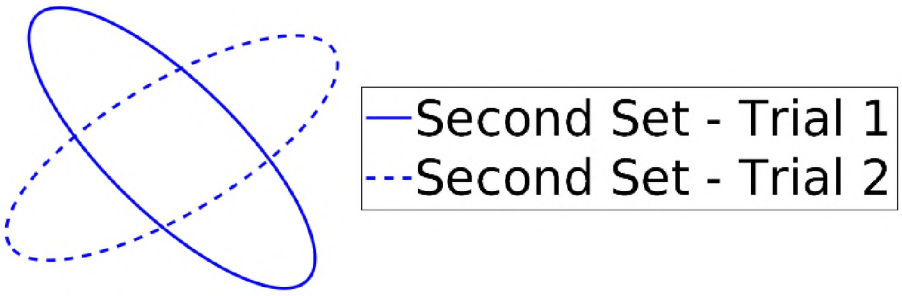

Figure 101: Convergence solutions from the second set of experiments ($W = [3, 5, 1, 1]$).

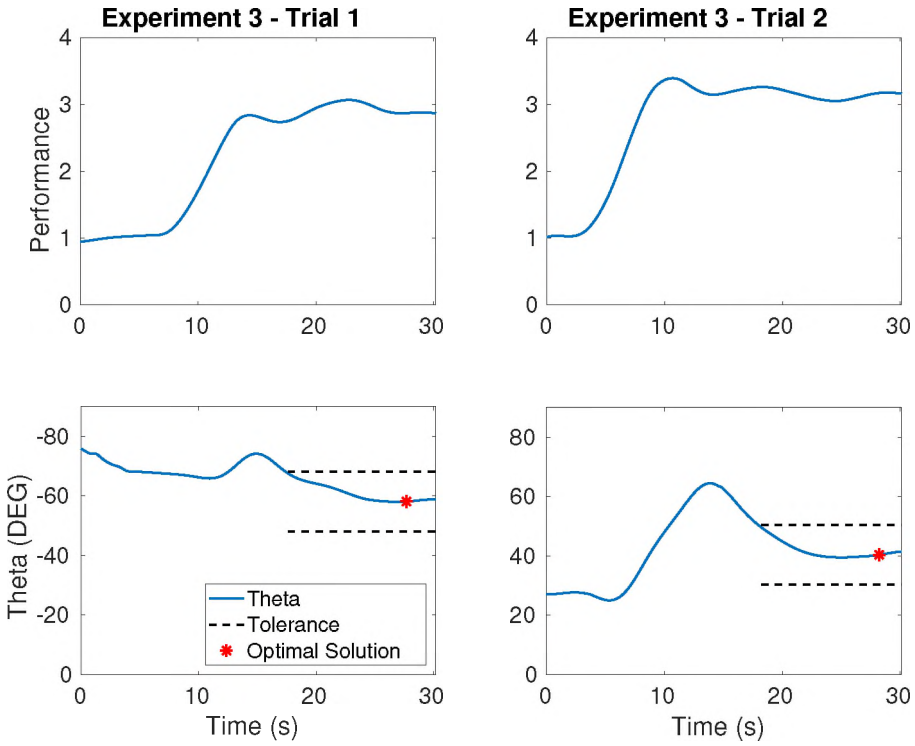

Figure 102: Third set of experiments with the muscle weight vector $W = [1, 1, 5, 5]$

Table XVIII: Table of the experimental results for the third set ($W = [1, 1, 5, 5]$).

Arm side	Trial	Convergence status	Solution (°)	Convergence time (s)
Dominant	1	Yes	-58.14	27.7
Dominant	2	Yes	40.40	28.2

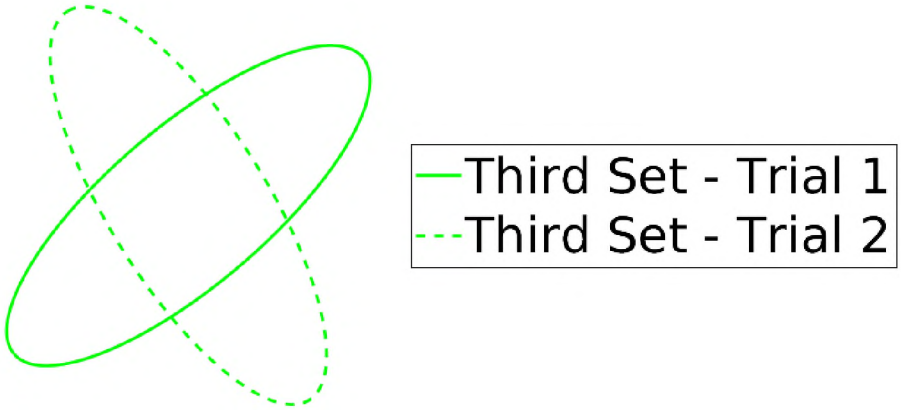

Figure 103: Convergence solutions from the third set of experiments ($W = [1, 1, 5, 5]$).

Upon completion of the 6 experimental trials, multiple outcomes and limitations were identified which were useful to elaborate some discussions and improve the framework during the following phases. For instance, differences in the muscle performance between trials from the same experimental set were revealed. A higher performance value was exhibited in the second trials during all the experimental sets. This result seems to be associated with the reduced effort capacity of the muscles to perform activity when they start to get fatigued. However, despite the difference in the muscle performance between trials, they converged to similar solutions depending on the initial conditions and the muscle weight vector. These results suggest that the formulated model-free optimization method successfully enabled the user to exercise optimally.

It is important to consider that muscle dynamics are permanently changing. Therefore, ESC remains varying slightly even after reaching the optimal solution. However, based on the established convergence criterion, the solutions were computed and found in the neighborhood from 30° to 40° and its symmetric respect to the axes from --60° to --45° (see Figure 104).

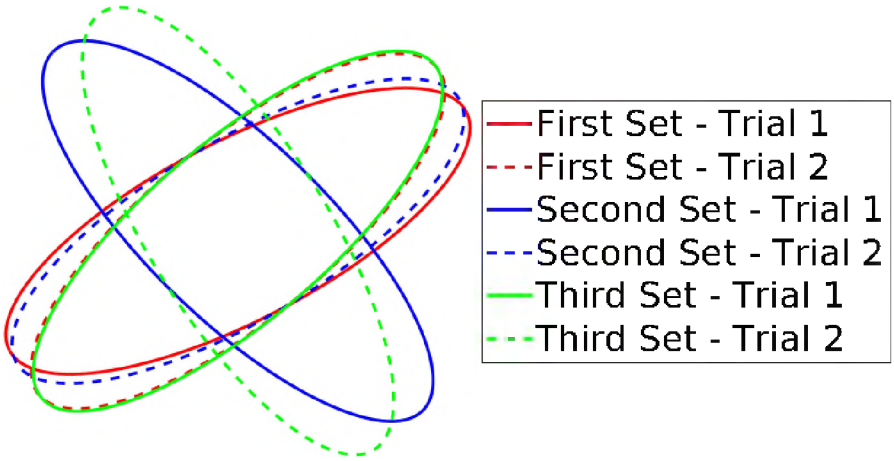

Figure 104: Convergence solutions from the 3 sets of experiments.

It is important to consider that the success of the method depends on the accuracy of the user to track the desired trajectory. Accordingly, it is recommended that the user get expertise with robot handling before the experiments. But although the user had practiced before, the mean of the RMS tracking error in all the experiments was 2.87 cm. However, the controller was robust enough to always converge to one of the local optima despite the lack of tracking. Nonetheless, it was assumed that future phases including resistances with multiple variables could significantly increase the tracking error, therefore the addition of a tracking error penalty was decided for the next phases.

It is important to note that at this point, only basic configurations (minimal viable development) were implemented. For instance, elbow immobilizers were not used, thus, the involuntary elbow rotations producing alterations in the muscle dynamics was one of the issues during this first phase of experiments. Another challenge faced was the EMG sensitivity associated with the electronic noise produced by the other systems (servos, motors, sensors). Furthermore, the high computational cost was limiting the accuracy of the parameter estimates. Finally, the only maximization muscle activations limited the versatility of the approach. During the next

phases, new features, configurations, and improvements were incorporated such as the minimization of a specific muscle or group of muscles.

6.4 Phase II - Single-Variable Optimization by Trajectory Regulation.

6.4.1 Methodology

During the second phase, the objective was to maximize the activation of a muscle while minimizing the others by regulating the orientation of the training trajectory. For this objective, the framework was set for trajectory parameter regulation to optimize the orientation of the ellipsoidal training trajectory. The model-free approach was implemented for minimization and the performance function was defined as the moving average of the sum between the multiplication of a muscle weight vector and the muscle activation and the multiplication of a tracking penalty gain and the tracking error as follows:

$$\min_{\theta} \quad J(t) = \frac{t_s}{t_{rev}} \sum_{(i=t-t_{rev}/t_s)}^{t} \left(\Big(W_m M(t)\Big) + \Big(W_t \big(P(t) - P_{des}(t)\big)^2\Big) \right), \tag{6.2}$$

where θ is the ellipse orientation, t_s is the sample time set at 5×10^{-4} seconds, t_{rev} is the period of revolution of the black dot (dot along the ellipsoidal path), t is the current time, W_m is the muscle weight vector of "1"s (positive for the muscles to be maximized and negative for the ones to be minimized), M the vector of muscle activations, W_t is the tracking penalty gain, and P and P_{des} are the current and desired position respectively (X_a or green dot and X_d or blue dot respectively).

One subject of the age of 29 (see Table XIX) performed a total of 4 experimental trials (2 per each body side). Each 2-trial set per each body side was

conducted by using the same settings and configuration parameters. The experimental order for each side of the body was randomly chosen, resulting in the experiments with the left side being performed first. The muscle weight vector (W_m in Tables. XX and XXI) was chosen to maximize the activations of the anterior deltoid (the first muscle) while minimizing the other muscles (lateral deltoid, posterior deltoid, and pectoralis major).

Table XIX: Organismic variables about the subject.

Variable	Description
Height	177 cm
Weight	77 kg
Gender	Male (M)
Age	29
Side dominant	Right (R)
Upper arm length	34.0 centimeters
Forearm length	28.0 centimeters

The settings and configuration parameters used during this phase of the experiments for the dominant and nondominant sides can be seen in the Tables. XX and XXI respectively.

Table XX: Framework settings and configuration parameters for the second phase of experiments with the dominant (right) side of the body.

Parameter	Description	Value	Units
a	Perturbation amplitude	0.1	-
ω	Perturbation frequency	1	rad/s
ω_l	Low-pass filter cutoff frequency	0.1	rad/s
ω_h	High-pass filter cutoff frequency	0.5	rad/s
k	Gain	1000	-
θ_{th}	Convergence tolerance for trajectory	8°	deg
t_{con}	Convergence time threshold	10	s
W_m	Muscle weight vector	$[-1, 1, 1, 1]$	-
W_t	Tracking penalty	1	-

Table XXI: Framework settings and configuration parameters for the second phase of experiments with the nondominant (left) side of the body.

Parameter	Description	Value	Units
a	Perturbation amplitude	0.1	-
ω	Perturbation frequency	1	rad/s
ω_l	Low-pass filter cutoff frequency	0.1	rad/s
ω_h	High-pass filter cutoff frequency	0.5	rad/s
k	Gain	600	-
θ_{th}	Convergence tolerance for trajectory	8°	deg
t_{con}	Convergence time threshold	10	s
W_m	Muscle weight vector	$[-1, 1, 1, 1]$	-
W_t	Tracking penalty	1	-

6.4.2 Results and Discussion

The results from the second phase of the experimental sets are presented in the plots and tables below:

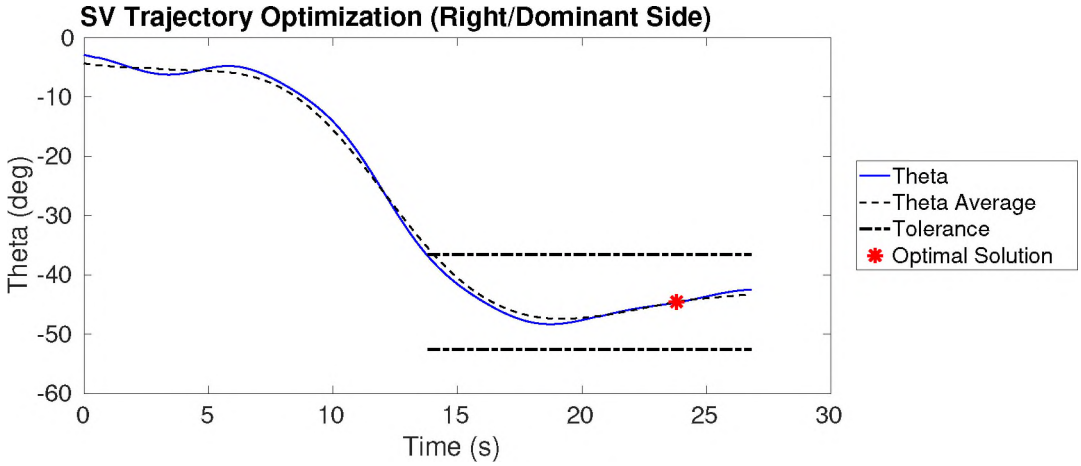

Figure 105: Results dominant side 1.

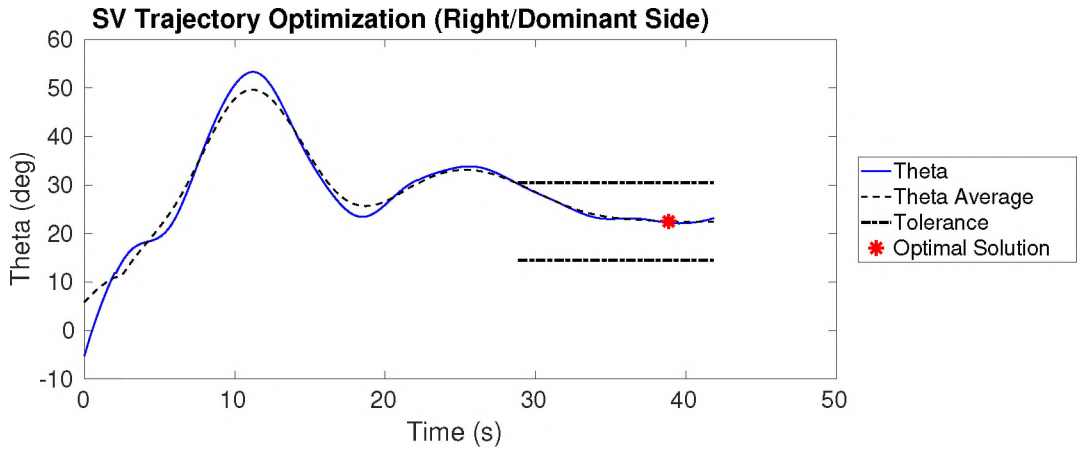

Figure 106: Results dominant side 2.

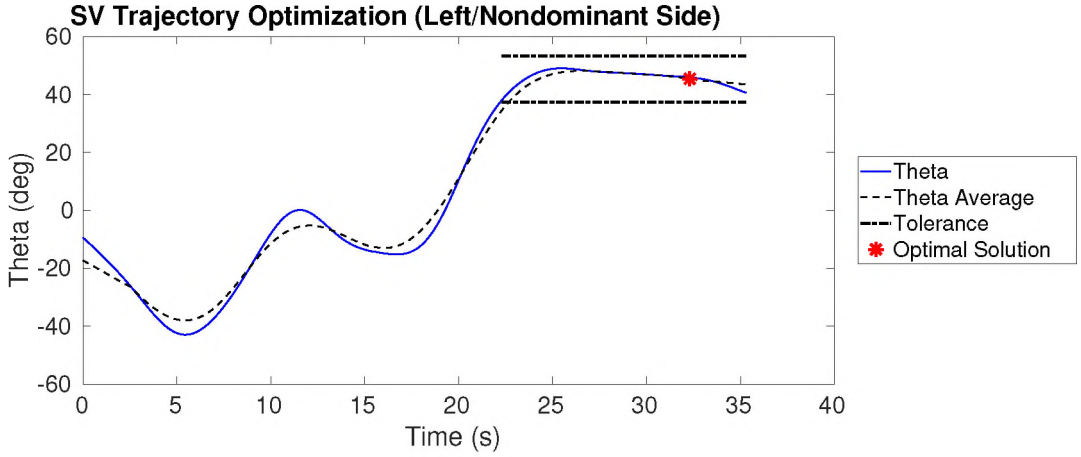

Figure 107: Results nondominant side 1.

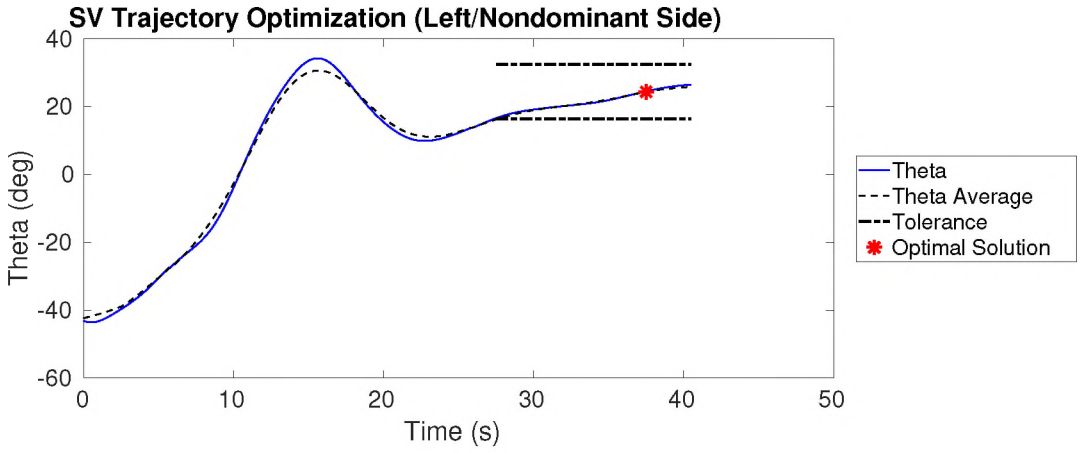

Figure 108: Results nondominant side 2.

Upon completion of the 4 experimental trials and based on the experimental results presented in Table XXII, some observations and discussions have been made. For instance, differences in the optimal trajectory orientation were observed between trials from the same body side. All the optimal solutions were in a neighborhood between 25° and 45° and its symmetric respect to the axes (see Figure 109). Coincidentally for both sides of the body, the first and second trials converged to similar solutions. Regarding the first trials, the optimal trajectories obtained are almost symmetric with respect to the axes. This result was previously observed during the first phase of the experiment supporting the possible existence of more than a local optimum. Regarding the second trials, the parameters converged to a more horizontal orientation (where the main or larger ellipsoidal axis was more aligned to the horizontal axis). Based on the fact that the second trial was performed after a few minutes of training, the orientation observed from the second trial could be associated with the optimal orientation for the user when the subject starts to get fatigued. In this particular case, where the posterior deltoid, lateral deltoid, and chest have to be minimized, a more horizontal orientation might contribute to the minimization of their muscle activations and likewise, in the optimization objective.

Table XXII: Summary of the experimental results from the second phase (single-variable trajectory optimization).

Side	Trial	Convergence status	Solution (°)	Convergence time (s)
Dominant	1	Yes	-44.54	23.80
Dominant	2	Yes	22.49	38.85
Nondominant	1	Yes	45.39	32.32
Nondominant	2	Yes	24.39	37.56

It was also observed that the second trials converged in longer periods on both sides of the body. This result seems to be associated with the increase of muscle activations as a result of fatigue producing a higher system sensitivity (similarly to an increasing in the framework gain). This effect is observed similarly, but in a lower

proportion, by comparing the convergence time results between the dominant and nondominant sides. During the first trials, the dominant side converged much faster than the nondominant side, and during the second trials, they converged at very similar times.

During this phase, the implementation of the impedance (training resistance) significantly increased the level of difficulty in the training protocol. Thus, was also expected a considerable increase in the tracking error which didn't result as expected suggesting that the implementation of the tracking error penalty was efficient in keeping the desired trajectory inside of feasible areas.

Regarding the issues noted during the first phase of the experiments, all of them were solved. The involuntary elbow rotations producing alterations in the muscle dynamics were successfully solved by using the elbow immobilizers. The EMG sensitivity associated with the electronic noise produced by the other systems (servos, motors, sensors) became neglected after using analog and digital filters. Finally, the high computational cost was significantly improved by using more efficient estimators and parameter configurations.

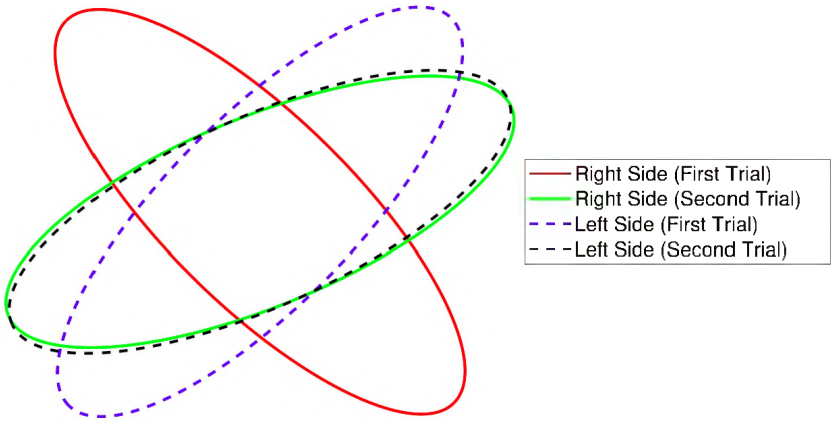

Figure 109: All results from the dominant and nondominant sides for the single variable trajectory optimization.

6.5 Phase III - Single-variable optimization by impedance regulation.

6.5.1 Methodology

During the third phase, the objective was to maximize the activation of a muscle while minimizing the others by only regulating the impedance. For this objective, the framework was set for impedance parameter regulation to optimize the impedance parameter associated with the stiffness property. During this phase, the orientation of the ellipsoidal training trajectory (orientation of its axis), damping, and inertia parameters remained constant. The model-free approach was implemented for minimization and the performance function was defined as the moving average of the sum between the multiplication of a muscle weight vector and the muscle activation and the multiplication of a tracking penalty gain and the tracking error as follows:

$$\min_{K} \quad J(t) = \frac{t_s}{t_{rev}} \sum_{(i=t-t_{rev}/t_s)}^{t} \left(\Big(W_m M(t)\Big) + \Big(W_t \big(P(t) - P_{des}(t)\big)^2\Big) \right), \tag{6.3}$$

where K is the stiffness variable, t_s is the sample time set at 5×10^{-4} seconds, t_{rev} is the period of revolution of the black dot (dot along the ellipsoidal path), t is the current time, W_m is the muscle weight vector of "1"s (positive for the muscles to be maximized and negative for the ones to be minimized), M the vector of muscle activations, W_t is the tracking penalty gain, and P and P_{des} are the current and desired position respectively (X_a or green dot and X_d or blue dot respectively).

The same subject from the second phase (see Table XIX) performed another experimental set of 4 trials (2 per each body side) on a different day. Similarly, each 2-trial set per body side was conducted by using the same settings and configuration parameters. The experimental order for each side of the body was also randomly

chosen, resulting in the experiments with the left side being performed first. The muscle weight vector (W_m in Tables. XXIII and XXIV) was chosen in the same way as during the second phase to maximize the activations of the anterior deltoid (the first muscle) while minimizing the other muscles (lateral deltoid, posterior deltoid, and pectoralis major). The settings and configuration parameters used during this phase of the experiments for the dominant and nondominant sides can be seen in the Tables. XXIII and XXIV respectively.

Table XXIII: Framework settings and configuration parameters for the third phase of experiments with the dominant (right) side of the body.

Parameter	Description	Value	Units
a	Perturbation amplitude	0.1	-
ω	Perturbation frequency	0.7	rad/s
ω_l	Low-pass filter cutoff frequency	0.1	rad/s
ω_h	High-pass filter cutoff frequency	0.5	rad/s
k	Gain	1000	-
δ_{th}	Convergence tolerance for impedance	0.025	Nm/rad
t_{con}	Convergence time threshold	10	s
W_m	Muscle weight vector	$[-1, 1, 1, 1]$	-
W_t	Tracking penalty	1	-

Table XXIV: Framework settings and configuration parameters for the third phase of experiments with the nondominant (left) side of the body.

Parameter	Description	Value	Units
a	Perturbation amplitude	0.1	-
ω	Perturbation frequency	0.7	rad/s
ω_l	Low-pass filter cutoff frequency	0.1	rad/s
ω_h	High-pass filter cutoff frequency	0.5	rad/s
k	Gain	600	-
δ_{th}	Convergence tolerance for impedance	0.025	Nm/rad
t_{con}	Convergence time threshold	10	s
W_m	Muscle weight vector	$[-1, 1, 1, 1]$	-
W_t	Tracking penalty	1	-

6.5.2 Results and Discussion

The results from the third phase of the experimental sets are presented in the plots and tables below:

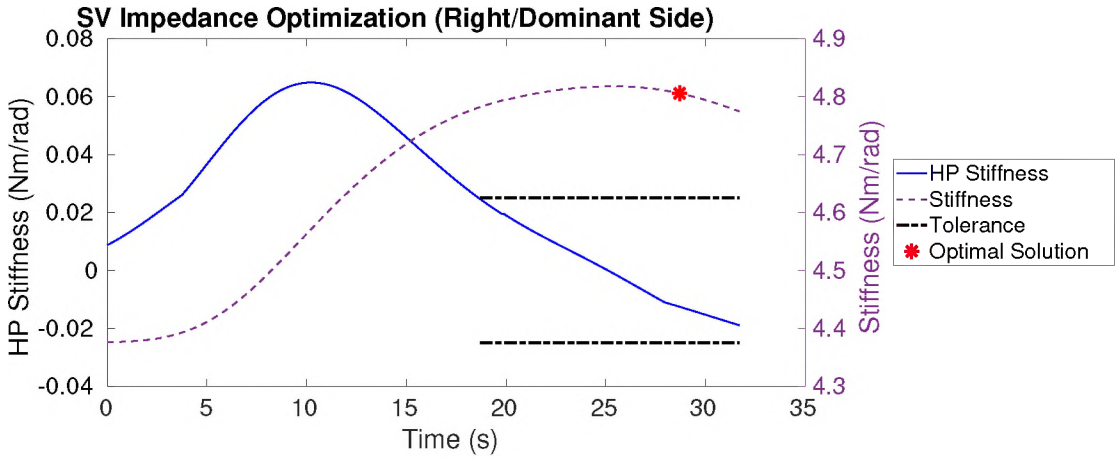

Figure 110: Results dominant side 1.

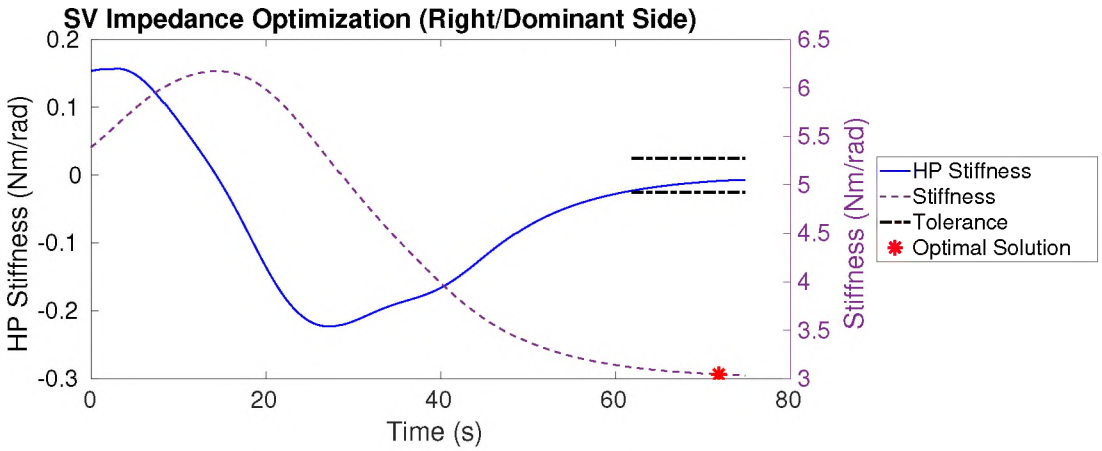

Figure 111: Results dominant side 2.

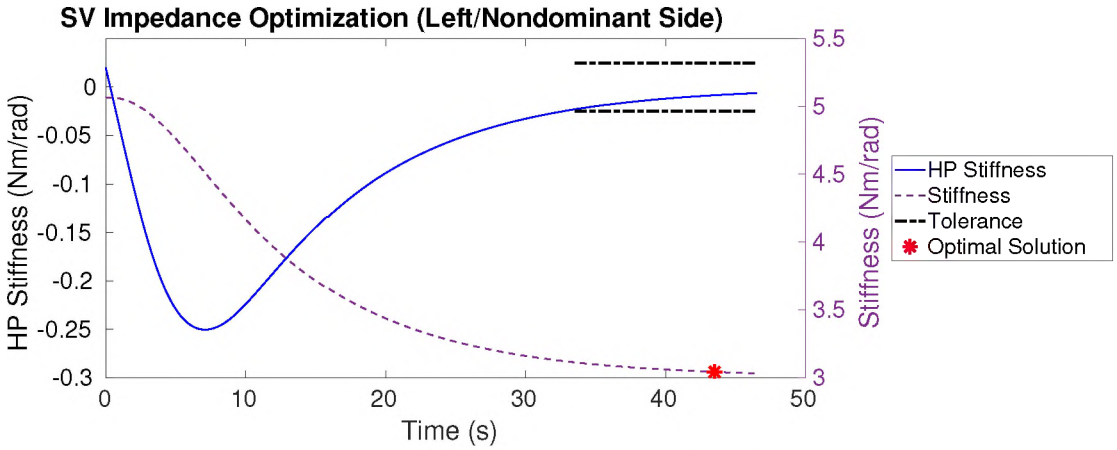

Figure 112: Results nondominant side 1.

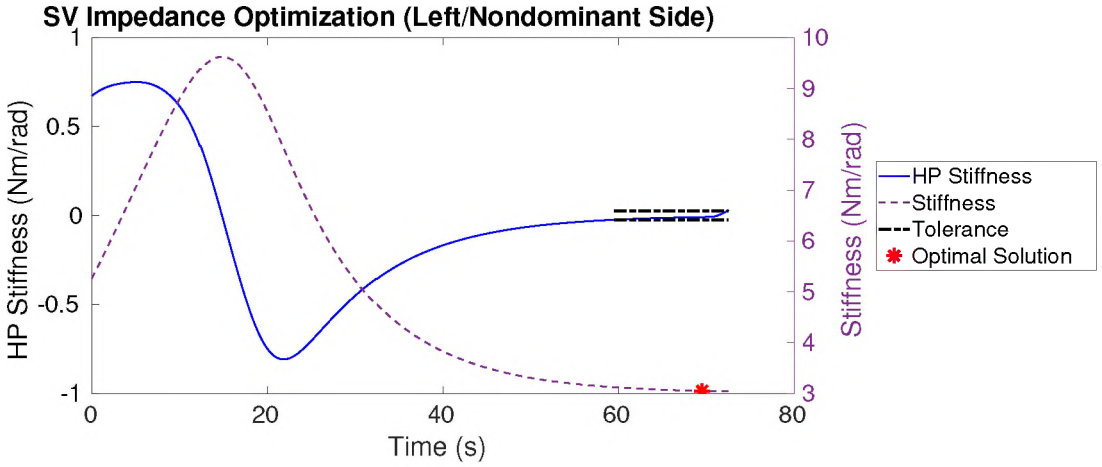

Figure 113: Results nondominant side 2.

Upon completion of the 4 experimental trials and based on the experimental results presented in Table XXV, some observations and discussions have been made. Except for the first trial, very similar optimal impedance parameters were observed between the other 3 trials (see all optimal solutions in Figure 114). These 3 results converged to values in the neighborhood of 3 Nm/rad, while the first trial from the dominant side converged to a value around 4.8 Nm/rad. Conclusions are difficult to make at this point with this sample size because the difference in the first trial could be associated with an error from the framework, as well as, the fact that the

dominant side is stronger especially during the first trial when the muscle is not fatigued. However, the similarity in the optimal solutions between 3 of the 4 trials suggests that the formulated model-free optimization method successfully enabled the user to optimize the impedance parameter in most cases.

Table XXV: Summary of the experimental results from the second phase (single-variable trajectory optimization).

Side	Trial	Convergence status	Solution (Nm/rad)	Convergence time (s)
Dominant	1	Yes	4.81	28.72
Dominant	2	Yes	3.04	71.83
Nondominant	1	Yes	3.09	43.56
Nondominant	2	Yes	3.05	69.57

Similar to the previous phases, longer convergence times were observed in the second trials on both sides of the body. This result supports the observation previously made about the possible relationship between long convergence periods and fatigue associated with the increase of muscle activations producing higher sensitivity.

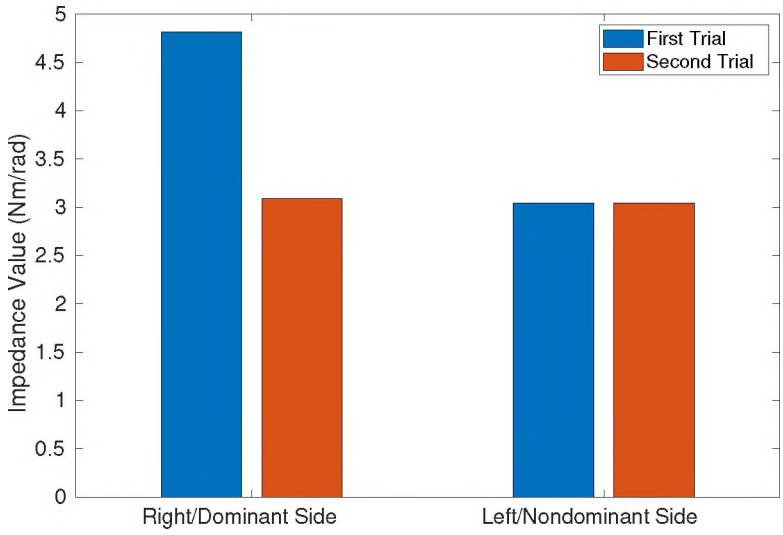

Figure 114: All results from the dominant and nondominant sides for the single variable impedance optimization.

6.6 Phase IV - Multi-variable optimization by simultaneous trajectory and impedance regulation.

During the fourth phase, the objective was to maximize the activation of a muscle while minimizing the others by simultaneous trajectory and impedance optimization. For this objective, the framework was set for multi-variable trajectory and impedance parameter regulation. Thus, the orientation of the ellipsoidal trajectory and the impedance parameter associated with the stiffness property were simultaneously optimized. The model-free approach was implemented for minimization and the performance function was defined as the moving average of the sum between the multiplication of a muscle weight vector and the muscle activation and the multiplication of a tracking penalty gain and the tracking error as follows:

$$\min_{\theta,K} \quad J(t) = \frac{t_s}{t_{rev}} \sum_{(i=t-t_{rev}/t_s)}^{t} \left(\left(W_m M(t) \right) + \left(W_t \left(P(t) - P_{des}(t) \right)^2 \right) \right), \tag{6.4}$$

where θ is the orientation of the ellipsoidal training trajectory, K is the stiffness variable, t_s is the sample time set at 5×10^{-4} seconds, t_{rev} is the period of revolution of the black dot (dot along the ellipsoidal path), t is the current time, W_m is the muscle weight vector of "1"s (positive for the muscles to be maximized and negative for the ones to be minimized), M the vector of muscle activations, W_t is the tracking penalty gain, and P and P_{des} are the current and desired position respectively (X_a or green dot and X_d or blue dot respectively).

The same subject from the second and third phase (see Table XIX) performed another experimental set of 4 trials (2 per each body side) on a different day. Similarly, each 2-trial set per body side was conducted by using the same settings and

configuration parameters. The experimental order for each side of the body was also randomly chosen, resulting in the experiments with the right side being performed first. The muscle weight vector (W_m in Tables. XXIII and XXIV) was chosen in the same way as during the second and third phase to maximize the activations of the anterior deltoid (the first muscle) while minimizing the other muscles (lateral deltoid, posterior deltoid, and pectoralis major). The settings and configuration parameters used during this phase of the experiments for the dominant and nondominant sides can be seen in the Tables. XXVI and XXVII respectively.

It is important to note the most of the configuration parameter values used for the previous 2 frameworks were reused during this phase except for the framework gain. The multi-variable framework, as previously stated in Section 4.2.1, results more demanding than the single-variable cases becoming harder to meet. For that reason, the selected framework gains were lower than the single-variable approach (40% and 50% of the value for the dominant and nondominant side respectively).

Table XXVI: Framework settings and configuration parameters for the fourth phase of experiments with the dominant (right) side of the body.

Parameter	Description	Value	Units
a	Perturbation amplitude	0.1	-
ω_1	Perturbation frequency	1	rad/s
ω_2	Perturbation frequency	0.7	rad/s
ω_l	Low-pass filter cutoff frequency	0.1	rad/s
ω_h	High-pass filter cutoff frequency	0.5	rad/s
k	Gain	400	-
θ_{th}	Convergence tolerance for trajectory	8°	deg
δ_{th}	Convergence tolerance for impedance	0.025	Nm/rad
t_{con}	Convergence time threshold	10	s
W_m	Muscle weight vector	$[-1, 1, 1, 1]$	-
W_t	Tracking penalty	1	-

Table XXVII: Framework settings and configuration parameters for the fourth phase of experiments with the nondominant (left) side of the body.

Parameter	Description	Value	Units
a	Perturbation amplitude	0.1	-
ω_1	Perturbation frequency	1	rad/s
ω_2	Perturbation frequency	0.7	rad/s
ω_l	Low-pass filter cutoff frequency	0.1	rad/s
ω_h	High-pass filter cutoff frequency	0.5	rad/s
k	Gain	300	-
θ_{th}	Convergence tolerance for trajectory	8°	deg
δ_{th}	Convergence tolerance for impedance	0.025	Nm/rad
t_{con}	Convergence time threshold	10	s
W_m	Muscle weight vector	$[-1, 1, 1, 1]$	-
W_t	Tracking penalty	1	-

6.6.1 Results and Discussion

The results from the fourth phase of the experimental sets are presented in the plots and tables below:

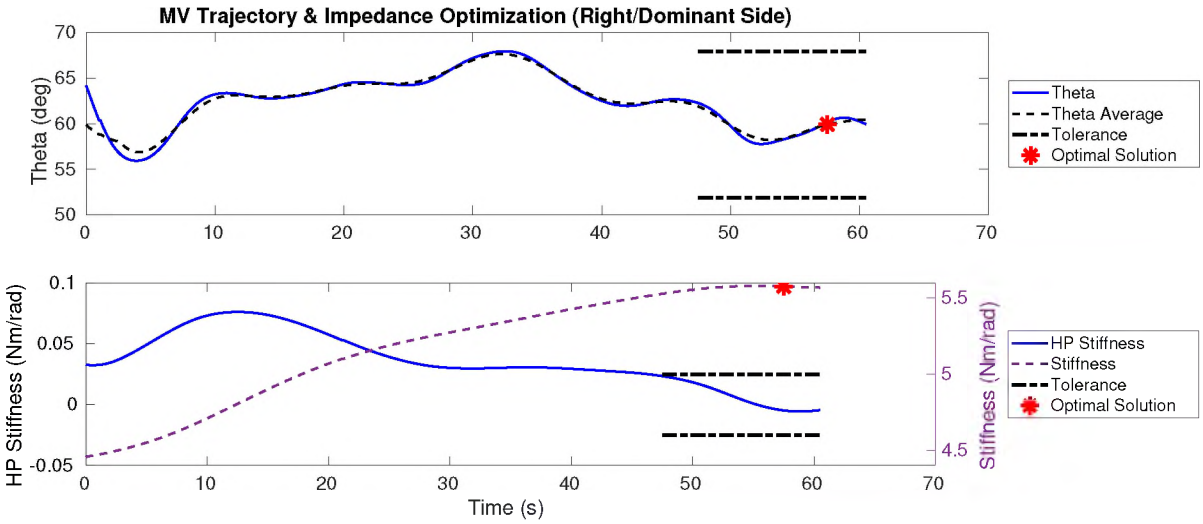

Figure 115: Results dominant side 1.

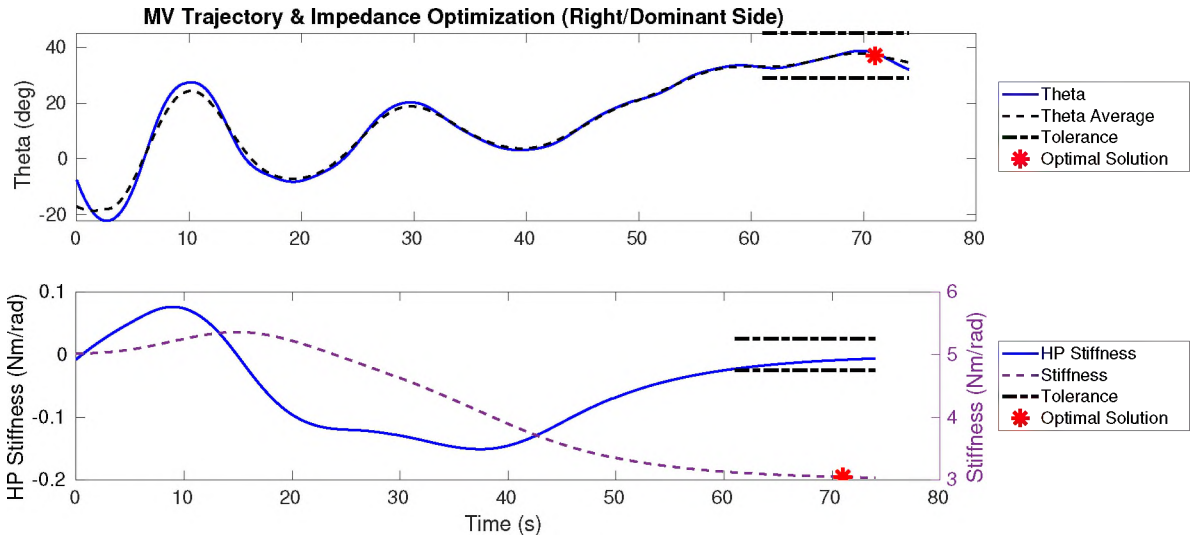

Figure 116: Results dominant side 2.

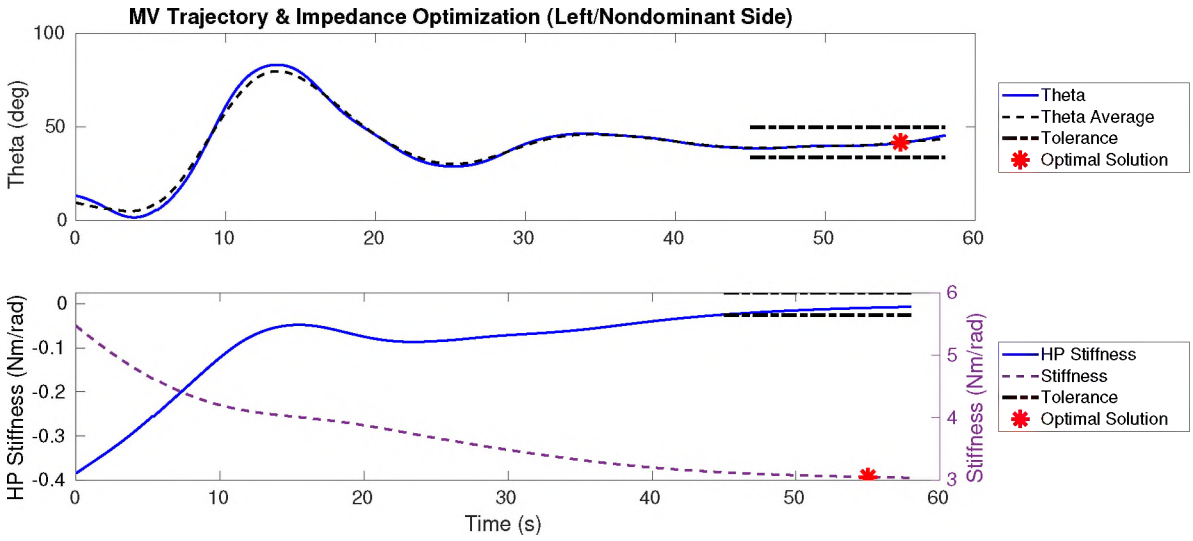

Figure 117: Results nondominant side 1.

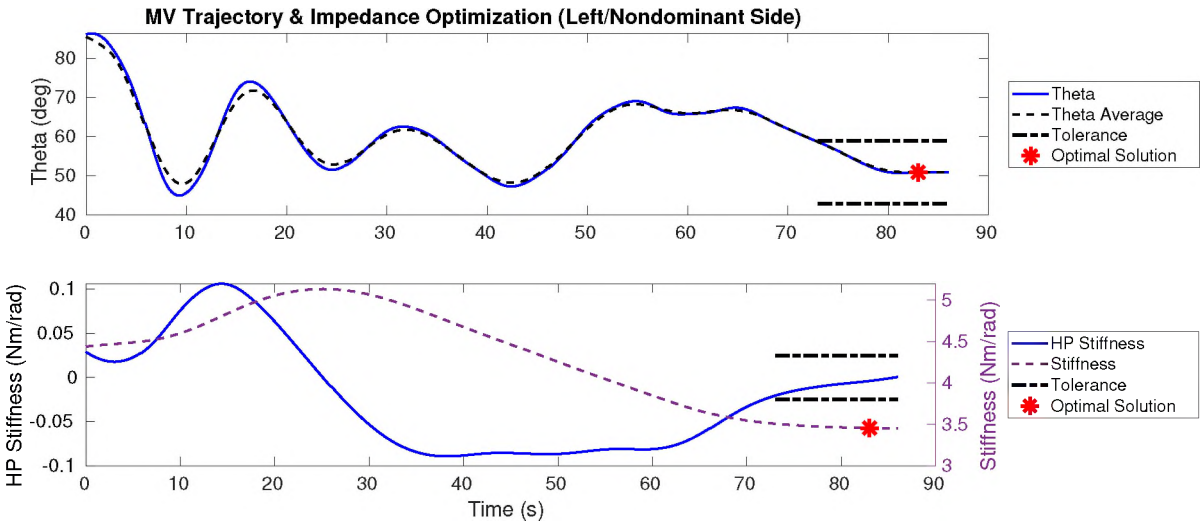

Figure 118: Results nondominant side 2.

Upon completion of the 4 experimental trials and based on the experimental results presented in Table XXVIII, some observations and discussions have been made.

Regarding the optimal trajectory parameter, the optimal values converged to similar solutions ($47.39° \pm 10.13°$ for the mean $\pm$ the standard deviation). Unlike the second phase (single-variable trajectory optimization), all the optimal solutions were in a neighborhood between 37° and 59° without converging out of the first quadrant (see Figure 109). Regarding the optimal impedance results, 3 of 4 parameters converged to values in a neighborhood between 3 Nm/rad and 3.5Nm/rad, while the first trial from the dominant side converged to a value around 5.8Nm/rad (see all optimal solutions in Figure 119). These results are very similar to the third phase, where the first trial produced a higher impedance parameter value with respect to the other 3 trials, while the other 3 trials converged to very similar optimal parameters. These results suggest that the dominant side (normally the stronger side) is able to reach higher impedances (resistance) at least before the user getting fatigued. Finally, regarding convergence times, similarly to the previous phases, longer periods were observed in the second trials on both sides of the body.

Table XXVIII: Summary of the experimental results from the fourth phase (single-variable trajectory optimization).

Side	Trial	Convergence status	Solutions (°) – (Nm/rad)	Convergence time (s)
Dominant	1	Yes	59.91 – 5.58	57.52
Dominant	2	Yes	37.04 – 3.05	71.03
Nondominant	1	Yes	41.72 – 3.05	55.03
Nondominant	2	Yes	50.87 – 3.45	83.09

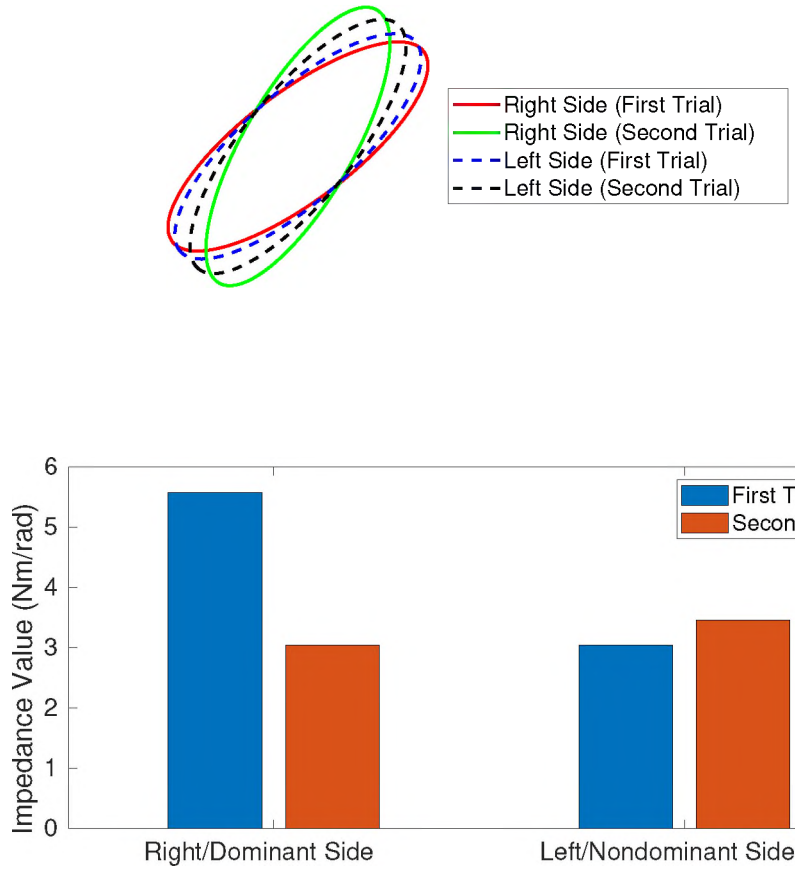

Figure 119: All results from the dominant and nondominant sides for the multi variable optimization.

6.7 Discussions

Based on the result observed from each of the experiments, the possible existence of more than a local optimum, especially for the trajectory orientation, is likely. Regarding the trajectory parameter, all the solutions were computed and found in the neighborhood between 30° and 60° and the symmetric results with respect to the axes between −60° and −30°. These results suggest that an inclined ellipsoidal trajectory seems to provide a desired performance for the selected weight muscle vector. Regarding the impedance parameters, most results were in the neighborhood of 3 Nm/rad suggesting that not big changes are expected between trials and body sides.

It is important to note that the success of the model-free approach strictly depends on the configuration and calibration parameters which are highly related to the physiology of the subject. Therefore, despite following a model-free methodology, the framework requires some pre-tests to find a good combination of setting parameters for each subject. For instance, higher gains or frequencies might produce faster convergence, but at the cost of a higher sensitivity which is not recommended on this approach because of undesired performances. On the other hand, low gains or frequencies might never achieve a convergence or not being able to deal with the time-varying dynamics due to the fatigue and the thermogenic effect of the muscles. Nonetheless, the parameters chosen for each of the 4 phases were accurate enough to produce robustness and a convenient convergence speed to deal with these variations. That means, the success rate of the convergence criteria was 100% (all the experimental trials converged). However, as it was previously stated, convergence is not always guaranteed. Some of the possible reasons for that high success rate might be:

- Subjects have performed several sets of experiments. Thus, the configuration

and tuning parameters that work for them are very well known.

- Subjects have a lot of practice with the exercise protocol leading to good tracking, and consequently to a good framework performance.

Coincidentally in all the phases, longer convergence times were observed in the second trials (after a few minutes of working out) (see Figure 120). Similarly, lightly longer convergence times were observed on the nondominant side than on the dominant side. This result strongly suggests that there is a possible relationship between convergence time and fatigue. It is known that muscles consist of many motor units that are not fully active at the beginning of the workout, but they start to activate together as fatigue increases [90, 39]. Besides, nondominant side (normally the less trained side) tends to fatigue faster and easier. The increase in the activation of motor units produces an increase in the muscle activations similarly to an increasing in the framework gain producing a higher sensitivity, and thus undesired performances. These sudden changes might not only delay the convergence but also they might even block it. Therefore, it can be concluded that independently of the accuracy in the initial setting parameter selection, recalibration might become needed after a few minutes of training. The increase in the sensitivity previously observed might be solved by decreasing the framework gain, thus future studies could include automatic parameter calibrations to overcome this current limitation.

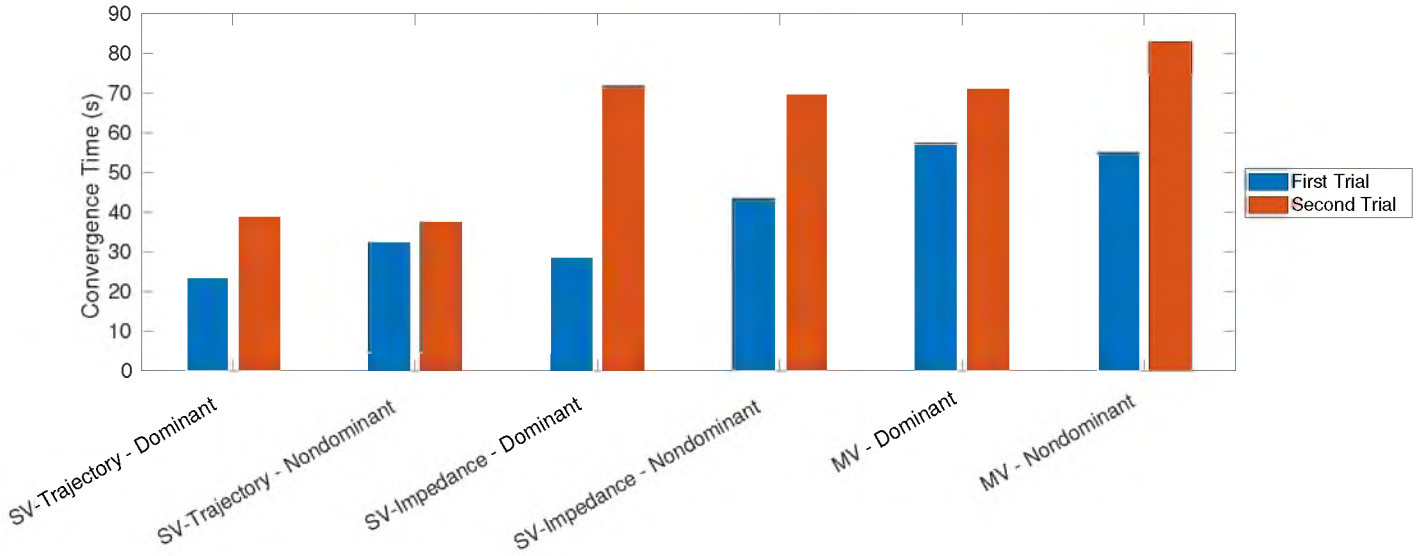

Figure 120: Comparison of convergence time between the trials from the second (SV-Trajectory), third (SV-Impedance), and fourth (MV) phase trials.

It is important to highlight that the success of the framework (accuracy of the optimal variables), especially for trajectory optimization, lies in the accuracy of the user to track accurately the desired trajectory. Accordingly, it is recommended the user gets expertise with robot handling before the experiments. During the trials, it was observed from the subject that conscious focus was put on activating the muscles being measured whilst maintaining proper alignment with the visual display. As the ellipsoid pattern was altered and moved, the level of difficulty was increased. The ellipse trajectory produces linear motion of the glenohumeral joint which in turn resulted in high muscular fatigue. As the ellipse rotates, the various muscles associated with the total glenohumeral movement were tasked. The orientation of the ellipse brought about an increased time of resistance which ultimately resulted in more muscular stimulation. With the ellipse pattern, the primary drivers in the shoulder were successfully activated as opposed to the stabilizers which were focused on in the smaller movement pattern. As a suggestion for future research, the combined modular resistance supplied by this technology might focus on the benefits of linear

movements to lead to typical exercise movements such as presses or lifts.

It is important to note that there are still multiple issues limiting the maximum capacity of the framework. Some of them have been overcome as the phases progressed, but others, including uncaptured ones, will be part of future works. For instance, results might be greatly affected by the psychological effects of training with an unconventional machine as a robot is.

In general, these results support the feasibility of the formulated model-free optimization method to successfully enable the user to exercise optimally, but more studies with bigger sample size are required for deeper analytical studies.

CHAPTER VII

CONCLUSION AND RECOMMENDATIONS FOR FUTURE WORK

7.1 Statement of Contributions

In this dissertation, we set out to explore the possibilities and limitations of smart frameworks able to optimize training parameters by using muscle activations as biofeedback. We aimed to investigate the capabilities of the AEMs and the physiological effects on people performing cardio-based and resistance-based training by using these machines. Then, we aimed to develop the framework for the smart regulation of the robotic training parameter. To achieve these goals, four objectives were set at the beginning of this dissertation.

Objective 1: Investigate the physiological effects as a result of different exercise protocols with different exercise machines.

The investigation of the physiological effects associated with exercise started in Chapter II exploring the characteristics of the exercise protocols and the machines used to perform these exercises. This pre-investigation played a key role because of the strict correlation between machine parameters (trajectory and resistance parameters) and physiological effects. Then, we formulated and planned the strategy to acquire the required information related to these physiological effects as a result of exercise.

In Chapter III, we explored these physiological effects by measuring and studying them through experimental trials with subjects of different ages, genders, and fitness levels. The physiological effects selected for this study were muscle activations, heart rate, and oxygen consumption associated with the musculoskeletal, cardiovascular, and cardiorespiratory systems respectively. Every training pattern produces a unique combination of training effects. For instance, resistance-based training such as weight lifting does not produce the same effects as cardio-based training such as aerobic fitness. Therefore, we measured the physiological effects as a result of both cardio-based training (by using a powered rowing machine) and resistance-based training (by using robotic systems).

Publications:

- [24] De las Casas, H., Richter, H., and van den Bogert, A. Design and hybrid impedance control of a powered rowing machine. In ASME 2017 Dynamic Systems and Control Conference, October 2017.

- [30] De las Casas, H. Design and control of a powered rowing machine with programmable impedance. Master's thesis, Cleveland State University, 2017.

- [28] De las Casas, H., Kleis, K., Richter, H., Sparks, K., and van den Bogert, A. Eccentric training with a powered rowing machine. Medicine in Novel Technology and Devices, 2:100008, 2019.

- [25] Humberto De las Casas, Santino Bianco, and Hanz Richter. Targeted muscle effort distribution with exercise robots: Trajectory and resistance effects. Medical Engineering & Physics, 2021.

Objective 2: Develop a model-free framework for single-variable optimization of a trajectory parameter using muscle activations as biofeedback.

In Chapter IV, we formulated the single-variable optimization framework by using perturbation-based Extremum Seeking Control (ESC) for the regulation of the ellipsoidal trajectory orientation to be tracked by the subject exercising. The objective was designed to follow a model-free approach using a physiological effect as biofeedback. Thus, based on the outcomes from the previous investigations, we decided to use muscle activations because of the following reasons:

1. Safety: The use of superficial muscle activation sensors doesn't produce any danger to the subject unlike to the other methods such as electrocorticography which can be dangerous.

2. Availability: We have muscle activation sensors available in one of our research laboratories.

3. Cost: The equipment purchase cost can be high, but the cost of its usage only lies in the sensor adhesive available at low cost (about 50 cents per adhesive).

4. Expertise: The use of muscle activations sensors doesn't require high knowledge or expertise.

After the complete development of the framework, we evaluated its performance in simulation by using 5 human arm models from our virtual population and comparing its results with the ones obtained by using Biogeography-Based Optimization. Later, in Chapter V, we used this framework to study the concept of training personalization by presenting early evidence about the unique combination of optimal trajectory parameters for each person/model by performing a total of 300 comparisons by using our virtual population of 25 female and 25 male models. Finally, in Chapter VI, real-

time experiments with 2 different robots (WAM and 4OptimX robots) were conducted to test the feasibility of the trajectory parameter optimization framework in real-time applications.

Publications:

- [31] Humberto De las Casas, Holly Warner, and Hanz Richter. Real-time optimization of an ellipsoidal trajectory orientation using muscle effort with extremum seeking control. Medical Engineering & Physics, 91:19–27, 2021.
- [26] De las Casas, H., Chambers, N., Richter, H., and Sparks, K. Real-time trajectory optimization in robot-assisted exercise and rehabilitation. Journal of Biomechanics. (under review)

Objective 3: Develop a model-free framework for single-variable optimization of an impedance parameter using muscle activations as biofeedback.

In Chapter IV, we used the single-variable optimization framework previously developed for trajectory parameter optimization to adapt it for impedance parameter optimization. For this objective, we used a fixed ellipsoidal trajectory orientation with a variable impedance automatically regulated by using muscle activation as biofeedback. Since impedance parameters are more stability sensitive than trajectory parameters, we decided to only regulate the stiffness impedance (constant damping and inertia parameters) to not compromise the system stability. After the successful adaptation of the framework, in Chapter V, we used this framework to study the concept of training personalization by presenting additional evidence about the unique combination of optimal impedance parameters for each person/model by using our virtual population. Finally, in Chapter VI, real-time experiments with the 4OptimX robot were conducted to test the feasibility of the impedance parameter optimization

framework in real-time applications.

Objective 4: Develop a model-free framework for multi-variable optimization of trajectory and impedance parameters using muscle activations as biofeedback.

After the successful development of the single-variable optimization frameworks for trajectory and impedance parameters, the multi-variable approach was formulated. In Chapter IV, we extended the single-variable framework to include multi-variable capabilities for simultaneous optimization of trajectory and impedance parameters. For this objective, we decided to use variable ellipsoidal trajectory orientation and stiffness impedance, same as before, automatically and simultaneously regulated by also using muscle activation as biofeedback. For the framework methodology selection, we developed 2 multi-variable frameworks based on the use of perturbation-based and Newton-based ESC. In Appendices C, we evaluated in simulation the performance of each framework to select the best fit based on specific criteria. After the successful selection and adaptation of the framework, in Chapter V, we used the framework to study the concept of training personalization by presenting additional evidence about the unique combination of optimal training parameters (trajectory and impedance parameters) for each person/model by using our virtual population. Finally, in Chapter VI, real-time experiments with the 4OptimX robot were conducted to test the feasibility of the multi-variable framework for the optimization of the trajectory and impedance parameters in real-time applications.

Other contributions

The use of these smart frameworks for the optimization of the training parameters in human performance and rehabilitation promises development enhancements in fitness and rehabilitation including for instance:

- Muscle training focalization and/or isolation.
- Safer and more controllable workout/rehabilitation environments.
- Reduced injuries and accidents in training facilities.
- Inclusive environments for beginner trainers, older populations, and people with reduced motor skills.

7.2 Limitations of The Study and Future Perspectives

7.2.1 Equipment

The framework is computationally expensive making it difficult to be replicated on systems with low computational speed, power, and data storage requirement. Similarly, it requires the use of high-end sensors able to measure signals with high precision and deal with electrical noise in the environment.

- In terms of precision, the correct selection of sensors plays the most important role. Previously, the integration of multiple systems showed how noise and delays can affect measurements due to inefficient electrical insulators, algorithm failures, and other technical issues.
- In terms of versatility, the framework requires running multiple processes related to software and hardware at the same time and in real-time.
- In terms of speed, the framework requires the computing of complex algorithms while it synchronizes multiple sub-systems with a sampling rate of at least 2 kHz.
- In terms of data storage requirement, the framework requires mass storage of data including more than a hundred variables been recorded with a high

sampling rate during protocols that can last hours.

This framework could be shrunk to the use of less sophisticated robots and training parameters reducing the computational cost and the requirement of high-precision sensors and devices. Oppositely, the framework could be extended to endless variations including but not limited to:

- The use of a more sophisticated robot and/or multiple robots simultaneously.
- The use of biofeedback based on other physiological systems such as the cardiorespiratory, cardiovascular, or simultaneous multiple-systems.
- The regulation of other training parameters such as damping, inertia, trajectory's dimension, frequency, etc.

7.2.2 Configuration, tuning, and calibration parameters

It is important to highlight that despite following a model-free methodology, the framework requires the manual selection of some parameters which are strictly related to the framework's performance. Among them, there are configuration, tuning, and calibration parameters. Configuration parameters are associated with the exercise protocol objective such as the weight muscle vector including the selection of muscles to be maximized, minimized, and their priorities. Tuning parameters are associated with the architecture framework including the ESC gain and frequencies. Calibration parameters are associated with the parameters which are modulated at the beginning of each experimental trial during the warm-up and isometric tests.

The configuration parameters which are associated with the exercise protocol objective are freely selectable. Therefore, any muscle or group of muscles can be selected for muscle maximization or minimization with any priority. However, some muscles work synergistically better with some muscles than with others. Thus, a bad

selection of these configuration parameters might not produce the expected performance by focusing or defocusing the wrong muscle or group of muscles. For that reason, it is recommended to be professionally selected by a professional trainer or therapist for maximum efficiency.

Unlike the configuration parameters, the tuning and calibration parameters are not freely selectable but require procedures for their correct identification to avoid undesired performances. For instance, bad tuning or calibration parameters might increase or decrease the framework's sensitivity. A high-sensitive framework configuration might accelerate the convergence process, but introducing disturbances that are not recommended because of undesired performances. On the other hand, a low-sensitive framework configuration might never achieve a convergence or not being able to deal with the time-varying dynamics due to the fatigue and the thermogenic effect of the muscles. Therefore, tuning and calibration procedures have to be carefully conducted.

The tuning parameters are related to the physiology of the subject. For instance, the muscle activations on untrained people are more difficult to measure and their muscles get fatigued easier and faster. Therefore, higher gains and lower frequencies are required to deal with the low muscle activation signals without increasing the sensitivity too much. These parameters can be selected by performing pre-tests following the same exercise protocol of the experiments. During these tests, the gain is set at a very low level, and by trial and error, it is increased until small oscillations start to happen. Then, a pilot test is performed for the modulation of the frequency (for the single-variable approach) or frequencies (for the multi-variable approach). During the pilot test, the frequencies are modulated by regulating the speed of the oscillations. There is not an ideal speed of oscillations, thus by trial and error, these frequencies can be selected. From experience, these pre-tests by trial and

error during 5 minutes have shown to be efficient enough to find a good combination of these parameters for each subject. However, it is recommended to perform these pre-tests on a different day than the experimental trials to avoid muscle tiredness.

Regarding the calibration parameters, there are parameters associated with the machine and others associated with the subject. The calibration parameters associated with the machine are related to the machine's sensors such as load cells, encoders, etc. The calibration parameters associated with the subject are related to the sensors measuring the subject's signals used for biofeedback which, in the case of this study, was the muscle activations. For this calibration, the warm-up process plays an important role to boost flexibility, performance, and activation of the first motor units. After the warm-up, the isometric tests are important for the sensors' calibration by assessing maximum forces (highest activations possible) [46]. For the isometric tests, the subject is required to perform static exercises (isometric resistances) including pull-up holds, static push-ups, static dumbbell curls (with different angles), lateral shoulder raises, and flexed-arm hangs. Next, the maximum muscle activation observed from each muscle is used to calibrate the sensors (normalize the data with respect to these maximum activations).

Another current limitation observed is the loss of precision in the muscle calibration parameters over time. This effect was observed during the real-time experiments where longer convergence times were coincidentally produced in the second trials (after a few minutes of working out) in all the phases. A similar effect (longer convergence times) was observed for the trials with the nondominant side in comparison with the trials with the dominant side. It is known that during fatigue, the maximum muscle activation is increased in comparison with the maximum activation measured during the calibration process (isometric tests). Besides, the nondominant side (normally the less trained side), tends to fatigue faster and easier. Furthermore,

based on the fact that new muscle motor units start to activate (increase in muscle activation) together with the increase of fatigue, results suggest that there is a possible relationship between convergence time, fatigue, and thus muscle calibration parameters. This increase in the muscle activations produces an increase in the framework's sensitivity introducing disturbances. As a result, the convergence might not only be delayed but also might even be blocked. Therefore, a recalibration process for the muscle parameters might be needed after a few minutes of training (when fatigue starts to show up). The increase in the sensitivity previously observed might be solved by simply decreasing the framework gain. However, an automatic muscle parameter calibration system would be optimal to overcome this current limitation.

7.2.3 User experience effects

It is important to note that the efficiency of the framework (accuracy of the optimal variables), especially for the optimization of the trajectory parameters, lies in the precision of the user to track accurately the desired trajectory. Thus, it is highly recommended the user gets expertise with the exercise protocol before the experiments. Furthermore, it was observed that sometimes the subject unconsciously focused more on activating the measured muscles than maintaining proper alignment with the visual display. As a result of the multi-tasking, the level of difficulty increases together with the tracking error. Therefore, it is important to aware the user of the priority focus of the exercise protocol.

7.2.4 Impedance regulation

It is a known fact that a negative impedance is an unstable impedance (unstable system), for that reason, real-time experiments were performed by using saturation blocks to limit the stiffness value from 0 to 10 Nm/rad. Unlike real-time experiments, simulation experiments were performed by using unconstrained optimization

to acquire data that wouldn't be possible (because it wouldn't be safe) with a real population. As a result, some models obtained negative optimal stiffness impedance values (unstable impedance parameters). Considering that the zero-effort path (the circular trajectory of zero effort) was located inside of the ellipsoidal trajectory, a positive stiffness impedance produces resistance forces acting centripetally, while negative stiffness impedance produces resistance forces acting centrifugally (see Figure 121). Therefore, based on the skeletal distribution and the weight muscle vector selected, optimal resistances might act centripetally as well as centrifugally.

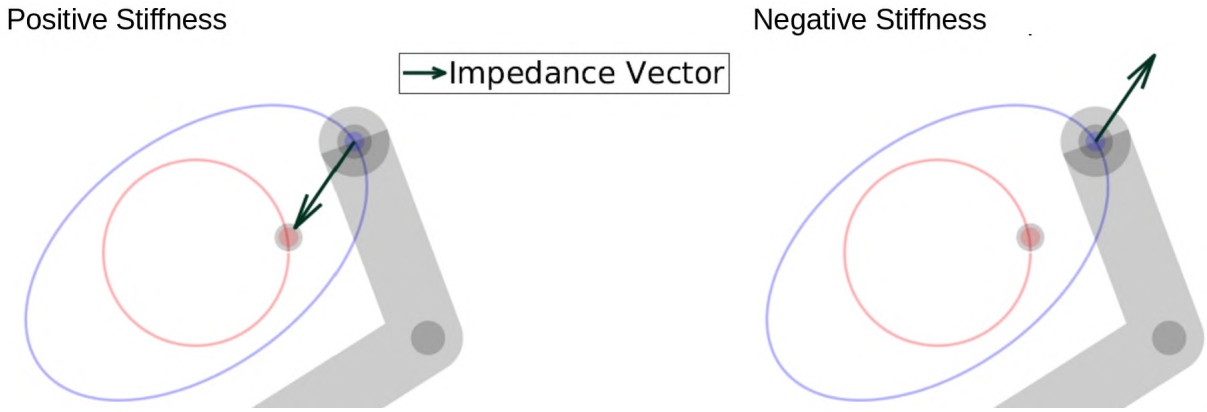

Figure 121: Centripetal and centrifugal resistances associated with positive and negative stiffness impedances respectively.

These results evidence another limitation of this study for the impedance optimization in real-time applications. Currently, if the optimal impedance value is negative, the value would converge to the tolerance limit (set at 0 Nm/rad) without being able to reach the real optimal value. However, a good variation for future work that would potentially overcome this limitation would be to replace the regulation of the stiffness impedance with the regulation of the radius of the circle or the radii of the ellipse. As a result, centrifugal forces would be possible without using unstable parameters (see Figure 122).

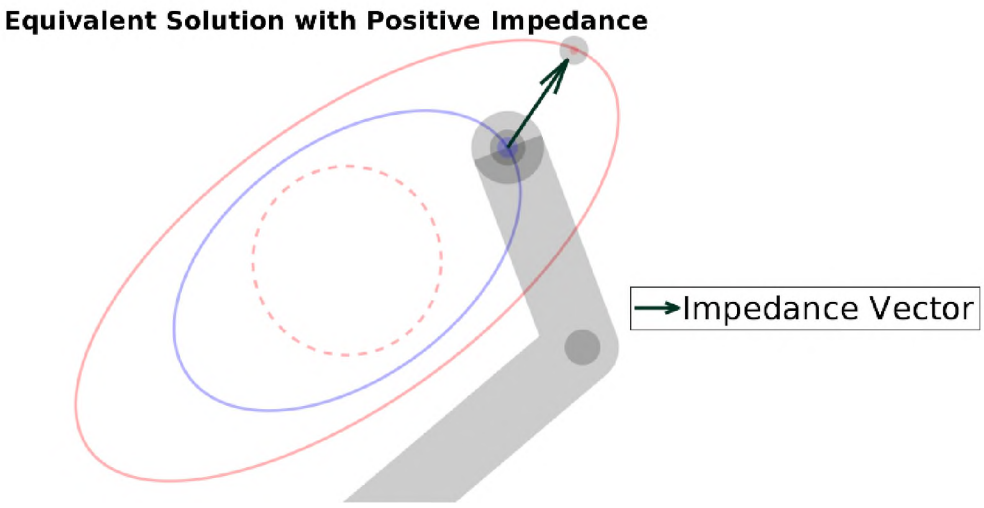

Figure 122: Centrifugal resistances with positive stiffness impedance (stable impedance).

7.2.5 Possibility of multiple local optima

The existence of more than one local optimum would complicate the fact of finding the optimal training parameters (the global optimum parameters).

Based on the results previously observed from the experiments, the possible existence of more than a local optimum for the trajectory orientation is likely. Regarding this parameter, similar solutions in neighboring quadrants were found (trajectories symmetric with respect to the axes). The sample size was not large enough to provide strong conclusions, thus, future experiments could explore deeper the existence of the multiple local optima for the trajectory parameter.

Unlike the trajectory parameter, based on the results previously observed, there is not any evidence about the possible existence of more than a local optimum for the impedance parameter. Nonetheless, based on the fact that optimal impedances were found acting in both directions (centripetally and centrifugally), there is a possibility that there is a local optimum for each direction. Similarly as before, the sample size was not large enough to provide strong conclusions. Thus,

future experiments could explore deeper the possible existence of the multiple local optima for the impedance parameter.

7.2.6 Population availability and self-experimentation

The recruitment of volunteers for experimental tests is never easy, especially during pandemic times. For that reason, the feasibility of the approach was performed by conducting self-experimentation where my person was the designer, researcher, operator, subject, and reporter.

Self-experiments provide some limitations against experimenting with volunteer subjects mainly when the subject is the same person who developed the framework and who best knows the system in detail and how it works intimately. These limitations present during the real-time experiments are related to the following criteria and they are presented below:

- **User experience:**

  As previously stated, the precision of the user to track accurately the desired trajectory plays an important role in the efficiency of the framework (accuracy of the estimation in the optimal variables). This precision can be enhanced by practice because, similarly to a game, practice leads to skill improvements.

  A normal subject from an experimental group might be exposed to practice sessions of 1 hour approximately which might be enough to reach acceptable dexterity levels. However, after years of research, the self-experimenting subject might have completed over 200 hours of practice. As a result, this subject's skill would be potentially better than the average volunteer subjects.

- **Configuration, tuning, and calibration parameters:**

  The parameters selection is also strictly related to the framework's performance.

Those parameters vary between people and during the time, so there is not any initial guess about the possible parameters that can work well for each new subject.

This selection can become very challenging, so a bad parameter selection is always possible. For this case, the parameters that work well for the self-experimenting subject are already known because they have been used several times. So, the selection is reduced to only tunning processes guarantying a good performance.

- **Population size:**

  Self-experiments are single-subject studies where the experimenter experiments on himself or herself. That means, there is only one subject available for the whole study.

  A limitation related to the single-subject population studies is the fact that they restrict the depth of the research. As a result, they can't provide enough or either strong conclusions.

For all those limitations previously stated, real-time experiments were limited to only test the feasibility of the framework and to provide early discussions. Additional experiments with a larger population are part of the future work.

In addition to the previous limitations, some general advantages self-experiments might include for instance:

- A better and more comfortable time management.
- Faster decision making.
- A more relaxed and less distracting environment.

Regarding the general disadvantages, self-experiments might include:

- It is hard to multi-task.
- Less help leads to more work.
- In case of an issue, it takes more time to solve it or find a solution.
- Lack of cooperation and brainstorming leading to reduced quality and quantity of ideas.
- It's not entertaining.

7.2.7 Other limitations

Some limitations of the study were overcome as the phases progressed, but there are still some others limiting the potential of this framework. Some of them have been already been reported, some others include for instance:

- The impedance controller in the robots guarantees passivity with the user, thus they create a safe environment for the exercise protocol. However, this doesn't prevent the psychological effects produced as a result of training with an unconventional machine as a robot. Some subjects felt afraid during the exercise protocol and their physiological effects such as muscle activation, heart rate, and ventilation significantly increased.
- High cost including purchase, installation, configuration, and maintenance.
- The presence of an operator is required.
- Others not yet identified.

BIBLIOGRAPHY

[1] Hervé Abdi. The kendall rank correlation coefficient. Encyclopedia of Measurement and Statistics, pages 213–223, 2007.

[2] Erhan Akdogan and Zeynep Şişman. A muscular activation controlled rehabilitation robot system. pages 271–279, 09 2011.

[3] Naji A. Alibeji, Nicholas Andrew Kirsch, and Nitin Sharma. A muscle synergy-inspired adaptive control scheme for a hybrid walking neuroprosthesis. Frontiers in Bioengineering and Biotechnology, 3:203, 2015.

[4] Kartik B. Ariyur and Miroslav Krstic. Multivariable extremum seeking feedback: Analysis and design. In Fifteenth International Symposium on Mathematical Theory of Networks and Systems, University of Notre Dame, pages 12–16.

[5] Kartik B. Ariyur and Miroslav Krstic. Real Time Optimization by Extremum Seeking Control. John Wiley & Sons, Inc., New York, NY, USA, 2003.

[6] S. Atay, M. Bryant, and G. Buckner. Real-time power optimization of a bimodal rolling-flying vehicle via extremum seeking control. In 2020 American Control Conference (ACC), pages 5114–5118, 2020.

[7] Nicolas Babault, Michel Pousson, Anne Michaut, and Jacques Van Hoecke. Effect of quadriceps femoris muscle length on neural activation during isometric and concentric contractions. Journal of Applied Physiology, 94(3):983–990, 2003.

[8] Barrett Technology. The wam® arm. https://advanced.barrett.com/wam-arm-1. Accessed: 2019-10-24.

[9] Ouriel Barzilay and Alon Wolf. Adaptive rehabilitation games. Journal of Electromyography and Kinesiology, 23(1):182 – 189, 2013.

[10] Santino Bianco. Robust impedance control of a four degree of freedom exercise robot. Master's thesis, Cleveland State University, May 2019.

[11] Yoann Blache, Mickaël Begon, Benjamin Michaud, Landry Desmoulins, Paul Allard, and Fabien Dal Maso. Muscle function in glenohumeral joint stability during lifting task. PLOS ONE, 12(12):1–15, 12 2017.

[12] Deborah Anne Burton, Keith Stokes, and George M Hall. Physiological effects of exercise. Continuing Education in Anaesthesia Critical Care & Pain, 4(6):185–188, 12 2004.

[13] D. Cabrera, A. Ruina, and V. Kleshnev. A simple 1+ dimensional model of rowing mimics observed forces and motions. In Human Movement Science, volume 25, pages 192 – 220, 2006.

[14] M. C. Carrozza, N. Ng Pak, E. Cattin, F. Vecchi, M. Marinelli, and P. Dario. On the design of an exoskeleton for neurorehabilitation: design rules and preliminary prototype. In The 26th Annual International Conference of the IEEE Engineering in Medicine and Biology Society, volume 2, pages 4807–4810, 2004.

[15] S.P. Chan, B. Yao, W.B. Gao, and M. Cheng. Robust impedance control of robot manipulators. International Journal of Robotics and Automation, 6(4):220–227, 1991.

[16] Won Hyuk Chang and Yun-Hee Kim. Robot-assisted therapy in stroke rehabilitation. Journal of Stroke, 15(3):174–181, 2013.

[17] Vincent C. K. Cheung, Andrea Turolla, Michela Agostini, Stefano Silvoni, Caoimhe Bennis, Patrick Kasi, Sabrina Paganoni, Paolo Bonato, and Emilio Bizzi. Muscle synergy patterns as physiological markers of motor cortical damage. Proceedings of the National Academy of Sciences, 109(36):14652–14656, 2012.

[18] Rubana Chowdhury, Mamun Reaz, Mohd Ali, Ashrif Bakar, Kalaivani Chellappan, and Tae Chang. Surface electromyography signal processing and classification techniques. Sensors, 13(9):12431–12466, Sep 2013.

[19] COSMED - The Metabolic Company. COSMED K4b2.

[20] Christophe Croux and Catherine Dehon. Influence functions of the spearman and kendall correlation measures. Tilburg University, Center for Economic Research, Discussion Paper, 19, 01 2010.

[21] Jasper R. Daube and Devon I. Rubin. Needle electromyography. Muscle & Nerve, 39(2):244–270, 2009.

[22] Andrea D'avella and Francesco Lacquaniti. Control of reaching movements by muscle synergy combinations. Frontiers in Computational Neuroscience, 7:42, 2013.

[23] Margie H. Davenport, Sarah Charlesworth, Dana Vanderspank, Maggie M. Sopper, and Michelle F. Mottola. Development and validation of exercise target heart rate zones for overweight and obese pregnant women. Applied Physiology, Nutrition, and Metabolism, 33(5):984–989, 2008.

[24] Humberto De las Casas. Design and control of a powered rowing machine with programmable impedance. Master's thesis, Cleveland State University, 2017.

[25] Humberto De las Casas, Santino Bianco, and Hanz Richter. Targeted muscle effort distribution with exercise robots: Trajectory and resistance effects. Medical Engineering & Physics, 2021.

[26] Humberto De las Casas, Nicholas Chambers, Hanz Richter, and Kenneth Sparks. Real-time trajectory optimization in robot-assisted exercise and rehabilitation. 2021.

[27] Humberto De las Casas, Kevin Kleis, Hanz Richter, Kenneth Sparks, and Antonie van den Bogert. Corrigendum to "eccentric training with a powered rowing machine". Medicine in Novel Technology and Devices, 7:100039, 2020.

[28] Humberto De las Casas, Kevin Kleiss, Hanz Richter, Keneth Sparks, and Antonie van den Bogert. Eccentric training with a powered rowing machine. Medicine in Novel Technology and Devices, 2:100008, 2019.

[29] Humberto De las Casas and Hanz Richter. Backstepping control of muscle driven systems with redundancy resolution, 2020.

[30] Humberto De las Casas, Hanz Richter, and Antonie van den Bogert. Design and hybrid impedance control of a powered rowing machine. In ASME 2017 Dynamic Systems and Control Conference, October 2017.

[31] Humberto De las Casas, Holly Warner, and Hanz Richter. Real-time optimization of an ellipsoidal trajectory orientation using muscle effort with extremum seeking control. Medical Engineering & Physics, 91:19–27, 2021.

[32] DELSYS. Trigno Wireless System - User Guide.

[33] M.U. Deutsch, G. J. Maw, D. Jenkins, and P. Reaburn. Heart rate, blood lactate and kinematic data of elite colts (under-19) rugby union players during competition. Journal of Sports Sciences, 16(6):561–570, 1998.

[34] Richard P. Di Fabio. Reliability of Computerized Surface Electromyography for Determining the Onset of Muscle Activity. Physical Therapy, 67(1):43–48, 01 1987.

[35] P. K. Diwakar, Young Keun Oh, Seung-Hun Park, and Young-Ro Yoon. Personal digital exercise trainer for managing, monitoring and recording the exercise. In 2005 IEEE Engineering in Medicine and Biology 27th Annual Conference, pages 3720–3723, Jan 2005.

[36] Alexander Dromerick. Nrh neuroscience research center. page 286, 06 2008.

[37] dSPACE. MicroLabBox - Compact Power in the Lab.

[38] C. Edwards and S. Spurgeon. Sliding mode control: theory and applications. CRC Press, 1998.

[39] RM Enoka. Morphological features and activation patterns of motor units. Journal of clinical neurophysiology : official publication of the American Electroencephalographic Society, 12(6):538—559, November 1995.

[40] Y. J. Fan, Y. H. Yin, L. D. Xu, Y. Zeng, and F. Wu. Iot-based smart rehabili-

tation system. IEEE Transactions on Industrial Informatics, 10(2):1568–1577, May 2014.

[41] Philip Felig and John Wahren. Fuel homeostasis in exercise. New England Journal of Medicine, 293(21):1078–1084, 1975.

[42] C. Fleischer and G. Hommel. A human–exoskeleton interface utilizing electromyography. IEEE Transactions on Robotics, 24(4):872–882, 2008.

[43] Richard B. Freeman. Chapter 6 demand for education. volume 1 of Handbook of Labor Economics, pages 357 – 386. Elsevier, 1986.

[44] Lina Fu. Model-Based Extremum Seeking Control for a Class of Nonlinear Systems. PhD thesis, The Ohio State University, 2010.

[45] Y. Furuhashi, M. Nagasaki, T. Aoki, Y. Morita, H. Ukai, and N. Matsui. Development of rehabilitation support robot for personalized rehabilitation of upper limbs. In 2009 IEEE International Conference on Rehabilitation Robotics, pages 787–792, June 2009.

[46] Stefan Garcia, Jeffrey Dueweke, and Christopher Mendias. Optimal joint positions for manual isometric muscle testing. Journal of Sport Rehabilitation, 01 2016.

[47] Azad Ghaffari, Miroslav Krstic, and Dragan Nesic. Multivariable newton-based extremum seeking. pages 1759–1767, June 2012.

[48] Jennie A. Gilbert. Using target heart-rate zones in your class. Journal of Physical Education, Recreation & Dance, 76(3):22–26, 2005.

[49] Claire C. Gordon. 1988 anthropometric survey of u.s. personnel: Summary

statistics. Technical report, United States Army Natick Research, Development and Engineering Center, March 1989.

[50] M. Gosselin, E. Neufeld, Heidi Moser, E. Huber, Silvia Farcito, Livia Gerber, Maria Jedensjö, I. Hilber, Fabienne Di Gennaro, B. Lloyd, E. Cherubini, D. Szczerba, W. Kainz, and N. Kuster. Development of a new generation of high-resolution anatomical models for medical device evaluation: the virtual population 3.0. Physics in medicine and biology, 59 18:5287–303, 2014.

[51] Grand View Research. Aqua gym equipment market size analysis report by product (cardiovascular, strength training), by distribution channel (online, specialty store, department stores & supermarkets), and segment forecasts, 2019 - 2025. https://www.grandviewresearch.com/industry-analysis/aqua-gym-equipment-market. Accessed: 2019-12-16.

[52] Grand View Research. Corporate wellness market size, share & trends analysis report by service (health risk assessment, stress management), by category (fitness & nutrition consultant, organization), by end use, and segment forecasts, 2019 - 2026. https://www.grandviewresearch.com/industry-analysis/corporate-wellness-market. Accessed: 2020-08-13.

[53] D. C. Guevara, G. Vietri, M. Prabakar, and J. Kim. Robotic exoskeleton system controlled by kinect and haptic sensors for physical therapy. In 2013 29th Southern Biomedical Engineering Conference, pages 71–72, May 2013.

[54] Bin Guo, Daqing Zhang, Zhu Wang, Zhiwen Yu, and Xingshe Zhou. Opportunistic iot: Exploring the harmonious interaction between human and the internet of things. Journal of Network and Computer Applications, 36(6):1531 – 1539, 2013.

[55] A. Haidar, M. E. Wilinska, J. A. Graveston, and R. Hovorka. Stochastic virtual population of subjects with type 1 diabetes for the assessment of closed-loop glucose controllers. IEEE Transactions on Biomedical Engineering, 60(12):3524–3533, 2013.

[56] F. Harashima. Human adaptive mechatronics. In IEEE Workshop on Advanced Robotics and its Social Impacts, 2005., pages 80–, June 2005.

[57] A. R. Hargens, S. Parazynski, M. Aratow, and J. Friden. Muscle changes with eccentric exercise: implications on earth and in space. Advances in myochemistry, 2:299–312, 1989.

[58] Joseph Hidler, Diane Nichols, Marlena Pelliccio, and Kathy Brady. Advances in the understanding and treatment of stroke impairment using robotic devices. Topics in stroke rehabilitation, 12:22–35, 02 2005.

[59] Archibald Vivian Hill. The heat of shortening and the dynamic constants of muscle. Proceedings of the Royal Society of London. Series B - Biological Sciences, 126(843):136–195, 1938.

[60] Neville Hogan. Impedance control: An approach to manipulation: Part ii—implementation. J. Dyn. Sys., Meas., Control., 1985.

[61] Neville Hogan, Hermano Igo Krebs, J. Charnnarong, P. Srikrishna, and Andre Sharon. MIT-MANUS: a workstation for manual therapy and training II. In Hari Das, editor, Telemanipulator Technology, volume 1833, pages 28 – 34. International Society for Optics and Photonics, SPIE, 1993.

[62] Neville Hogan, Hermano Igo Krebs, Jain Charnnarong, Padmanabhan Srikrishna, and Andre Sharon. MIT-manus: a workstation for manual therapy and

training. i. [1992] Proceedings IEEE International Workshop on Robot and Human Communication, pages 161–165, 1992.

[63] T. Hortobagyi. The positives of negatives: clinical implications of eccentric resistance in exercise in older adults. Journal of Gerontology, 58A:417–418, 2003.

[64] Alun Hughes and Nish Chaturvedi. Estimation of maximal oxygen consumption and heart rate recovery using the tecumseh sub-maximal step test and their relationship to cardiovascular risk factors. Artery Research, 18:29–35, 06 2017.

[65] Insurance Information Institute. Facts + statistics: Sports injuries. https://www.iii.org/fact-statistic/facts-statistics-sports-injuries. Accessed: 2021-1-7.

[66] Steven J Elmer, Camden Marshall, Keith R McGinnis, Timothy A Van Haitsma, and Paul C Lastayo. Eccentric arm cycling: Physiological characteristics and potential applications with healthy populations. European journal of applied physiology, 113, 07 2013.

[67] Kathleen Jagodnik and Antonie van den Bogert. Optimization and evaluation of a proportional derivative controller for planar arm movement. Journal of biomechanics, 43:1086–91, 04 2010.

[68] Jem Arnold. The problem with vo2max. https://sparecycles.blog/2017/11/22/the-problem-with-vo2max/, 11 2017. Accessed: 2019-12-5.

[69] John LaRosa. U.s. physical therapy clinics constitute a growing $34 billion industry. https://blog.marketresearch.com/u.s.

-physical-therapy-clinics-constitute-a-growing-34-billion-industry. Accessed: 2019-11-19.

[70] Lewis G. Coggins Jr., William E. Pine III, Carl J. Walters, and Steven J. D. Martell. Age-structured mark–recapture analysis: A virtual-population-analysis-based model for analyzing age-structured capture–recapture data. North American Journal of Fisheries Management, 26(1):201–205, 2006.

[71] Da-Woon Jung, Dae-Sung Park, Bum-Suk Lee, and Min Kim. Development of a motor driven rowing machine with automatic functional electrical stimulation controller for individuals with paraplegia; a preliminary study. Annals of rehabilitation medicine, 36:379–85, 06 2012.

[72] Arnold Henry Kadish, Robert L. Litle, and James C. Sternberg. A new and rapid method for the determination of glucose by measurement of rate of oxygen consumption. Clinical Chemistry, 14(2):116–131, 1968.

[73] Juha Karvonen and Timo Vuorimaa. Heart rate and exercise intensity during sports activities. Sports Medicine, 5(5):303–311, May 1988.

[74] B Katz. The relation between force and speed in muscular contraction. The Journal of physiology, 96(1):45–64, 1939.

[75] Joosup Kim, Tharshanah Thayabaranathan, Geoffrey A Donnan, George Howard, Virginia J Howard, Peter M Rothwell, Valery Feigin, Bo Norrving, Mayowa Owolabi, Jeyaraj Pandian, Liping Liu, Dominique A Cadilhac, and Amanda G Thrift. Global stroke statistics 2019. International Journal of Stroke, 0(0):1747493020909545, 0. PMID: 32146867.

[76] H Krebs, N Hogan, Bruce Volpe, Mindy Aisen, L Edelstein, and C Diels. Overview of clinical trials with MIT-manus: A robot-aided neuro-rehabilitation

facility. Technology and health care : official journal of the European Society for Engineering and Medicine, 7:419–23, 02 1999.

[77] H. Krebs, J. Palazzolo, Laura Dipietro, M. Ferraro, J. Krol, K. Rannekleiv, Bruce Volpe, and N. Hogan. Rehabilitation robotics: Performance-based progressive robot-assisted therapy. Autonomous Robots, 15:7–20, 07 2003.

[78] Hermano Krebs, Mark Ferraro, Stephen Buerger, Miranda Newbery, Antonio Makiyama, Michael Sandmann, Daniel Lynch, Bruce Volpe, and Neville Hogan. Rehabilitation robotics: Pilot trial of a spatial extension for mit-manus. Journal of neuroengineering and rehabilitation, 1:5, 11 2004.

[79] Miroslav Krstić and Hsin-Hsiung Wang. Stability of extremum seeking feedback for general nonlinear dynamic systems. Automatica, 36(4):595 – 601, 2000.

[80] Miroslav Kubat. Chapter 5. Artificial Neural Networks. Springer International Publishing, Springer, 2017.

[81] D. N. Kulund, J. B. Dewey, C. E. Brubaker, and J. R. Roberts. Olympic weight-lifting injuries. The Physician and Sportsmedicine, 6(11):111–119, 1978.

[82] S. Kumar, A. Mohammadi, D. Quintero, S. Rezazadeh, N. Gans, and R. D. Gregg. Extremum seeking control for model-free auto-tuning of powered prosthetic legs. IEEE Transactions on Control Systems Technology, pages 1–16, 2019.

[83] M König and K Biener. [sport-specific injuries in weight lifting]. Schweizerische Zeitschrift fur Sportmedizin, 38(1):25—30, April 1990.

[84] LabJack - Measurement & Automation. Labjack t7. https://labjack.com/products/t7. Accessed: 2019-11-15.

[85] LabJack - Measurement & Automation. Labjack u3. https://labjack.com/products/U3. Accessed: 2019-11-15.

[86] LegalMatch. Gym accident statistics. https://www.legalmatch.com/law-library/article/gym-accident-statistics.html#:~:text=From%201990%20to%202007%2C%20114,and%2014%20years%20old%20annually. Accessed: 2021-1-7.

[87] Der-Chang Li, Long-Sheng Chen, and Yao-San Lin. Using functional virtual population as assistance to learn scheduling knowledge in dynamic manufacturing environments. International Journal of Production Research, 41(17):4011–4024, 2003.

[88] Perry Y. Li and Roberto Horowitz. Control of smart exercise machines part ii: Self-optimizing control. IFAC Proceedings Volumes, 29(1):5727 – 5732, 1996. 13th World Congress of IFAC, 1996, San Francisco USA, 30 June - 5 July.

[89] Perry Y. Li and Roberto Horowitz. Control of smart exercise machines. i. problem formulation and nonadaptive control. In IEEE/ASME TRANSACTIONS ON MECHATRONICS, 1997.

[90] Jing Z. Liu, Robert W. Brown, and Guang H. Yue. A dynamical model of muscle activation, fatigue, and recovery. Biophysical Journal, 82(5):2344 – 2359, 2002.

[91] Firstbeat Technologies Ltd. Automated fitness level (vo2max) estimation with heart rate and speed data. Technical report, Firstbeat Technologies, 11 2014.

[92] Firstbeat Technologies Ltd. Vo2 estimation method based on heart rate measurement. Technical report, Firstbeat Technologies, 2 2015.

[93] Carlo J. De Luca. The use of surface electromyography in biomechanics. Journal of Applied Biomechanics, 13(2):135 – 163, 1997.

[94] Alec MacCall. Virtual population analysis (vpa) equations for nonhomogeneous populations, and a family of approximations including improvements on pope's cohort analysis. Canadian Journal of Fisheries and Aquatic Sciences, 43:2406–2409, 04 2011.

[95] Duncan J. Macfarlane. Open-circuit respirometry: a historical review of portable gas analysis systems. European Journal of Applied Physiology, 117(12):2369–2386, Dec 2017.

[96] Pawel Maciejasz, Jörg Eschweiler, Kurt Gerlach-Hahn, Arne Jansen-Toy, and Steffen Leonhardt. A survey on robotic devices for upper limb rehabilitation. Journal of neuroengineering and rehabilitation, 11:3, 01 2014.

[97] Constantinos Mavroidis, Jason Nikitczuk, Brian Weinberg, Gil Danaher, Katherine Jensen, Philip Pelletier, Jennifer Prugnarola, Ryan Stuart, Roberto Arango, Matt Leahey, Robert Pavone, Andrew Provo, and Dan Yasevac. Smart portable rehabilitation devices. Journal of neuroengineering and rehabilitation, 2:18, 08 2005.

[98] Roberto Merletti, Dario Farina, Marco Gazzoni, Andrea Merlo, P. Ossola, and Alberto Rainoldi. Surface electromyography for noninvasive characterization of muscle. Europa Medicophysica, 37:57–68, 01 2001.

[99] B. Michel, S. Peter, and T. Jean-Yves. Smart interface-to-device architecture for hmi. In IEEE SMC'99 Conference Proceedings. 1999 IEEE International Conference on Systems, Man, and Cybernetics (Cat. No.99CH37028), volume 6, pages 1063–1068 vol.6, Oct 1999.

[100] W. Moase, C. Manzie, and M. Brear. Newton-like extremum-seeking for the control of thermoacoustic instability. pages 2094–9105, September 2010.

[101] Y. Morita, Masaya Nagasaki, H. Ukai, N. Matsui, and M. Uchida. Development of rehabilitation training support system of upper limb motor function for personalized rehabilitation. In 2008 IEEE International Conference on Robotics and Biomimetics, pages 300–305, Feb 2009.

[102] Motive8. When to update corporate gym equipment. https://m8group.co.uk/blog/when-to-update-gym-equipment/. Accessed: 2020-10-07.

[103] S. Hutchinson M.W. Spong and M. Vidyasagar. Robot Modeling and Control. Wiley, 2005.

[104] A. Möller, L. Roalter, S. Diewald, J. Scherr, M. Kranz, N. Hammerla, P. Olivier, and T. Plötz. Gymskill: A personal trainer for physical exercises. pages 213–220, March 2012.

[105] NASA. Advanced resistive exercise device (ared) man-in-theloop test (milt). Technical report, NASA, May 2006.

[106] NASA. Lost in space: Bone density. https://www.nasa.gov/pdf/516065main_ALG_ST_BoneDensity%2012-23-10.pdf, 2010. Accessed: March 2017.

[107] TJ Neviaser. Weight lifting. risks and injuries to the shoulder. Clinics in sports medicine, 10(3):615—621, July 1991.

[108] Jorge Nocedal and Stephen J. Wright. Numerical Optimization. Springer, New York, NY, 1999.

[109] Joseph Nuamah and Younho Seong. Human machine interface in the internet of things (iot). pages 1–6, 06 2017.

[110] Tiago Roux Oliveira, Luiz Rennó Costa, and Alexandre Visintainer Pino. Extremum seeking applied to neuromuscular electrical stimulation. IFAC-PapersOnLine, 49(32):188 – 193, 2016. Cyber-Physical & Human-Systems CPHS 2016.

[111] Parker Hannifin - Human Motion & Control Lab. Home webpage, December 2018. http://hmc.csuohio.edu/.

[112] P. Paz and T. R. Oliveira. Neuromuscular electrical stimulation for stroke patients by deterministic extremum seeking. In 2018 IEEE Conference on Decision and Control (CDC), pages 6692–6698, Dec 2018.

[113] P. Paz, T. R. Oliveira, A. V. Pino, and A. P. Fontana. Model-free neuromuscular electrical stimulation by stochastic extremum seeking. IEEE Transactions on Control Systems Technology, pages 1–16, 2019.

[114] L. Ploutz-Snyder, J. Ryder, K. English, F. Haddad, and K. Baldwin. Risk of impaired performance due to reduced muscle mass, strength, and endurance. Technical report, NASA, March, 9 2015.

[115] Polar. Polar H7 Heart Rate Sensor - User Manual.

[116] Jg Pope. An investigation of the accuracy of virtual population analysis using cohort analysis. 1972.

[117] Brahm Powell. Investigation of extremum seeking control for adaptive exercise machines. Master's thesis, Cleveland State University, August 2017.

[118] Protectivity Insurance. 41% of gym users have been injured whilst working out. https://www.protectivity.com/knowledge-centre/41-of-gym-users-have-been-injured-whilst-working-out/. Accessed: 2021-1-7.

[119] WL Risser. Weight-training injuries in children and adolescents. American family physician, 44(6):2104—2108, December 1991.

[120] C. Rodriguez Guerrero, J. Fraile Marinero, J. Perez Turiel, and P. Rivera Farina. Bio cooperative robotic platform for motor function recovery of the upper limb after stroke. In 2010 Annual International Conference of the IEEE Engineering in Medicine and Biology, pages 4472–4475, 2010.

[121] TIAGO ROUX-OLIVEIRA, LUIZ R. COSTA, ALEXANDRE V. PINO, and PAULO PAZ. Extremum Seeking-based Adaptive PID Control applied to Neuromuscular Electrical Stimulation. Anais da Academia Brasileira de Ciencias, 91, 00 2019.

[122] Seyed Safavynia, Gelsy Torres-Oviedo, and Lena Ting. Muscle synergies: Implications for clinical evaluation and rehabilitation of movement. Topics in spinal cord injury rehabilitation, 17:16–24, 05 2011.

[123] S. Scalzi, P. Tomei, and C. M. Verrelli. Nonlinear control techniques for the heart rate regulation in treadmill exercises. IEEE Transactions on Biomedical Engineering, 59(3):599–603, March 2012.

[124] Peter Schantz, Jane Salier Eriksson, and Hans Rosdahl. The heart rate method for estimating oxygen uptake: analyses of reproducibility using a range of heart rates from commuter walking. European Journal of Applied Physiology, 119(11):2655–2671, Dec 2019.

[125] Peter Schantz, Jane Salier Eriksson, and Hans Rosdahl. The heart rate method for estimating oxygen uptake: Analyses of reproducibility using a range of heart rates from cycle commuting. PLOS ONE, 14(7):1–20, 07 2019.

[126] E. M. Schearer, Y. Liao, E. J. Perreault, M. C. Tresch, and K. M. Lynch. Optimal sampling of recruitment curves for functional electrical stimulation control. In 2012 Annual International Conference of the IEEE Engineering in Medicine and Biology Society, pages 329–332, 2012.

[127] E. M. Schearer, Y. Liao, E. J. Perreault, M. C. Tresch, W. D. Memberg, R. F. Kirsch, and K. M. Lynch. Evaluation of a semi-parametric model for high-dimensional fes control. In 2015 7th International IEEE/EMBS Conference on Neural Engineering (NER), pages 304–307, 2015.

[128] E. M. Schearer, Y. W. Liao, E. J. Perreault, M. C. Tresch, W. D. Memberg, R. F. Kirsch, and K. M. Lynch. Semiparametric identification of human arm dynamics for flexible control of a functional electrical stimulation neuroprosthesis. IEEE Transactions on Neural Systems and Rehabilitation Engineering, 24(12):1405–1415, 2016.

[129] Henning Schmidt, Cordula Werner, Rolf Bernhardt, Stefan Hesse, and Jörg Krüger. Gait rehabilitation machines based on programmable footplates. Journal of NeuroEngineering and Rehabilitation, 2007.

[130] Seeking Alpha. Opportunity within the multi-billion physical therapy industry: Examining u.s. physical therapy and ewellness. https://seekingalpha.com/article/3975610-opportunity-within-multi-billion-physical-therapy-industry-examining Accessed: 2019-11-19.

[131] Chandan K Sen and Lester Packer. Thiol homeostasis and supplements in physical exercise. The American Journal of Clinical Nutrition, 72(2):653S–669S, 08 2000.

[132] Roy J. Shephard. Occupational demand and human rights. Sports Medicine, 12(2):94–109, Aug 1991.

[133] Fady Shibata Alnajjar, Tytus Wojtara, hidenori kimura, and Shingo Shimoda. Muscle synergy space: learning model to create an optimal muscle synergy. Frontiers in Computational Neuroscience, 7:136, 2013.

[134] Yuri Shtessel, Christopher Edwards, Leonid Fridman, and Arie Levant. Sliding Mode Control and Observation. Birkhäuser Basel, 2014.

[135] S. Siegel. The kendall rank correlation coefficient. Nonparametric Statistics for the Behavioral Sciences, pages 213–223, 01 1956.

[136] D. Simon. Biogeography-based optimization. IEEE Transactions on Evolutionary Computation, 12(6):702–713, 2008.

[137] D. Simon. Evolutionary optimization algorithms : biologically-inspired and population-based approaches to computer intelligence. 2013.

[138] Rajat Emanuel Singh, Kamran Iqbal, Gannon A. White, and Tarun E Hutchinson. A systematic review on muscle synergies: From building blocks of motor behavior to a neurorehabilitation tool. In Applied bionics and biomechanics, 2018.

[139] S. Smith, S. Zwart, and M. Heer. Human Adaptation to Spaceflight: The Role of Nutrition. NASA, December 2014.

[140] Juhani Smolander, Marjo Ajoviita, Tanja Juuti, Ari Nummela, and Heikki Rusko. Estimating oxygen consumption from heart rate and heart rate variability without individual calibration. Clinical Physiology and Functional Imaging, 31(4):266–271, 2011.

[141] Juhani Smolander, Tanja Juuti, Marja-Liisa Kinnunen, Kari Laine, Veikko Louhevaara, Kaisa Männikkö, and Heikki Rusko. A new heart rate variability-based method for the estimation of oxygen consumption without individual laboratory calibration: Application example on postal workers. Applied Ergonomics, 39(3):325 – 331, 2008.

[142] Statista. North america sports market size from 2009 to 2023 (in billion u.s. dollars)*. https://www.statista.com/statistics/214960/revenue-of-the-north-american-sports-market/. Accessed: 2021-2-28.

[143] Katherine Steele, Matthew Tresch, and Eric Perreault. The number and choice of muscles impact the results of muscle synergy analyses. Frontiers in Computational Neuroscience, 7:105, 2013.

[144] K. Stegath, N. Sharma, C. M. Gregory, and W. E. Dixon. An extremum seeking method for non-isometric neuromuscular electrical stimulation. In 2007 IEEE International Conference on Systems, Man and Cybernetics, pages 2528–2532, Oct 2007.

[145] S. W. Su, Lu Wang, B. G. Celler, A. V. Savkin, and Y. Guo. Modelling and control for heart rate regulation during treadmill exercise. In 2006 International Conference of the IEEE Engineering in Medicine and Biology Society, pages 4299–4302, Aug 2006.

[146] S. W. Su, L. Wang, B. G. Celler, and A. V. Savkin. Heart rate control during

treadmill exercise. In 2005 IEEE Engineering in Medicine and Biology 27th Annual Conference, pages 2471–2474, Jan 2005.

[147] S. W. Su, L. Wang, B. G. Celler, A. V. Savkin, and Y. Guo. Identification and control for heart rate regulation during treadmill exercise. IEEE Transactions on Biomedical Engineering, 54(7):1238–1246, July 2007.

[148] Juri Taborri, Valentina Agostini, Panagiotis K. Artemiadis, Marco Ghislieri, Daniel A Jacobs, Jinsook Roh, and Stefano Rossi. Feasibility of muscle synergy outcomes in clinics, robotics, and sports: A systematic review. In Applied bionics and biomechanics, 2018.

[149] George Thomas, Paul Lozovyy, and Dan Simon. Fuzzy robot controller tuning with biogeography-based optimization. In Kishan G. Mehrotra, Chilukuri K. Mohan, Jae C. Oh, Pramod K. Varshney, and Moonis Ali, editors, Modern Approaches in Applied Intelligence, pages 319–327, Berlin, Heidelberg, 2011. Springer Berlin Heidelberg.

[150] Ø. Ulltang. Sources of errors in and limitations of Virtual Population Analysis (Cohort Analysis). ICES Journal of Marine Science, 37(3):249–260, 09 1977.

[151] J. v. Zitzewitz, G. Rauter, R. Steiner, A. Brunschweiler, and R. Riener. A versatile wire robot concept as a haptic interface for sport simulation. In 2009 IEEE International Conference on Robotics and Automation, pages 313–318, 2009.

[152] Salim S. Virani, Alvaro Alonso, Emelia J. Benjamin, Marcio S. Bittencourt, Clifton W. Callaway, April P. Carson, Alanna M. Chamberlain, Alexander R. Chang, Susan Cheng, Francesca N. Delling, Luc Djousse, Mitchell S.V. Elkind, Jane F. Ferguson, Myriam Fornage, Sadiya S. Khan, Brett M. Kissela, Kris-

ten L. Knutson, Tak W. Kwan, Daniel T. Lackland, Tené T. Lewis, Judith H. Lichtman, Chris T. Longenecker, Matthew Shane Loop, Pamela L. Lutsey, Seth S. Martin, Kunihiro Matsushita, Andrew E. Moran, Michael E. Mussolino, Amanda Marma Perak, Wayne D. Rosamond, Gregory A. Roth, Uchechukwu K.A. Sampson, Gary M. Satou, Emily B. Schroeder, Svati H. Shah, Christina M. Shay, Nicole L. Spartano, Andrew Stokes, David L. Tirschwell, Lisa B. VanWagner, Connie W. Tsao, and null null. Heart disease and stroke statistics—2020 update: A report from the american heart association. Circulation, 141(9):e139–e596, 2020.

[153] Michael Vogt and Hans Hoppeler. Eccentric exercise: Mechanisms and effects when used as training regime or training adjunct. In The American Physiological Society, volume 116, pages 1446–1454, 02 2014.

[154] Q. Wang, W. Chen, A. A. A. Timmermans, C. Karachristos, J. B. Martens, and P. Markopoulos. Smart rehabilitation garment for posture monitoring. In 2015 37th Annual International Conference of the IEEE Engineering in Medicine and Biology Society (EMBC), pages 5736–5739, Aug 2015.

[155] Yi Wang, Yi Li, Hongbao Cao, Momiao Xiong, Yin Shugart, and Li Jin. Efficient test for nonlinear dependence of two continuous variables. BMC bioinformatics, 16:260, 08 2015.

[156] Susan Ward. Open-circuit respirometry: real-time, laboratory-based systems. European Journal of Applied Physiology, 118, 05 2018.

[157] Holly Warner. Simulation and Control at the Boundaries Between Humans and Assistive Robots. PhD thesis, Cleveland State University, December 2019.

[158] Holly Warner, Hanz Richter, and Antonie van den Bogert. Backstepping Control

of Open-Chain Linkages Actuated by Antagonistic Hill Muscles. Journal of Dynamic Systems, Measurement, and Control, 06 2020.

[159] Jack M. Winters and Savio L-Y. Woo. Hill-Based Muscle Models: A Systems Engineering Perspective, pages 69–93. Springer New York, New York, NY, 1990.

[160] Tytus Wojtara, Fady Alnajjar, Shingo Shimoda, and Hidenori Kimura. Muscle synergy stability and human balance maintenance. Journal of neuroengineering and rehabilitation, 11:129, 08 2014.

[161] D. N. Wolf and E. M. Schearer. Developing a quasi-static controller for a paralyzed human arm: A simulation study. In 2019 IEEE 16th International Conference on Rehabilitation Robotics (ICORR), pages 1153–1158, 2019.

[162] Chunlei Zhang and Raul Ordonez. Extremum-Seeking Control and Applications A Numerical Optimization-Based Approach. Springer London Dordrecht Heidelberg New York, 01 2012.

[163] Juanjuan Zhang, Pieter Fiers, Kirby A. Witte, Rachel W. Jackson, Katherine L. Poggensee, Christopher G. Atkeson, and Steven H. Collins. Human-in-the-loop optimization of exoskeleton assistance during walking. Science, 356(6344):1280–1284, 2017.

[164] X. T. Zhang, D. M. Dawson, W. E. Dixon, and B. Xian. Extremum seeking nonlinear controllers for a human exercise machine. In 2004 43rd IEEE Conference on Decision and Control (CDC) (IEEE Cat. No.04CH37601), volume 4, pages 3950–3955 Vol.4, Dec 2004.

[165] X. T. Zhang, D. M. Dawson, W. E. Dixon, and B. Xian. Extremum-seeking nonlinear controllers for a human exercise machine. IEEE/ASME Transactions

on Mechatronics, 11(2):233–240, April 2006.

[166] H. Zheng, R. Davies, T. Stone, S. Wilson, J. Hammerton, S. J. Mawson, P. M. Ware, N. D. Black, N. D. Harris, C. Eccleston, H. Hu, H. Zhou, and G. A. Mountain. Smart rehabilitation: Implementation of ict platform to support home-based stroke rehabilitation. In Constantine Stephanidis, editor, Universal Acess in Human Computer Interaction. Coping with Diversity, pages 831–840, Berlin, Heidelberg, 2007. Springer Berlin Heidelberg.

[167] H. Zheng, R. J. Davies, and N. D. Black. Web-based monitoring system for home-based rehabilitation with stroke patients. In 18th IEEE Symposium on Computer-Based Medical Systems (CBMS'05), pages 419–424, June 2005.

APPENDICES

APPENDIX A

Virtual Population Models

A.1 Baseline Model - Muscle Actuated Linkage Model

The virtual population used in this research includes 50 human models with 25 female and 25 male models. It was built by using a muscle-actuated linkage model developed by Dr. Warner [158] as a baseline. This muscle-actuated linkage model was built by using physical parameters of a scaled real human arm [67]. The model includes two subsystems: the linkages (as a frame), and 6 muscles (as the actuators). The muscles were oriented as shown in Figure 123. The human arm's dynamics are given by

$$D(q)\ddot{q} + C(q,\dot{q})\dot{q} + g(q) - J^T F_{ext} = AF_{muscles}, \tag{A.1}$$

where q is the state vector representing the shoulder and elbow position, D is the mass matrix, C is the Coriolis matrix, g is the gravity vector, J is the Jacobian, F_{ext} is the external force representing the interaction between the arm and the exercise machine, A is the matrix of muscle moment arms, and $F_{muscles}$ is the vector of muscle forces calculated based on the muscle dynamics [158, 159, 59].

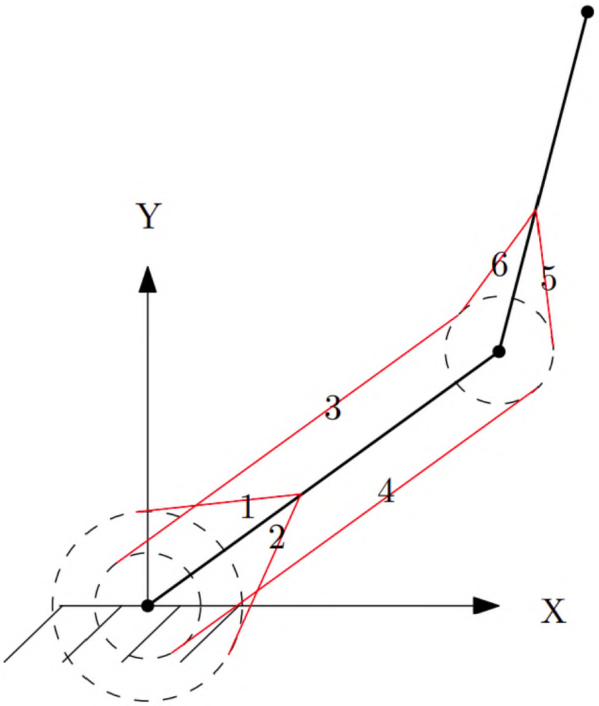

Figure 123: Locations of muscles: Anterior Deltoid (1), Posterior Deltoid (2), Biceps Brachii (3), Triceps Brachii (long head) (4), Triceps Brachii (short head) (5), and Brachialis (6) [31].

This muscle-actuated linkage model has a Lyapunov-based backstepping controller to generate a closed-loop tracking simulation while providing insight into muscle redundancy resolution. Furthermore, it has an optimization framework to produce an efficient human movement by using the insight from this controller [157].

Therefore, for the simulation experiments, the muscle actuated the linkage model receives the target position to be tracked by the end-effector (X_d) and the external/interaction force (F_{ext}), and then the internal controller in the linkage model computes the muscle activations required to accomplish the target motion (see Figure 124).

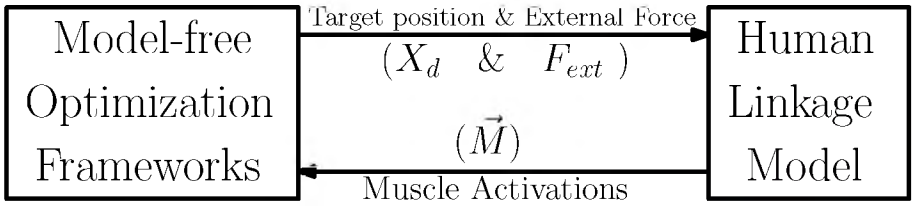

Figure 124: Model-free optimization framework in the simulation environment.

The linkage model is based on the Hill muscle model [29] (see Figure 125) including the following elements:

- A series elastic element (SEE) modeled as a nonlinear spring with a slack region (that simulates the effects of the human tendon).
- A parallel elastic element (PEE) representing the nonlinear stiffness of the human muscle produced after the muscle has been drawn beyond its optimal length.
- A contractile element (CE) that produces the activation and it is the active force generating element.
- The control input (neural input) to the system.

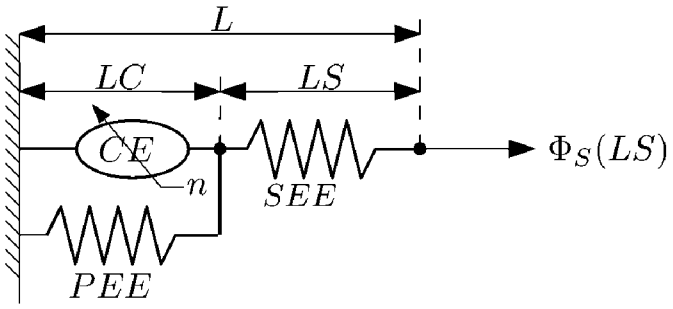

Figure 125: Hill muscle model used for the muscle-actuated arm model. The variables SEE, PEE, CE, and n represent the series elastic element, parallel elastic element, contractile element, and control input. The tendon force is represented by $\Phi_S(LS)$ [157].

For more details or intentions to make use of this muscle-actuated linkage model, please refer to the bibliography [157].

A.2 Generation Process

Each of the models from the virtual population was generated based on anthropometric data (reported on [49]) and the parameters of the linkage arm model. This anthropometric data report includes descriptions, measurements, statistics, and percentile values built from almost 9000 subjects (males and females) of different ages and racial categories (see Figure 126).

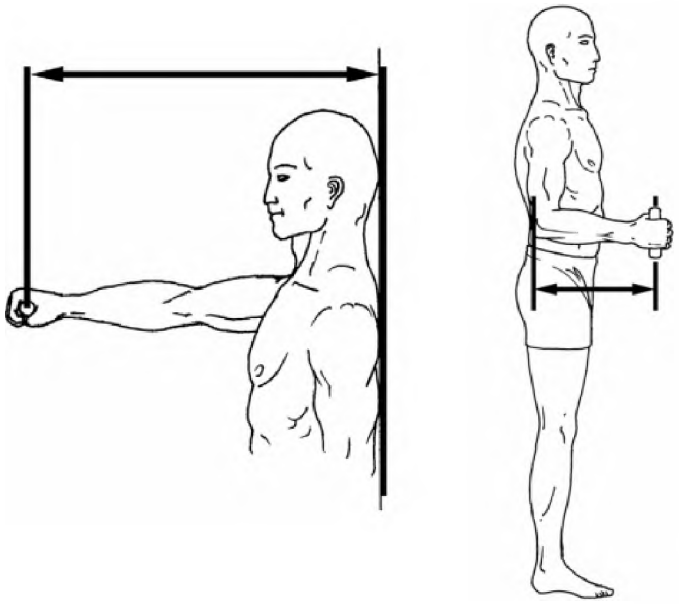

Figure 126: Examples of anthropometric data points [49].

A total of 8 parameters representing the lengths, masses, inertia, and center of masses of the upper and lower arms were generated for each model. The first 2 generated parameters were the lengths of the upper and lower arms. These 2 parameters received the values from the percentiles on the male and female anthropometric datasets as follows:

Table XXIX: Relationship between the generated models and the percentiles in the anthropometric data.

Model	Percentile
1	1^{th}
2	2^{th}
3	3^{th}
4	5^{th}
5	10^{th}
6	15^{th}
7	20^{th}
8	25^{th}
9	30^{th}
10	35^{th}
11	40^{th}
12	45^{th}
13	50^{th}
14	55^{th}
15	60^{th}
16	65^{th}
17	70^{th}
18	75^{th}
19	80^{th}
20	85^{th}
21	90^{th}
22	95^{th}
23	97^{th}
24	98^{th}
25	99^{th}

Then, the set of physical parameters of the scaled linkage model (see Table XXX) was used to generate the remaining 6 parameters for each of the 50 models (25 female and 25 male models).

Table XXX: Physical parameters of the linkage scaled to a real human arm [67].

Parameter	Value
$L1_M$ (kg)	2.24
$L2_M$ (kg)	1.76
$L1_I$ (kgm)	0.0253
$L2_I$ (kgm)	0.0395
$L1_L$ (m)	0.33
$L2_L$ (m)	0.32
$L1_{CM}$ (m)	0.1439
$L2_{CM}$ (m)	0.2182

The generation of the remaining 6 parameters was performed by finding the ratio between the upper and lower arm lengths of each model and the linkage in Table XXX, multiplying the parameter for that ratio and then adding a random value between the ±5% of the linkage parameter value. For example, the inertia parameter associated with the lower arm was calculated as follows:

$$L1_I = \frac{L1_L}{0.33}(0.0253) + \frac{R\Big([-0.0253, 0.0253]\Big)}{20}, \tag{A.2}$$

where $R([x, y])$ is a function producing a random number between x and y.

Regarding the muscles, the lengths from the original linkage model were used and scaled based on the same ratio previously used as follows:

Table XXXI: Original muscle lengths from the linkage model and the scale factors [67]. The variables L_o, L_s, a_0 represent the optimal length of the contractile element, the slack length of the muscle, and the length of the muscle when the arm is completely extended respectively.

Muscle	L_o	L_s	a_0	Scale factor
Anterior Deltoid (1)	0.1280	0.0538	0.1840	$L1_L/0.33$
Posterior Deltoid (2)	0.1280	0.0538	0.1055	$L1_L/0.33$
Biceps Brachii (3)	0.1422	0.2298	0.4283	$L1_L/0.33$
Triceps Brachii (longhead) (4)	0.0877	0.1905	0.1916	$L1_L/0.33$
Triceps Brachii (shorthead) (5)	0.0877	0.1905	0.2387	$L2_L/0.32$
Brachialis (6)	0.1028	0.0175	0.1681	$L2_L/0.32$

Regarding the remaining muscle properties, they were selected as the default values (they were not varied) and they can be seen in Table XXXII).

Table XXXII: Default muscle parameters based on the musculoskeletal representation of a human model [158, 159, 59, 74].

Muscle	F_{max} (N)	d_1 (m)	d_2 (m)
Anterior Deltoid (1)	800	0.05	0
Posterior Deltoid (2)	800	-0.05	0
Biceps Brachii (3)	1000	0.03	0.03
Triceps Brachii (longhead) (4)	1000 -0.03	-0.03	
Triceps Brachii (shorthead) (5)	700	0	-0.03
Brachialis (6)	700	0	0.03

A.2 Model Parameters

A.2.1 Female arm model parameters

Table XXXIII: Female arm model parameters. The subscripts M, I, L, and CM represent the mass, inertia, length, and center of mass properties of the links respectively.

Model	$L1_M$ (kg)	$L2_M$ (kg)	$L1_I$ (kgm)	$L2_I$ (kgm)	$L1_L$ (m)	$L2_L$ (m)	$L1_{CM}$ (m)	$L2_{CM}$ (m)
1	1.9159	1.7175	0.021916	0.038909	0.2893	0.3258	0.13192	0.22972
2	1.9767	1.7876	0.023645	0.042078	0.2935	0.3277	0.13128	0.22141
3	2.1124	1.7835	0.021983	0.039178	0.2963	0.3292	0.12619	0.23291
4	2.0423	1.8957	0.02195	0.042655	0.3002	0.3317	0.1295	0.21998
5	2.1022	1.8281	0.023062	0.042273	0.3063	0.3363	0.13594	0.23569
6	2.0406	1.9502	0.023653	0.042482	0.3104	0.3399	0.1384	0.2245
7	2.2257	1.8911	0.025121	0.040955	0.3137	0.3429	0.13861	0.23776
8	2.1279	1.8678	0.024249	0.043868	0.3166	0.3456	0.14085	0.24418
9	2.1278	1.9228	0.024918	0.044253	0.3192	0.348	0.13759	0.24595
10	2.0963	1.8872	0.023485	0.042977	0.3217	0.3502	0.14413	0.2326
11	2.2971	1.8963	0.023643	0.043501	0.324	0.3524	0.14229	0.23723
12	2.2875	1.9079	0.025415	0.043097	0.3262	0.3546	0.13571	0.23626
13	2.2649	1.8761	0.023997	0.043659	0.3284	0.3567	0.14634	0.24085
14	2.2925	2.0481	0.026349	0.045746	0.3306	0.3589	0.15113	0.25527
15	2.3271	1.9957	0.025914	0.046011	0.3329	0.3611	0.144	0.23809
16	2.2248	2.0586	0.025112	0.043486	0.3352	0.3634	0.13999	0.24515
17	2.3216	1.979	0.026494	0.043216	0.3377	0.3657	0.15386	0.24933
18	2.3342	2.0391	0.027054	0.047051	0.3404	0.3683	0.15286	0.25452
19	2.2531	1.9875	0.026049	0.04503	0.3434	0.3712	0.15393	0.24353
20	2.4072	1.9906	0.026678	0.045265	0.3469	0.3746	0.15548	0.2616
21	2.2898	2.1055	0.026011	0.046563	0.3515	0.3788	0.14644	0.24874
22	2.4714	2.1813	0.027006	0.048108	0.3584	0.3852	0.15626	0.25281
23	2.5275	2.1051	0.028063	0.048223	0.3629	0.3895	0.15822	0.27254
24	2.4492	2.1438	0.027996	0.047939	0.3664	0.3926	0.164	0.26428
25	2.5653	2.1993	0.028263	0.049002	0.372	0.3977	0.1644	0.27099

A.2.2 Male arm model parameters

Table XXXIV: Male arm model parameters. The subscripts M, I, L, and CM represent the mass, inertia, length, and center of mass properties of the links respectively.

Model	$L1_M$ (kg)	$L2_M$ (kg)	$L1_I$ (kgm)	$L2_I$ (kgm)	$L1_L$ (m)	$L2_L$ (m)	$L1_{CM}$ (m)	$L2_{CM}$ (m)
1	2.0927	1.9093	0.025312	0.044252	0.3226	0.35	0.14742	0.24478
2	2.273	2.0074	0.024041	0.043286	0.3264	0.354	0.14622	0.25183
3	2.2308	1.9187	0.025789	0.042627	0.3289	0.3566	0.13676	0.25351
4	2.1767	2.0188	0.025251	0.043089	0.3323	0.3605	0.14319	0.23657
5	2.3599	2.0926	0.02635	0.044291	0.3378	0.3667	0.14017	0.25332
6	2.3956	2.0048	0.026943	0.046643	0.3416	0.3711	0.14215	0.24417
7	2.4033	2.0821	0.026188	0.045251	0.3447	0.3746	0.15499	0.24528
8	2.3545	2.1444	0.025443	0.04526	0.3475	0.3777	0.14838	0.25971
9	2.4506	2.0391	0.027266	0.0452	0.35	0.3805	0.15737	0.25592
10	2.4445	2.1064	0.026705	0.045751	0.3524	0.383	0.16005	0.25657
11	2.5118	2.1084	0.027211	0.046906	0.3547	0.3855	0.14869	0.26759
12	2.4801	2.1926	0.027206	0.046529	0.357	0.3879	0.15213	0.26525
13	2.4607	2.2236	0.027666	0.047891	0.3592	0.3903	0.15099	0.27486
14	2.376	2.1154	0.027347	0.049553	0.3615	0.3927	0.15688	0.26849
15	2.5556	2.2143	0.028256	0.047299	0.3639	0.3951	0.15734	0.27168
16	2.4855	2.154	0.027898	0.047247	0.3663	0.3977	0.16086	0.28086
17	2.6002	2.2764	0.029008	0.049458	0.3689	0.4003	0.15882	0.26772
18	2.5377	2.2501	0.029625	0.048177	0.3718	0.4032	0.15626	0.28306
19	2.6229	2.3078	0.02913	0.049724	0.375	0.4065	0.15649	0.2777
20	2.604	2.3035	0.028473	0.052001	0.3787	0.4104	0.16623	0.28272
21	2.5868	2.3068	0.029151	0.051466	0.3835	0.4152	0.17203	0.2781
22	2.6388	2.2517	0.029768	0.050325	0.3906	0.4225	0.17384	0.27789
23	2.7885	2.3546	0.031264	0.05179	0.3951	0.4274	0.17818	0.28889
24	2.7952	2.4405	0.030707	0.054772	0.3983	0.4311	0.17222	0.29668
25	2.6735	2.3162	0.030274	0.054499	0.4033	0.437	0.18134	0.2922

APPENDIX B

Extremum Seeking Control - Application Example

An application example is presented below to provide a better understanding of Extremum Seeking Control (ESC) performance. Considering the following function:

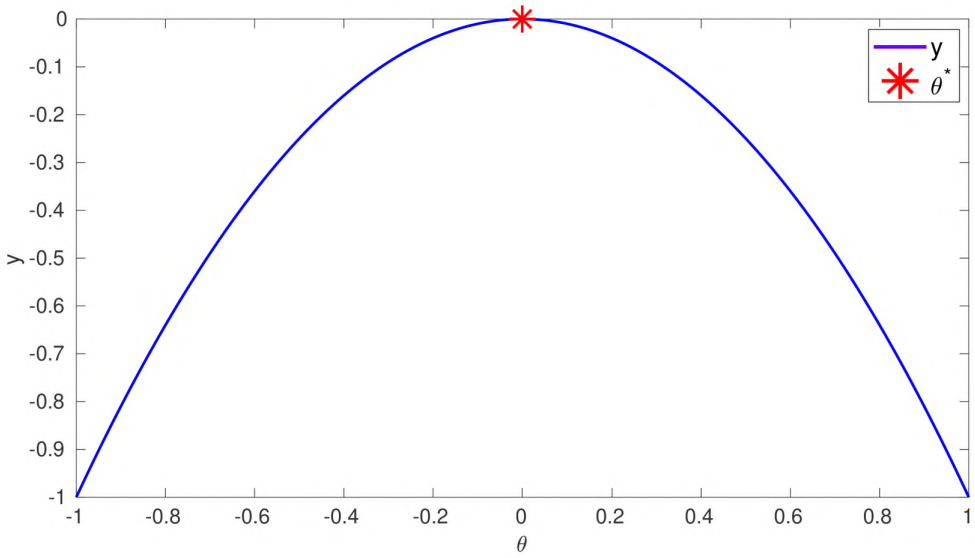

Figure 127: Performance output of the function $y(\theta) = -\theta^2$.

$$y(\theta) = -\theta^2, \tag{B.1}$$

with its maximizer at $\theta^* = 0$ (see Figure 127), the variable θ is derived as follows:

$$\theta = \hat{\theta} + a\sin(\omega t) \tag{B.2}$$

where $\hat{\theta}$ is the estimated theta and $a\sin(\omega t)$ is the input perturbation.

For this example, an input perturbation with an amplitude and frequency of $a = 0.1$ and $\omega = 10$ Hz respectively was used.

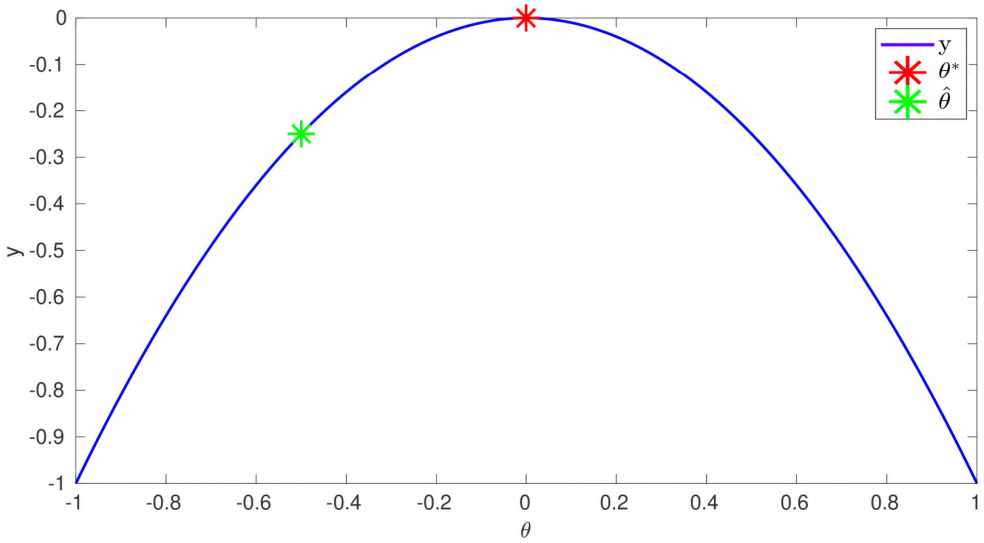

Figure 128: Estimated variable ($\hat{\theta} < \theta^*$) on the performance output.

Considering that the estimated variable is $\hat{\theta} = -0.5$ (see Figure 128), the variable θ and the output y respect to time can be seen in Figure 129.

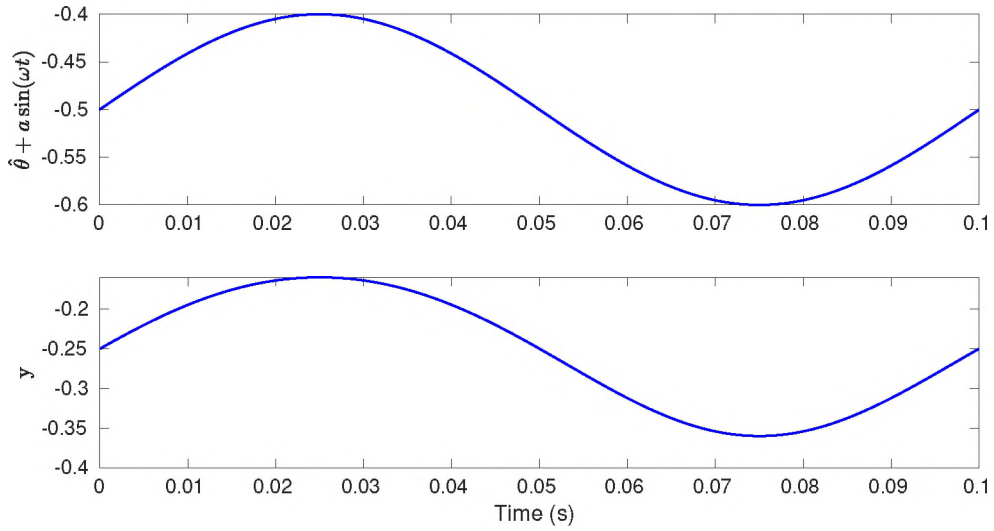

Figure 129: Parameterized variable (θ) and performance output.

Figure 129 shows that both variables, θ and y, are in phase. Thus, by applying a zero-mean normalization by using a high-pass filter, and then, by multiplying both variables, a common-sign result is obtained.

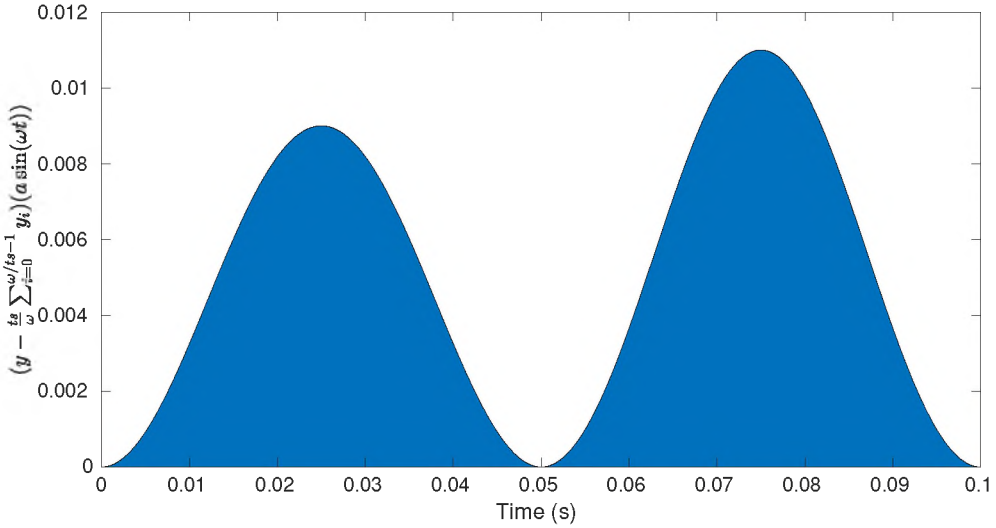

Figure 130: Result of $\theta(y)$ for $\hat{\theta} > \theta^*$.

In this example, the result from the previous multiplication became positive, thus, after integrating it, a positive result is obtained (see Figure 130). This positive

number makes the estimated variable $\hat{\theta}$ increased proportionally to the k gain variable in direction to θ^*.

Analogously, on the case of the estimated variable be $\hat{\theta} = 0.5$ (see Figure 131), the variable θ (Eq. B.2) and the output (y) would be out of phase by π. Therefore, the result from the multiplication between these two variables would produce a negative signal (see Figure 132). The resulted from the integration of this signal would make that the estimated variable $\hat{\theta}$ decrease in direction to θ^*.

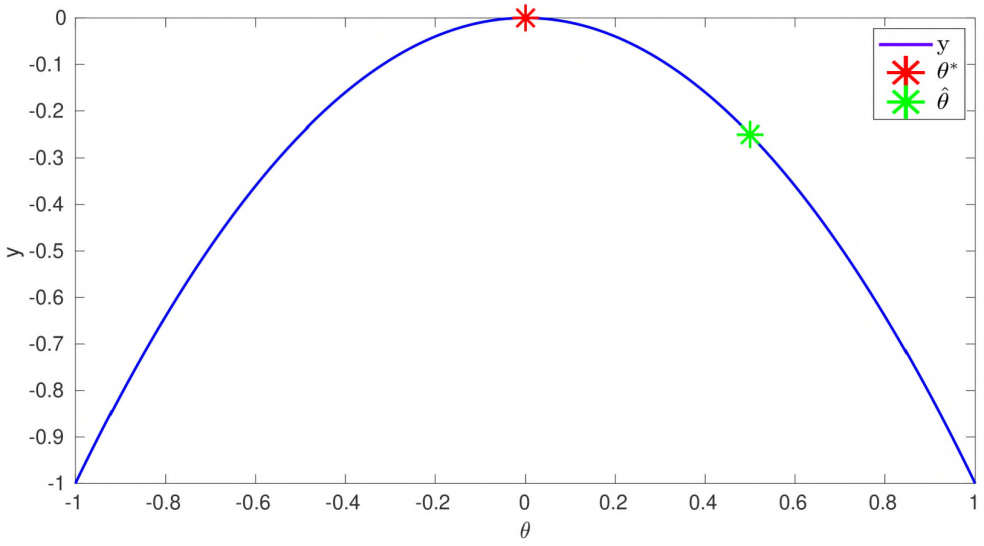

Figure 131: Estimated variable ($\hat{\theta} > \theta^*$) on the performance output.

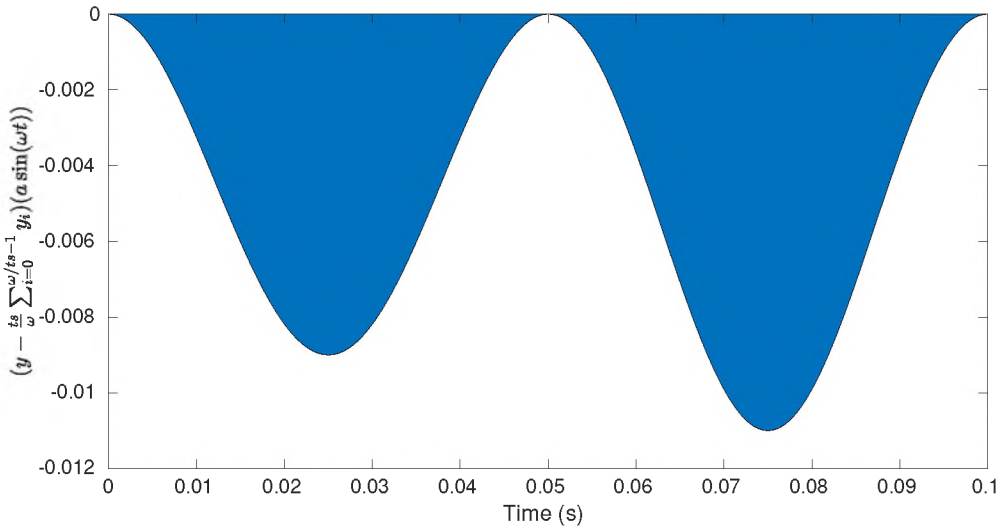

Figure 132: Result of $\theta(y)$ for $\hat{\theta} < \theta^*$.

In the case of seeking minimization, the k gain variable should be negative. Its negative value would force the system to go in the opposite direction of the maximizer.

APPENDIX C

Multi-variable Methodology Comparison

These simulations have been performed to evaluate the performances of these methods by minimizing the following cost:

$$\min_{u_1,u_2} \quad f^* + w(1)(u_1 - u^*(1))^2 + w(2)(u_2 - u^*(2))^2, \tag{C.1}$$

To make an impartial evaluation, each of the methods was tested under the same conditions (same parameter configurations). These parameters can be seen in Table XXXV.

Table XXXV: Simulation parameters.

Variable	Description	Value
ts	Sample time (fixed)	$5(10^{-4})$ s
u_0	Initial input conditions	$[2, 2]$
$u*$	Optimal values	$[1, 1.5]$
Γ_0	Initial estimator condition	$\begin{bmatrix} 0.001 & 0 \\ 0 & 0.001 \end{bmatrix}$
f^*	Optimal cost	2
w	Weight vector	$[2, 2]$
a	Amplitude of perturbations	0.01
k	Gain	-10
ω_1	Frequency of the first perturbation	10
ω_2	Frequency of the second perturbation	40
ω_h	Frequency of the high pass filter	1
ω_r	Frequency of the derivative filter	0.01

C.1 Results - Multi-variable perturbation-based ESC

The first plot (Figure 133) shows the cost function for the perturbation-based method. The time of convergence seems to be close to 1200 seconds, however, Figure 134 evidence that the convergence time is longer for both variables (close to 1800 seconds).

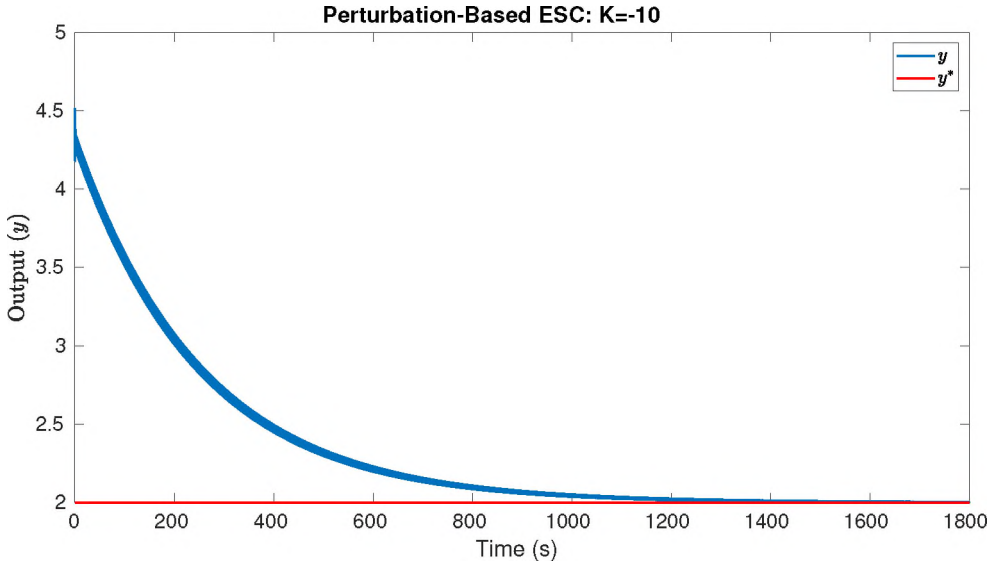

Figure 133: Cost function for the multi-variable perturbation-based with gain $K = -10$.

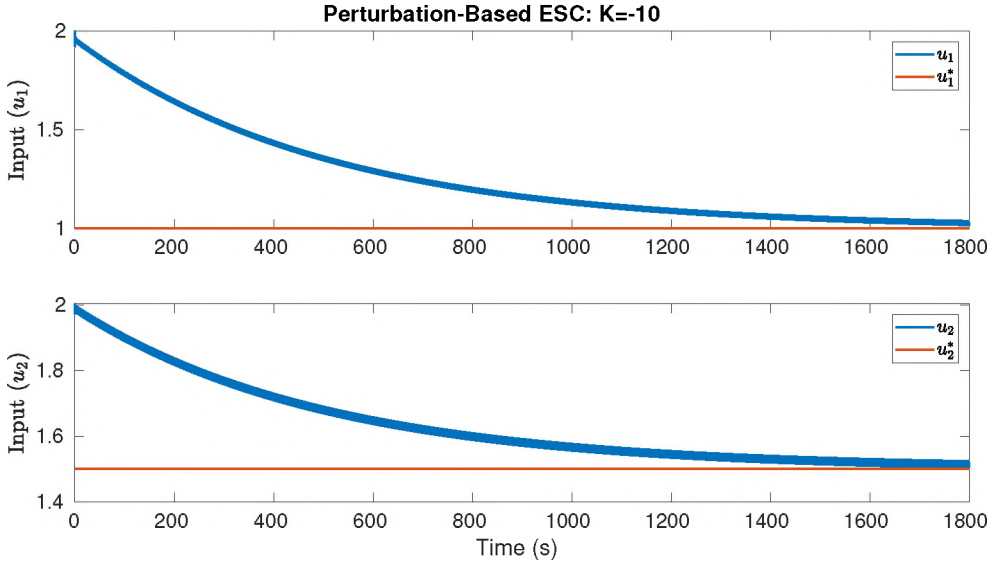

Figure 134: Solution convergence for the multi-variable perturbation-based with gain $K = -10$.

One of the biggest advantages of the multi-variable perturbation-based method is its robustness. The same parameters previously used were also simulated but changing only the gain variable (K) from -10 to -500. Figure 135 and Figure 136 show the very high speed of convergence (about 25 seconds for both variables).

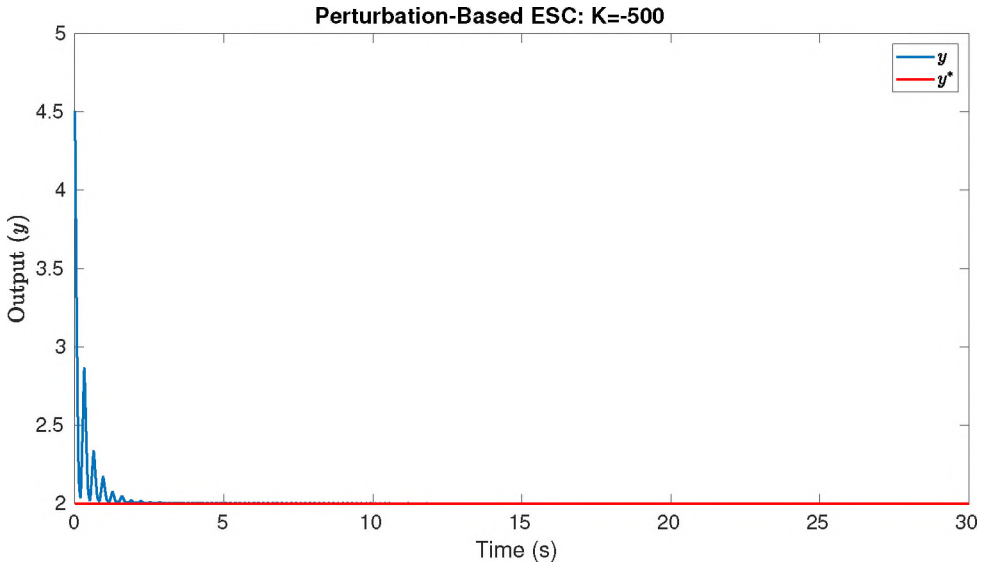

Figure 135: Cost function for the multi-variable perturbation-based with gain $K = -500$.

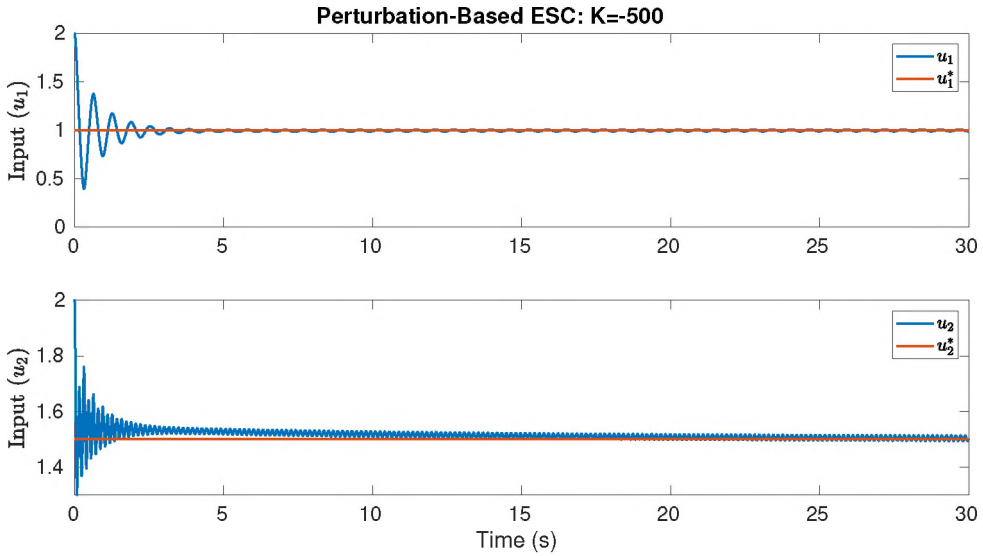

Figure 136: Solution convergence for the multi-variable perturbation-based with gain $K = -500$.

C.2 Results - Newton-based ESC

For the case of the Newton-based, Figure 137 and 138 show faster convergence with respect to the perturbation-based under the same parameters (about 120 seconds). This fact confirms the big advantage of Newton-based respect to the perturbation-based related to the convergence speed. However, the biggest disadvantage of this approach is its lack of robustness. To make this approach work depends on the guessing of several parameters. Furthermore, these parameters are very sensitive. Therefore, small variations could produce a much better performance as easily as break the controller loop.

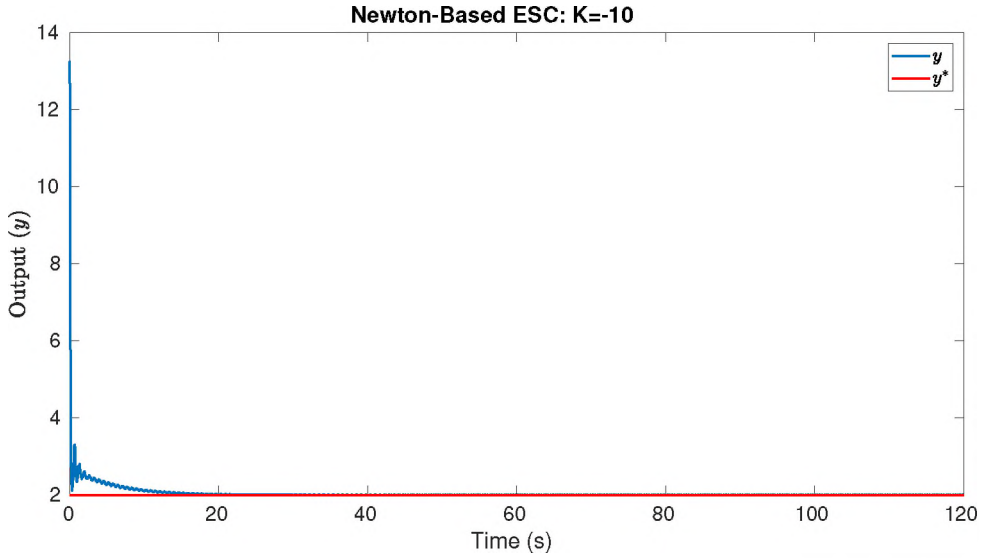

Figure 137: Cost function for the Newton-based with gain $K = -10$.

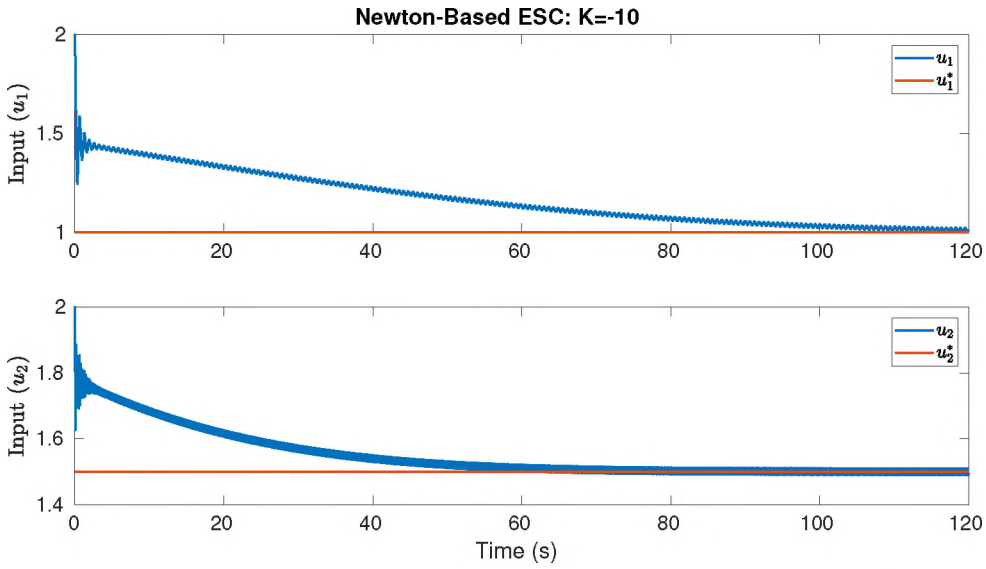

Figure 138: Solution convergence for the Newton-based with gain $K = -10$.

C.3 Discussion

Some advantages and disadvantages of each of the approaches have been seen in these simulations. On the one side, the perturbation-based approach proved to be more robust by providing a good performance against any cost function and by using any combination of configuration parameters. On the other hand, the Newton-based approach proved to be faster (up to 15 times faster under the same configuration parameters) but highly unstable. It is important to highlight that during these simulation tests, this Newton-based method worked by using a very limited range of configuration parameters showing to be very sensitive to the parameter selection. Thus, despite being a model-free approach, this methodology requires good parameter guesses which are not possible under this research environment involving highly nonlinear dynamics from the human body.

Finally, during these early stages of experimentation, the stability and robustness of the system represent the most important factors in the selection of the

methodology because they are strictly related to the safety of the training environment. Other factors such as the computational cost and processing time can always be part of improvements and future research, so they do not represent part of our design requirements. For those reasons, it was decided to use the multi-variable perturbation-based ESC for this research.

APPENDIX D

Informed Consent Form for Training with a Powered Rowing Machine

Introduction

My name is Kevin Kleis and I am inviting you to participate in a research study that I am conducting for my Master's Thesis in the Human Performance Laboratory at Cleveland State University. The research study will be conducted under the supervision of Dr. Kenneth Sparks and Dr. Douglas Wajda, and partnered with the Mechanical Engineering Department at CSU. The purpose of my thesis is to examine the effects of varying eccentric workloads on muscular contraction and metabolic cost. Please read all sections carefully and understand the testing protocol, as the informed consent is very important in helping you decide if you would like to participate in the study.

Procedures

Testing will include two sessions on the powered rower and one session gathering maximal isometric contraction data of predetermined muscle groups. Before beginning tests, height, age, and weight will be collected to be entered into the COSMED K4b2. Rowing sessions will include a full body row and lower body row on a powered rower machine (adapted from the Concept 2 model) that was designed in the mechanical

engineering department of Cleveland State University. The type of rowing (low vs. full) will be randomized to prevent and order effect. Before beginning the tests, you will have eight electromyography (EMG) sensors placed on selected muscles. A Polar heart rate sensor will also be worn. Next, the COSMED K4b2 will be attached through a harness to collect metabolic data while rowing.

Once all equipment is on, you will have a two-minute warm-up period to prepare for the test. Following the two-minute warm-up period, two minutes of resting data will be collected. Next, when instructed to start, you will begin a twelve-minute session in which every three minutes, the power rower eccentric workload will be increased.

During this time, there will be a cadence provided for you to follow in order to control the speed of the exercise.

Risks and Discomforts

Risks of this test are minimal and do not exceed those of a standard exercise session. Possible risks and discomforts could be muscle strain and soreness from the powered rower testing. Other potential risks that may arise from exercise include abnormal heart rate and/or blood pressure, fainting, and in rare cases, heart attack, stroke, or death.

Every effort will be made to minimize potential risks through a proper warm-up prior to testing. In addition, you must have no physical limitations that prevent you from participating in regular exercise. In an event that you are injured, please notify the research team as soon as possible and seek medical attention from you primary physician.

Benefits

There are no direct benefits to you from this investigation. The results of this research will help exercise and engineering professionals in the improvement and design of exercise machines for space travel and rehabilitation.

Privacy and Confidentiality

To ensure that all information is confidential, your data will be kept in a folder and stored in a secure file in the CSU Human Performance Laboratory where only the researchers will have access. Your name will not be used in any publications of this research to ensure confidentiality. However, data obtained from this study may be used for statistical or scientific purposes to benefit future research with your right of privacy retained.

Participation

I understand that participation in this study is voluntary and that I have the right to withdraw myself at any time with no consequences.

If I have any questions about my rights as a subject, I understand that I can contact the Cleveland State University Institutional Review Board at (216) 687-3630.

If I have any questions regarding the procedures, I can contact Dr. Kenneth Sparks at (216) 687-4831 or Graduate Student Kevin Kleis at (440) 429-5110 or kleis.kevin@yahoo.com.

Acknowledgement

The purpose, procedures, risks and discomforts and possible benefits have been explained to me. I attest that I am 18 years of age, understand this form, and agree to participate in the study. I have been given a copy of this informed consent form.

Participant Signature: _____ **Date:** _____

Witness Signature: _____ **Date:** _____

APPENDIX E

Informed Consent Form for Training with Cyber Exercise Machines

Introduction

My name is Humberto De las Casas and I am inviting you to participate in a research study that I am conducting for my PhD's Dissertation in the Center for Human-Machine Systems (CHMS) at Cleveland State University. The purpose of my study is to examine the feasibility of the automatic regulation of the robot parameters able to optimize muscle activations using them as biofeedback. Please read all sections carefully and understand the testing protocol, as the informed consent is very important in helping you decide if you would like to participate in the study.

Procedures

Testing will include 3 sessions performed on different days. Before beginning tests, some measurements will be performed (see Table XXXVI). The experimental procedure begins with a conventional calibration process. This calibration consists of warm-up and isometric tests. The warm-up process is to boost flexibility and performance, meanwhile, the isometric tests to assess muscle strength for the EMG sensor calibration. For the isometric tests, the subject moves to multiple fixed positions where muscles are capable to produce maximum forces. Then, the experiment pro-

ceeds with the real-time optimization frameworks. One session will be performed by using a single-variable optimization framework for the automatic regulation of the trajectory parameter associated with the ellipsoidal curve orientation. The other will be performed by using a single-variable optimization framework for the automatic regulation of the impedance associated with the resistance of the training. And the last one will be performed by using a multi-variable optimization framework for the automatic and simultaneous regulation of the trajectory and impedance parameters previously described.

Table XXXVI: Subject measurements.

Variable	Description
Height	In centimeters
Weight	In kilograms
Gender	Male (M) or female (F)
Age	In years
Side dominant	Left (L), right (R), or both (B)
Arm length	From shoulder to wrist

During each of the experiments, the subject requires to follow a desired position while receiving visual feedback from his or her current position (GUI can be seen on Figure. 139). This GUI consists of 4 curves and 2 dots. The black curve represented the reference trajectory which is tracked by the robot in the absence of an external force. The blue curve represented the ellipsoidal trajectory of fixed axis lengths and programmable orientation to be followed by the user. The 2 red dashed line curves represented the tolerance limits where the subject position is suggested to remain during the performance of the experiments. The 2 dots represent the desired and the actual positions. The desired position (rotating periodically over the blue ellipsoidal trajectory) is labeled with the black dot. The actual position defined by the end-effector of the robot (user's position) is labeled with the red dot. The user position (red dot) is required to track the desired position (black dot) as best as possible while

remaining within the tolerance limits.

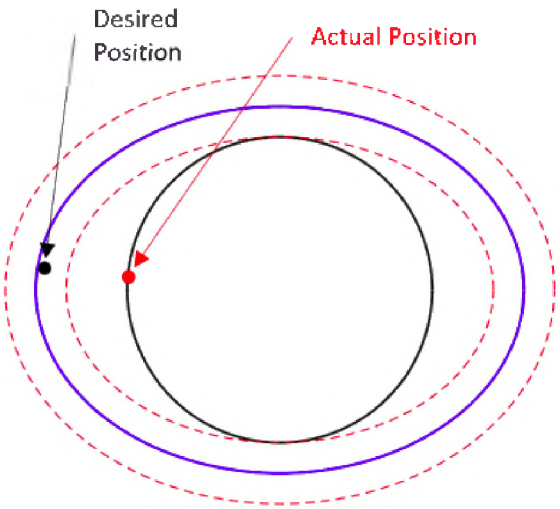

Figure 139: GUI for the experiments.

Risks and Discomforts

Risks of this test are minimal and do not exceed those of a standard exercise session. Possible risks and discomforts could be muscle strain and soreness from the testing. Every effort will be made to minimize potential risks through a proper warm-up prior to testing. In addition, you must have no physical limitations that prevent you from participating in regular exercise. In an event that you are injured, please notify the research team as soon as possible and seek medical attention.

Benefits

There are no direct benefits to you from this investigation. The results of this research will help exercise and engineering professionals in the improvement and design of exercise machines for space travel and rehabilitation.

Privacy and Confidentiality

To ensure that all information is confidential, your data will be kept in a folder and stored in a secure file in the CSU Human Performance Laboratory where only the researchers will have access. Your name will not be used in any publications of this research to ensure confidentiality. However, data obtained from this study may be used for statistical or scientific purposes to benefit future research with your right of privacy retained.

Participation

I understand that participation in this study is voluntary and that I have the right to withdraw myself at any time with no consequences. If I have any questions about my rights as a subject, I understand that I can contact the Cleveland State University Institutional Review Board at (216) 687-3630.

If I have any questions regarding the procedures, I can contact Humberto De las Casas at h.delascasas@pucp.pe or (216) 804-6434 or Dr. Hanz Richter at h.richter@csuohio.edu.

Acknowledgement

The purpose, procedures, risks and discomforts and possible benefits have been explained to me. I attest that I am 18 years of age, understand this form, and agree to participate in the study. I have been given a copy of this informed consent form.

Participant Signature: _____ **Date:** _____

Witness Signature: _____ **Date:** _____

APPENDIX F

Muscle Activations in training with the 4OptimX

Muscle activations encountered during training with the 4OptimX are presented below. These muscle activations are related to training with different configurations of impedance and trajectory.

Muscle Activation - Low Impedance and Slow Trajectory

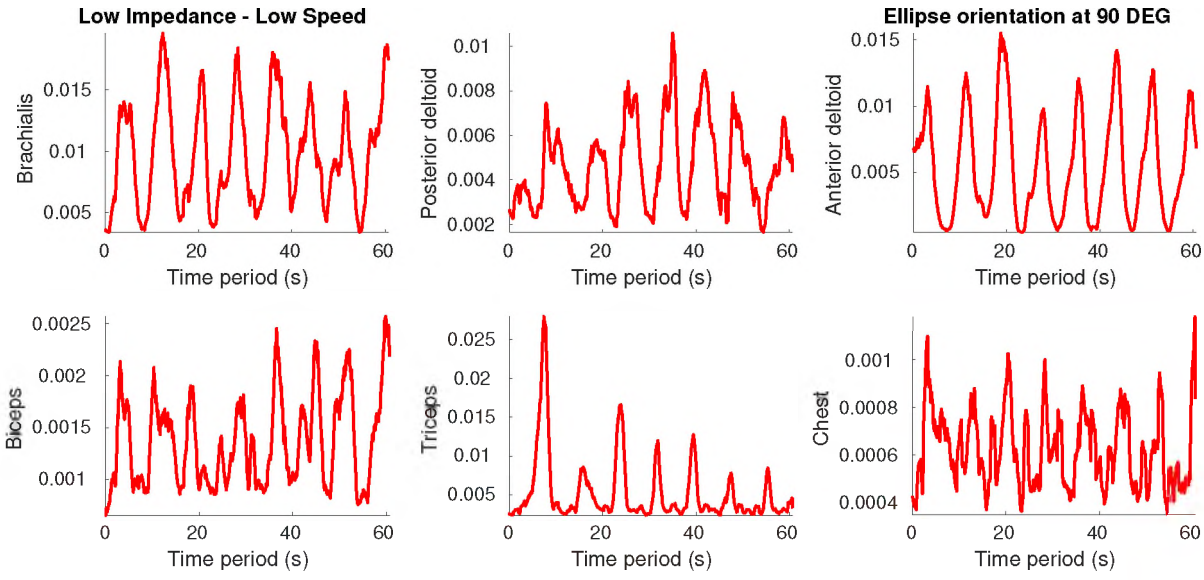

Figure 140: Muscle activation during training with low impedance and slow ellipsoidal trajectory oriented at 90 degrees.

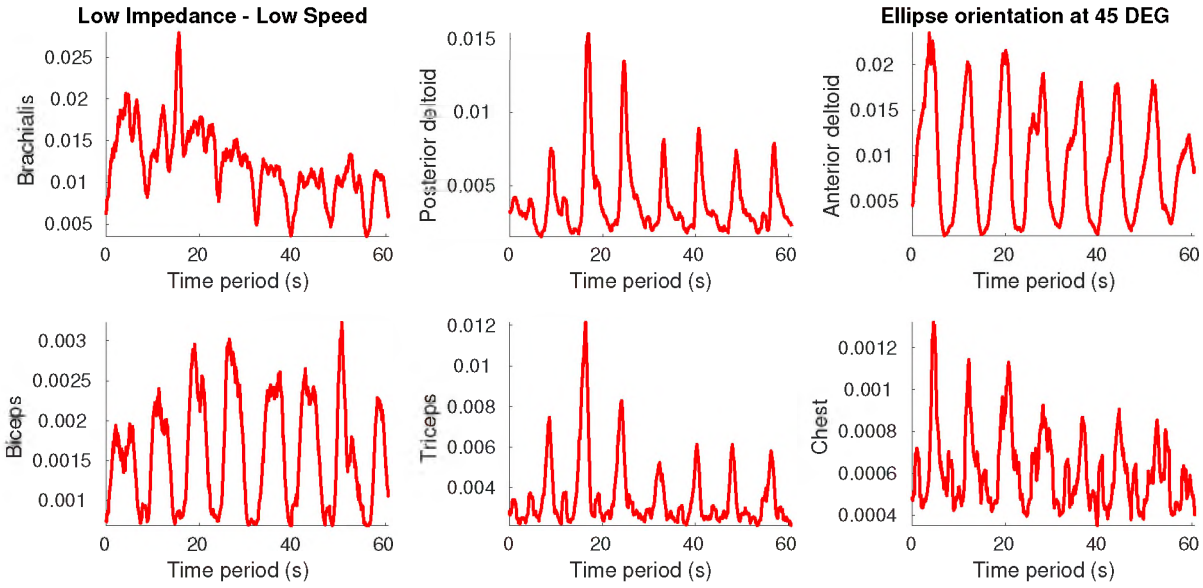

Figure 141: Muscle activation during training with low impedance and slow ellipsoidal trajectory oriented at 45 degrees.

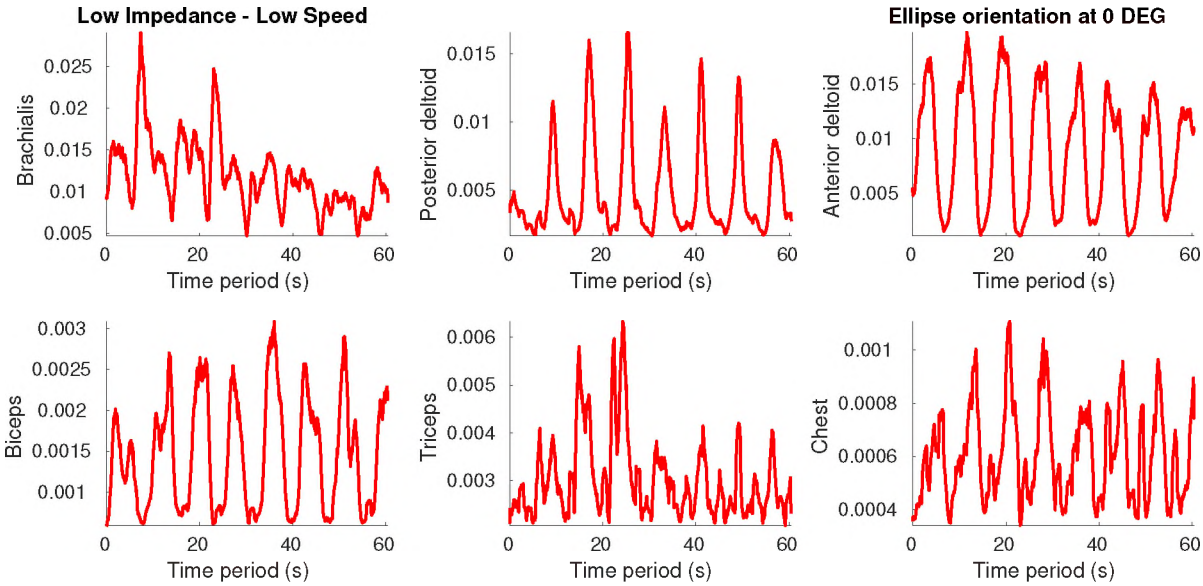

Figure 142: Muscle activation during training with low impedance and slow ellipsoidal trajectory oriented at 0 degrees.

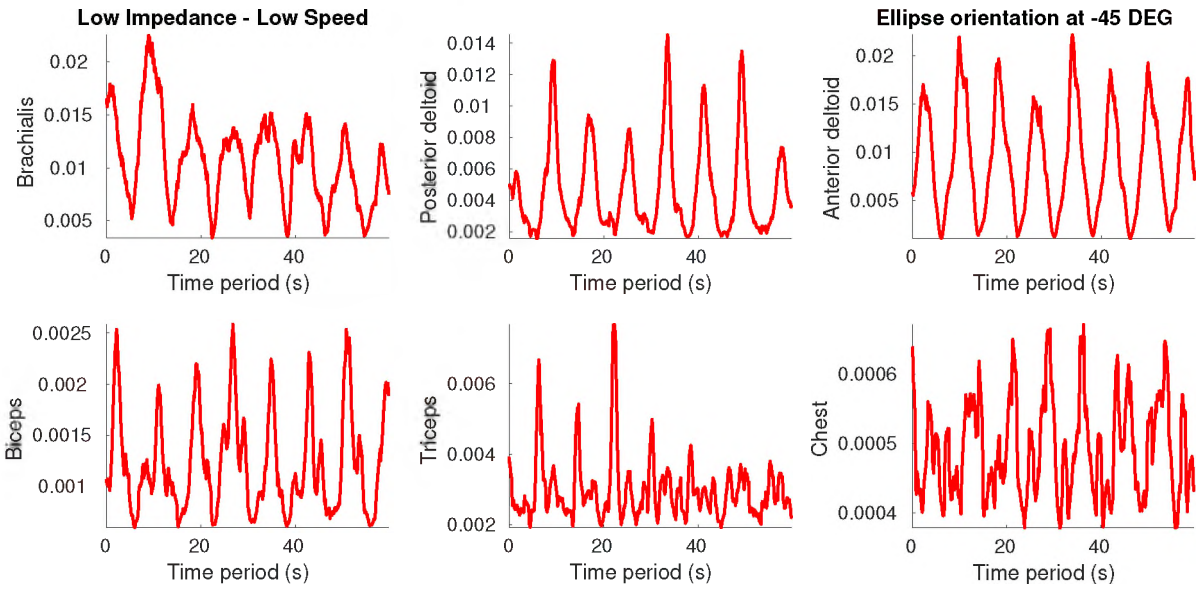

Figure 143: Muscle activation during training with low impedance and slow ellipsoidal trajectory oriented at -45 degrees.

Muscle Activation - Low Impedance and Fast Trajectory

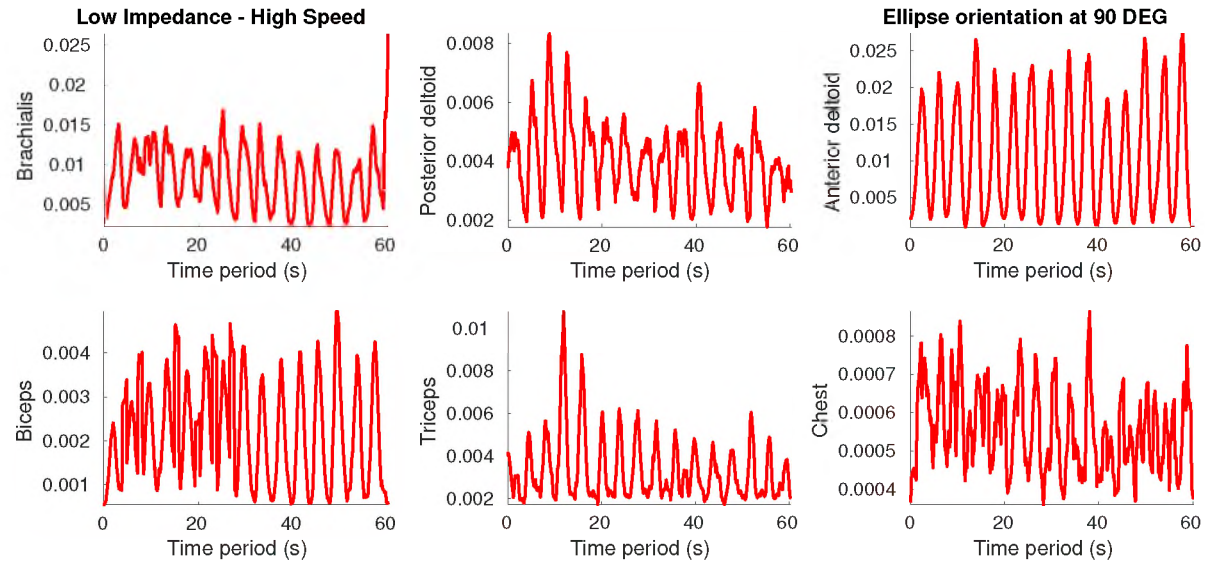

Figure 144: Muscle activation during training with low impedance and fast ellipsoidal trajectory oriented at 90 degrees.

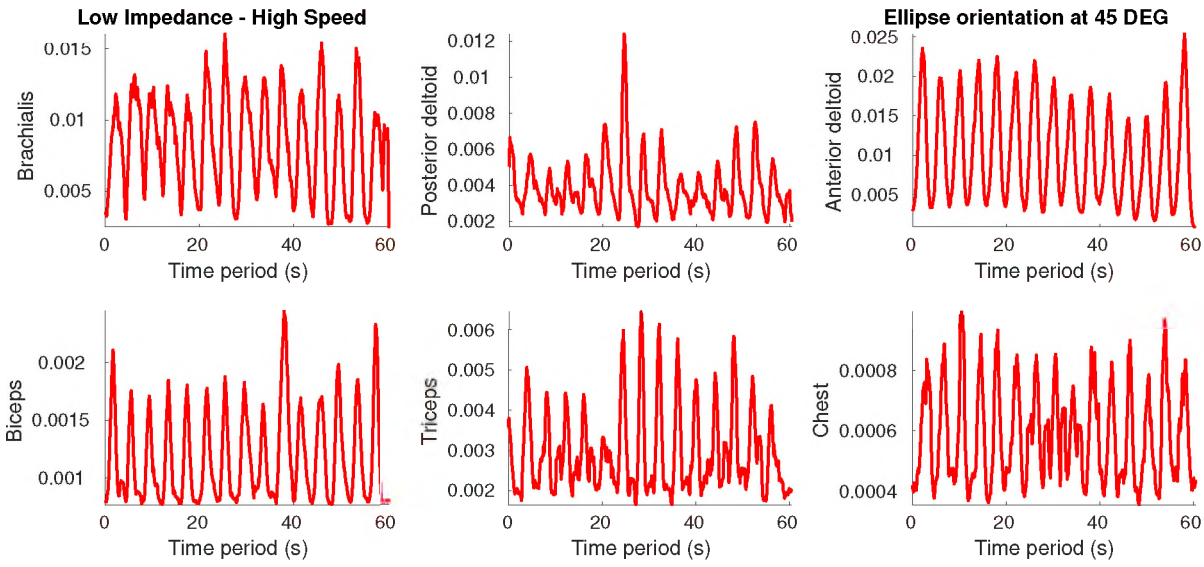

Figure 145: Muscle activation during training with low impedance and fast ellipsoidal trajectory oriented at 45 degrees.

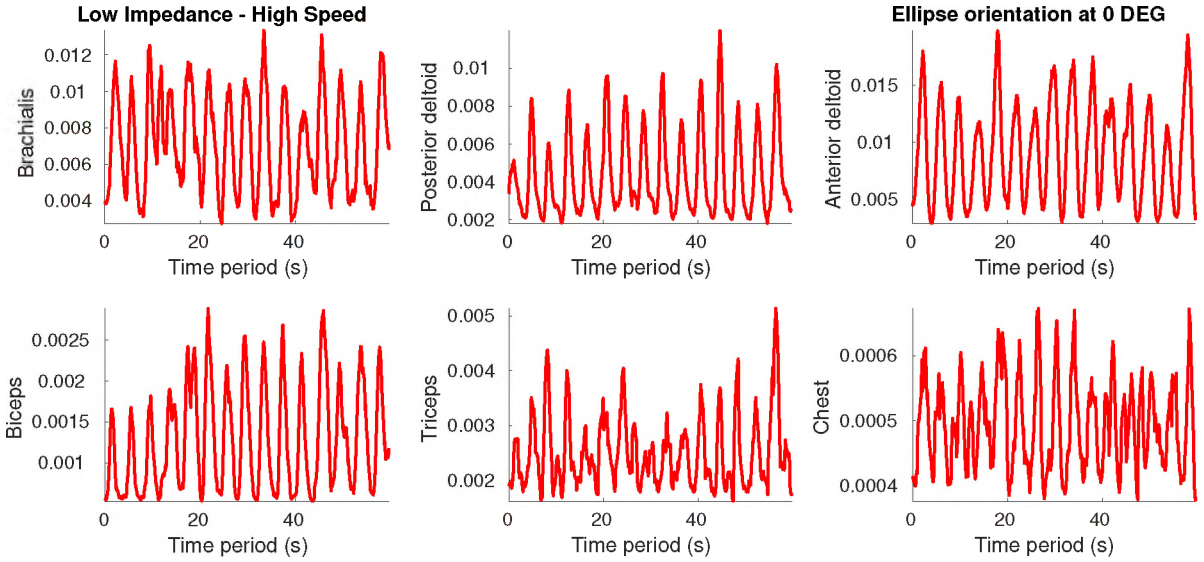

Figure 146: Muscle activation during training with low impedance and fast ellipsoidal trajectory oriented at 0 degrees.

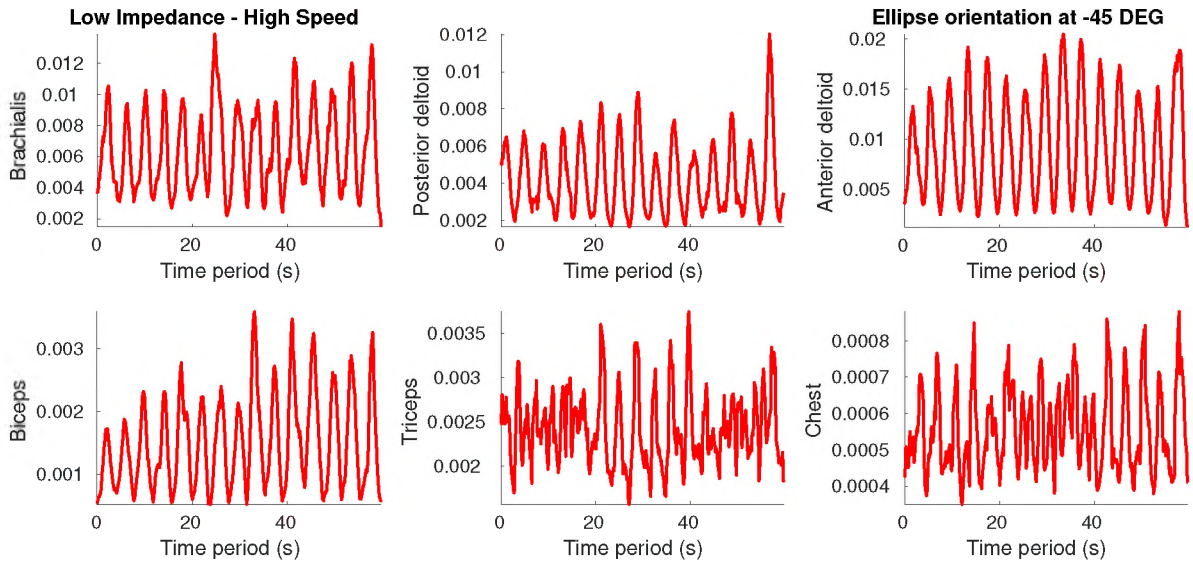

Figure 147: Muscle activation during training with low impedance and fast ellipsoidal trajectory oriented at -45 degrees.

Muscle Activation - High Impedance and Slow Trajectory

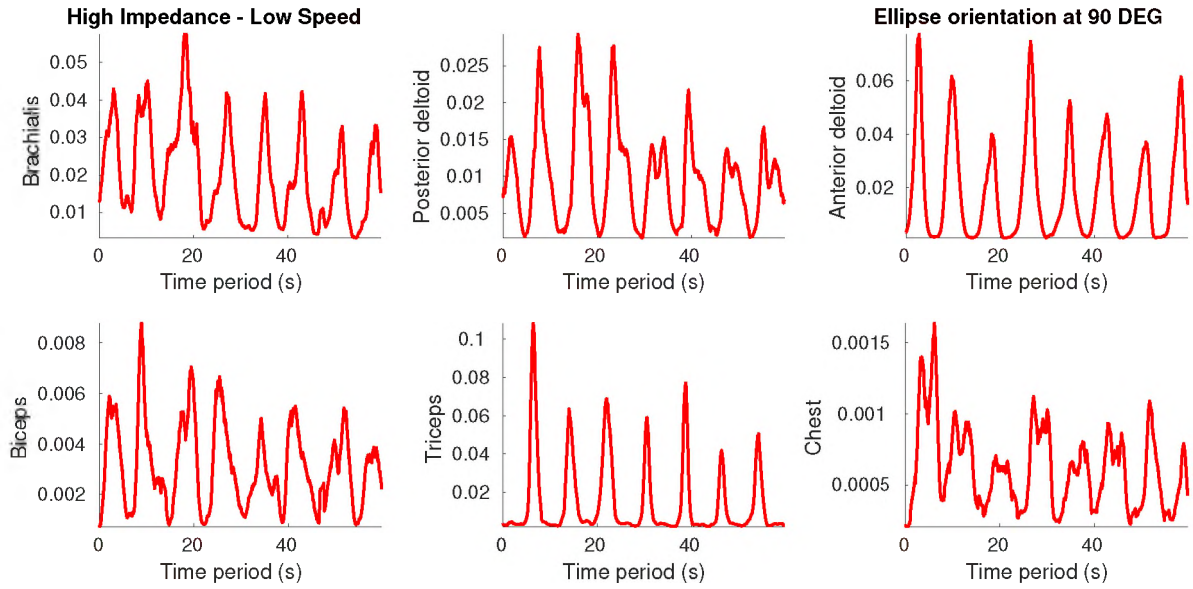

Figure 148: Muscle activation during training with high impedance and slow ellipsoidal trajectory oriented at 90 degrees.

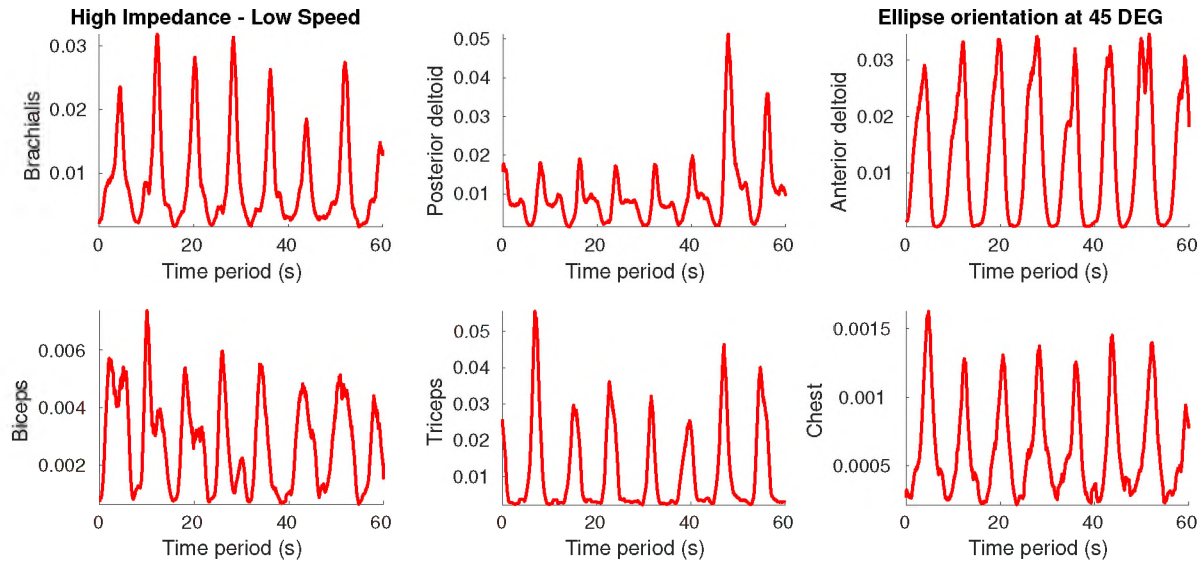

Figure 149: Muscle activation during training with high impedance and slow ellipsoidal trajectory oriented at 45 degrees.

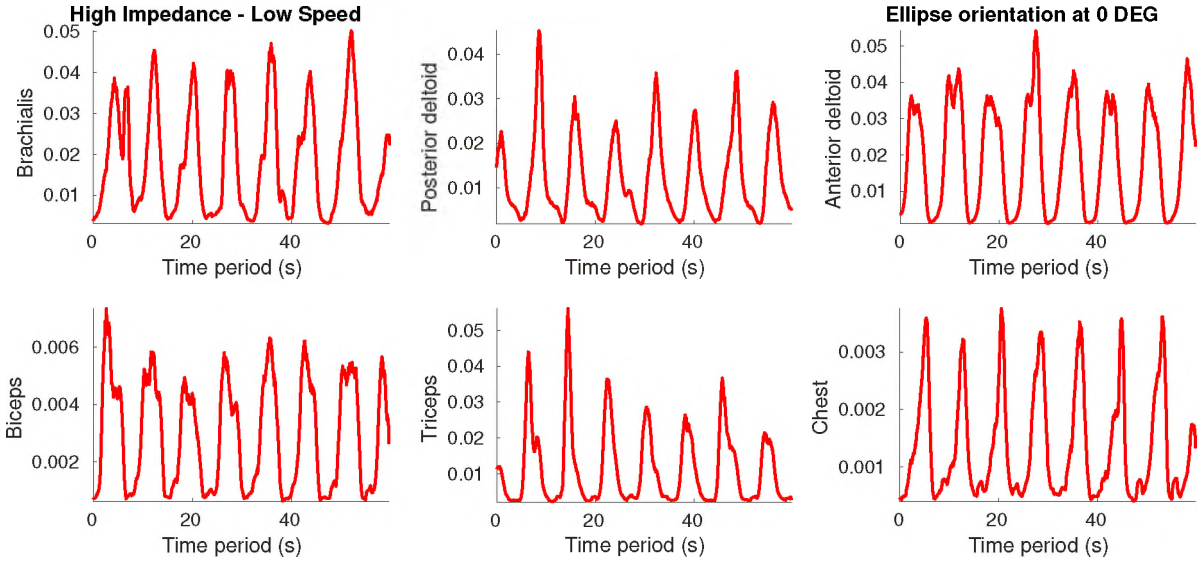

Figure 150: Muscle activation during training with high impedance and slow ellipsoidal trajectory oriented at 0 degrees.

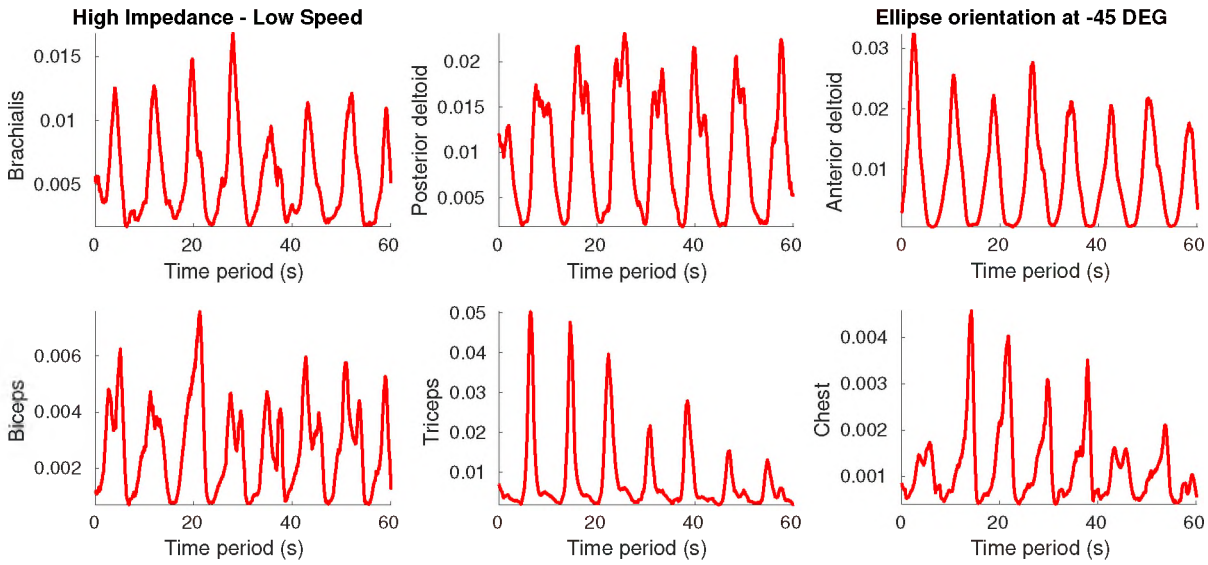

Figure 151: Muscle activation during training with high impedance and slow ellipsoidal trajectory oriented at -45 degrees.

Muscle Activation - High Impedance and Fast Trajectory

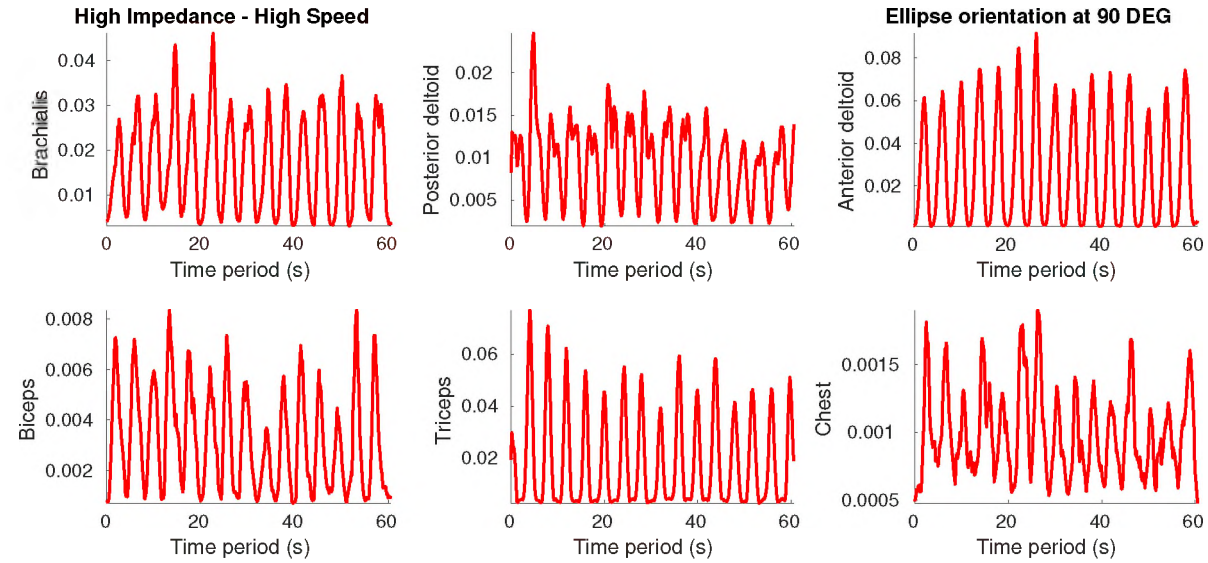

Figure 152: Muscle activation during training with high impedance and fast ellipsoidal trajectory oriented at 90 degrees.

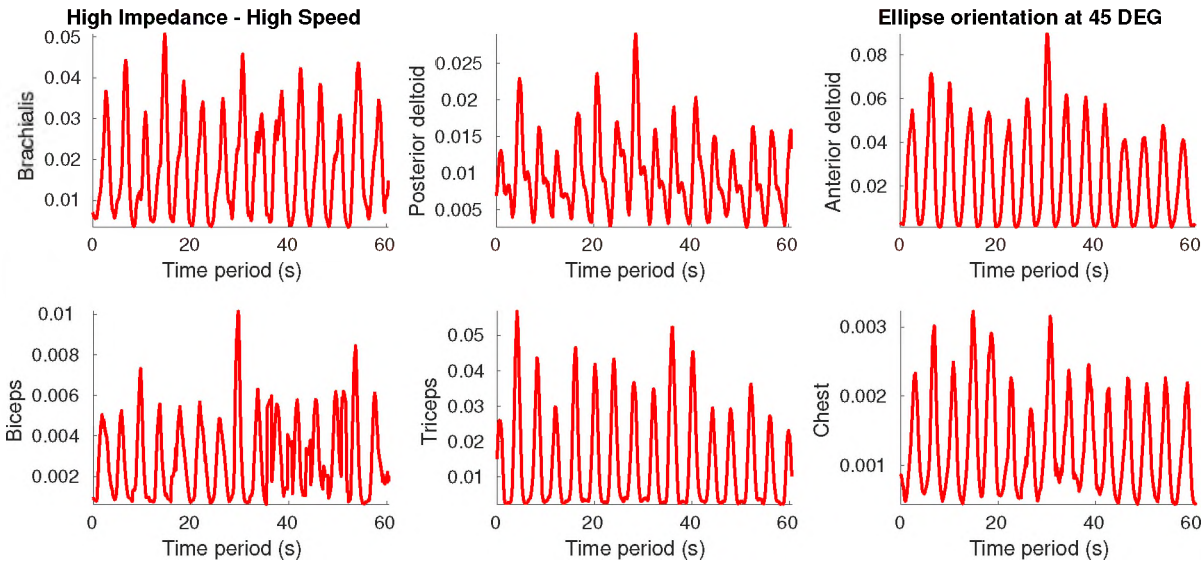

Figure 153: Muscle activation during training with high impedance and fast ellipsoidal trajectory oriented at 45 degrees.

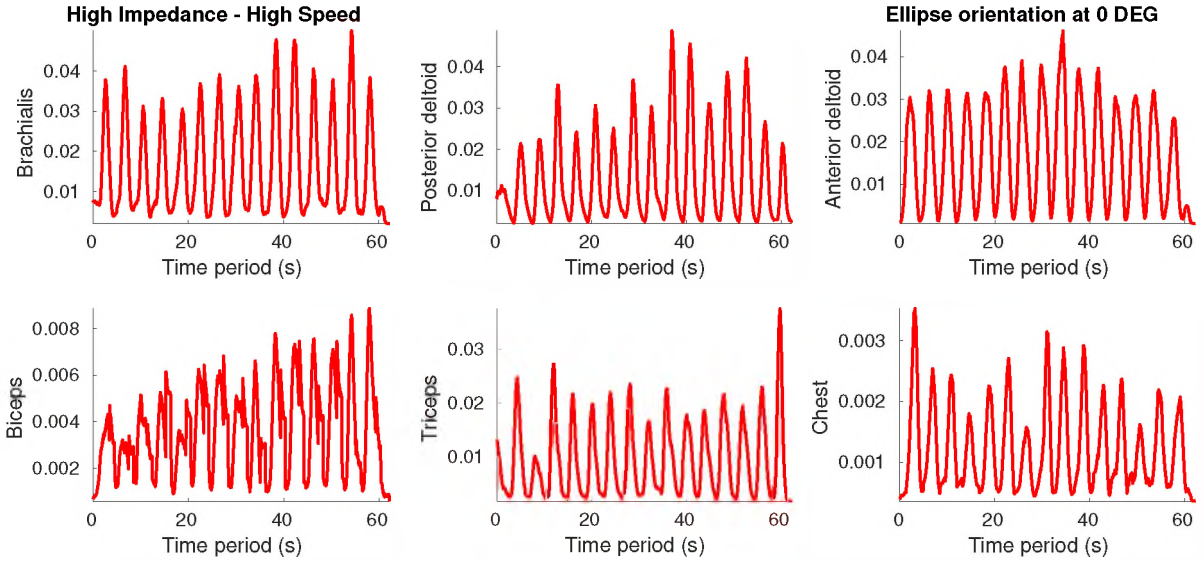

Figure 154: Muscle activation during training with high impedance and fast ellipsoidal trajectory oriented at 0 degrees.

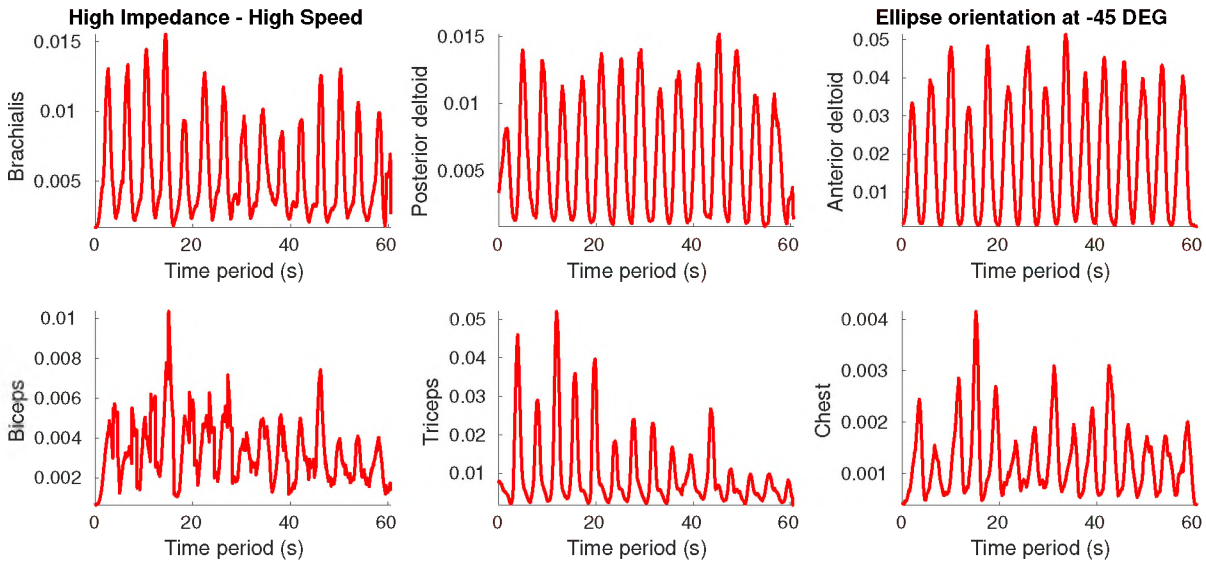

Figure 155: Muscle activation during training with high impedance and fast ellipsoidal trajectory oriented at -45 degrees.

Muscle Activation - Low Impedance and Super-Fast Trajectory

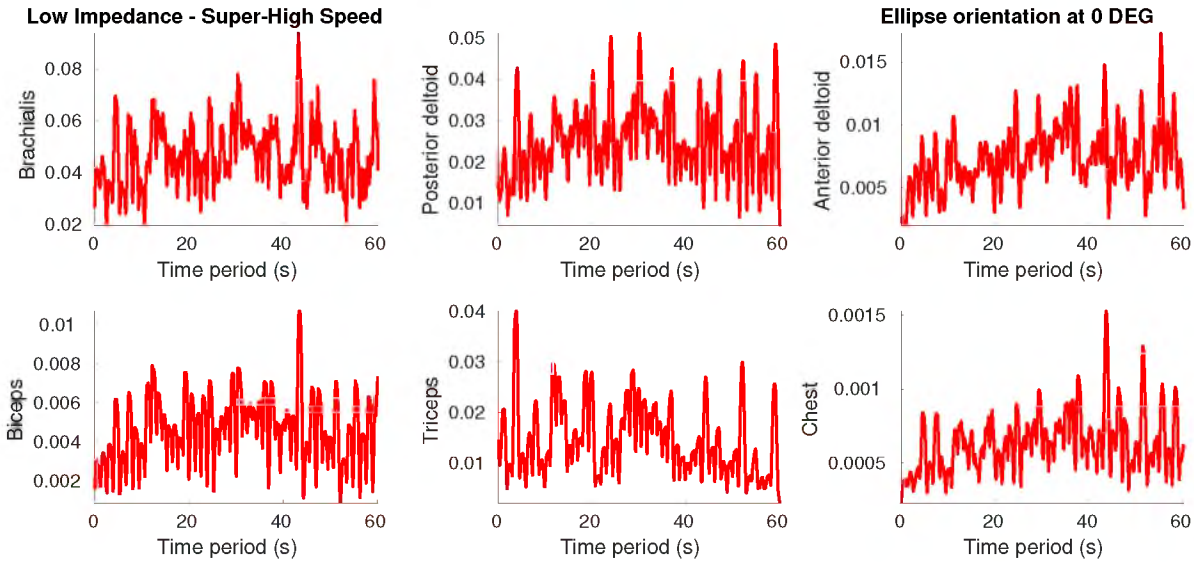

Figure 156: Muscle activation during training with low impedance and super-fast ellipsoidal trajectory oriented at 0 degrees.